R-01-45

Nuclear data for accelerator-driven transmutation

Annual report 2000/2001

Blomgren J, Johansson C, Klug J,
Olsson N, Pomp S, Renberg P-U

Department of Neutron Research
and The Svedberg Laboratory
Uppsala Unviersity

September 2001

SKB

Nuclear data for accelerator-driven transmutation

Annual Report 2000/2001

Blomgren J, Johansson C, Klug J,
Olsson N, Pomp S, Renberg P-U

Department of Neutron Research
and The Svedberg Laboratory
Uppsala University

September 2001

Contents

Appendices:

I. J. Blomgren, Charge-exchange giant resonances as probes of nuclear structure, Proceedings of IX Seminar on Electromagnetic Interactions of Nuclei at Low and Intermediate Energies, Moscow September 20-22, 2000. (Invited talk, in press.)

II. T. Peterson, L.C. Bland, J. Blomgren, W.W. Jacobs, T. Kinashi, A. Klyachko, P. Nadel-Turonski, L. Nilsson, N. Olsson, J. Rapaport, T. Rinckel, E.J. Stephenson, S.E. Vigdor, S.W. Wissink, Y. Zhou, Development of a Tagged Neutron Facility for Neutron Scattering Experiments at Intermediate Energies, *Proc. 15th Int. Conference on Particles and Nuclei (PANIC99), Uppsala, Sweden*, ed. G. Fäldt, B. Höistad and S. Kullander, Nucl. Phys. **A 663&664** (2000) 1057c.

III. T. Peterson for the TNT collaboration, Tagged Neutron Production with a Storage Ring, *Proceedings of 4th International Conference on Nuclear Physics at Storage Rings (STORI99), Bloomington, Indiana, September 12-16, 1999.* AIP conference proceedings **512** (2000) 235.

IV. P.-O. Söderman, J. Blomgren, A. Ringbom, N. Olsson, L. Nilsson, J.A. Bordewijk, S. Brandenburg, G. van 't Hof, M.A. Hofstee, H. van der Ploeg, S.Y. van der Werf, A. van der Woude, A. Krasznahorkay, A. Balanda, D. Chmielewska and H. Laurent, Neutron decay of deep hole states and isobaric analog states in ^{115}Sn populated by the (^{3}He,α) reaction at 102 MeV, Nucl. Phys. **A683** (2001) 79.

V. J. Rahm, J. Blomgren, H. Condé, K. Elmgren, N. Olsson, T. Rönnqvist, R. Zorro, A. Ringbom, G. Tibell, O. Jonsson, L. Nilsson, P.-U. Renberg, T.E.O. Ericson and B. Loiseau, np scattering measurements at 96 MeV, Phys. Rev. C **63** (2001) 044001.

VI. J. Thun, J. Blomgren, K. Elmgren, J. Källne, N. Olsson, J.F. Lecolley, F. Lefebvres, C. Varignon, F. Borne, X. Ledoux, Y. Patin, O. Jonsson, P.-U. Renberg, The response of a liquid scintillator detector to 21-100 MeV neutrons, accepted for publication in Nucl. Instr. Meth. **A**.

VII. J. Klug, The SCANDAL facility - how to measure elastic neutron scattering in the 50-130 MeV range, PhL thesis.

VIII. Notes from the OECD/NEA Nuclear Science Committee (NSC) meeting, Paris, France, 2001-06-11–13 (in Swedish).

1 Background

The present project, supported as a research task agreement by Statens Kärnkraftsinspektion (SKI), Svensk Kärnbränslehantering AB (SKB), Barsebäck Kraft AB (BKAB) and Vattenfall AB, started 1998-07-01. From 1999-01-01 the project also receives support from Totalförsvarets forskningsinstitut (FOI). The primary objective from the supporting organizations is to promote research and research education of relevance for development of the national competence within nuclear energy.

The aim of the project is in short to:

- promote development of the competence within nuclear physics and nuclear technology by supporting licenciate and PhD students,

- push forward the international research front regarding fundamental nuclear data within the presently highlighted research area "accelerator-driven transmutation",

- strengthen the Swedish influence within the mentioned research area by expanding the international contact network,

- constitute a basis for Swedish participation in the nuclear data activities at IAEA and OECD/NEA.

The project is run by the Department of Neutron Research (INF) at Uppsala University, and is utilizing the unique neutron beam facility at the national The Svedberg Laboratory (TSL) at Uppsala University.

In this document, we give a status report after the third year (2000-07-01–2001-06-30) of the project.

2 Introduction

Transmutation techniques in accelerator-driven systems (ADS) involve high-energy neutrons, created in the proton-induced spallation of a heavy target nucleus. The existing nuclear data libraries developed for reactors of today go up to about 20 MeV, which covers all available energies for that application; but with a spallator coupled to a core, neutrons with energies up to $1-2$ GeV will be present. Although a large majority of the neutrons will be below 20 MeV, the relatively small fraction at higher energies still has to be characterized. Above ~ 200 MeV, direct reaction models work reasonably well, while at lower energies nuclear distortion plays a non-trivial role. This makes the $20-200$ MeV region the most important for new experimental cross section data.

Very little high-quality neutron-induced data exist in this energy domain. Only the total cross section (Finlay et al., 1993) and the np scattering cross section have been investigated extensively. Besides this, there are data on neutron elastic scattering from UC Davis at 65 MeV on a few nuclei (Hjort et al., 1994). Programmes to measure neutron elastic scattering have been proposed or begun at Los Alamos (Rapaport and Osborne) and IUCF (Finlay et al., 1992), with the former resulting in a thesis on data in the $5° - 30°$ range on a few nuclei.

The situation is similar for (n,xp) reactions, where programmes have been run at UC Davis (Ford et al., 1989), Los Alamos (Rapaport and Sugarbaker, 1994), TRIUMF

(Alford and Spicer, 1998) and TSL Uppsala (Olsson, 1995, Blomgren, 1997), but with limited coverage in secondary particle energy and angle. Better coverage has been obtained by the Louvain-la-Neuve group up to 70 MeV (Slypen et al., 1994).

Thus, there is an urgent need for neutron-induced cross section data in the region around 100 MeV, which is an area where very few facilities in the world can give contributions. By international collaboration within an EU supported Concerted Action, which has been followed by the full scale project HINDAS, the level of ambition for the present project has been increased, and the potential of the unique neutron beam facility at The Svedberg Laboratory in Uppsala can be fully exploited.

3 Experimental setup and techniques

3.1 The TSL neutron beam facility

At TSL, quasi-monoenergetic neutrons are produced by the reaction ^{7}Li(p,n)^{7}Be in a ^{7}Li target bombarded by $50-180$ MeV protons from the cyclotron, as is illustrated in Fig. 1 (Condé et al., 1990, Klug et al., 2001). After the target, the proton beam is bent by two
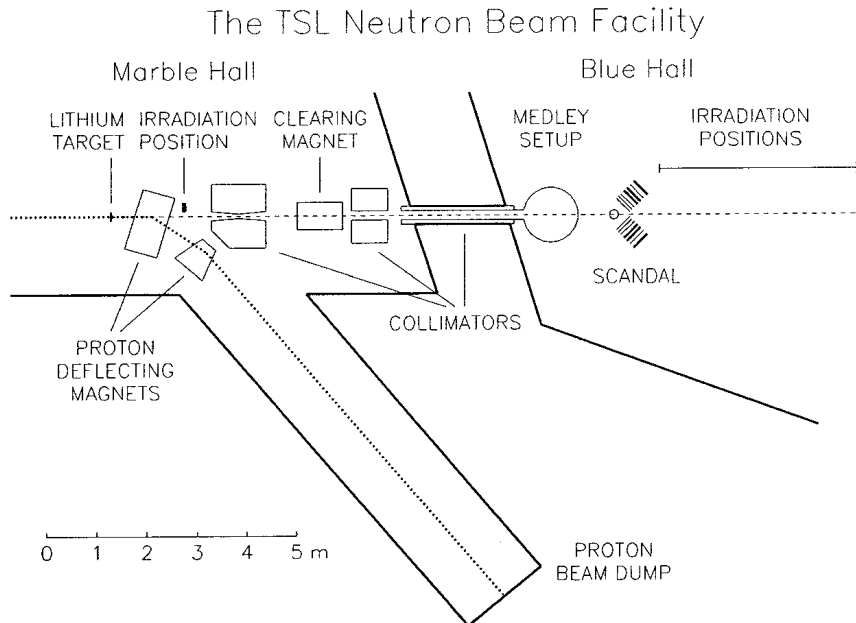
Figure 1: The TSL neutron beam facility.

dipole magnets into an 8 m long concrete tunnel, where it is focused and stopped in a well-shielded Faraday cup, which is used to measure the proton beam current. A narrow neutron beam is formed in the forward direction by a system of three collimators, with a total thickness of more than four metres.

The energy spectrum of the neutron beam consists of a high-energy peak, having approximately the same energy as the incident proton beam, and a low-energy tail. About half of all neutrons appear in the high-energy peak, while the rest are roughly equally distributed in energy, from the maximum energy and down to zero. The thermal contribution is small. The low-energy tail of the neutron beam can be reduced using

time-of-flight (TOF) techniques over the long distance between the neutron source and the reaction target (about 8 m).

The relative neutron beam intensity is monitored by integrating the charge of the primary proton beam, as well as by using thin film breakdown counters, placed in the neutron beam, measuring the number of neutron-induced fissions in ^{238}U (Prokofiev et al., 1999).

Two multi-purpose experimental setups are semi-permanently installed at the neutron beam line, namely MEDLEY and SCANDAL. These were described in detail in the annual report 1999/2000, and only a brief presentation is given here.

3.2 The MEDLEY setup

The MEDLEY detector array (Dangtip et al., 2000), shown in Fig. 2, is designed for measurements of neutron-induced light-ion production cross sections of relevance for
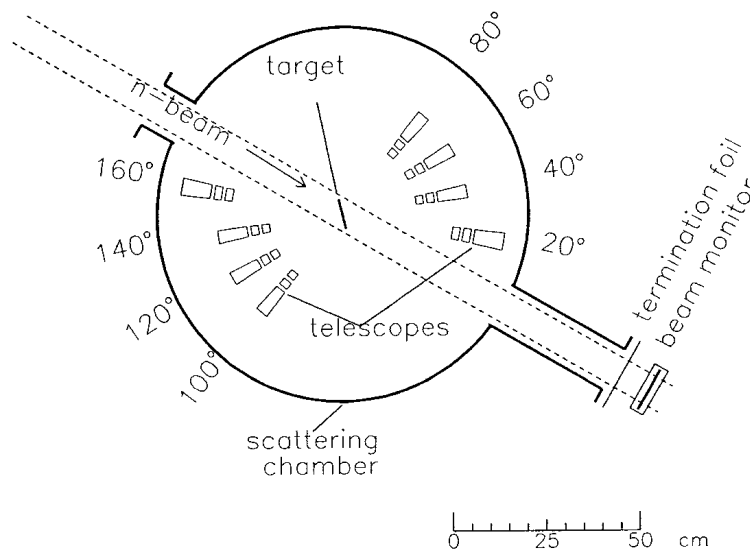

Figure 2: The MEDLEY detector array.

applications within ADS and fast-neutron cancer therapy and related dosimetry. It consists of eight particle telescopes, installed at scattering angles of $20° - 160°$ with $20°$ separation, in a 1 m diameter scattering chamber, positioned directly after the last neutron collimator. All the telescopes are fixed on a turnable plate at the bottom of the chamber, which can be rotated without breaking the vacuum.

Each telescope is a $\Delta E - \Delta E - E$ detector combination, where the ΔE detectors are silicon surface barrier detectors with thicknesses of 50 or 60 μm and 400 or 500 μm, respectively, while the E detector is a 50 mm long inorganic CsI(Tl) crystal. $\Delta E - \Delta E$ or $\Delta E - E$ techniques are used to identify light charged particles (p, d, t, ^{3}He, α). The chosen design gives a sufficient dynamic range to distinguish all charged particles from a few MeV up to more than 100 MeV.

The solid angle of the telescopes is defined by active collimators, designed as thin hollow plastic scintillator detectors, mounted on small photomultiplier tubes. A signal

6

from such a detector is used to veto the corresponding event, thereby ensuring that only particles that pass inside the collimator are registered.

3.3 The SCANDAL setup

The SCANDAL setup (Klug et al., 2001) is primarily intended for studies of elastic neutron scattering, i.e., (n,n) reactions. Neutron detection is accomplished via conversion to protons by the H(n,p) reaction. In addition, (n,xp) reactions in nuclei can be studied by direct detection of protons. This feature is also used for calibration, and the setup has therefore been designed for a quick and simple change from one mode to the other.

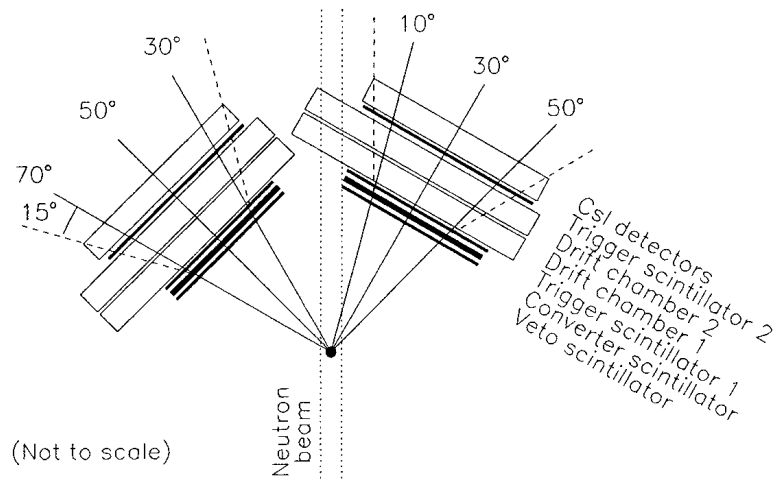The device is illustrated in Fig. 3. It consists of two identical systems, in most cases

Figure 3: The SCANDAL setup

located on each side of the neutron beam. The design allows the neutron beam to pass through the drift chambers of the right-side setup, making low-background measurements close to zero degrees feasible.

In neutron detection mode, each arm consists of a 2 mm thick veto scintillator for fast charged-particle rejection, a neutron-to-proton converter which is a 10 mm thick plastic scintillator, a 2 mm thick plastic scintillator for triggering, two drift chambers for proton tracking, a 2 mm thick ΔE plastic scintillator, which is also part of the trigger, and an array of 12 large CsI detectors for energy determination. The trigger is provided by a coincidence of the two trigger scintillators, vetoed by the front scintillator. The compact geometry allows a large solid angle for protons emitted from the converter. Recoil protons are selected using the ΔE and E information from the plastic scintillators and the CsI detectors, respectively.

The energy resolution is about 3.7 MeV (FWHM), which is sufficient to resolve elastic and inelastic scattering in several nuclei. The angular resolution is calculated to be about 1.4° (rms) when using a cylindrical scattering sample of 5 cm diameter.

When SCANDAL is used for (n,xp) studies, the veto and converter scintillators are removed. A multitarget arrangement can be used to increase the target content without impairing the energy resolution, which is typically 3.0 MeV (FWHM). This multitarget

7

box allows up to seven targets to be mounted simultaneously, interspaced with multi-wire proportional counters (MWPC). In this way it is possible to determine in which target layer the reaction took place, and corrections for energy loss in the subsequent targets can be applied. In addition, different target materials can be studied simultaneously, thus facilitating absolute cross section normalization by filling a few of the multitarget slots with CH_2 targets. The first two slots are normally kept empty, and used to identify charged particles contaminating the neutron beam.

4 Results and analysis

4.1 Elastic scattering

A two-week experiment was performed in September 2000 with SCANDAL on neutron scattering from hydrogen. The aim of this measurement is to establish this cross section as an absolute reference, i.e., all other data are measured relative to it. It has therefore high priority not only for our project, but for neutron data measurements in general in our energy range.

Elastic scattering of neutrons on ^{208}Pb was studied in March, 2001. This measurement was a follow-up experiment on a previous run (May 2000) to get improved statistics. The analysis of the scattering data has now reached a stage where final data are expected in a near future. A preliminary two-point "angular distribution" of neutrons scattered from carbon and lead at 9° and 16° is shown in Fig. 4. Some work remains on assessment of the systematical uncertainties before a complete angular distribution in the region 10° − 70° can be presented. It will be very interesting to see how well these data can be described by recent optical model representations (Koning).

4.2 (n,xlcp) reactions

In parallel with the elastic scattering measurement with SCANDAL in September 2000, we performed experiments with MEDLEY to measure double differential cross sections $d^2\sigma/d\Omega dE$ for protons and other light charged particles (d, t, ^{3}He, α) emitted in reactions of 100 MeV neutrons on ^{16}O and ^{28}Si targets. These experiments aim at providing data for medical effects and electronics sensitivity due to cosmic rays.

A French group lead by Jean-François Lecolley, Caen, has previously run experiments at TSL in collaboration with us on (n,xp) reactions. Up to now, ^{56}Fe and ^{208}Pb targets have been studied, and a ^{238}U experiment is planned. Analysis of the first two nuclei is in progress, and preliminary spectra look very promising.

4.3 (n,xn) reactions

We have launched another collaboration project with the Caen group; (n,xn) reactions. For these studies, a modified SCANDAL converter has been designed and built in Caen. It was tested and mounted at SCANDAL for the first time in April 2001. Preliminary analysis seems to indicate that it worked as expected, and the test experiment provided guidance for further equipment development.
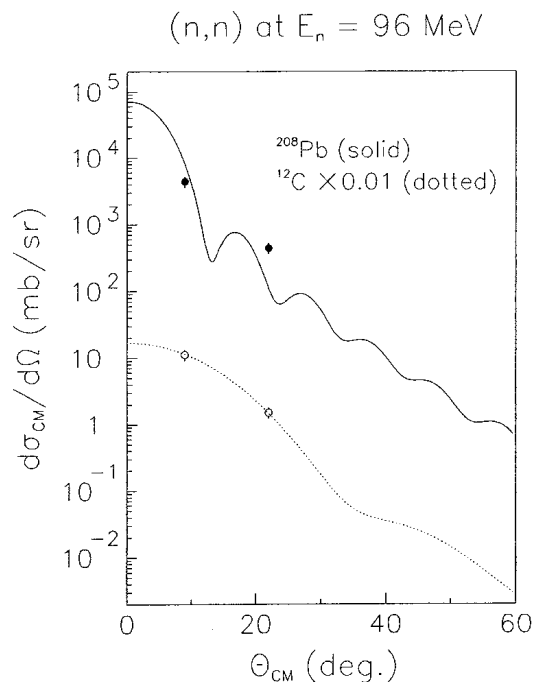
Figure 4: Preliminary data on neutron elastic scattering from ^{12}C and ^{208}Pb. The 9° point of ^{12}C has been normalized to the theoretical curve. All the other points are experimentally normalized to the 9° point of ^{12}C. The calculations are provided by D. Madland, LANL.

5 International activities

5.1 Collaboration

INF participates in the EU project HINDAS (High- and Intermediate Energy Nuclear Data for Accelerator-Driven Systems), which involves 16 European institutions from Belgium, France, Germany, The Netherlands, Spain, Sweden and Switzerland. The experimental work will be performed at six European laboratories (UCL in Louvain-la-Neuve, TSL in Uppsala, KVI in Groningen, PSI in Villigen, COSY at Jülich and GSI in Darmstadt). Work on the theoretical interpretation of the experimental results is also included. The project, which started 2000-09-01 and runs over three years, is coordinated by Prof. Jean-Pierre Meulders, Louvain-la-Neuve, Belgium.

HINDAS has a total budget of 2.1 MEUR, whereof 210 kEUR falls on the Uppsala partner, while the collaborators that use the TSL neutron facility have received in total about 500 kEUR. Most of the money is intended for PhD students or postdocs. This means an increasing engagement for the Uppsala group and TSL, but also more focus on the activities here.

A substantial fraction of the Uppsala funding is used to employ Stephan Pomp, who acts as liaison between the Uppsala group and the collaborating groups, as well as supervisor for PhD students at INF.

9

To our judgement, HINDAS is well organized and focused. It involves a major part of the competence and equipment available in Europe, and will also contribute to the development of nuclear data activities in Europe, by bringing new scientists into this area.

The group participates in an experiment at Indiana University Cyclotron Facility (IUCF), Bloomington, Indiana, USA on neutron-proton scattering measurements. An experimental campaign during 1999 has resulted in two publications during the present year, and a new experiment is being planned for late summer 2001.

5.2 Meetings and conferences

Cecilia Johansson and Joakim Klug, together with four other Uppsala students participated in the "Fredric Joliot - Otto Hahn Summer School" in Cadarache, August 2000.

Nils Olsson has taken on duty as Swedish representative in the OECD/NEA Nuclear Science Committee (NSC) and its Executive Group. He participated in a meeting with these bodies 2001-06-11–13. Notes from the meeting are enclosed in appendix VIII.

Jan Blomgren was invited speaker at a Symposium on Electromagnetic Interactions in Nuclei at Low and Intermediate Energies, Moscow, Russia, September 2000 (enclosed).

6 Administrative matters

6.1 Personnel and PhD students

INF has had three PhD dissertations during the year, Somsak Dangtip who has worked with cross section measurements with MEDLEY of medical relevance, Alexander Prokofiev who has performed neutron-induced fission cross section measurements, and Michael Österlund who has studied fundamental nuclear medium effects.

During the project year, Nils Olsson has accepted a new position as research director at FOI. He is still active within the project on a part-time basis (30 %). The project leadership has been taken over by Jan Blomgren. In December 2000, Stephan Pomp was employed as research associate. Two PhD students are directly connected to and financed by the present project, namely Cecilia Johansson and Joakim Klug, which both are connected to the research school AIM (Advanced Instrumentation and Measurements). Two other students, Bel Bergenwall who is financed by AIM, and Udomrat Tippawan with a schoolarship from Thailand, have tasks strongly related to the present project, and especially to the line of development emerging from the collaboration with the French groups within HINDAS.

Jan Blomgren has obtained a permanent position as associate professor (universitetslektor) in applied nuclear physics at INF, Uppsala university, starting June 1, 2001.

Starting September 1, 2000, Jan Blomgren has taken on the duty as director of studies of the recently created Research School for Nuclear Technology, based at the Swedish Centre for Nuclear Technology. The main activity during the first year has been to identify a course curriculum, and to re-shape courses to fit national requirements. First courses will be given September 2001.

January 30, 2001, Joakim Klug defended his licentiate thesis "The SCANDAL facility - how to measure elastic neutron scattering in the 50–130 MeV range" (enclosed). Dr. A. Håkansson from the neighbouring department of radiation sciences acted as opponent.

May 5, 2001, Jonas Söderberg at Linköping University defended his licentiate thesis in radiophysics. It contains a section on the MEDLEY setup, which he participated in the development of.

An agreement with Chiang Mai university, Thailand has been reached to have Somsak Dangtip and a PhD student working part-time on development work for the SCANDAL facility. Somsak graduated with a PhD from our group in September 2001 and has been staff physicist at Chiang Mai university since.

Members of our group participate in several courses on nuclear physics as well as on energy technology. Some of these include problems related to transmutation. Also a number of outreach talks, seminars, articles and interviews related to this project have been given.

6.2 Reference group

A reference group meeting, with participation by Per-Eric Ahlström (SKB), Benny Sundström (SKI), Thomas Lefvert (Vattenfall AB), Fredrik Winge (BKAB) and Anders Ringbom (FOA), was held in Uppsala 2001-01-16. Scientific and administrative reports on the progress of the project were given at this meeting.

In addition to the meetings, the progress of the work is continously communicated to the reference group members by short, written, quarterly reports.

References

Alford W.P. and Spicer B.M., 1998, Nucleon charge-exchange reactions at intermediate energy, Advances in Nuclear Physics 24, 1.

Blomgren J., The (n,p) reaction - Not So Boring After All? Proceedings from International Symposium on New Facet of Spin Giant Resonances in Nuclei, Tokyo, 1997, p. 70. (Invited talk)

Condé H., Hultqvist S., Olsson N., Rönnqvist T., Zorro R., Blomgren J., Tibell G., Håkansson A., Jonsson O., Lindholm A., Nilsson L., Renberg P.-U., Brockstedt A., Ekström P., Österlund M., Brady P., Szeflinski Z., 1990, A facility for studies of neutron induced reactions in the 50 - 200 MeV range, Nucl. Instr. Meth. A292, 121.

Dangtip S., Ataç A., Bergenwall B., Blomgren J., Elmgren K., Johansson C., Klug J., Olsson N., Alm Carlsson G., Söderberg J., Jonsson O., Nilsson L., Renberg P.-U., Nadel-Turonski P., Le Brun C., Lecolley F.-R., Lecolley J.-F., Varignon C., Eudes Ph., Haddad F., Kerveno M., Kirchner T., Lebrun C., 2000, A facility for measurements of nuclear cross sections for fast neutron cancer therapy, Nucl. Instr. Meth., in press.

Finlay R., Abfalterer W.P., Fink G., Montei E., Adami T., Lisowski P.W., Morgan G.L., Haight R.C., 1993, Neutron total cross sections at intermediate energies, Phys. Rev. C47, 237.

Finlay R., 1992, Proposal to the NSF for support of CHICANE/Spectrometer System for the IUCF Cooler Ring.

Ford T.D., Brady F.P., Castaneda C.M., Drummond J.R., McEachern B., Romero J.L., Sorenson D.S., 1989, A large dynamic range detector for measurement of neutron-induced charged particle spectra down to zero degrees, Nucl. Instr. Meth. A274, 253.

Hjort E.L., Brady F.P., Romero J.L, Drummond J.R., Sorenson D.S., Osborne J.H., McEachern B., 1994, Measurements and analysis of neutron elastic scattering at 65 MeV, Phys. Rev. C50, 275.

Klug J., Blomgren J., Ataç A., Bergenwall B., Dangtip S., Elmgren K., Johansson C., Olsson N., Rahm J., Jonsson O., Nilsson L., Renberg P.-U., Nadel-Turonski P., Ringbom A., Oberstedt A., Tovesson F., Le Brun C., Lecolley J.-F., Lecolley F.-R., Louvel M., Marie N., Schweitzer C., Varignon C., Eudes Ph., Haddad F., Kerveno M., Kirchner T., Lebrun C., Stuttgé L., Slypen I., Prokofiev A., Smirnov A., Michel R., Neumann S., Herpers U., 2000, SCANDAL - A facility for elastic neutron scattering studies in the 50 − 130 MeV range, to be published.

Koning A., private communication.

Olsson N., 1995, Studies of spin-isospin excitations at TSL in Uppsala, Nucl. Phys. News 5, no. 2, 28.

Prokofiev A.V., Smirnov A.N., Renberg P.-U., 1999, A monitor for intermediate-energy neutrons based on thin film breakdown counters, Report TSL/ISV-99-0203, Uppsala University.

Rahm J., Blomgren J., Condé H., Elmgren K., Olsson N., Rönnqvist T., Zorro R., Ringbom A., Tibell G., Jonsson O., Nilsson L., Renberg P.-U., Ericson T.E.O. and Loiseau B., np scattering measurements at 96 MeV, Phys. Rev. C 63 (2001) 044001.

Rapaport J. and Sugarbaker E., 1994, Isovector excitations in nuclei, Annu. Rev. Nucl. Part. Sci. 44, 109.

Rapaport J., private communication, and Osborne J., thesis, unpublished.

Slypen I., Corcalciuc V., Ninane A., Meulders J.P., 1994, Charged particles produced in fast neutron induced reactions on ^{12}C in the 45 − 80 MeV energy range, Nucl. Instr. Meth. A337, 431.

Thun J., Blomgren J., Elmgren K., Källne J., Olsson N., Lecolley J.-F., Lefebvres F., Varignon C., Borne F., Ledoux X., Patin Y., Jonsson O., Renberg P.-U., 2000, The response of a liquid scintillator detector to 21–100 MeV neutrons, accepted for publication in Nucl. Instr. Meth. A.

Appendix I

CHARGE-EXCHANGE GIANT RESONANCES AS PROBES OF NUCLEAR STRUCTURE

J. Blomgren
Department of Neutron Research, Uppsala University, Sweden

Abstract

Giant resonances populated in charge-exchange reactions can reveal detailed information about nuclear structure properties, in spite of their apparent featurelessness.

The (p,n) and (n,p) reactions - as well as their analog reactions - proceed via the same nuclear matrix elements as beta decay. Thereby, they are useful for probing electroweak properties in nuclei, especially for those not accessible to beta decay. The nuclear physics aspects of double beta decay might be investigated in double charge-exchange reactions.

Detailed nuclear struture information, such as the presence of ground-state correlations, can be revealed via identification of "first-forbidden" transitions. In addition, astrophysics aspects and halo properties of nuclei have been investigated in charge exchange.

Finally, these experiments have questioned our knowledge of the absolute strength of the strong interaction.

1 Introduction

How come there is a talk about spin-isospin properties of nuclei, exemplified by Gamow-Teller giant resonances, in a symposium on electromagnetic interactions?

Being among the younger speakers, I have lived more than half my life *after* the unification of the electromagnetic and weak forces. Thus, for me it is natural to study the *electroweak* rather than the electromagnetic response in nuclei.

In the middle of the previous century, beta decay - one of the most prominent electroweak manifestations in nuclei - was a major spectroscopic tool in nuclear physics, however plagued with profound problems. For a long time, the theoretical decay rates deviated severely from the experimental results. Compared to simple model predictions, almost any beta decay rate was orders of magnitudes slower. Part of the discrepancy was removed with the discovery of the isobaric analogue state (IAS). This state corresponds to a collective Fermi transition, which locates all Fermi strength in a single, narrow state. The Coulomb displacement energy puts this state energetically out of reach for beta decay in most nuclei.

This observation stimulated speculations that a major part of the Gamow-Teller (GT) strength could similarly be found in a giant resonance, located at a slightly higher excitation energy than the IAS, due to the spin dependence of the nuclear force. Soon it was indeed found that intermediate energy (p,n) reactions were dominated by GT transitions to states at low excitation energy.

Studies of the intrinsic propeties of the Gamow-Teller resonance grew into an entire industry around 1980, and a number of conferences have been devoted to these investigations. I will therefore not go into details here; see, e.g., [1, 2, 3] for a review. Instead this article is focused on another aspect; the use of Gamow-Teller resonances as probes of nuclear properties.

I will present a few examples on this, most of them taken from (n,p) experiments at the The Svedberg Laboratory (TSL) in Uppsala, Sweden. The TSL neutron beam has a very extensive agenda, with studies of both fundamental and applied physics on its agenda [4, 5].

The field of detailed (n,p) experiments was opened up by UC Davis, from which a series of experiments at about 65 MeV neutron energy were conducted up to about ten years ago. The torch then passed on to TRIUMF, where the 200–500 MeV region was exhausted by a very ambitious programme, spanning over 20 nuclei ranging from ^{3}He to ^{208}Pb. Los Alamos has contributed to the field by studying the (n,p) reaction with the white neutron source, thus providing good data on energy dependences. It can be noted that these four laboratories seem to be a quartet of harmony. In all cases where the same cross section has been measured by more than one place, there is agreement on the results. As we will return to in the end, that is nothing to be taken for granted...

2 Why employing the (n,p) reaction?

The original motivation for (n,p) studies came from the (p,n) reaction, which has been studied systematically during the last twenty years. The (p,n) reaction and nuclear β^- decay are both responses to an isospin change (Fermi) or a combined spin and isospin change (Gamow-Teller) of the nucleus. In popular terms, the (p,n) reaction can be described as β^- decay governed by the strong interaction.

This simple picture was corroborated by the finding that the Gamow-Teller (GT) strength found in the (p,n) reaction and the GT strength from β^- decay for the same transition are proportional. Thus, the (p,n) reaction can be used to explore β^- decay where it is inaccessible, e.g. from excited states or unstable nuclei.

Soon it was realized that the (n,p) reaction should be complementary in such studies, allowing the β^+ decay to be investigated. Besides the inherent nuclear physics interest, it has also a considerable astrophysics impact, because the beta decay and electron capture rates in iron-region nuclei play important roles in stars prior to supernova explosion.

Lately, great attention has been paid to accelerator-based transmutation of nuclear waste, and the possibilities to use this also for energy production. For this purpose, many neutron-induced cross sections in this energy domain are useful as design parameters as well as for model validation. Luckily, among the nuclei studied for purely fundamental nuclear physics reasons we find some of the most important materials to be used in a transmutation facility, e.g., iron, zirconium and lead. What was originally curiosity-driven research is today important data in the applied world!

3 Precision studies of nuclear ground states

From figure 1, it can be seen that there should be no GT strength in ^{90}Zr to first order. All filled proton orbitals correspond to filled neutron shells, so all strength should be Pauli
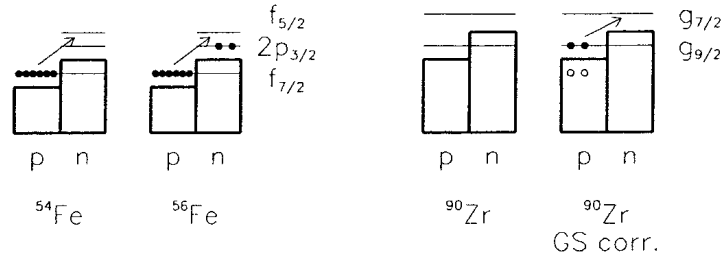
Figure 1: Simple shell-model illustrations of the (n,p) reaction on ^{54}Fe, ^{56}Fe and ^{90}Zr.

blocked. However, if the ^{90}Zr ground state is not the simplest configuration given by the naive shell model, but has an admixture of protons in the $g_{9/2}$ shell, a GT transition could occur to the empty neutron $g_{7/2}$ orbital. Thus, GT strength in the ^{90}Zr(n,p) reaction should be a probe for such ground-state correlations [6].

It turns out that such first-forbidden GT strength actually shows up, corresponding to an occupation of - on average - 0.9 protons in the $g_{9/2}$ shell. This is in agreement with results from other techniques, like pick-up or knock-out experiments.

The (n,p) reaction on ^{54}Fe and ^{56}Fe reveals Gamow-Teller properties which deviate from the simplest expectations [7]. These two nuclei differ by two neutrons in an orbital that should not participate in any GT transition (see figure 1). Hence, it could be anticipated that the GT strength should be the same for them. That is far from true. The GT strength is instead 3.5 ± 0.5 and 2.3 ± 0.5 for the two nuclei.

Auerbach et al. [8] have shown that RPA correlations can reduce the GT strength substantially. They also found a relation to the quadrupole moment, such that the strength is inversely proportional to it. This is in agreement with the iron data, as illustrated by the table below.

	^{54}Fe	^{56}Fe
$S_{\beta+}$	3.5 ± 0.5	2.3 ± 0.5
$B(E2)$ (W.u.)	10.6	16.8
$S_{\beta+} * B(E2)$	37 ± 5	39 ± 8

4 Halo properties of nuclei

Recently, there has been a vivid activity about halo nuclei, and indeed lots of really amazing physics has come out from this. Two such halo nuclei are accessible by the (n,p) reaction, ^{11}Be and ^{6}He, which are one- and two-neutron halos, respectively.

It has long been speculated that a new dipole mode should be present in halo nuclei, the so-called soft dipole resonance. The classical giant dipole resonance (GDR) is popularily described as an oscillation of protons versus neutrons, while in a halo nucleus the halo neutron could oscillate in opposite phase to the core. Such an oscillation has a much weaker restoring force than when all nucleons participate, and has therefore to reside at a lower excitation energy, like a few MeV. The total dipole strength in a nucleus is determined by the model-independent energy-weighted sum rule (EWSR), which states

that the sum of the strength multiplied with its excitation energy should be given by the number of protons and neutrons in the nucleus, insensitive to the spatial distribution of the nucleons. If the presence of a neutron halo places strength at low excitation energy, this has then to be compensated by an enlarged absolute stength to conserve the sum rule.

Thus, dipole strength at low excitation energy and larger absolute strength should be two features to look for. A third observable should be a proposed downward shift of the centroid of the classical GDR. What about Gamow-Tellers? Well, conventional wisdom tells that there should be no differences due to a halo, because the Gamow-Teller excitation has no radial dependence.

A recent experiment on the $^{10}B(n,p)^{10}Be$ and $^{11}B(n,p)^{11}Be$ reactions turned most expectations upside down [9]. The search for a soft dipole turned out to be negative by all measures; there was no hint whatsoever of it. This should not be over-interpreted though; it is not evident that the (n,p) reaction has to populate the soft dipole strongly even if it exists.

What was more intriguing was that the Gamow-Teller strength to three low-lying states was significantly reduced compared to shell-model expectations, in agreement with a previous $(t,^{3}He)$ experiment [10]. Is this due to the halo configuration of the final nucleus? A follow-up experiment is being planned on $^{6}Li(n,p)^{6}He$.

In contrast to the medium-weight nuclei above, the total Gamow-Teller strength appears to follow a simple picture, at least on a relative scale. Back-of-the-envelope estimates based on that the strength should be proportional to the number of protons in $p_{3/2}$ and to the number of neutron vacancies in any p shell result in a prediction that the strength in ^{10}B should be 50 % large than in ^{11}B, which is in agreement with data. To be more specific, the extracted strengths below 30 MeV excitation energy are 2.0 ± 0.2 for ^{10}B and 1.3 ± 0.2 for ^{11}B.

5 $^{9}Be(n,p)$ and the unit cross section puzzle

In the (p,n) reaction, it has been found that the GT unit cross section, $\hat{\sigma}_{GT}$, varies smoothly as a function of mass A, at a given energy, and that it is slightly larger for odd than for even nuclei. This unit cross section is given by

$$\hat{\sigma}_{GT} = \sigma_{GT}/B_{GT}, \tag{1}$$

where σ_{GT} is the experimental GT cross section at 0°, corrected for optical model distortions and the finite momentum and energy transfer in the reaction, and B_{GT} is the strength obtained from the corresponding β decay.

The unit cross section for odd nuclei is systematically $20 - 30\%$ larger than for even. This behaviour is not fully understood. Furthermore, for some odd nuclei, e.g., ^{13}C and ^{15}N (and possibly ^{35}Cl), the GT unit cross section for the ground state transition is $30 - 40\%$ larger than a smooth trend through the data points for other odd nuclei would indicate. In contrast, the transition to the 15.1 MeV state in the $^{13}C(p,n)^{13}N$ reaction does not show any such effects.

A number of possible explanations have been discussed in the literature. Taddeucci et al. [1] suggested that optical potential parameter differences between odd and even nuclei could lead to uncertainties in distorted wave calculations. Systematic studies of optical potentials, especially for nonzero-spin targets, are thus motivated.
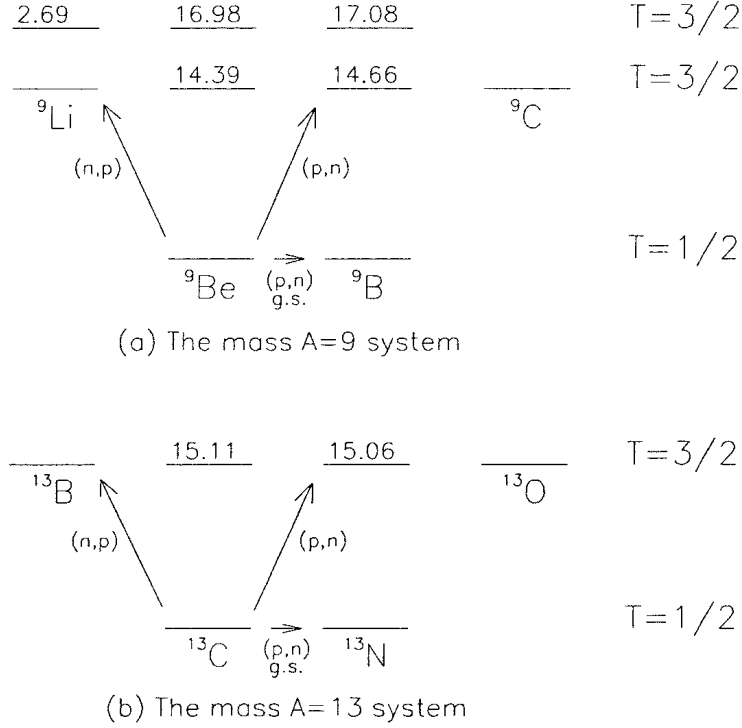
Figure 2: Isobar diagrams of the mass (a) $A = 9$ and (b) $A = 13$ systems.

The unit cross section proportionality (eq. 1) relies on the dominance of central interactions and direct reaction mechanisms. Possible contributions from non-central interactions and non-direct reaction mechanisms as a reason for such effects have been discussed [1, 3].

Another possibility of why the unit cross sections differ is because of problems with the axial vector current g_A. The Gamow-Teller transition in nuclear β decay is determined by $(g_A/g_V)^2 B_{GT}$, while $\hat{\sigma}_{GT}$ is a function of B_{GT} and A only. It has been found that in the nuclear medium, the value of g_A for the free neutron is reduced to an effective value of $(g_A)_{eff} = (0.8 - 0.9)g_A$, resulting in quenching values $[(g_A)_{eff}/g_A]^2$ of 60 − 80% [2]. In addition, the importance of heavy-meson exchange for GT matrix elements has been pointed out [11, 12], which could possibly have some implications for the value of g_A. It is not known whether such effects could be different for odd and even nuclei.

Lack of data prevents systematic studies of such effects by the (n,p) reaction. Although with fewer data points available, the data base on unit cross sections for (n,p) on even nuclei shows a trend similar to that of (p,n) data. For odd nuclei, there are only two cases where the corresponding B_{GT} is known; ^{3}He [13] and ^{13}C [14, 15].

Hence, further (n,p) reaction studies on nuclei, where corresponding data on (p,n) at about the same energy are available, should be most useful. One of the best cases among several candidates is ^{9}Be (see figure 2a).

The data for the ^{9}Be(n,p)^{9}Li ground state were used to determine a GT unit cross section of $\hat{\sigma} = 7.4 \pm 1.2$ mb/sr [16]. This is in good agreement with the intrinsic value obtained from shell-model calculations, but is considerably lower than that estimated from the ^{9}Be(p,n)^{9}Li ground state reaction ($\hat{\sigma} = 11.0 \pm 1.6$ mb/sr) [17]. Thus, it seems as the $T = \frac{1}{2} \to T = \frac{3}{2}$ transitions are about 30% weaker than the $T = \frac{1}{2} \to T = \frac{1}{2}$ (ground-state) transition. This resembles the situation of the $A = 13$ system, where the $T = \frac{1}{2} \to T = \frac{3}{2}$ transition has a unit cross section of around 10–11 mb/sr, whilst the $T = \frac{1}{2} \to T = \frac{1}{2}$ (ground-state) transition has $\hat{\sigma} = 14.4 \pm 1.2$ mb/sr, i.e. also here the former is about 30 % weaker. The puzzle which motivated this investigation seems therefore to remain.

6 Are there double Gamow-Teller resonances?

Recently, double beta decay has been identified in several experiments. (See e.g. ref. [18] for a review.) Like in the beta decay studies half a century ago mentioned in section 1, also in this case only a minor fraction of the total appropriate strength can be studied. Experiments aiming at examining a major part of the double Gamow-Teller strength might improve our understanding of spin-isospin properties of nuclei, as did the single Gamow-Teller resonance investigations.

Lately, double giant resonances have been of considerable interest, both theoretically and experimentally. Up to now the double isobaric analogue state (DIAS), the double isovector dipole resonance (DIVDR), and the dipole built on the analogue state have been identified, using the (π^+, π^-) reaction and its inverse at LAMPF [19]. In addition, evidence of Gamow-Teller strength built on the isobaric analogue state has been found. It is expected that double giant resonances are general features of nuclei, and evidence for two-phonon resonances have now been found in several experiments. For a review of the field, see ref. [20].

Among the two-phonon resonances, the double Gamow-Teller (DGT) resonance is of particular interest, because of links to particle and astrophysics via the connection to the double beta decay and its implications for the neutrino mass [21, 22].

Auerbach, Zamick and Zheng predicted the existence of collective isotensor resonances in double charge-exchange reactions as a new mode of collectivity in nuclei [23]. Observation of DGT strength will be experimentally difficult, since there are no simple elementary probes available (the pion has zero spin and at the nucleon level a probe like (p, Δ^-) would be required). The DGT resonance can in principle be excited in pion double charge exchange, but the mechanism is assumed to be weak.

The only giant resonance for which both the one- and two-phonon cross sections have been measured with similar reactions is the IVDR, which has been studied by the $(\pi^\pm, \pi^0)$ (one-phonon) [24] and the (π^+, π^-) (two-phonon) [19] reactions. The ratio of the two- to one-phonon cross sections, taken at the maximum of the two excitations, is about 0.003. The single Gamow-Teller cross section at zero degrees in heavy-ion reactions are typically a few mb/sr for light nuclei. An estimate based on such an approach, using a B(GT) calibration from single charge exchange, the shell model calculation above, and a simple model for the DCX cross section in terms of the SCX cross sections by Bertsch [25], predicted a cross section of 24 μb/sr. In this model, it was assumed that the ratio SCX/DCX is the same as for pion-induced charge exchange.

Bertulani [26] has developed an eikonal approximation model for heavy-ion charge exchange reactions, in which he predicted that the cross sections for DGT excitation in heavy-ion reactions should be - at most - in the μb/sr region, but probably much smaller. It was pointed out that there is a suppression mechanism of heavy-meson exchange in heavy-ion reactions. Instead of a large contribution from ρ mesons in the reaction mechanism - which is the case for reactions induced by pions and nucleons - the larger interaction distance in heavy-ion reactions favour pion exchange. This results in a much weaker charge-exchange, and hence much smaller cross sections. Thus, these two predictions differ by several orders of magnitude.

Guided by this, we have carried out a search for double Gamow-Teller excitations, employing the $^{24}\text{Mg}(^{18}\text{O},^{18}\text{Ne})^{24}\text{Ne}$ reaction at 100 and 76 MeV/nucleon at NSCL-MSU and GANIL, respectively [27].

A very small cross section at low excitation energies was found, about 20 nb/sr, but the angular distribution did not support a double Gamow-Teller interpretation. Thus the results provide evidence for a strong suppression of double Gamow-Teller excitations. Thereby, they are qualitatively compatible with the Bertulani model. However, since we can only deduce an upper limit of the cross section, it cannot be excluded that the DGT excitation is even weaker. This result seems to discourage the use of heavy ions at intermediate energies for probing double Gamow-Teller strength.

7 A major surprise: the calibration was off!

All (n,p) data above have been normalized to the $^1\text{H}(\text{n},\text{p})$ reaction, i.e. the fundamental np scattering process. When designing this programme it was anticipated that the best way of establishing the absolute scale would be to measure relatively to the np scattering cross section, which was then believed to be well known.
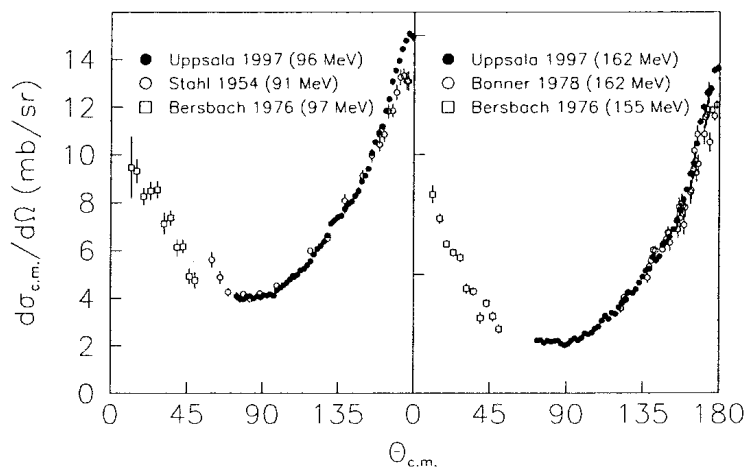

Figure 3: The np scattering differential cross section at 96 and 162 MeV.

The first data [28] revealed a true surprise! The angular distribution differed from the global partial-wave analyses by 15 % at 0° $^1\text{H}(\text{n},\text{p})$, i.e. at 180° c.m. np scattering. This was shocking for two different resons.

Firstly, this is one of the best places to determine the pion-nucleon coupling constant, and thus establishing the absolute strength of the strong interaction. Secondly, this cross section has been used to normalize virtually every neutron-induced cross section. All cross sections for transmutation of waste, future accelerator-based energy production, fast-neutron cancer therapy, cosmic neutron induced failures in electronics and other applications - multi-billion dollar cross sections - are therefore uncertain with the same amount.

This has motivated new measurements with good precision, and also at another energy. The discrepancy is still there [29, 30, 31], which is illustrated in figure 3. An obvious next step has been to make a thorough investigation of the entire world data base on np scattering [32]. We have found that it is in a much worse condition than we had thought. The largest data sets tend to fall into two families with respect to shape, with a 15 % difference at backward angles. In addition, there are normalization inconsistencies, also of about 15 %, between the two most frequently used normalization techniques.

There has been an intense debate during the last few years on whether the pion-nucleon coupling constant should have the classical value of 14.4, or 13.6 which recent global analyses of the world np data base seem to indicate. The data base is in such a condition that either one of the two discrepancies mentioned above could account for the difference alone. Making order out of this mess has therefore become a very important activity. An international workshop was recently organized to scrutinize this problem [33].

Thereby, what begun as studies of fundamental nuclear properties employing the (n,p) reaction has now grown into multi-disciplinary research, where basic physics and emerging large-scale applications are developed in a joint endeavour. To my opinion, this is a good raw model for the future of nuclear physics.

References

[1] T.N. Taddeucci, C.A. Goulding, T.A. Carey, R.C. Byrd, C.D. Goodman, C. Gaarde, J. Larsen, D. Horen, J. Rapaport and E. Sugarbaker, Nucl. Phys. **A469** (1987) 125, and references therein.

[2] J. Rapaport and E. Sugarbaker, Ann. Rev. Nucl. Part. Sci. 44 (1994) 109.

[3] W.P. Alford and B.M. Spicer, Adv. Nucl. Phys. **24** (1998) 1.

[4] H. Condé, S. Hultqvist, N. Olsson, T. Rönnqvist, R. Zorro, J. Blomgren, G. Tibell, A. Håkansson, O. Jonsson, A. Lindholm, L. Nilsson, P.-U. Renberg, A. Brockstedt, P. Ekström, M. Österlund, F.P. Brady and Z. Szeflinski, Nucl. Instr. Meth. **A292** (1990) 121.

[5] J. Klug, J. Blomgren, A. Ataç, B. Bergenwall, S. Dangtip, K. Elmgren, C. Johansson, N. Olsson, J. Rahm, O. Jonsson, L. Nilsson, P.-U. Renberg, P. Nadel-Turonski, A. Ringbom, A. Oberstedt, F. Tovesson, C. Le Brun, J.-F. Lecolley, F.-R. Lecolley, M. Louvel, N. Marie, C. Schweitzer, C. Varignon, Ph. Eudes, F. Haddad, M. Kerveno, T. Kirchner, C. Lebrun, L. Stuttgé, I. Slypen, A. Prokofiev, A. Smirnov, R. Michel, S. Neumann, U. Herpers, to be published.

[6] H. Condé, N. Olsson, E. Ramström, T. Rönnqvist, R. Zorro, J. Blomgren, A. Håkansson, G. Tibell, O. Jonsson, L. Nilsson, P.-U. Renberg, M. Österlund, W. Unkelbach, J. Wambach, S.Y. van der Werf, J. Ullmann and S.A. Wender, Nucl. Phys. **A545** (1992) 785.

[7] T. Rönnqvist, H. Condé, N. Olsson, E. Ramström, R. Zorro, J. Blomgren, A. Håkansson, A. Ringbom, G. Tibell, O. Jonsson, L. Nilsson, P.-U. Renberg, S.Y. van der Werf, W. Unkelbach and F.P. Brady, Nucl. Phys. **A563** (1993) 225.

[8] N. Auerbach, L. Zamick and A. Klein, Phys. Lett. **B118** (1982) 256.

[9] A. Ringbom, G. Tibell, J. Blomgren, H. Condé, K. Elmgren, N. Olsson, J. Rahm, T. Rönnqvist, O. Jonsson, L. Nilsson, P.-U. Renberg, Chr. Bargholtz, K. Fransson, K. Lindh, P.-E. Tegnér, P. Thörngren-Engblom, accepted for publication in Nucl. Phys. A.

[10] I. Daito, H. Akimune, S.M. Austin, D. Bazin, G.P.A. Berg, J.A. Brown, B.S. Davids, Y. Fujita, H. Fujimura, M. Fujiwara, R. Hazama, T. Inomata, K. Ishibashi, J. Jaenecke, S. Nakayama, K. Pham, D.A. Roberts, B.M. Sherrill, M. Steiner, A. Tamii, M. Tanaka, H. Toyokawa and M. Yosoi, Phys. Lett. **B418** (1998) 27.

[11] T.-S.H. Lee and D.O. Riska, Phys. Rev. Lett. **70** (1993) 2237.

[12] C. Horowitz, H.O. Meyer and D.K. Griegel, Phys. Rev. **C49** (1994) 1337.

[13] A. Celler, S. Yen, W.P. Alford, R. Abegg, B.A. Brown, S. Burzynski, D. Frekers, O. Häusser, R. Helmer, R.S. Henderson, K. Hicks, K.P. Jackson, R. Jeppesen, C.A. Miller, M.A. Moinester, B.W. Pointon, A. Trudel and M. Vetterli, Phys. Rev. **C47** (1993) 1563.

[14] D.S. Sorensen, X. Aslanoglou, F.P. Brady, J.R. Drummond, R.C. Haight, C.R. Howell, N.S.P. King, A. Ling, P.W. Lisowski, B.K. Park, J. Rapaport, J.L. Romero, W. Tornow and J.L. Ullmann, Phys. Rev. **C45** (1992) R500.

[15] J.L. Mildenberger, W.P. Alford, A. Celler, O. Häusser, K.P. Jackson, B. Larson, B. Pointon, A. Trudel, M.C. Vetterli and S. Yen, Phys. Rev. **C43** (1991) 1777.

[16] S. Dangtip, J. Blomgren, N. Olsson, H. Condé, K. Elmgren, J. Rahm, A. Ringbom, G. Tibell, O. Jonsson, L. Nilsson, P.-U. Renberg, S.Y. van der Werf, Nucl. Phys. **A677** (2000) 3.

[17] B. Pugh, Ph.D. Thesis, MIT (1985) (unpublished).

[18] M. Moe and P. Vogel, Ann. Rev. Nucl. Part. Sci. **44** (1994) 247.

[19] S. Mordechai and C. Fred Moore, Nature **352** (1991) 393.

[20] Ph. Chomaz and N. Frascaria, Phys. Rep. **252** (1995) 275.

[21] H. Primakoff and S. P. Rosen, Ann. Rev. Nucl. Part. Sci. **31** (1981) 145.

[22] W. C. Haxton and J. Stephenson, Prog. Part. Nucl. Phys. **12** (1984) 409.

[23] N. Auerbach, L. Zamick and D. C. Zheng, Ann. Phys. **192** (1989) 77.

[24] A. Erell, J. Alster, J. Lichtenstadt, M.A. Moinester, J.D. Bowman, M.D. Cooper, F. Irom, H.S. Matis, E. Piasetzky, U. Sennhauser, Phys. Rev. **C34** (1986) 1822

[25] G. Bertsch, private communication.

[26] C. Bertulani, Nucl. Phys. **A554** (1993) 493.

[27] J. Blomgren, K. Lindh, N. Anantaraman, Sam M. Austin, G.P.A. Berg, B.A. Brown, J.-M. Casandjian, M. Chartier, M.D. Cortina-Gil, S. Fortier, M. Hellström, J.R. Jongman, J.H. Kelley, A. Lepine-Szily, I. Lhenry, M. Mac Cormick, W. Mittig, J. Nilsson, N. Olsson, N.A. Orr, E. Ramakrishnan, P. Roussel-Chomaz, B. Sherrill, P.-E. Tegnér, J.S. Winfield, J.A. Winger, Phys. Lett. **B362** (1995) 34.

[28] T. Rönnqvist, H. Condé, N. Olsson, R. Zorro, J. Blomgren, G. Tibell, O. Jonsson, L. Nilsson, P.-U. Renberg and S.Y. van der Werf, Phys. Rev. **C45** (1992) R496.

[29] T.E.O. Ericson, B. Loiseau, J. Nilsson, N. Olsson, J. Blomgren, H. Condé, K. Elmgren, O. Jonsson, L. Nilsson, P.-U. Renberg, A. Ringbom, T. Rönnqvist, G. Tibell, R. Zorro, The πNN Coupling from High Precision np Charge Exchange at 162 MeV, Phys. Rev. Lett. **75** (1995) 1046.

[30] J. Rahm, J. Blomgren, H. Condé, S. Dangtip, K. Elmgren, N. Olsson, T. Rönnqvist, R. Zorro, A. Ringbom, G. Tibell, O. Jonsson, L. Nilsson, P.-U. Renberg, T.E.O. Ericson and B. Loiseau, Phys. Rev. **C57** (1998) 1077.

[31] J. Rahm, J. Blomgren, H. Condé, S. Dangtip, K. Elmgren, N. Olsson, T. Rönnqvist, R. Zorro, O. Jonsson, L. Nilsson, P.-U. Renberg, A. Ringbom, G. Tibell, S.Y. van der Werf, T.E.O. Ericson and B. Loiseau, (submitted for publication).

[32] J. Blomgren, N. Olsson, J. Rahm, Physica Scripta **T87** (2000) 33.

[33] Proceedings of Workshop on critical issues in the determination of the pion-nucleon coupling constant, ed. J. Blomgren, Physica Scripta **T87**.

Appendix II

Development of a Tagged Neutron Facility for Neutron Scattering Experiments at Intermediate Energies *

T. Peterson[a], L.C. Bland[a], J. Blomgren[b], W.W. Jacobs[a], T. Kinashi[a], A. Klyachko[a], P. Nadel-Turonski[c], L. Nilsson[c], N. Olsson[b], J. Rapaport[d], T. Rinckel[a], E.J. Stephenson[a], S.E. Vigdor[a], S.W. Wissink[a], and Y. Zhou[a]

[a]Indiana University Cyclotron Facility, Bloomington, Indiana 47408, USA

[b]Department of Neutron Research, Uppsala University, Uppsala, Sweden

[c]The Svedberg Laboratory, Uppsala University, Uppsala, Sweden

[d]Ohio University, Athens, Ohio 45701, USA

We describe the ongoing development of a tagged neutron facility at the Indiana University Cooler. The neutrons are produced via the interaction of a stored 200 MeV proton beam with a deuterium gas jet target. Energy and position measurements of the two low-energy recoil protons in the reaction $p + d \rightarrow n + 2p$ provide the information necessary to determine the neutron four-momentum event by event and to thereby measure the absolute flux of neutrons incident on the secondary target directly. The first proposed experiment using this tagged neutron beam will be an absolute $\pm$ 1% measurement of the np backscattering cross section.

1. INTRODUCTION

A difficulty which has plagued neutron scattering experiments in the past is that of accurately determining the flux of neutrons incident upon the target. The uncertainty in neutron flux has often been the dominant source of systematic uncertainty, and the data from many neutron differential cross section measurements have been presented as relative only.

One specific area where an absolute neutron scattering cross section measurement would be of great impact is in np backscattering and its use in determining the charged pion-nucleon coupling constant, g_c^2. The uncertainty in recent determinations of g_c^2, both from phase-shift analyses [1] and pole extrapolation [2], is dominated by the normalization uncertainty in the np differential cross section. An absolute measurement of the np differential cross section to $\pm$ 1% would further provide an important check of the Nijmegen PWA [3], which its creators claim gives $\pm 0.7\%$ accuracy for the normalization, although none of the cross section data included in their fits has a normalization uncertainty that approaches this level of precision.

2. EXPERIMENTAL TECHNIQUE

2.1. Neutron Tagging

The tagged neutron facility is located in the T-region of the Indiana Cooler. The neutrons are produced via the reaction $p + d \to n + 2p$ with a circulating proton beam of bombarding energy 200 MeV incident on a deuterium gas jet target (GJT). The presence of a 6° bending magnet in the ring allows for the centering of the secondary target at 14° exiting neutron angle. At small neutron angles the predominance of the $^1S_0$ final state interaction for the two protons results in a neutron beam of narrow energy spread (~ 10 MeV).

The 'tagging' of the neutrons is accomplished by detection of the associated recoil protons in a silicon detector array located in vacuum. The detection of two protons in coincidence signals the production of a neutron, while energy and position measurements on the recoil protons allow for reconstruction of the four-momentum of the neutron. Knowledge of the neutron's four-momentum then makes it possible not only to determine whether the neutron is incident on the secondary target, but also where it is incident on the target and with what bombarding energy.

It is important to point out some aspects of this 'beam' of tagged neutrons. First, not all neutrons that are incident on the secondary target are tagged. However, by requiring that a tag be associated with all neutron scattering events, these untagged neutrons do not enter into the analysis. Second, not all neutrons that are tagged are incident on the secondary target. Good energy and position measurements on the recoil protons from the production reaction are thus required in order to accurately identify those neutrons that do impinge on the secondary target. We expect to achieve $\lesssim 100$ keV neutron energy resolution and $\lesssim 1$ mm position uncertainty for location on target. For a time-averaged primary luminosity of 10^{31} cm^{-2}s^{-1}, the expected tagged neutron rate is ~ 2 kHz.

The recoil proton detectors (the 'tagger') consist of an array of four silicon double-sided strip detectors (DSSDs), each backed by a large area silicon pad detector. Each detector has an active area of approximately 6.4 × 6.4 cm^2 and thickness of 500 μm. The strips on the two sides of the DSSDs are orthogonal, and the readout pitch is ~ 0.5 mm, yielding a total of 1024 channels (excluding the silicon pad detectors). The front-end electronics for the DSSDs are comprised of pairs of 32-channel application specific integrated circuits (ASICs) located in vacuum. The ASICs, the VA32_hdr2 and TA32C [4], provide pulse-height information for each channel along with a single fast logic output from each chip set for triggering and timing purposes. This allowance for self-triggering of the DSSD readout is a novel feature of the front-end electronics, and one essential to measuring the absolute tagged neutron flux on the secondary target. The silicon pad backing detectors are needed in order to relieve neutron reconstruction ambiguities caused by recoil protons that have sufficient energy to penetrate through a DSSD. A schematic view of the arrangement of the tagging detectors is shown in Fig. 1.

2.2. Neutron Scattering

For the np differential cross section measurement, the tagged neutrons will impinge upon a liquid hydrogen target of 4 cm thickness located approximately 1 m from the gas jet target and subtending a solid angle of ~ 15 msr. The detection of neutron backscattering events will be achieved via the detection of the forward scattered proton in a detector
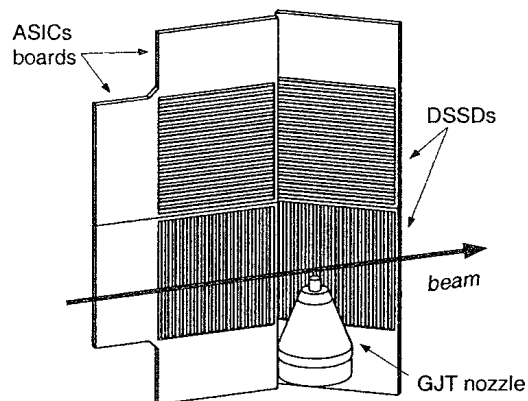
Figure 1. Schematic view of the tagger. The silicon pad detectors, one located immediately behind each DSSD, are not visible in this figure.
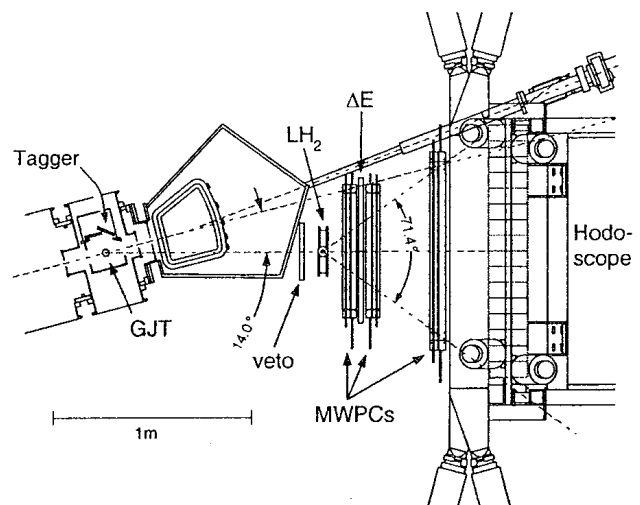
Figure 2. A top view of the experimental setup for the np scattering experiment.

array of large acceptance. This forward detector array, shown in Fig. 2, consists of 9 planes of wire chambers for proton tracking, as well as a large area ΔE/start scintillator and 20 element scintillator hodoscope for triggering and energy measurements. Nearly complete azimuthal coverage is provided for neutron scattering with $\theta_{cm} \gtrsim 90°$. The angular resolution for scattered protons will be $\approx 0.5°$. Comparison of the interaction position in the target from scattered proton tracking to that predicted from the neutron tag will provide a check on the accuracy of the four-momentum reconstruction of the tagged neutrons. In addition, data for neutron scattering at mid-angles $(60° \lesssim \theta_{cm} \lesssim 90°)$ will be gathered simultaneously, though with poorer statistics, via the detection of the scattered protons and neutrons in coincidence. This mid-angle data will facilitate comparison of the measured angular distribution to the total np cross section.

The experiment has many built-in crosschecks aimed at controlling possible sources of error. In addition to the primary event streams that measure the neutron flux and np backscattering, data from pd elastic scattering is acquired simultaneously. The pd elastic scattering is to be used as a luminosity monitor to aid in normalizing empty target background runs to full-target runs. The forward going protons from pd scattering also provide a tagged proton beam with which to measure pp scattering in the LH_2 for the purpose of monitoring the product of the target thickness and solid angle of the forward detector array. The setup also allows for a direct measurement of the hodoscope neutron detection efficiency, providing both calibration information for the mid-angle coincidence events and an additional test of the accuracy of the tagged neutron reconstruction. The accuracy of the tagged neutron beam profile can further be checked by observing the consistency of np absolute cross sections extracted from different interaction position regions on the secondary target.

3. STATUS AND PLANS

The forward detector stack for the neutron scattering measurements is in place and has been commissioned with beam. The recoil detector system for performing the neutron tagging is undergoing beam commissioning during summer 1999. The liquid hydrogen target for use in the np scattering experiment is currently under construction. Neutron tagging tests and initial np scattering measurements on a plastic scintillator target will be conducted in 1999, with the primary np scattering data taking with the LH_2 target scheduled to take place in 2000.

Other possible experiments using the tagged neutron facility are under consideration. The method can be extended to other neutron energies in a straightforward manner. Depending on the results of the initial np scattering measurement, further np measurements at other energies may be performed. By simply replacing the hydrogen in the LH_2 target with deuterium, an absolute measurement of the nd elastic scattering cross section could be made. Such an experiment might shed light on the nature of the three-nucleon force, which has been predicted [5] to play an important role in the region of the angular distribution minimum.

It should also be possible to create a beam of polarized tagged neutrons, taking advantage of the sizable spin transfer coefficient, D_{SS}, in the neutron production reaction. One could then, for example, measure the cross section and analyzing power in the reaction $\vec{n} + p \rightarrow 2p + \pi^-$ near threshold. In this case it is the event-by-event knowledge of the neutron four-momentum that facilitates a near threshold measurement not possible with traditional neutron sources due to the rapid cross section variation with energy.

REFERENCES

1. D.V. Bugg and R. Machleidt, Phys. Rev. C **52** (1995) 1203.
2. T.E.O. Ericson *et al.*, Phys. Rev. Lett. **75** (1995) 1046.
3. V.G.J. Stoks, R.A.M. Klomp, M.C.M. Rentmeester, and J.J. de Swart, Phys. Rev. C **48** (1993) 792.
4. Manufactured by Integrated Detectors & Electronics AS, Veritasveien 9, N-1322 Hovik, Norway.
5. H. Witala *et al.*, Phys. Rev. Lett. **81** (1998) 1183.

Appendix III

Tagged Neutron Production with a Storage Ring[1]

Todd Peterson* for the TNT collaboration

*Indiana University Cyclotron Facility
Bloomington, Indiana 47408

Abstract. We describe the ongoing development of TNT, the T-region Neutron Tagger. As a way of overcoming the problem of normalization in neutron scattering experiments, we are developing a facility to tag the production of neutrons on an event-by-event basis. The neutrons are produced using the reaction $p + d \rightarrow n + 2p$ with a 200 MeV circulating proton beam incident on a deuterium gas jet target in the Indiana Cooler. The tagging of a neutron is accomplished via the detection of the two low energy recoil protons in an array of double-sided silicon strip detectors. A tagged neutron beam makes possible absolute neutron cross section measurements, and the first experiment that will be done using this tagged neutron facility is a measurement of the np backscattering cross section. Some other possible experiments using tagged neutrons are also presented.

INTRODUCTION

A difficulty which has plagued neutron scattering experiments in the past is that of accurately determining the flux of neutrons incident upon the target. The uncertainty in neutron flux has often been the dominant source of systematic uncertainty, and the data from many neutron induced charged particle differential cross section measurements have been presented as relative only.

One specific area where an absolute neutron scattering cross section measurement would be of great impact is in np backscattering. Not only does the existing data suffer from the problem with normalization, but there are large datasets which are in apparent disagreement with one another. In spite of this, the Nijmegen group claims that their PWA [1] gives $\pm 0.7\%$ accuracy for the normalization, although none of the cross section data included in their fits has a normalization uncertainty that approaches this level of precision. A measurement with an absolute uncertainty near this level would provide an important test of the Nijmegen claim. Furthermore, the normalization of np cross sections is an issue in the ongoing controversy over the proper value of the charged pion-nucleon coupling constant, g_c^2. The largest source

---

of systematic error in recent determinations of g_c^2 using np scattering data, both from phase-shift analyses [2] and pole extrapolation [3], is due to the normalization uncertainty in the np differential cross section. In order to try to address these issues, we set about developing a tagged neutron facility with the goal of measuring the absolute np differential cross section at back angles to $\sim \pm 1\%$.
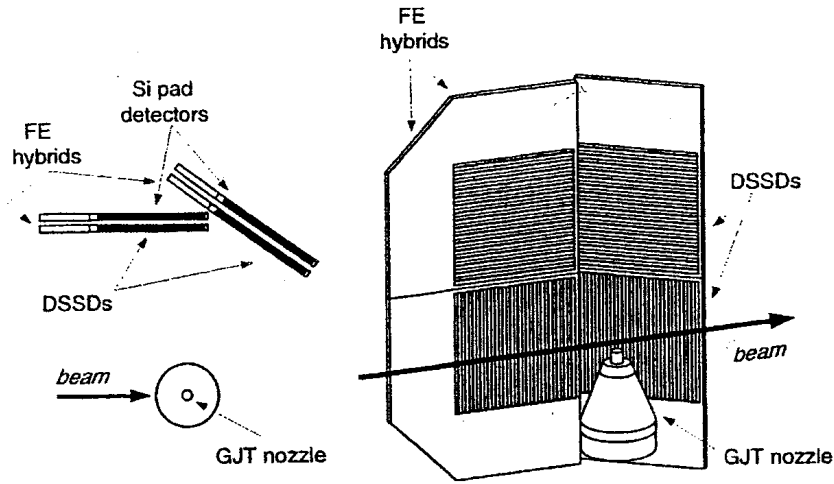
TAGGING NEUTRONS

The TNT (T-region Neutron Tagger) facility is located in the T-region of the Indiana Cooler. The neutrons are produced via the reaction $p + d \rightarrow n + 2p$ with a circulating proton beam of bombarding energy 200 MeV incident on a deuterium gas jet target (GJT). The presence of a 6° bending magnet in the ring allows for the centering of the secondary target at 14° exiting neutron angle. At small neutron angles the predominance of the $^1S_0$ final state interaction for the two protons results in a neutron beam of narrow energy spread ($\sim$10 MeV).

The "tagging" of the neutrons is accomplished by detection of the two recoil protons in a silicon detector array (the "tagger") located in vacuum. The detection of two protons in coincidence signals the production of a neutron, while energy and position measurements on the recoil protons allow for complete reconstruction of the four-momentum of the neutron. Knowledge of the neutron's four-momentum then makes it possible not only to determine whether the neutron is incident on the secondary target, but also where it is incident on the target and with what bombarding energy.

It is important to point out some aspects of this "beam" of tagged neutrons. First, not all neutrons that are incident on the secondary target are tagged. Simulations indicate that the tagging efficiency for neutrons incident on the secondary target will be $\sim$40%. However, by requiring that a tag be associated with all neutron scattering events, the untagged neutrons do not enter into the analysis. Second, not all neutrons that are tagged are incident on the secondary target. Good energy and position measurements on the recoil protons from the production reaction are thus required in order to accurately identify those neutrons that do impinge on the secondary target. We hope to achieve $\lesssim$100 keV neutron energy resolution (FWHM) and $\lesssim$1 mm position uncertainty for location on target. While the uncertainty in position has a lower limit arising from the granularity of the recoil detectors, the resolution achieved for both neutron impact position and energy ultimately depend on the energy resolution attained in the detection of the recoil protons. For a time-averaged primary luminosity of 10^{31} cm^{-2}s^{-1}, the expected tagged neutron rate is $\sim$2 kHz. The actual operating luminosity used will depend on the rate of false neutron tags arising from accidental coincidences.

The tagger consists of an array of four silicon double-sided strip detectors (DSSDs), each backed by a large area silicon pad detector. Each detector has an active area of approximately 6.4×6.4 cm^2 and thickness of 500 μm. The strips on the two sides of the DSSDs are orthogonal, and the readout pitch is $\simeq$0.5 mm,

FIGURE 1. Top and side views showing the arrangement of the neutron tagging detectors with respect to the gas jet target (GJT).

yielding a total of 1024 channels (excluding the silicon pad detectors). The front-end electronics for the DSSDs are comprised of pairs of 32-channel application specific integrated circuits (ASICs) located in vacuum. The ASICs, the VA32_hdr2 and TA32C [4], provide pulse-height information for each channel along with a single fast logic output from each chip set for triggering and timing purposes. This allowance for self-triggering of the DSSD readout is a novel feature of the front-end electronics, and one essential to measuring the absolute tagged neutron flux on the secondary target. The trigger electronics are set up such that, in most cases, a neutron can be tagged even when both recoil protons impinge upon the same silicon detector. The silicon pad detectors located behind the DSSDs are needed in order to relieve neutron reconstruction ambiguities caused by recoil protons that have sufficient energy to penetrate through a DSSD. A schematic view of the arrangement of the tagging detectors is shown in Figure 1.

One issue with which we must contend is the fact that the gas jet target is an extended target. Because only one (x, y) position measurement is made on each recoil proton, we need to know the event origin in order to determine the proton angles and, therefore, the neutron angles. The event vertex is determined by calculating the magnitude of the outgoing neutron's momentum using both conservation of energy and conservation of momentum. The neutron's momentum using energy conservation is

$$p_{EC} = \sqrt{(E_i - E_{p1} - E_{p2})^2 - m_n^2} \qquad (1)$$

where E_i is the initial energy of the system (beam proton plus target deuteron), E_{p1} and E_{p2} are the energies of the two recoil protons, and the quantity is independent of the vertex position. In calculating the neutron's momentum using momentum conservation, we take the event origin to be along the central beam axis. The

237

momentum is then only a function of z, the location along the beam direction,

$$\vec{p}_{MC}(z) = \vec{p}_i - \vec{p}_{p1}(z) - \vec{p}_{p2}(z). \tag{2}$$

By forming the quantity,

$$\Delta p(z) \equiv p_{EC} - p_{MC}(z), \tag{3}$$

we can determine the event origin by using a bisection method to find where $\Delta p(z) = 0$. Simulations show that the quantity $\Delta p(z)$ is single-valued, and the distribution of event origins from experimental data reproduce the expected product of the longitudinal density profile of the gas jet target and the tagging acceptance.

NEUTRON SCATTERING

For the np differential cross section measurement, the tagged neutrons will impinge upon a liquid hydrogen target of 4 cm thickness located approximately 1 m from the gas jet target and subtending a solid angle of $\approx$15 msr. The detection of neutron backscattering events will be achieved via the detection of the forward scattered proton in a detector array of large acceptance. This forward detector array, shown in Figure 2, consists of 9 planes of wire chambers for proton tracking, as well as a large area ΔE/start scintillator and 20 element scintillator hodoscope for triggering and energy measurements. Nearly complete azimuthal coverage is provided for neutron scattering with $\theta_{cm} \geq 90°$. The angular resolution for scattered protons will be about 0.5°.

As previously mentioned, the four-momentum reconstruction of the neutron will allow us to predict where it passes through the target. We can then do a traceback to the target volume for the forward scattered proton and determine the distance of closest approach of the two tracks. This comparison of the interaction position in the target from scattered proton tracking to that predicted from the neutron tag will provide a check on the accuracy of the four-momentum reconstruction of the tagged neutrons. Good agreement here is necessary in order to attain confidence in the neutron flux determination, since this will depend critically on our ability to determine whether the tagged neutrons which do not undergo scatterings in the secondary target actually passed through it.

Because the detectors comprising the scintillator hodoscope have reasonable neutron detection efficiency ($\approx$20%) in this energy range, we will also be able to collect some neutron scattering data via the detection of neutrons in coincidence with the scattered protons. This coincidence data can be obtained simultaneously with the primary scattering data and extends the angular coverage to $\theta_{cm} \gtrsim 60°$. Although this mid-angle data will be collected with poorer statistics, it will facilitate comparison of the measured angular distribution to the total np cross section.

The experiment has been designed with many built-in crosschecks aimed at controlling possible sources of systematic error. In addition to the primary event
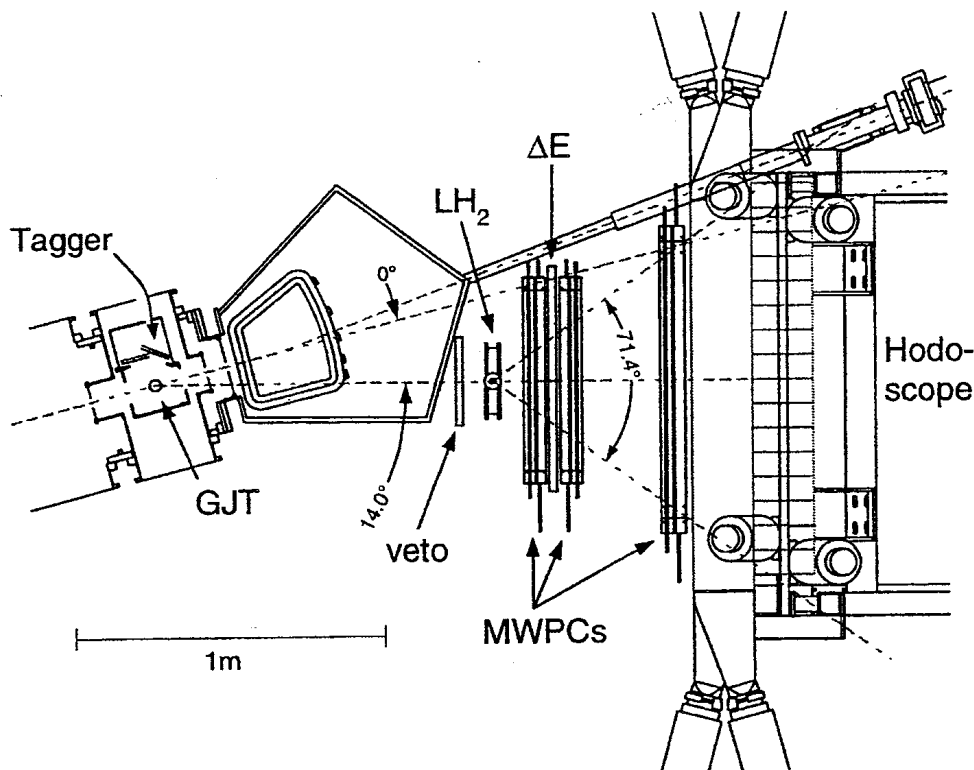
FIGURE 2. A top view of the experimental setup for the np scattering experiment. The circulating proton beam is bent by 6° (indicated by the upper right track) by a dipole magnet, allowing the secondary target and forward detector stack to be centered at 14° neutron emission angle.

streams that measure the neutron flux and np backscattering, data from pd elastic scattering are acquired simultaneously. The pd elastic scattering data will be used as a luminosity monitor to aid in normalizing empty target background runs to full-target runs. The forward going protons from pd scattering also provide a tagged proton beam with which to measure pp scattering in the LH_2 for the purpose of monitoring the product of the target thickness and solid angle of the forward detector array. Because tagged neutrons will also be incident on the scintillator hodoscope, the setup allows for a direct measurement of the hodoscope neutron detection efficiency. This efficiency data provides calibration information for the mid-angle coincidence events, while at the same time giving us an additional means for testing the accuracy of the tagged neutron reconstruction. A particularly powerful crosscheck will be made possible by the combination of the large area target together with a prediction for where each neutron passes through it. By subdividing the target into smaller target bins in the analysis, a comparison can be made of the cross section determinations for each bin. The requirement of agreement for these logically separate measurements will impose a stringent test on the accuracy of the neutron flux determination. Taken as a whole, these many crosschecks should make it possible to approach the goal of ±1% absolute accuracy.

STATUS

We have conducted a test of the neutron tagging method, where a two-dimensional position-sensitive silicon detector (2D-PSD) used in previous Cooler experiments took the place of the full tagger. The forward detector stack for the neutron scattering measurements was in place for this test. While the 2D-PSD had much lower tagging efficiency and poorer position resolution than the final tagger will have, this beam test was useful for both commissioning the forward detectors and demonstrating that the general tagging principle is sound. Figure 3 demonstrates that we were able both to predict the neutron position on target and to detect and trace back the scattered proton with reasonable precision in that first test. This test run also yielded important information for the design of the final tagger system. In particular, the points falling above the diagonal in Figure 3(a) were determined to come from cases where one of the recoil protons possessed sufficient energy to pass all the way through the 2D-PSD. This effect is clearly seen in the simulated events shown in Figure 3(b). It was the neutron reconstruction errors from these cases that led us to include silicon pad detectors behind the DSSDs, as described previously in the section on tagging neutrons.

After extensive development work on the interface electronics for the tagger readout, the tagger underwent its first beam test in July of 1999. The primary focus of this run was on setting up the trigger logic and timing for the various event streams. Data was collected for pd elastic scattering, where the deuteron is detected in the tagger array. Figure 4 shows the energy deposited in the tagger versus the position of the forward-going charged particle at the first wire chamber. The kinematic
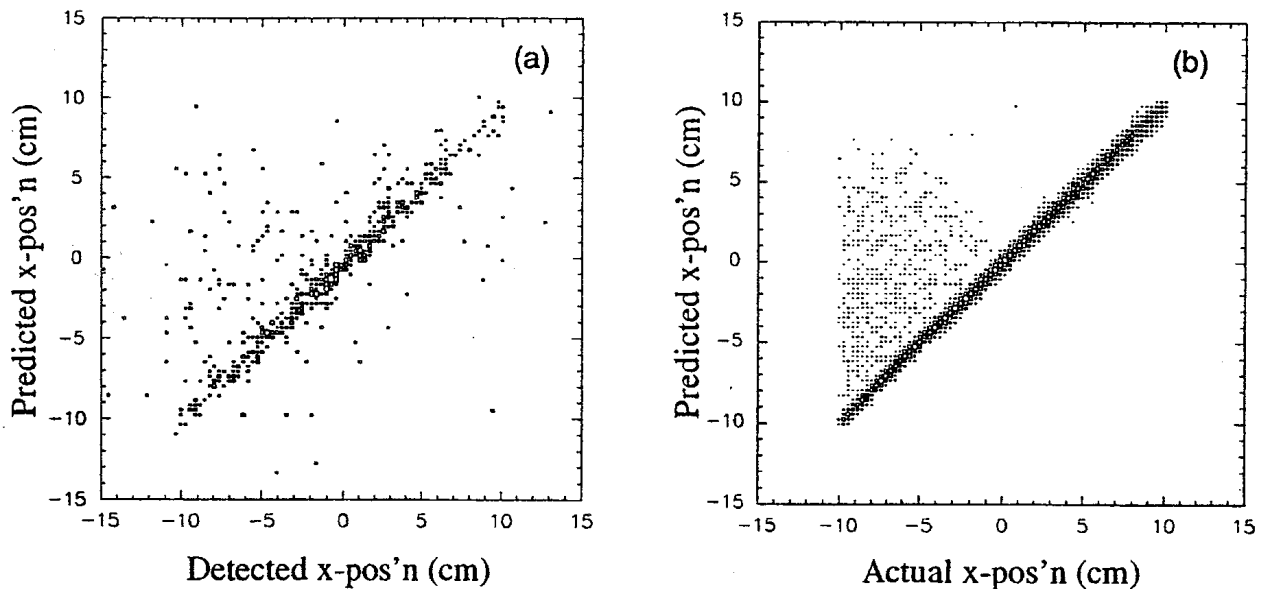

FIGURE 3. (a) Plot of predicted neutron position on the secondary target vs. the target position determined from the scattered proton traceback. (b) Results of a simulation showing the predicted neutron position on the secondary target vs. the actual position on target.
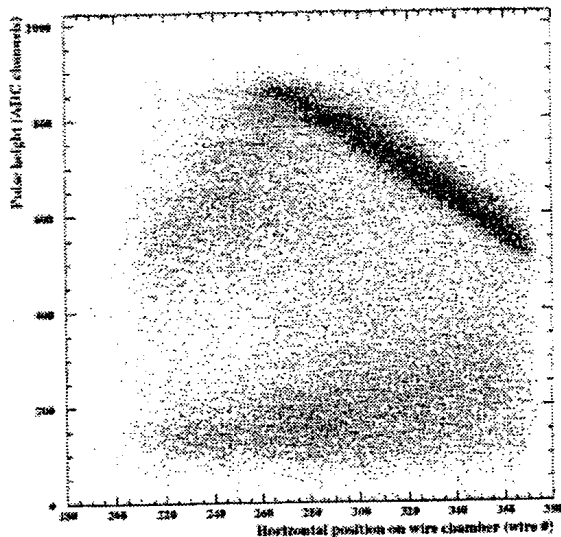
FIGURE 4. Plot of the pulse height in a silicon detector versus the position of the forward-going particle in the first wire chamber. The dark band corresponds to *pd* elastic scattering events where the deuteron is incident on the silicon detector array.
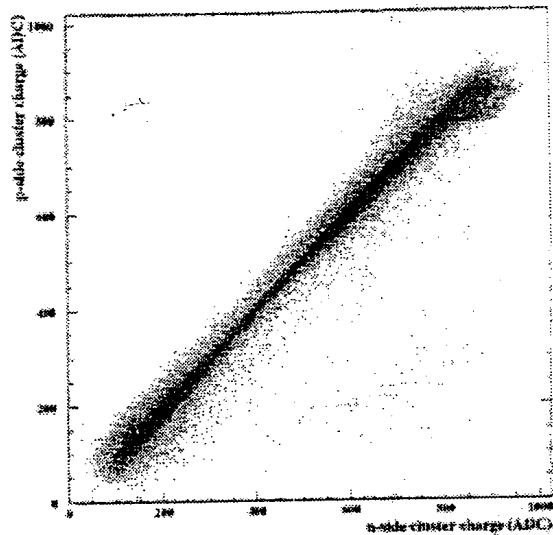
FIGURE 5. Plot of the charge correlation for the two sides of a silicon detector for the events shown in Figure 4.

correlation from the *pd* elastic events can be clearly distinguished. An important issue in the tagged neutron reconstruction will be the ability to correctly assign the (x, y) coordinates to the recoil protons in cases where they impinge on the same silicon detector. This task depends on the energy resolution and gain matching of the readout of the two sides of the detector. Figure 5 shows the charge correlation between the two sides of a detector for the events appearing in Figure 4. Given the improvement in noise reduction subsequent to the first beam test, we are confident that we should be able reliably reconstruct the vast majority of events with two particles in a single tagging detector.

The liquid hydrogen target for use in the *np* scattering experiment is currently under construction. Additional tagging tests and initial *np* scattering measurements will be conducted using a plastic scintillator target. The primary *np* scattering data taking with the LH$_2$ target is scheduled to take place in 2000.

FUTURE POSSIBILITIES

Other possible experiments using the tagged neutron facility are under consideration. The method should be extendable to other neutron energies in a straightforward manner, although further study is necessary to determine how the tagged neutron flux varies with incident proton beam energy. Depending on the results of the initial *np* scattering measurement, further *np* measurements at other energies may be performed. By simply replacing the hydrogen in the LH$_2$ target with deuterium, an absolute measurement of the *nd* elastic scattering cross section could

be made. Such an experiment might shed light on the nature of the three-nucleon force, which has been predicted [5] to play an important role in the region of the angular distribution minimum.

It should also be possible to create a beam of polarized tagged neutrons, taking advantage of the sizable spin transfer coefficient, D_{SS}, in the neutron production reaction. One could then, for example, measure the cross section and analyzing power in the reaction $\vec{n} + p \rightarrow 2p + \pi^-$ near threshold. In this case it is the event-by-event knowledge of the neutron four-momentum that facilitates a near threshold measurement not possible with traditional neutron sources due to the rapid cross section variation with energy.

CONCLUSION

The TNT facility currently under development will be a unique facility for medium energy neutron scattering experiments. The method used to tag neutrons capitalizes on the low energy recoil detection made possible by the storage ring environment. The ability to produce a beam of tagged neutrons opens up a number of interesting experimental possibilities. In particular, knowledge of the neutron flux will make possible an absolute np differential cross section measurement.

ACKNOWLEDGMENTS

REFERENCES

1. V.G.J. Stoks, R.A.M. Klomp, M.C.M. Rentmeester, and J.J. de Swart, Phys. Rev. C **48**, 792 (1993).
2. D.V. Bugg and R. Machleidt, Phys. Rev. C **52**, 1203 (1995).
3. J. Rahm *et al.*, Phys. Rev. C **57**, 1077 (1998).
4. Manufactured by Integrated Detectors & Electronics AS, Veritasveien 9, N-1322 Hovik, Norway.
5. H. Witala *et al.*, Phys. Rev. Lett. **81** (1998) 1183.

Appendix IV

Neutron decay of deep hole states and isobaric analog states in ^{115}Sn populated by the (^{3}He,α) reaction at 102 MeV

P.-O. Söderman [a], A. Ringbom [a], J. Blomgren [b,*], N. Olsson [b], L. Nilsson [c],
J.A. Bordewijk [d], S. Brandenburg [d], G. van 't Hof [d], M.A. Hofstee [d],
H. van der Ploeg [d], S.Y. van der Werf [d], A. Krasznahorkay [e], A. Bałanda [f],
D. Chmielewska [g], H. Laurent [h]

[a] Department of Radiation Sciences, Uppsala University, Box 535, S-75121 Uppsala, Sweden
[b] Department of Neutron Research, Uppsala University, Box 525, S-75120 Uppsala, Sweden
[c] The Svedberg Laboratory, Uppsala University, Box 533, S-75121 Uppsala, Sweden
[d] Kernfysisch Versneller Instituut, Zernikelaan 25, 9747 AA Groningen, The Netherlands
[e] Nuclear Research Institute of the Hungarian Academy of Sciences, Debrecen, PO Box 51, H-4001, Hungary
[f] Jagiellonian University, Cracow, Poland
[g] Soltan Institute for Nuclear Studies, 05-400 Swierk, Poland
[h] Institut de Physique Nucleaire, 91406 Orsay cedex, France

Abstract

Neutron decay of excited hole states and isobaric analog states (IAS) populated by the ^{116}Sn(^{3}He,α) reaction at an energy of 102 MeV has been investigated. The α-particles were analysed in a magnetic spectrograph positioned at 1.4° and detected with a multiwire drift chamber. Excitation energies in ^{115}Sn up to 23 MeV were studied. An array of neutron detectors was positioned around the target at angles ranging from 68° to 209°. The neutron data were analysed in terms of decay into final states, using statistical model calculations as a tool to extract lower limits of nonstatistical decay. Nonstatistical decay was observed from states up to an excitation energy of about 18 MeV. The neutron emission of the IAS is compatible with 100% statistical decay. © 2001 Elsevier Science B.V. All rights reserved.

---

* Corresponding author.
  E-mail address: jan.blomgren@tsl.uu.se (J. Blomgren).

1. Introduction

Deep-hole states have been observed using pickup reactions with light-ion beams since the beginning of the seventies. By now, a large body of information on their excitation energies, spins and spectroscopic factors have been extracted. For a comprehensive summary see Ref. [1].

To gain insight into the microscopic structure and damping mechanism of these relatively simple states in nuclei new approaches are needed. One very promising approach, previously applied to giant resonances [2–5], is the investigation of their neutron decay. The deep-hole states above the nucleon emission thresholds decay, due to the height of the Coulomb barrier in medium-weight to heavy nuclei, predominantly by neutron emission.

One of the most studied nuclei when it comes to deep-hole states is ^{115}Sn. Neutron-hole states in ^{115}Sn have been studied via the (p,d), (d,t) and (^{3}He,α) reactions by a large number of authors up to an excitation energy of about 15 MeV with good energy resolution (see, e.g., Refs. [6–12]). Deep neutron-hole states in ^{115}Sn up to $E_x = 50$ MeV have been studied by Langevin-Joliot et al. [13] using the (^{3}He,α) reaction at a beam energy of 283 MeV. Spectroscopic factors and spins for all low-lying well-resolved states have been determined and suggestions for spin and spectroscopic factors for the broader structures up to 50 MeV exist.

Around 14 MeV in ^{115}Sn, a cluster of isobaric analog states (IAS), $T_> = T_0 + 1$, where $T_0 = 15/2$ is the ^{115}Sn ground-state isospin, have been observed. The neutron decay of these states is isospin forbidden since the only states that are energetically reachable with neutron decay have isospin $T_0 - 1/2$, i.e. $\Delta T = 3/2$. The IAS can, however, decay by neutron emission through an isospin impurity, $T = T_0$, in the IAS. The square of the amplitude of this isospin impurity is of the order of one percent. Proton decay, on the other hand, is strongly hindered by the Coulomb barrier. It is interesting to determine the neutron branching ratio for these IAS and to see if the neutron decay is statistical or not, i.e., in which way it contributes to the width of the IAS. The neutron decay of an IAS has previously been observed in only one experiment, Bordewijk et al. [14], where a neutron branching ratio of 37% for the IAS in ^{208}Bi and a completely statistical decay of the neutrons was found.

This paper is devoted to the study of the neutron decay of deep hole and IAS in ^{115}Sn, populated by the (^{3}He,α) reaction at a beam energy of 102 MeV. The experimental techniques and procedure are described in Section 2, while the data reduction and the experimental results are presented in Section 3. Section 4 is devoted to the analysis of the experimental data in terms of statistical and nonstatistical decay, and the results are discussed in Section 5. Finally, a summary and the conclusions are given in Section 6.

2. Experimental apparatus and procedure

The neutron decay of hole states in ^{115}Sn has been studied with the ^{116}Sn(^{3}He,α) reaction at the KVI, Groningen, The Netherlands. A general overview of the experimental

equipment can be found in one of our previous papers [15] where we used the same experimental setup.

A ^{3}He beam, provided from an external ECR ion source, was accelerated to 102 MeV using the KVI AVF cyclotron. The target was a 20.2 mg/cm^2 thick tin foil, enriched to 98.0% in ^{116}Sn, tilted an angle of 45° with respect to the beam direction. The beam intensity (at the target position) was 2 nA.

The emerging α-particles were detected using the QMG/2 magnetic spectrograph [16, 17], for which the entrance aperture was adjusted to accept particles within ±2.9° vertically, and ±2.6° horizontally, giving a solid angle of 8.7 msr. A multiwire drift chamber (MWDC), placed in the focal plane of the spectrograph, gave information on momentum and horizontal scattering angle [18]. The ^{3}He beam was stopped in a Faraday cup inside the first dipole. Special care was taken to avoid rescattering of the beam in the beam stop and to make sure that the α-particles in the focal plane could be selected with gates on the time-of-flight (TOF) in the spectrograph, the horizontal angle in the focal plane, and the energy loss in a plastic scintillator, positioned behind the MWDC. Since the cross sections for exciting deep-hole states are rather small and the angular distributions peak at 0°, it is advantageous to put the spectrometer close to 0° to optimize the coincidence count rate. To obtain axial symmetry one would like to put the spectrometer exactly at zero degrees. As a compromise, satisfying as closely as possible these requirements, the spectrograph was set at an angle of +1.4°, thus covering the horizontal angular range $\theta_\alpha = -1.2°$ to +4.0°.

Neutrons in coincidence with α-particles were detected using the multidetector system EDEN. This detector system has been described in detail in a recent publication [19], and only a brief summary will be given here. EDEN consists of 40 liquid scintillators (NE213), each with a diameter of 20 cm and a thickness of 5 cm, optically coupled via a light guide to a 12.5 cm diameter photomultiplier (PM) tube. For this experiment 39 detectors were used, positioned at angles ranging from 68° to 209° with respect to the ^{3}He-beam direction. The distance from the target to the neutron detectors was 1.75 m, and thus a solid angle of 410 msr was covered. Fifteen detectors were positioned in the horizontal plane, the remaining 24 either just above or just below it. The neutron detectors were shielded from the beam stop inside the first dipole by a wall, consisting of 10 cm of lead and 10 cm of concrete.

Neutron energies were determined using TOF techniques. For each detector the anode pulse was used to start a time-to-digital converter (TDC), while a common stop pulse was derived from the cyclotron RF. This experiment was performed with the cyclotron operating at a frequency of about 10 MHz, which corresponds to a beam burst separation of 100 ns.

It is of special importance in measurements close to zero degrees to have a beam of high quality in order to achieve good resolution in the neutron energy determination, and to reduce the background in the coincidence experiment. High quality means in this context a halo-free beam with short beam bursts and no ghost pulses between the main bursts. This was obtained by taking special care during the beam development [20]. Furthermore, the phase of the cyclotron RF must be extremely stable and was therefore monitored during

the experiment with a small BaF_2 detector placed on top of the scattering chamber. If the phase changed significantly during a run, the run was stopped and a new one started, in order to keep the phase stable within each run. With these precautions, the width of the beam pulse could be kept below 1.2 ns, and the overall time resolution in the neutron TOF spectra was better than 1.6 ns.

Pulse-shape discrimination (PSD) techniques were used to separate neutrons from γ-rays. The pulse-height stability of the neutron detectors was checked repeatedly using ^{241}Am, ^{137}Cs, ^{60}Co and ^{22}Na γ-ray sources between the runs.

The α-particle spectra range from $E_x = 0$ to 23 MeV in ^{115}Sn, corresponding to a maximum neutron energy of 16 MeV. The data set consists of about 120 000 true coincidence events. The experiment was done in two sessions, with slightly different settings of the magnetic field in the spectrograph. The first part, covered $E_x = 0.0$–19.5 MeV, while the second part covered $E_x = 3.5$–23.0 MeV.

3. Data reduction and experimental results

The data were analysed off-line on an event-by-event basis, using the acquisition and analysis program PAX (Ref. [21]). The α-particles were selected by gates on the TOF in the spectrograph, the angle in the focal plane, and the energy loss in the plastic scintillator. Down-scaled singles data were stored in a spectrum with a bin width of 20 keV. Singles α-particle spectra for the two spectrograph magnetic settings are shown (with 80 keV/channel) as dashed and dotted lines in Fig. 1a.

For the coincidence events, the neutron detector pulse-height spectra for all the detectors were brought to the same scale by multiplicative factors and offsets. This could be done using the spectra taken with the γ-ray sources between the runs. A low-level threshold corresponding to a neutron energy of 500 keV was applied, following the procedure described in Ref. [15]. Neutrons were separated from γ-rays by creating a two-dimensional spectrum with the PSD signal versus anode pulse height for each of the 39 detectors. The separation was obtained via individual two-dimensional gates in these spectra. Above the threshold used in this experiment, the neutron–gamma (n–γ) separation was very good.

The neutron TOF versus the cyclotron RF was generated as the difference between two TDC signals, namely the time difference between the neutron detectors and the spectrograph scintillator, and the time difference between the spectrograph scintillator and the cyclotron RF. Both these time spectra were found to be slightly nonlinear and were corrected off line. The neutron TOF spectra were also given different offsets for each of the 39 detectors to align them and facilitate later addition. Neutron-energy spectra were generated from the neutron TOF spectra. Two windows in these spectra were used, one corresponding to prompt neutrons and the other to random coincidences, as is illustrated in the upper panel of Fig. 4 in Ref. [15]. A true coincidence neutron spectrum was obtained for each detector as the difference between these two spectra. Neutron energy spectra gated on 1.6 MeV wide excitation energy bins in ^{115}Sn between $E_x = 8.0$ and 22.4 MeV are shown in Figs. 2 and 3.
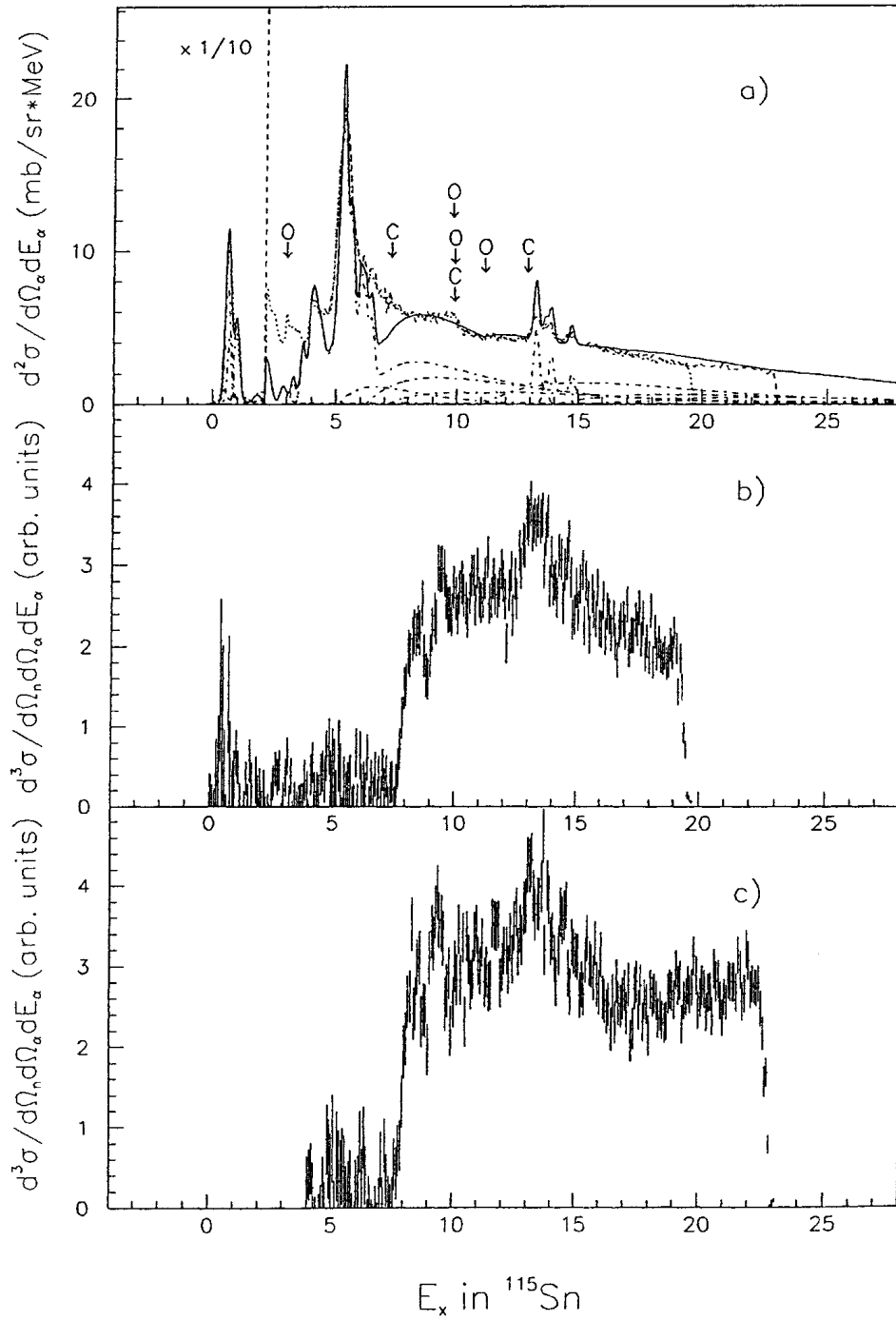
Fig. 1. (a) The α-energy spectrum of the ^{116}Sn(^{3}He,α)^{115}Sn reaction at an incident energy of 102 MeV and an effective angle of 2.5° with a 29.3 mg/cm^2 thick target giving an energy resolution of 300 keV (FWHM). The dot-dashed and dotted lines correspond to different magnetic field settings. The dashed lines are the one-step pick-up contributions for different single-particle orbitals calculated with DWUCK4. The full line is the sum of all single-particle orbitals and represents the prediction for single-step pickup from ^{116}Sn. (b) Alpha spectrum in coincidence with neutrons, obtained with the high-field setting of the spectrograph magnets. The error bars represent statistical uncertainties only. (c) Alpha spectrum in coincidence with neutrons, obtained with the low-field setting of the spectrograph magnets. The error bars represent statistical uncertainties only.

Fig. 2. Experimental neutron-energy spectra gated on 1.6 MeV wide excitation energy bins in [115]Sn between 8.0 and 22.4 MeV (solid circles). The solid and dashed lines represents the CASCADE calculations, using the literature and fitted sets of level-density parameters, respectively (see text). The error bars represent statistical uncertainties only.

Events with an α-particle in coincidence with an emitted neutron were stored in two α-particle spectra with 20 keV bin width, one prompt and one random, the difference giving the true coincident α-particle spectrum. Such a spectrum is shown (with 80 keV/channel) in Figs. 1b and 1c. The opening of the one- and two-neutron decay channels at $E_x =$ 7.6 MeV and 17.8 MeV, respectively, can be seen.

Final-state spectra were generated by subtracting the neutron separation energy and the neutron energy from the [115]Sn excitation energy for each event. A final-state spectrum for

Fig. 3. The same figure as Fig. 2, but the solid and dashed lines represents the PACE calculations, using the literature and fitted sets of level-density parameters, respectively (see text).

the total excitation energy region covered in this experiment is shown in Fig. 4. Below the two-neutron threshold ($E_x = 17.8$ MeV), this is identical to the actual final-state spectrum in ^{114}Sn. Above this threshold this statement is no longer strictly true, but in the following it will for convenience be referred to as the final-state spectrum. It is worth noting the clear separation of the ground state in ^{114}Sn from the rest of the spectrum (Fig. 4). The first excited state ($E_{fs} = 1.3$ MeV) can also be distinguished. The wide bump beginning at about $E_{fs} = 10$ MeV is due to the opening of the two-neutron decay channel. Final-state spectra were also generated for 1.6 MeV wide excitation energy bins in the compound nucleus (^{115}Sn), as is shown in Figs. 5 and 6.
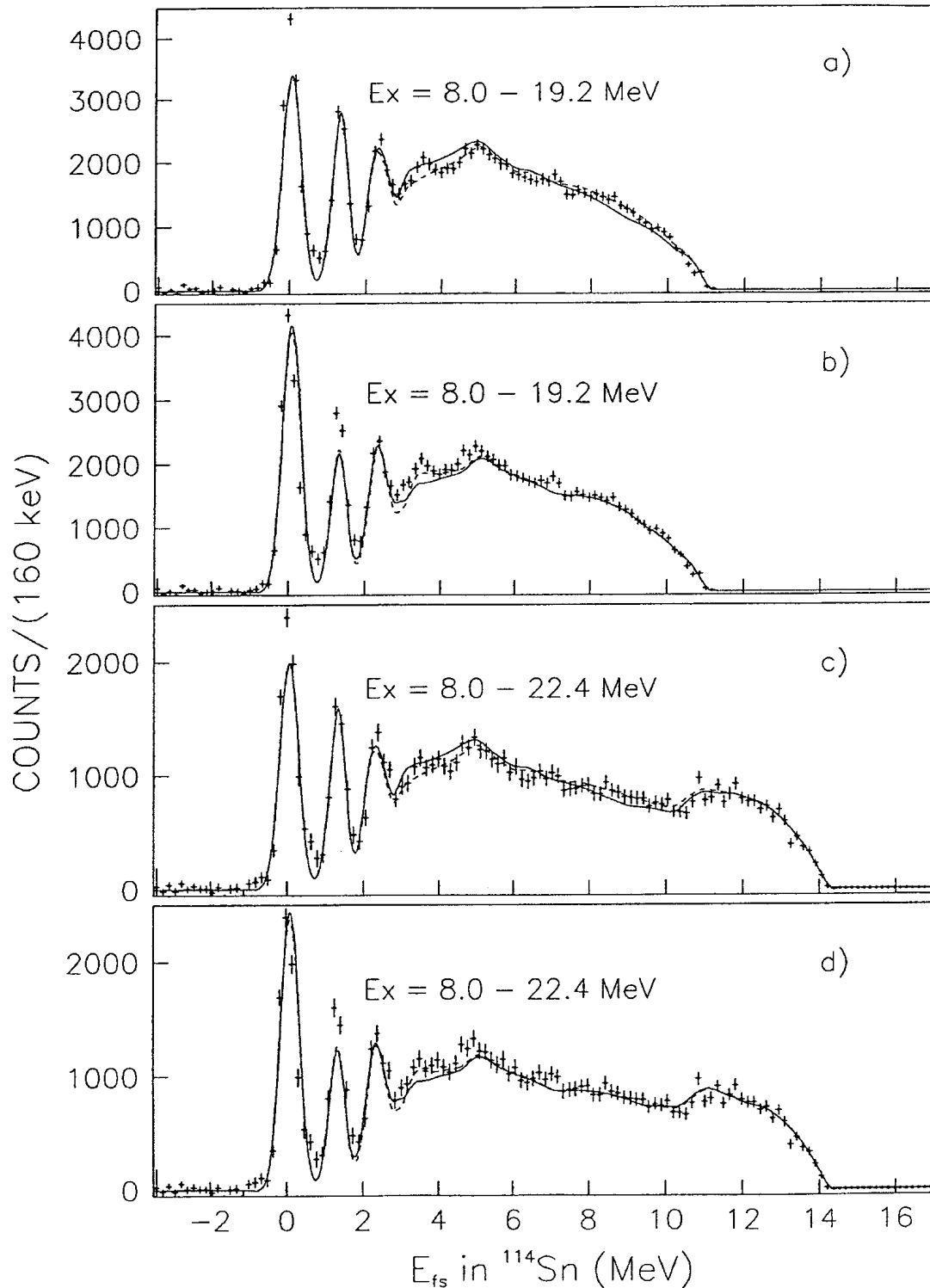
Fig. 4. Experimental final-state spectra in ^{114}Sn for the full excitation energy region in ^{115}Sn covered in this experiment (solid circles). In (a) and (c) the data taken with the low and high magnetic field settings of the spectrograph, respectively, are compared with the CASCADE calculation, using the literature (solid line) and the fitted (dashed line) level-density parameters (see text). In (b) and (d) the same data are compared with the corresponding PACE calculations. The error bars represent statistical uncertainties only.
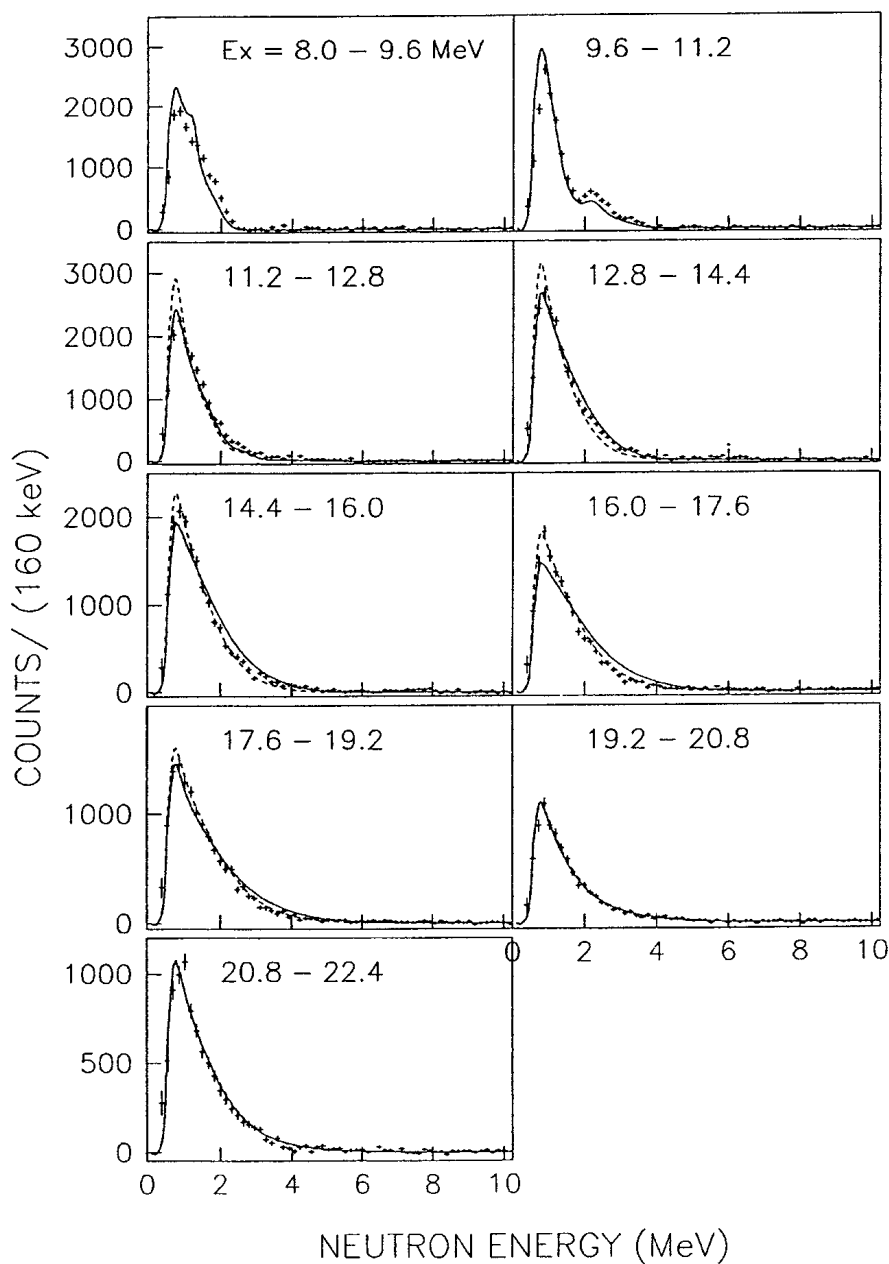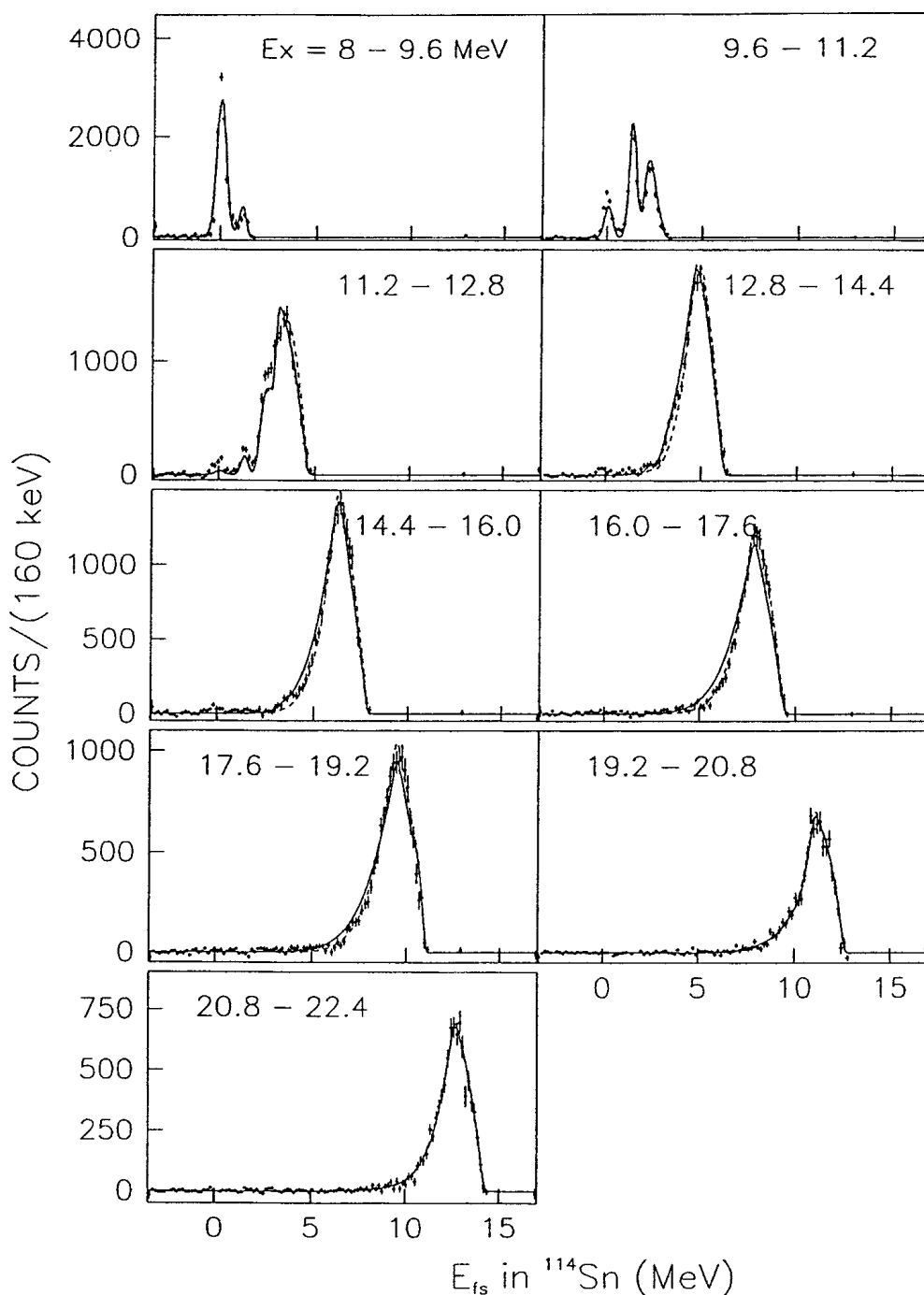
Fig. 5. Experimental final-state spectra gated on 1.6 MeV wide excitation energy bins in ^{115}Sn between 8.0 and 22.4 MeV (solid circles). The solid and dashed lines represent the CASCADE calculations, using the literature and fitted sets of level-density parameters, respectively (see text). The error bars represent statistical uncertainties only.

Furthermore, the angular correlations for the decay from $E_x = 8.0$–22.4 MeV in ^{115}Sn to the ground state, the first excited state, and to the excitation energy bins $E_{fs} = 1.8$–2.9, 2.7–4.3, 4.2–6.2 and 6.2–10.2 MeV in ^{114}Sn, have been measured and are displayed in Fig. 7. Angular correlations for the decay to the ground state in ^{114}Sn,
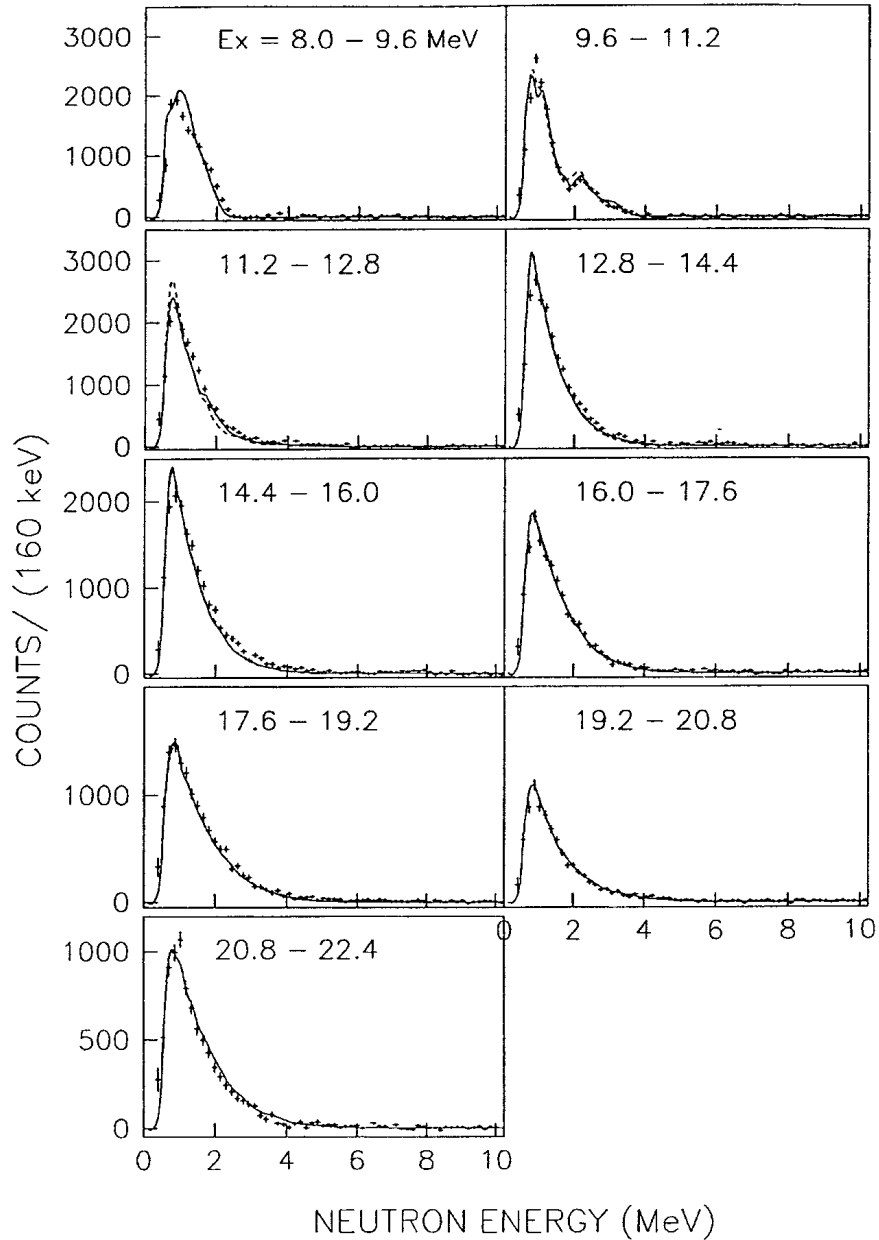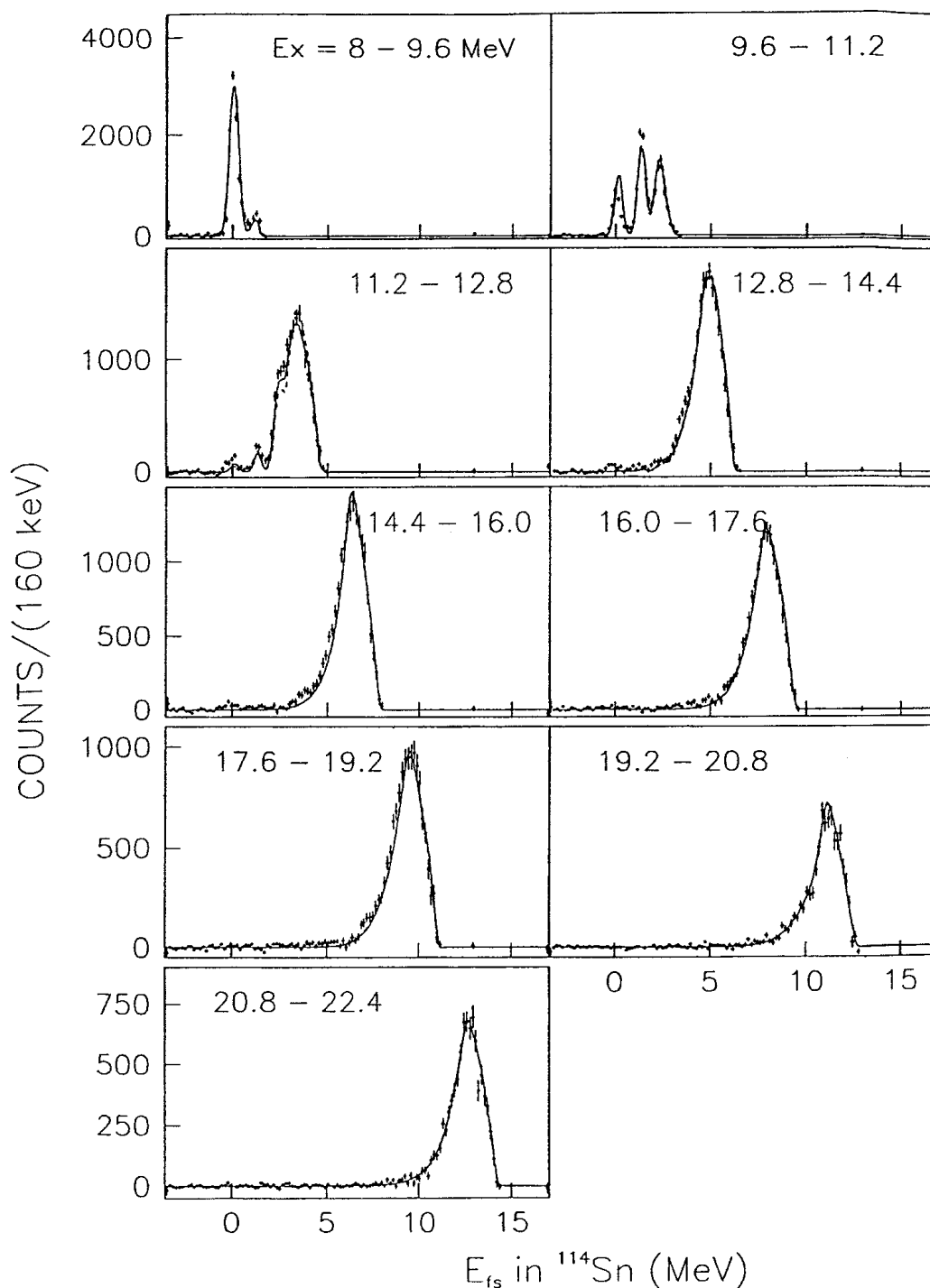
Fig. 6. The same figure as Fig. 5, but the solid and dashed lines represent the PACE calculations, using the literature and fitted sets of level-density parameters, respectively (see text).

from different excitation energy bins in the compound nucleus [115]Sn, have also been studied, and the results are shown in Fig. 8. The data points represent the sum over two or three neutron detectors, one in the horizontal plane and the other(s) just above or below this plane. The angular correlations for the decay to the ground state in [114]Sn
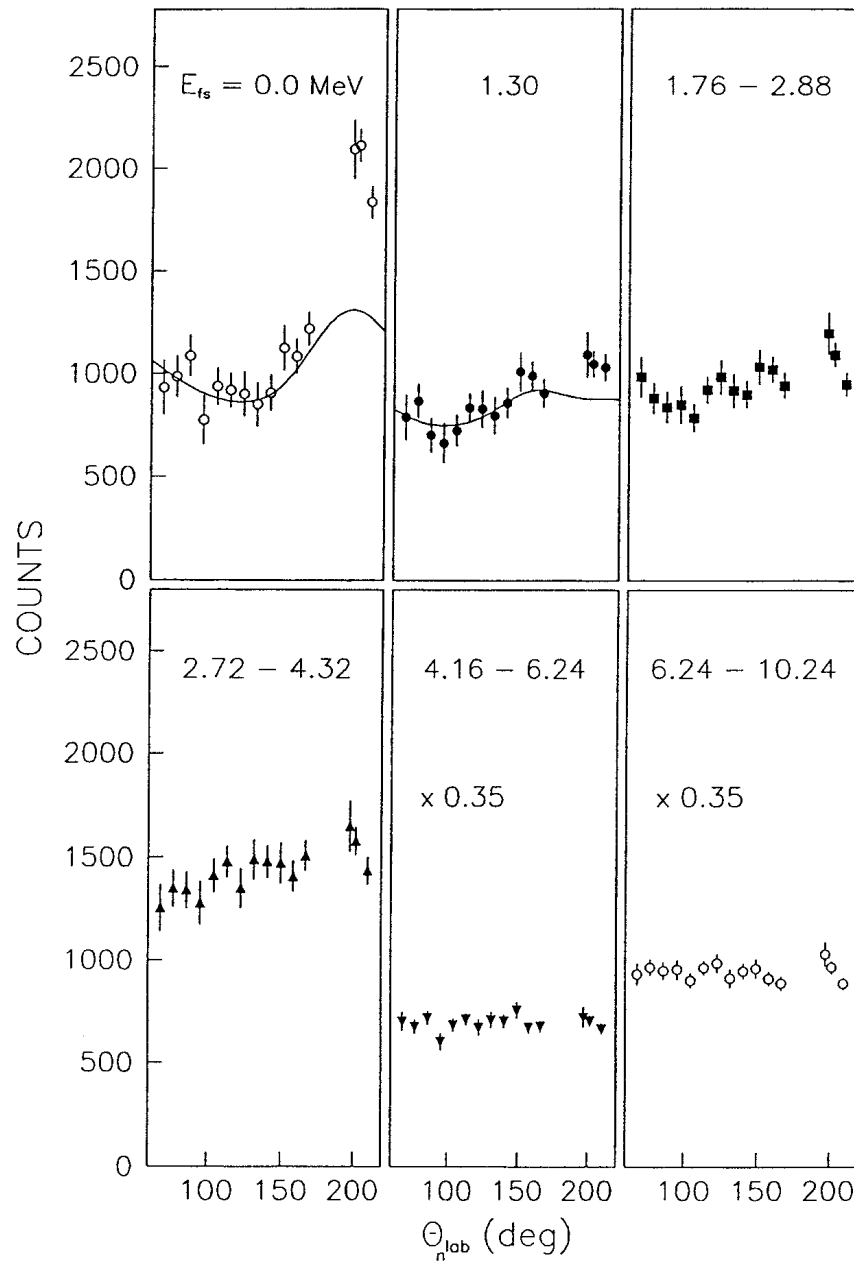
Fig. 7. Angular correlations for the decay from $E_x = 8.0–23.0$ MeV in [115]Sn to the ground state, the first excited state, and four excitation energy intervals between 1.76 and 10.24 MeV in [114]Sn. The full line is the ANGCOR calculation. The error bars represent statistical uncertainties only.

are peaked at 0 degrees with respect to the direction of the recoiling nucleus. The angular correlation for the decay to the first exited state has also a forward-backward asymmetry. Decay to states at higher excitation energies shows more or less isotropic angular distributions.
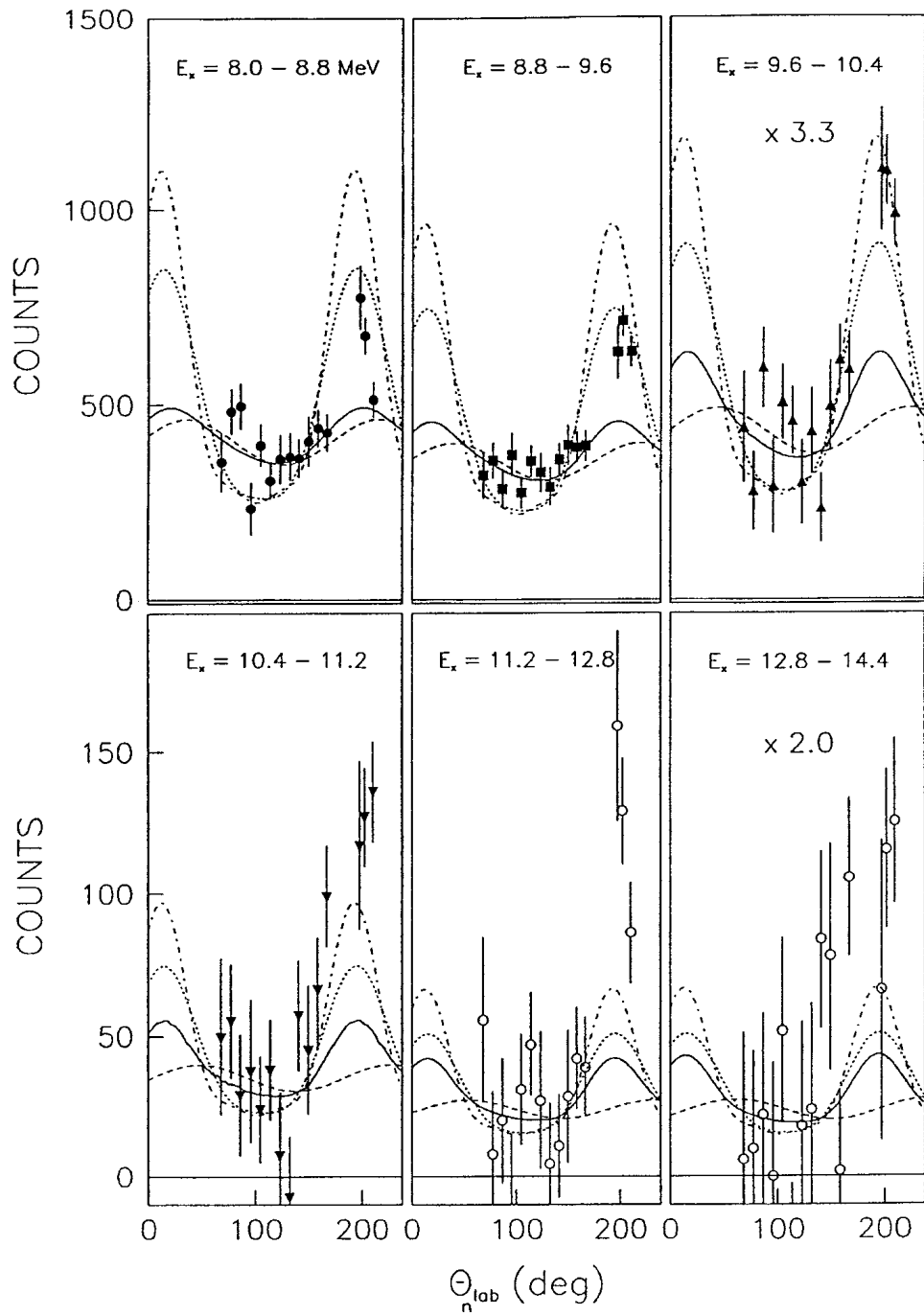
Fig. 8. Angular correlations for the decay to the ground state in ^{114}Sn gated on four 0.8 MeV and two 1.6 MeV wide excitation energy bins in ^{115}Sn. The full line represents the ANGCOR calculation with the spin distribution derived in this experiment. The dashed, dotted and dot-dashed lines represent calculations for decay from pure hole states, i.e., $2p_{3/2}$, $1f_{5/2}$ and $1g_{7/2}$, respectively. The error bars represent the statistical uncertainties only.

4. Data analysis

The experimental singles spectra obtained in this work are due to direct pickup of single-particle strength, superimposed on a continuum of more complex nature. The continuum is partly the result of two-step processes, such as pickup followed by inelastic scattering, or inelastic scattering followed by pickup, but more complex processes may also contribute. Both the single-hole states and the continuum are expected to decay predominantly by neutron emission in a statistical way.

This expectation is in contrast to the behaviour of single-particle states or giant resonances, i.e. particle–hole states. If a particle occupies a high-lying orbital, it could either be emitted directly (direct decay) or dissipate its excitation energy to more complex configurations, resulting in pre-equilibrium or statistical decay. This is not expected for hole states, because the only way to reach a stable residual nucleus is that a nucleon in the least bound orbitals falls down into the hole. This process is quite unlikely because the phase space available is very small. Instead, dissipation of excitation energy by coupling to more complex configurations is far more likely, based on statistical considerations.

To determine the degree of nonstatistical neutron decay, the experimental data were compared with calculations of the statistical decay. Such calculations were performed using two computer codes, CASCADE (Refs. [22,23]) and PACE (Ref. [24]). The reason for using two different codes was to increase the probability that observed deviations between experiment and calculations really are due to nonstatistical decay, rather than to shortcomings of the applied code.

The statistical and nonstatistical decay show typically rather different patterns. Statistical decay results in a maxwellian distribution at low particle emission energy, while the nonstatistical decay preferentially populates distinct states, in particular low-lying states in the residual nucleus. For decay from states at moderate and high excitation energy, these two decay modes are well separated in final-state energy, and thereby the extraction of nonstatistical strength is not very controversial. For decaying states at low excitation energy, however, there is no such separation in final-state energy, which makes the extraction technique less reliable.

This technique is well established in decay studies of, e.g., giant resonances. Although it in principle minimizes the nonstatistical strength because the statistical part is assumed to account for the entire distribution at high final-state energy, i.e., low emission energy, this is generally not believed to be a major concern. The only way a large error in the extraction of nonstatistical decay can occur is if there is direct decay strongly resembling the statistical distribution, which is considered highly unlikely.

The spin distribution in the compound nucleus is needed as input to statistical model calculations. In order to calculate the spin distribution of single-hole states as a function of excitation energy in ^{115}Sn, all relevant hole states in ^{115}Sn, their excitation energies, widths, shapes and cross sections should be considered. The cross sections can be calculated using the distorted-wave Born approximation (DWBA), provided spectroscopic factors and appropriate optical potentials are available. After adding the individual contributions the result should be compared with the experimental singles spectra.

Agreement would indicate that the calculated spin distribution as a function of excitation energy is reasonable. In addition, agreement with the experimental singles spectra would tell that deep-hole states dominate, and that the "background" from other processes than one-step pickup of a neutron is small.

Another important input to the statistical model calculations is the level densities of the nuclei considered in the decay cascade. Often, these are determined by evaluation of experimental data and from systematics of nearby nuclei. Alternatively, the level-density parameters could be determined by fitting to the present experimental coincidence spectra in regions where the statistical decay is expected to be totally dominating.

When comparing the statistical model calculations directly with the experimental spectra isotropic decay is assumed. This is not exactly true since, in general, neutron decay proceeds through a mixture of several angular momentum, l, values. Most of the neutrons have, however, a low l, because of the small transmission coefficients for high-l neutron decay. The experimental angular correlations between the scattered α-particles and the emitted neutrons show if the neutron decay is isotropic or nearly isotropic in the regions of interest. Some of the experimental angular correlations were compared with DWBA-based calculations (Fig. 8) performed with the code ANGCOR (Ref. [25]). If the decay is predominantly statistical, the calculations should describe the data well, provided that the spin distributions are appropriate.

In the following subsections the different steps of the analysis are described in some detail. The results are discussed and compared with existing data.

4.1. DWBA calculations

As was mentioned above, the experimental singles spectrum is expected to be due to direct pickup of single-particle strength, superimposed on a continuum of more complex nature. This continuum is poorly known. We have therefore tried an approach where single-hole states are used to fit as much as possible of the experimental spectrum. As will be seen below, such an approach seems to be able to describe the full spectrum reasonably well. This should not, however, be overinterpreted. The reason for this procedure is not to determine the precise fraction of single-hole and continuum excitation, but to provide reasonable input concerning the nature of the decaying states, to be used in the statistical decay calculations. The statistical decay spectra calculated on the basis of this technique are not very sensitive to its details.

The single-hole distribution and the one-step pickup spectrum in ^{115}Sn, were calculated using the DWBA. Excitation energies, spins and spectroscopic factors for states up to $E_x = 3.2$ MeV were taken mostly from the compilation in Nuclear Data Sheets based primarily on the ^{116}Sn(d,t)^{115}Sn experiments at 23 and 40 MeV (polarized) performed by Berrier-Ronsin et al. [10] and Perrin et al. [8]. For the remaining states up to $E_x = 15$ MeV we used results from the ^{116}Sn(^{3}He,α)^{115}Sn reaction obtained by Gerlic et al. [11], Sekiguchi et al. [12] and Langevin-Joliot et al. [13]. Spectroscopic factors for the IAS were derived from the proton pickup experiment on ^{116}Sn by Hesselink et al. [26].

^{116}Sn is not a closed neutron subshell nucleus. The orbitals $3s_{1/2}$, $2d_{3/2}$, $1g_{7/2}$, $1h_{11/2}$ and $2d_{5/2}$ are only partially filled. Therefore it is impossible to use the simple sum rule for filled shells to determine the spectroscopic factors for these states. Instead we used a procedure based on the very reasonable assumption that the total number of neutrons in these orbitals should be sixteen. The experimentally known strength for all these subshells corresponds to 14.39 neutrons. The remaining 1.61 neutrons were distributed in proportion to the known strength in the states referred to above.

For the remaining single-hole orbitals the excitation energies were taken from Ref. [27] with widths comparable to the experimentally known widths of other deep-hole states and spectroscopic factors corresponding to filled shells.

Gaussian distributions, with the experimental width of 300 keV (FWHM), were assigned to all low-lying states and the narrow IAS. The high-lying states, which have larger widths, were described by maxwellian distributions. These distributions were positioned with the maxima at the proper excitation energies and widths as described in Table 1. The use of maxwellian distributions gives these states a substantial high energy tail. When summing up the cross section for each orbital, making sure that the desired cross section is obtained, the high-energy tails were put equal to zero above $E_x = 50$ MeV. The results are not sensitive to the exact choice of this upper limit. The 1.61 neutrons that were distributed in the partially filled subshells were given triangular shaped distributions with their maxima 2.5 MeV above the first state in that subshell and extending up to $E_x = 50$ MeV.

The DWBA calculations were performed with the code DWUCK4 (Ref. [28]), using optical potential parameters derived by Duhamel et al. [29]. The experimental one-nucleon pickup cross sections are related to the calculated differential cross sections $(d\sigma^{lsj}/d\Omega)_{DW}$ through the formula:

$$\frac{d\sigma^{lsj}}{d\Omega} = N \frac{C^2 S}{2J+1} \left(\frac{d\sigma^{lsj}}{d\Omega}\right)_{DW}, \tag{1}$$

where the reaction dependent constant N was given the normally adopted value, $N = 23$, for the (^{3}He,α) reaction [29]. The single-particle orbitals, excitation energies and widths used in the calculations are given together with the resulting cross sections in Table 1.

The results of the calculations for the individual states given in Table 1 are shown as dot-dashed curves in Fig. 1a. All contributions were added to obtain a "theoretical" singles spectrum (solid line) for comparison with the experimental one.

The experimental singles spectrum recorded at the high magnetic field setting of the spectrograph were normalized to the calculated singles spectrum in such a way that the sum of the yield in the three lowest, unresolved, states, at $E_x = 0.50, 0.61$ and 0.71 MeV, were the same in calculation and experiment. These states are considered to be fairly pure single-hole states. The singles spectrum obtained at the lower magnetic field was normalized to the spectrum obtained at the higher magnetic field, over the full overlapping energy region.

There is a clear discrepancy between experiment and calculation for $E_x = 2$–3.5 MeV. One reason for this might be that we included in our calculation the states with known spin. There exists, however, a number of states in this region, of which the spin is not unambiguously known. Since this is well below the neutron threshold, the discrepancy does

Table 1

Single-particle orbitals, excitation energies, widths and cross sections for hole states in ^{115}Sn used in the calculation of the one-step pickup spectrum and its spin distribution. The DWBA calculations were averaged over the opening angle of the spectrograph. The eight lines containing a Σ shows the total spectroscopic factor employed for that subshell

nlj	E_x (MeV)	Width (MeV)	C^2S	σ (mb/sr)
$3s_{1/2}$	0.00	0.30	0.7^g	0.28
$3s_{1/2}$	1.96	0.30	0.14^g	0.10
$3s_{1/2}$	2.50		0.09^f	0.08
$3s_{1/2}$			Σ 0.93	
$2d_{3/2}$	0.50	0.30	0.9^g	2.47
$2d_{3/2}$	1.28	0.30	0.10^g	0.31
$2d_{3/2}$	1.64	0.30	0.13^g	0.42
$2d_{3/2}$	3.00		0.13^f	0.48
$2d_{3/2}$			Σ 1.26	
$1g_{7/2}$	0.61	0.30	5.9^g	19.71
$1g_{7/2}$	1.86	0.30	0.33^g	1.06
$1g_{7/2}$	3.11		0.70^f	2.11
$1g_{7/2}$			Σ 6.93	
$1h_{11/2}$	0.71	0.30	1.6^g	11.93
$1h_{11/2}$	3.21		0.18^f	1.12
$1h_{11/2}$			Σ 1.78	
$2d_{5/2}$	0.99	0.30	4.0^g	14.41
$2d_{5/2}$	1.42	0.30	0.074^g	0.28
$2d_{5/2}$	1.73	0.30	0.15^g	0.60
$2d_{5/2}$	2.06	0.30	0.08^g	0.33
$2d_{5/2}$	2.21	0.30	0.13^g	0.55
$2d_{5/2}$	2.36	0.30	0.05^g	0.22
$2d_{5/2}$	2.52	0.30	0.014^g	0.04
$2d_{5/2}$	2.81	0.30	0.05^g	0.23
$2d_{5/2}$	2.95	0.30	0.03^g	0.14
$2d_{5/2}$	3.19	0.30	0.013^g	0.06
$2d_{5/2}$	3.49		0.51^f	2.49
$2d_{5/2}$			Σ 5.10	
$1g_{9/2}$	3.67	0.30	0.05^g	0.27
$1g_{9/2}$	5.30	1.0	4.67^d	22.98
$1g_{9/2}$	7.60	3.5	2.40^b	10.00
$1g_{9/2}$	10.10^b	6.0	2.27^f	7.35
$1g_{9/2}$	13.26^{IAS}	0.30	0.44^h	0.99
$1g_{9/2}$	14.73^{IAS}	0.30	0.17^h	0.31
$1g_{9/2}$			Σ 10.00	
$2p_{1/2}$	6.6^c	3.0	1.90^f	4.54
$2p_{1/2}$	13.63^{IAS}	0.30	0.10^h	0.39
$2p_{1/2}$			Σ 2.00	

Table 1 —continued

nlj	E_x (MeV)	Width (MeV)	C^2S	σ (mb/sr)
$2p_{3/2}$	9.2^c	4.0	3.88^f	14.08
$2p_{3/2}$	13.89^{IAS}	0.30	0.12^h	0.57
$2p_{3/2}$			$\Sigma\ 4.0$	
$1f_{5/2}$	3.29	0.30	0.16^a	0.38
$1f_{5/2}$	10.1	6.0	3.5^b	6.18
$1f_{5/2}$	15.1^b	8.0	2.34^f	2.54
$1f_{5/2}$			$\Sigma\ 6.00$	
$1f_{7/2}$	15.1^b	8.00	8.00^f	15.16
$2s_{1/2}$	19.0^e	10.0	2.00^f	8.54
$1d_{3/2}$	20.0^e	10.0	4.00^f	3.28
$1d_{5/2}$	22.0^e	10.0	6.00^f	5.33
$1p_{1/2}$	27.0^e	10.0	2.00^f	0.94
$1p_{3/2}$	28.0^e	10.0	4.00^f	2.26
$1s_{1/2}$	34.0^e	10.0	2.00^f	0.49

[a] From Gerlic et al. [11].
[b] From Langevin-Joliot et al. [13].
[c] E_x from Sekiguchi et al. [12].
[d] A sum of 22 neighbouring states, from Gerlic et al. [11].
[e] E_x from p. 239 [27].
[f] To obtain full sum rule.
[g] From Nuclear Data Sheets [45].
[h] From Hesselink et al. [26].

not in any crucial way influence the conclusions drawn in this paper and it was decided not to guess the spin of the states, but to leave them out. This strength will obviously show up somewhere else in our calculations since we exhaust the simple sum rule of 16 neutrons. On the other hand, it will be smeared out over the full singles spectrum. The effects of this are most likely negligible. The singles spectrum above $E_x = 5$ MeV can be fully described by one-step pickup processes. The agreement between experiment and calculation suggests that the extracted single-hole distribution is reasonable and can be used with confidence in the statistical model calculations.

4.2. Statistical model calculations

Calculations have been performed for the neutron decay of excited states in ^{115}Sn, using the Hauser–Feshbach formalism, with the two codes CASCADE (Refs. [22,23]) and PACE (a modified version [24] of the Monte-Carlo based code JULIAN–PACE, Ref. [30]).

The two most important inputs to the statistical model decay calculations are the spin of the decaying state and the level density in the residual nucleus. A different spin of the decaying state can completely change the decay spectrum: this is particularly true for states close to the neutron emission threshold. Even a modest change of the level-density

parameters can cause a substantial difference in the resulting decay spectrum. Hence, the conclusion of whether there is nonstatistical decay or not is strongly dependent on the accuracy of the spin distributions and level densities used in the calculations. Special attention was paid to this problem in the present work.

The spin distribution for [115]Sn obtained from the analysis described in Section 4.1 was used.

Both the CASCADE and PACE codes have the option that individual levels with speci-fied spin can be used at low excitation energies in a nucleus. Above the region of individual levels, and up to about 8 MeV, the level density is described by the Fermi gas model. From about $E_x = 18$ MeV and upwards the level density is obtained from the liquid-drop model. A smooth interpolation is performed in the region between the Fermi gas model and the liquid-drop model. The methods used to interpolate differ in the two codes.

The code CASCADE employs the back-shifted Fermi gas model as expressed by Pühlhofer [22]. In PACE the level-density scheme of Gilbert and Cameron [31] is used. The expression for the level density differs slightly from that used by Pühlhofer and is called the shifted Fermi gas model. Two parameters are determined for each nucleus, namely the level-density parameter, a, and a pairing energy, the parameter Δ. The parameter a determines the energy dependence of the level density, while Δ determines the zero point of the effective excitation energy. The small difference in the level-density expressions has the effect that the parameters a and Δ do not become numerically exactly the same when a fit is performed to experimental data using the two approaches. Approximately the same value for a but different values for Δ are obtained.

In the actual calculations individual levels were used up to $E_{fs} = 3.027$ MeV in [114]Sn and up to about 2 MeV for the other nuclei in the decay chain, the only really important one being [113]Sn. Values for a in the Fermi gas model were taken from Dilg et al. [32] and Gilbert and Cameron [31] for the CASCADE and PACE calculations, respectively. The pairing energy parameter Δ was obtained by studying the cumulative number of levels, making sure that the transition from individual levels to the Fermi gas region was smooth. Since the Δ obtained in this way for [114]Sn in the PACE calculation was close to the value suggested by Gilbert and Cameron [31] the latter value was used. The parameters used are given in Table 2 (literature).

In the calculation of the neutron transmission coefficients the optical potential parame-ters derived by Rapaport et al. [33] were used in the CASCADE calculation. In the PACE code this option was not available and we used the default option in PACE, i.e., optical potential parameters from Perey and Perey [34].

When calculating the statistical decay using the parameters a and Δ obtained according to the procedure described above, it was found that the CASCADE calculations did not describe the data very well in all the energy bins. To investigate this problem, the level-density parameter a for [114]Sn was varied to make the agreement between experiment and calculation as good as possible for the excitation energy bins $E_x = 14.4–16.0$ and 16.0–17.6. These two bins are above the region where the parameter Δ plays a prominent role for the shape of the level-density curve, and below the energy where two-neutron emission becomes energetically possible and the level-density parameters for [113]Sn enter.

Table 2

Level-density parameters a and Δ used in the statistical model calculations

Calculation	^{114}Sn		^{113}Sn	
	a (MeV^{-1})	Δ (MeV)	a (MeV^{-1})	Δ (MeV)
CASCADE (literature)	12.65	1.03	12.53	−0.17
CASCADE (fit)	16.30	1.73	15.90	0.53
PACE (literature)	16.30	2.33	15.90	1.19
PACE (fit)	16.30	2.03	15.90	0.89

This excitation energy region should be well suited for a determination of a. With the fitted a for ^{114}Sn fixed, Δ was determined from the requirement that the cumulative sum of levels varies smoothly in the transition from individual levels to the Fermi gas region. The corresponding parameters for ^{113}Sn could not easily be determined by fitting, since the calculations are not very sensitive to these parameters.

Therefore, since the fitted value of a for ^{114}Sn was so close to the value of Gilbert and Cameron, their value for a was used also for ^{113}Sn, as can be seen in Table 2 (fit). The PACE calculation describes the data well and there was no need for a fitted parameter. However, as a comparison a calculation using the fitted value for Δ was performed.

Calculations were performed with two sets of parameters for each code, one following the published compilations [31,32], called the "literature" set, and the other being derived from the fitting procedure described in the preceding paragraph, called the "fit" set. The actual calculations were done in a number of steps; for a more detailed description see Ref. [15].

The calculations are presented both in terms of neutron-energy spectra (Figs. 2 and 3) and final-state spectra, (Figs. 5 and 6), since these two representations are to some extent complementary, see Ref. [15].

In the analysis, the energy-dependent efficiency and energy resolution of the neutron detectors has to be taken into account. The procedures to obtain this efficiency function have been described in detail in a separate publication [35]. To take into account the velocity of the decaying nucleus relative to each separate neutron detector, the calculated neutron-energy distributions were transformed to the laboratory frame and folded with the neutron time-of-flight resolution and the calculated efficiency of the neutron detector. The finite resolution in the excitation-energy spectrum was accounted for by smearing these calculations with the spectrometer resolution. As a final step, this folded spectrum was transformed back to the frame of the emitting nucleus, resulting in final-state energy spectra which can be compared with the data.

When comparing the experimental neutron-energy spectra with the calculated ones, the calculations were normalized separately for each excitation energy bin to the experimental spectra in the low energy region ($E_n < 1.5$ MeV). The normalization of the final-state spectra was inspected to check that the calculated spectra did not exceed the experimental ones significantly in any region, which was never the case.

The experimental final-state spectra are generally well described both by the CASCADE (Fig. 5) and the PACE (Fig. 6) calculations. Exceptions can be seen at low excitation energy in ^{115}Sn where there are some discrepancies, and for the ground-state decay from the higher E_x bins, which is clearly visible in the experimental spectra up to $E_x = 17.6$ MeV, not being reproduced by the calculations. Moreover, the curves for the literature (solid lines) and fitted (dashed lines) sets of level-density parameters are very similar, except in the CASCADE calculation where in the excitation energy range 14.4–17.6 MeV (in ^{115}Sn), a better description is obtained with the fitted parameters. This is seen even more clearly in the neutron energy spectra (Fig. 2), which are better suited to check that the applied level densities and detector efficiencies are correct.

4.3. Angular correlations

Neutron–alpha angular correlations can in principle give information on the spin of the initial state. The more angular momentum the neutron removes the more prominent is the angular correlation. In reality, this is not straight forward and a number of complications arise. The decaying state is not a single state but many overlapping states with different spins. The final state should preferably be a spin-0 state in order to make the neutron angular momentum unambiguous, which would facilitate the interpretation. Furthermore, the final state has to be resolved experimentally, and the branching ratio for decay to this state reasonably large.

The only well resolved final states in this experiment are the $J^\pi = 0^+$ ground state and the $J^\pi = 2^+$ first excited state in ^{114}Sn. Since the spin and parity of the first excited state complicates the interpretation of the decay to this state we are particularly interested in the angular correlations for the decay to the ground state.

The spectrograph was positioned at 1.4° resulting in a direction of the recoiling nucleus at around 190° with respect to the beam. This is the angle where the angular correlations for the decay to the ground state are expected to peak which is also the case (see Figs. 7 and 8).

Angular distributions for decay to the ground state from six excitation energy regions in ^{115}Sn were compared with model calculations using a modified version [36] of the DWBA-based code ANGCOR [25] (solid lines in Fig. 8). The same optical-model parameters [29] and spin distribution as presented in Section 4.1 were used in the calculations. Branching ratios for the decay from states with different spins were obtained from CASCADE. All the contributions were added incoherently. Agreement between experiment and calculation would indicate that the decay is predominantly statistical. Also shown in the same figure are calculations of angular correlations for decay from pure hole states, $2p_{3/2}$, $1f_{5/2}$, and $1g_{9/2}$ as dashed, dotted and dash-dotted curves, respectively.

The experimental angular distributions for the decay from the excitation energy region 8.0–23.0 MeV in ^{115}Sn to the ground state and first excited state in ^{114}Sn were also compared (Fig. 7) with ANGCOR calculations using the same spin distribution and method as described above. The result is shown as solid curves in Fig. 7. The angular correlations become more pronounced the higher the angular momentum of the neutron. High-l neutron

decay is, however, hindered by the small transmission coefficients, so that when high-spin states in ^{114}Sn become energetically accessible the neutron decay will to a large extent proceed to these, giving a less pronounced angular correlation. The angular correlations for neutrons decaying to final states in ^{114}Sn between 1.8 and 10.2 MeV do not show any pronounced structure.

Angular correlations represent a potential problem when comparing the statistical model decay calculations with experiment, since in such a comparison isotropic decay is assumed. In reality this requirement is not completely satisfied. The angular distributions are peaked (for neutrons with $l > 0$) at $0°$ and $180°$ with respect to the direction of the recoiling nucleus. This peaking becomes more pronounced with increasing neutron angular momentum.

However, prominent angular correlations were observed only in the decay to the ground state and first excited state of ^{114}Sn. Moreover, the neutron detectors were arranged in almost a full semicircle around the target, which makes the assumption of isotropy less important. We have investigated the possible misidentification of strength due to anisotropies in the decay by ANGCOR calculations, taking the present experimental geometry into account. The effect of nonisotropy of the neutron angular correlations can be expressed as the ratio of the sum over all detectors of the calculated correlations, divided by the sum for an isotropic distribution. The result is that this ratio is 1.00, 0.99, 1.16 and 1.29 for decay to $J^{\pi} = 0^{+}$ from $p_{1/2}$, $p_{3/2}$, $f_{7/2}$ and $g_{9/2}$, respectively; i.e., such effects are very small for low angular momenta, which are the dominating decay multipolarities. The main effect of not taking angular correlations explicitly into account in the extraction of nonstatistical decay is thus that the extracted strength for high angular momenta has to be corrected by at most up to about 30%, while the correction is negligible for low angular momenta.

The results on branching ratios of nonstatistical decay presented in Tables 3 and 4 are given with statistical uncertainties only. Hence, the model uncertainty described above should be included in the total uncertainty. The calculations presented in Figs. 2–6 are weighted sums of contributions to different subshells, and are therefore also subject to similar effects. In this case, however, these uncertainties are much smaller, because at all excitation energies, the calculated sum is composed of many multipolarities, which makes the maximum possible effect due to nonisotropy rather small.

Table 3
The neutron branching ratio (Γ_n/Γ_{tot} (%)) for two IAS clusters, the "background" under the two IAS clusters as defined in Fig. 10 and a 2 MeV wide E_x bin above the IAS is presented. The errors quoted are statistical

E_x in ^{115}Sn (MeV)	12.8–14.2	14.2–15.1	15.1–17.1
"background"	98.6 ± 2.2	98.7 ± 2.7	101.7 ± 1.8
IAS	99.1 ± 11.1	114.0 ± 34.0	

Table 4

Branching ratios for the nonstatistical neutron decay from five excitation energy bins in ^{115}Sn to the ground state, the first excited state, the region containing the first 3^- vibration (at 2.27 MeV), and a 2 MeV wide region centered at 3.59 MeV in ^{114}Sn. The errors quoted are statistical. These results should be considered lower limits of nonstatistical decay; see the text for details

E_{fs} in ^{114}Sn (MeV)	E_x in ^{115}Sn (MeV)				
	11.2–12.8 (%)	12.8–14.4 (%)	14.4–16.0 (%)	16.0–17.6 (%)	17.6–19.2 (%)
0.0	1.68 ± 0.26	1.20 ± 0.22	1.14 ± 0.20	0.81 ± 0.21	0.42 ± 0.20
1.3	1.80 ± 0.35	0.88 ± 0.23	0.75 ± 0.20	0.10 ± 0.17	0.12 ± 0.19
1.95–2.59	2.54 ± 0.32	0.64 ± 0.17	0.18 ± 0.16	0.16 ± 0.16	0.43 ± 0.13
2.59–4.59		3.21 ± 0.47	1.92 ± 0.33	1.42 ± 0.30	1.21 ± 0.28
0–4.59	6.02 ± 0.54	5.93 ± 0.59	3.99 ± 0.46	2.49 ± 0.43	2.18 ± 0.41

5. Discussion

The neutron decay of deep-hole states in ^{115}Sn agrees nicely with statistical model calculations. Both the neutron energy spectra (Figs. 2 and 3) and the final-state spectra (Figs. 5 and 6), are well described by all the calculations. The most striking deviation is seen in the decay to the ground state. Almost no decay to the ground state is predicted by the statistical model calculations above $E_x = 12.8$ MeV. Experimentally, however, decay to final states around $E_{fs} = 0$ is clearly seen in the bins $E_x = 12.8–14.4$ and $14.4–16.0$ MeV. On a closer examination some decay to the ground state can even be found in the next bins, $E_x = 16.0–17.6$ MeV and $17.6–19.2$ MeV. The observation of nonstatistical decay to the ground state from excitation energies above 12.8 MeV is not sensitive to uncertainties in the statistical model calculations. No reasonable assumption regarding the angular momentum of this decay results in statistical decay of such high neutron energies.

The statistical decay for the low excitation energy region ($E_x = 8.0–11.2$ MeV), where only one or a few final states are available for neutron decay, is very difficult to calculate. The decay from this region is very sensitive to the spin and parity of the decaying deep-hole state, the detailed energy dependence of the transmission coefficients and the amount of competing gamma- and charged-particle decay. The two codes give rather different results in these bins although they are very similar. Therefore, too much attention should not be paid to the discrepancies found in this region.

Branching ratios for the nonstatistical decay observed to final states in ^{114}Sn up to an energy $E_{fs} = 4.59$ MeV from five excitation energy bins in ^{115}Sn, $E_x = 11.2–19.2$ MeV are presented in Table 4. Since the decay from the bin $E_x = 11.2–12.8$ MeV has its energy threshold in the final-state bin 2.59–4.59 MeV no value for this branching ratio is given. The values cited in the table are an average over the four calculations. For the next two final-state regions the branching ratios are obtained from a difference between experiment (a large number) and calculation (also a large number). This means that these values are sensitive to the finer details of the shape of the neutron spectra. The values given for the

decay to these two final-state regions are therefore obtained using the average over only the two calculations with best general description of the data.

As an illustration, the difference between experimental final-state spectra and statistical model calculations for the final-state region in Table 4 is shown in Fig. 9. There one can see that above $E_x = 19.2$ MeV no nonstatistical decay can be observed. The branching ratio for the nonstatistical decay to the ground state drops smoothly from 1.7% ($E_x = 11.2–12.8$ MeV) to 0.4% ($E_x = 17.6–19.2$ MeV). This can be interpreted as the analog of the electron "Auger process" in that one neutron in a "Cooper pair" is picked up, creating the deep-hole, and the other neutron escapes to the continuum, leaving the daughter nucleus in a 0^+ state (e.g. the ground state). The branching ratios for the decay to the first excited state start at 1.8% ($E_x = 11.2–12.8$ MeV) and drop off rather quickly so that already at $E_x = 16.0$ MeV it is consistent with zero. The "Auger process" mentioned above can be used to explain also this decay, but then the "Cooper pair" is not split; instead two neutrons with different spin overlap enough to make the decay mode possible.

The region 1.95–2.59 MeV contains the first 3^- vibration (2.27 MeV) in ^{114}Sn. Nonstatistical decay to this final-state region can then be interpreted as a sign of preequilibrium decay: the damping of the initial deep hole has to a significant extent proceeded via coupling to this 3^- surface vibration. A number of authors [37–40] have suggested this kind of surface vibration damping scheme to be important in the damping of giant resonances, and possible candidates have been reported in experiments on the neutron decay of giant resonances in ^{90}Zr [41,42]. The last final-state region under consideration, $E_{fs} = 2.59–4.59$ MeV contains a large number of final states, some of which are 2^+ or 3^- collective vibrations. It is not easy even to guess what mechanism might be responsible for this decay, even though the surface vibration damping scheme sounds appealing.

The summed nonstatistical branching ratio for decay to $E_{fs} = 0–4.59$ MeV starts at 6.0% (11.2–12.8 MeV), falls off slowly to 2.2% (17.6–19.2 MeV), and above 19.2 MeV no nonstatistical decay is found. This is a rather low branching ratio for nonstatistical decay compared with the decay of giant resonances in ^{124}Sn where a 15-20% nonstatistical decay branch was observed [43]. On the other hand, if one compares with earlier experiments [15, 44] on the neutron decay of deep-hole states, 2% and 14% nonstatistical decay was observed in ^{89}Zr and ^{207}Pb, respectively. The 4–5% nonstatistical decay branch found in this paper is somewhere in between these values. It is, however, only in the decay from deep-hole states in ^{115}Sn that clear evidence of nonstatistical decay to the ground state in the daughter nucleus is observed. The reason for this might be that ^{116}Sn is not a closed neutron-shell nucleus whereas both ^{90}Zr and ^{208}Pb are.

Between $E_x = 13.2$ and 14.8 MeV in ^{115}Sn a cluster of IAS can be seen. They are not resolved but from other experiments [45] we know that the main components are two $1g_{9/2}$ states at $E_x = 13.26$ and 14.73 MeV, a $2p_{1/2}$ state at 13.63 MeV and a $2p_{3/2}$ state at 13.89 MeV. The branching ratio for neutron decay can be determined from the neutron detector solid angle and efficiency if one knows the singles and coincidence yields. Since the primary aim of this experiment was not to determine absolute branching ratios but rather to determine the statistical (or nonstatistical) fraction of the neutron decay, large efforts were not spent during data acquisition to ensure a proper determination of

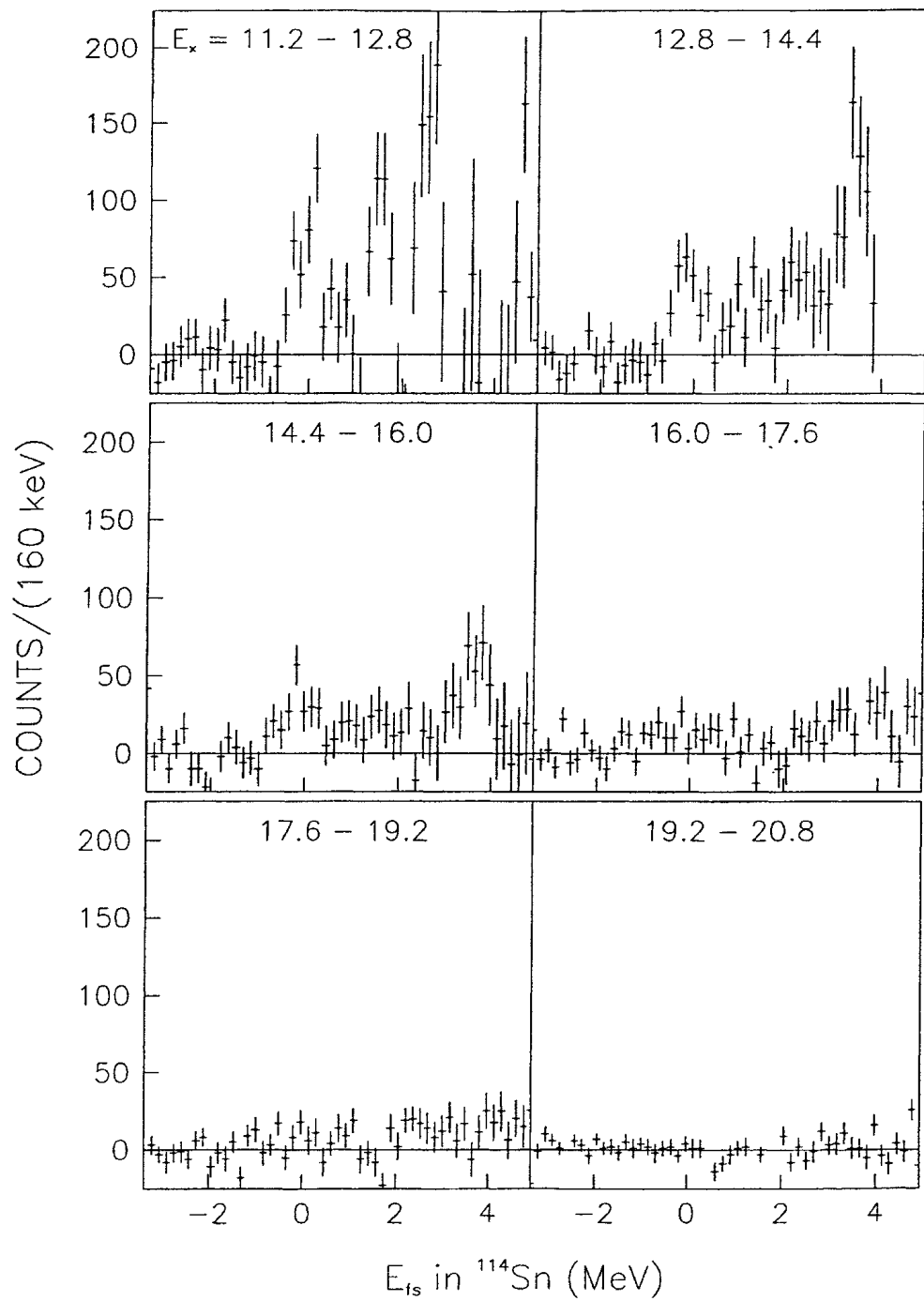Fig. 9. Spectra obtained as the difference between the experimental final-state spectra and a statistical model calculation (CASCADE with the "fit" set of input parameters), illustrating the observed nonstatistical decay. The spectra are gated on 1.6 MeV wide excitation energy bins in [115]Sn between 11.2 and 20.8 MeV. Final states up to 4.9 MeV are shown. The error bars represent statistical uncertainties only.

the singles downscaling factor. Therefore we cannot use the method described above to determine the neutron branching ratio. Instead, we compare the branching ratio of the IAS cluster with that of the deep-hole states in the same energy region and slightly above. CASCADE calculations predict the branching ratio for neutron decay from $E_x = 12$–17 MeV to be 1, see Fig. 10c. The experimental branching ratio for all states other than the IAS in the energy region $E_x = 12.0$–17.0 MeV is thus normalized to one. Using the normalization factor obtained in this way, the branching ratio for each E_x region separate and for the IAS cluster divided into two parts can be obtained, see Table 3. The errors given are statistical. The IAS cluster is riding on a "background" of deep-hole states. In order to extract the singles and coincidence yield of the IAS cluster, this "background" level was estimated as shown in Fig. 10, (a) and (b). Within the uncertainties, the branching ratio for both of the IAS clusters is the same as that obtained for surrounding states, which from statistical model calculations is expected to be consistent with 100%. The neutron spectrum for the decay from the $E_x = 12.8$–14.4 MeV bin is statistical to 94%, see Table 4. This is not significantly different from the surrounding E_x bins and the decay of the IAS is therefore consistent with 100% statistical neutron decay.

Angular correlations have been obtained for the decay from the 8.0–23.0 MeV excitation energy interval in ^{115}Sn to six excitation energy intervals in ^{114}Sn (Fig. 7), and for the decay to the ground state in ^{114}Sn from six E_x intervals in ^{115}Sn (Fig. 8). Prominent angular correlations are only seen for the decay to the ground state, and to some extent for the decay to the first excited state, while they are completely featureless above $E_x = 4.16$ MeV. The angular correlations for the decay to the ground state in ^{114}Sn are not very well described by the ANGCOR calculation using branching ratios from CASCADE and the spin distribution obtained as described earlier. The experiment overshoots the calculation by a large amount, suggesting nonstatistical decay. This is in agreement with the result from the CASCADE and PACE calculations, that could not completely account for the observed decay to the ground state. The angular correlations for the decay to the ground state from the E_x bins 8.0–8.8 MeV and 8.8–9.6 MeV are best described by the dotted curve in Fig. 8 that represents decay from a pure $1f_{5/2}$ state, whereas the decay from the other four E_x bins are better described by the dot-dashed curve in Fig. 8, i.e., decay from a pure $1g_{7/2}$ state.

Studies of the neutron decay of giant resonances have shown that the direct decay branch accounts for about 5–10% in ^{90}Zr [42], 15–20% in ^{124}Sn [42] and about 5% in ^{208}Pb [46,47]. The corresponding numbers for deep-hole states are 0% in ^{90}Zr [44], about 5% in ^{115}Sn (present work) and about 5–15% in ^{208}Pb [15]. Finally, the direct neutron decay of single-particle states in ^{209}Pb [48] amounts to about 7%. Experimental studies of the neutron decay of single-particle states in ^{90}Zr and in tin nuclei would be valuable to make the systematics complete. The experimental information already available seems not to indicate a very significant difference in direct decay strength for these kinds of excitations.
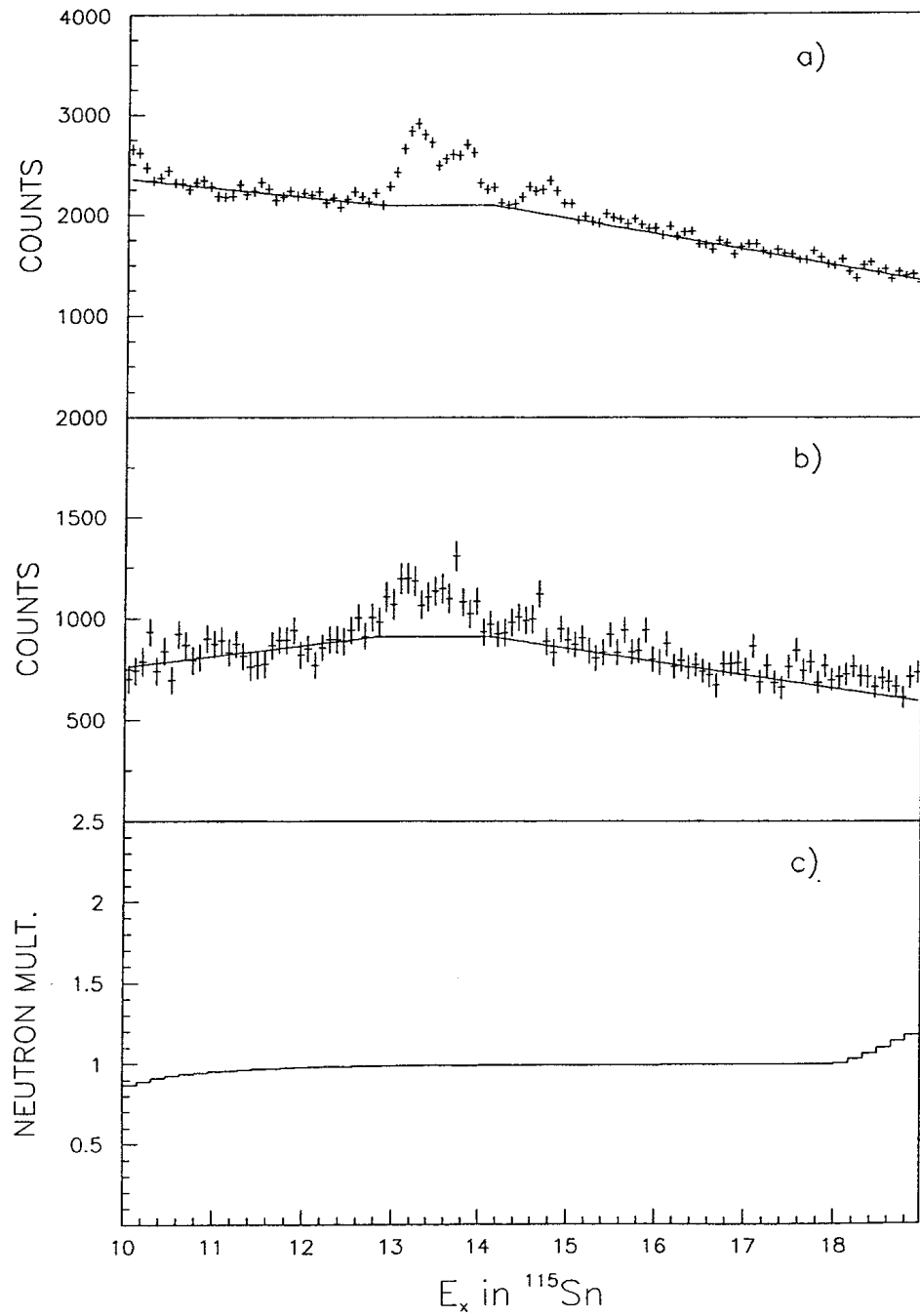
Fig. 10. (a) The part of the α-energy spectrum that contains the IAS cluster, obtained as in Fig. 1a. The solid line represents the estimated "background" used when extracting the IAS yield. (b) Alpha spectrum in coincidence with neutrons for the same excitation energy region as above. The solid line represents the estimated "background" used when extracting the IAS yield. (c) Neutron multiplicity calculated with CASCADE for the same excitation energy region as above.

6. Summary and conclusions

The neutron decay of deep-hole states and IAS in ^{115}Sn was measured using the multidetector system EDEN. Final-state and neutron-energy spectra were compared with statistical model calculations performed with the codes CASCADE and PACE, using level-density parameters found in the literature as well as parameters obtained by fitting to the experimental data.

The analysis framework adopted is very similar to what has been used in many other neutron decay experiments, like in decay of giant resonances and high-lying single-particle states, which facilitates comparisons of results. With this scheme, however, in principle only lower limits of nonstatistical decay are obtained.

The deep-hole states and IAS were created using the (^{3}He,α) reaction at a beam energy of 102 MeV. The singles spectrum can be fully accounted for using one-step pickup reactions only. This makes the study of the neutron decay of deep-hole states populated by this pickup reaction feasible.

The neutron decay of deep-hole states in ^{115}Sn are observed to be statistical to about 95% up to $E_x = 19.2$ MeV. Above this excitation energy the decay is consistent with decay from a completely thermalized system, i.e., 100% statistical. Nonstatistical decay to the ground state is observed rather high up in excitation energy in ^{115}Sn. This was not seen in the previous works [15,44] on the decay of deep-hole states in ^{89}Zr and ^{207}Pb, respectively.

The branching ratio for neutron decay of the IAS in ^{115}Sn is determined to be compatible with 100%, and the corresponding neutron spectrum is consistent with 100% statistical decay.

Acknowledgements

References

[1] S. Galès, Ch. Stoyanov, A.I. Vdovin, Phys. Rep. 166 (1988) 125.
[2] Electric and Magnetic Giant Resonances in Nuclei, International Review of Nuclear Physics, Vol. 7, J. Speth (Ed.), World Scientific, Singapore, 1991.
[3] A. van der Woude, Prog. Part. Nucl. Phys. 18 (1987) 217.
[4] S. Brandenburg, W.T.A. Borghols, A.G. Drentje, L.P. Ekström, M.N. Harakeh, A. van der Woude, A. Håkansson, L. Nilsson, N. Olsson, M. Pignanelli, R. de Leo, Nucl. Phys. A 466 (1987) 29.
[5] S. Strauch, Nucl. Phys. A 649 (1999) 85c.
[6] M. Matoba, H. Ijiri, H. Kametani, I. Kumabe, M. Hyakutake, N. Koori, T. Sakae, T. Maki, Nucl. Phys. A 456 (1986) 235.

[7] R.H. Siemssen, C.C. Foster, W.W. Jacobs, W.P. Jones, D.W. Miller, M. Saber, F. Soga, Nucl. Phys. A 405 (1983) 205.

[8] G. Perrin, G. Duhamel, C. Perrin, E. Gerlic, S. Galès, V. Comparat, Nucl. Phys. A 356 (1981) 61.

[9] S.Y. van der Werf, M.N. Harakeh, L.W. Put, O. Scholten, R.H. Siemssen, Nucl. Phys. A 289 (1977) 141.

[10] G. Berrier-Ronsin, G. Duhamel, E. Gerlic, J. Kalifa, H. Langevin-Joliot, G. Rotbard, M. Vergnes, J. Vernotte, K.K. Seth, K. Heyde, Nucl. Phys. A 288 (1977) 279.

[11] E. Gerlic, G. Berrier-Ronsin, G. Duhamel, S. Galès, E. Hourani, H. Langevin-Joliot, M. Vergnes, J. van de Wiele, Phys. Rev. C 21 (1980) 124.

[12] M. Sekiguchi, Y. Shida, F. Soga, Y. Hirao, M. Sakai, Nucl. Phys. A 278 (1977) 231.

[13] H. Langevin-Joliot, E. Gerlic, J. Guillot, M. Sakai, J. van de Wiele, A. Deveaux, P. Force, G. Landaud, Phys. Lett. B 114 (1982) 103.

[14] J.A. Bordewijk, A. Bałanda, D. Beaumel, J. Blomgren, S. Brandenburg, G. van 't Hof, M.N. Harakeh, M.A. Hofstee, J. Jänecke, A. Krasznahorkay, H. Laurent, L. Nilsson, N. Olsson, R. Perrino, R. Siebelink, P.O. Söderman, S.Y. van der Werf, A. Van der Woude, Nucl. Phys. A 574 (1994) 453.

[15] P.O. Söderman, J. Blomgren, A. Ringbom, N. Olsson, L. Nilsson, J.A. Bordewijk, S. Brandenburg, G. van 't Hof, M.A. Hofstee, H. van der Ploeg, S.Y. van der Werf, A. van der Woude, A. Krasznahorkay, A. Bałanda, D. Chmielewska, H. Laurent, Nucl. Phys. A 576 (1994) 215.

[16] A.G. Drentje, H.A. Enge, S.B. Kowalski, Nucl. Instrum. Methods 122 (1974) 485.

[17] A.G. Drentje, R.J. de Meijer, H.A. Enge, S.B. Kowalski, Nucl. Instrum. Methods 133 (1976) 267.

[18] J.M. Schippers, W.T.A. Borghols, S.Y. van der Werf, Nucl. Instrum. Methods A 247 (1986) 467.

[19] H. Laurent, H. Lefort, D. Beaumel, Y. Blumenfield, S. Fortier, S. Galès, J.C. Roynette, P. Volkov, S. Brandenburg, Nucl. Instrum. Methods A 326 (1993) 517.

[20] S. Brandenburg, PhD thesis, Rijksuniversiteit, Groningen, 1985, unpublished.

[21] P. Kroon, F. Sporrel, in: Program PAX, KVI Annu. Rep., 1981, p. 87, unpublished.

[22] F. Pühlhofer, Nucl. Phys. A 280 (1977) 267.

[23] M.N. Harakeh, Program CASCADE, extended version, private communication, 1990 (unpublished).

[24] D.G. Sarantites, M. Jäskeläinen, R. Woodward, F.A. Dilmanian, D.C. Hensley, J.H. Barker, J.R. Beene, M.L. Halbert, W.T. Milner, Phys. Lett. B 115 (1982) 441.

[25] M.N. Harakeh, L.W. Put, Program ANGCOR, KVI Internal Report 67 (1980).

[26] W.H.A. Hesselink, B.R. Kooistra, L.W. Put, R.H. Siemssen, S.Y. van der Werf, Nucl. Phys. A 226 (1974) 229.

[27] A. Bohr, B. Mottelsson, Nuclear Structure, Vol. 1, Benjamin, 1969.

[28] P.D. Kunz, Program DWUCK4 (unpublished); J.R. Comfort, extended version 1979; KVI-version 1981 (unpublished).

[29] G. Duhamel, G. Perrin, J.P. Didelez, E. Gerlic, H. Langevin-Joliot, J. Guillot, J. Van de Wiele, J. Phys. (London) G 7 (1981) 1415.

[30] M. Hillman, Y. Eyal, Program JULIAN (unpublished); A. Gavron modification PACE, Phys. Rev. C 21 (1980) 230.

[31] A. Gilbert, A.G.W. Cameron, Can. J. Phys. 43 (1965) 1446.

[32] W. Dilg, W. Schantl, H. Vonach, M. Uhl, Nucl. Phys. A 21 (1973) 269.

[33] J. Rapaport, V. Kulkarni, R.W. Finlay, Nucl. Phys. A 330 (1979) 15, optical model parameter set B.

[34] C.M. Perey, F.G. Perey, At. Data Nucl. Data Tables 17 (1976) 1.

[35] N. Olsson, P.-O. Söderman, L. Nilsson, H. Laurent, Nucl. Instrum. Methods A 349 (1994) 231.

[36] S. Brandenburg, private communication.

[37] B. Schwesinger, J. Wambach, Nucl. Phys. A 426 (1984) 253.

[38] P.F. Bortignon, R.A. Broglia, Nucl. Phys. A 371 (1981) 405.

[39] G.F. Bertsch, P.F. Bortignon, R.A. Broglia, Rev. Mod. Phys. 55 (1983) 287.

[40] P.F. Bortignon, R.A. Broglia, G.F. Bertsch, Phys. Lett. B 148 (1984) 20.

[41] W.T.A. Borghols, S. Brandenburg, J.H. Meier, J.M. Schippers, M.M. Sharma, A. van der Woude, M.N. Harakeh, A. Lindholm, L. Nilsson, S. Crona, A. Håkansson, L.P. Ekström, N. Olsson, R. de Leo, Nucl. Phys. A 504 (1989) 231.

[42] J. Blomgren, A.M. van den Berg, Y. Blumenfeld, D. Chmielewska, N. Alamanos, F. Auger, J. Bordewijk, S. Brandenburg, N. Frascaria, A. Gillibert, L. Nilsson, N. Olsson, P. Roussel, J.C. Roynette, J.A. Scarpaci, T. Soumijärvi, R. Turcotte, A. van der Woude, Nucl. Phys. A 578 (1994) 267.

[43] W.T.A. Borghols, S. Brandenburg, J.H. Meier, J.M. Schippers, M.M. Sharma, A. van der Woude, M.N. Harakeh, A. Lindholm, L. Nilsson, S. Crona, A. Håkansson, L.P. Ekström, N. Olsson, R. de Leo, Nucl. Phys. A 515 (1990) 173.

[44] P.-O. Söderman, J. Blomgren, A. Ringbom, N. Olsson, L. Nilsson, J.A. Bordewijk, S. Brandenburg, G. van 't Hof, M.A. Hofstee, H. van der Ploeg, S.Y. van der Werf, A. Krasznahorkay, A. Balanda, D. Chmielewska, H. Laurent, Nucl. Phys. A 587 (1995) 55.

[45] Nucl. Data Sheets 52 (1987) 565.

[46] A.M. van den Berg, Y. Blumenfeld, D. Chmielewska, N. Alamanos, F. Auger, J. Blomgren, J. Bordewijk, S. Brandenburg, N. Frascaria, A. Gillibert, L. Nilsson, N. Olsson, P. Roussel, J.C. Roynette, J.A. Scarpaci, T. Soumijärvi, R. Turcotte, A. van der Woude, Nucl. Phys. A 578 (1994) 238.

[47] D. Chmielewska, A.M. van den Berg, Y. Blumenfeld, N. Alamanos, F. Auger, J. Blomgren, J.A. Bordewijk, S. Brandenburg, N. Frascaria, A. Gillibert, L. Nilsson, N. Olsson, P. Roussel-Chomaz, J.C. Roynette, J.A. Scarpaci, T. Soumijärvi, R. Turcotte, A. van der Woude, Nucl. Phys. A 569 (1994) 383c.

[48] S. Galès, Nucl. Phys. A 569 (1994) 393c.

Appendix V

np scattering measurements at 96 MeV

J. Rahm, J. Blomgren, H. Condé, S. Dangtip, K. Elmgren, N. Olsson, T. Rönnqvist,[*] and R. Zorro[†]

Department of Neutron Research, Uppsala University, Box 535, S-75121 Uppsala, Sweden

O. Jonsson, L. Nilsson, and P.-U. Renberg

The Svedberg Laboratory, Uppsala University, Box 533, S-75121 Uppsala, Sweden

A. Ringbom[‡] and G. Tibell

Department of Radiation Sciences, Uppsala University, Box 535, S-75121 Uppsala, Sweden

S. Y. van der Werf

Kernfysisch Versneller Instituut, 9747 AA Groningen, The Netherlands

T. E. O. Ericson

CERN, CH-1211 Geneva 23, Switzerland
and The Svedberg Laboratory, Uppsala University, Box 533, S-75121 Uppsala, Sweden

B. Loiseau

Laboratoire de Physique Nucléaire et de Hautes Energies,[§] LPTPE, Université P. & M. Curie, 4 Place Jussieu,
75252 Paris Cedex 05, France

The differential np scattering cross section has been measured at 96 MeV in the angular range $\theta_{c.m.}$ = 74–180° at the neutron beam facility of the The Svedberg Laboratory in Uppsala. A subset of the data, covering 116–180°, has previously been published. The new, extended angular distribution has been normalized to the experimental total np cross section. Between 150° and 180°, the angular distribution is steeper than for most previous measurements and nucleon-nucleon potential predictions. At 180°, the difference amounts to about 10%, implying serious consequences because of the fundamental importance of this cross section. A value of the charged πNN coupling constant consistent with our earlier result at 162 MeV has been extracted from the data.

PACS number(s): 13.75.Cs, 13.75.Gx, 21.30.–x

I. INTRODUCTION

Recently, we have performed an np scattering measurement at 162 MeV [1,2], aiming at a higher accuracy than previous experiments. The np scattering cross section is not only of importance for investigations of the fundamental properties of the NN interaction, but has also a large impact on several applications, such as fast neutron cancer therapy and accelerator-driven transmutation technologies. The reason is that the np cross section is used as a primary standard for measurements of other neutron-induced cross sections in the 0–350-MeV region [3], i.e., other cross sections are normalized to that of np scattering. In particular the 180° np cross section, i.e., the H(n,p) cross section at 0°, is used for normalization purposes. This cross section therefore has to be known to high precision.

We have shown in our previous work that precision data of the np cross section in the backward hemisphere are useful for a determination of the charged πNN coupling constant. Both the shape of the angular distribution and the absolute normalization of the data are of crucial importance in this context. The πNN coupling constant is fundamental for quantitative discussions of many phenomena in nuclear and particle physics, and it is important to have determinations of it with full control of uncertainties. At present, a discussion goes on concerning appropriate methods to determine this quantity [4,5]. The specific issues concerning precision and systematics using backward np scattering to extract the coupling constant are addressed in Refs. [2,6,7], providing answers to criticisms discussed in Ref. [8]. The present experiment contributes additional material.

An investigation of the np scattering data situation, from 100 to 1000 MeV, up to the present date [9], shows that most of the data seem to fall into two main "families" with respect to the angular shape. Two of the largest data sets, i.e., those of Bonner et al. [10] (160–800 MeV) and of Hürster et al. [11] (200–590 MeV), agree reasonably well in shape above 500 MeV, but differ at 200 MeV by as much as 10–15 % in the 180°/150° cross section ratio. The shape of our previous angular distribution at 162 MeV is in good agreement with that of the Hürster data when plotted as $d\sigma/dt$ (t is the Mandelstam variable), but is, accordingly, in conflict

with the Bonner data. It is an experimental fact that there is a scaling with energy of the backward differential cross section (see, e.g., p. 376 of Ref. [12]). This is natural, since any potential model with pion exchange gives a $d\sigma/dt$ which varies slowly with energy in the laboratory system to leading order. The observed similarities in shape and normalization at different energies are therefore relevant and they are a clear signature of the charged pion exchange.

Normalization of np scattering differential cross sections has been—and is—a notorious problem [9]. To measure absolute cross sections, either the neutron beam intensity, or some other cross section to which the np scattering can be related, has to be known to high precision. The beam intensity can only be measured using a nuclear reaction, most frequently np scattering. Therefore most experimental data are assigned an absolute precision of no better than 5–10%, or are just given as relative cross sections.

Below the opening of the pion-production channel at about 270 MeV there is, however, a very direct and precise way of solving the normalization problem in principle. The total np cross section can be determined very accurately (better than 1%) without knowledge of the absolute beam intensity. The total cross section and the differential np cross section are closely linked; if the full angular distribution of the differential cross section is known, an unambiguous normalization to the total cross section can be performed, because all channels but elastic scattering are very small. This technique has been employed in several previous measurements, and is also utilized in the present work. A prerequisite is, however, that a large fraction of the angular distribution is measured.

Recently, the development of a well characterized tagged neutron beam at IUCF [13] opens up another possibility to measure absolute neutron cross sections directly of, e.g., np scattering, to the 1–2% level. Agreement between precision data taken with these very different techniques would strongly increase the confidence in the absolute scale.

These facts motivate new, precise determinations of the np scattering cross section at several energies, with an angular coverage that is as large as possible. In this paper, we present data from a measurement of the differential np scattering cross section at 96 MeV in the angular range $\theta_{c.m.}$ $=74°-128°$. These data have been linked to the angular distribution measured in 1991 at $\theta_{c.m.}=116°-180°$ by Rönnqvist *et al.* [14]. Both experiments were performed by the same collaboration and with the same experimental setup at the neutron beam facility at The Svedberg Laboratory (TSL) in Uppsala. Thus the present work is an extension of the Rönnqvist data, now covering the angular range $\theta_{c.m.}$ $=74°-180°$.

Section II of the paper contains a brief description of the experimental arrangement, while the analysis procedure and the important normalization technique are described and discussed in Sec. III. The results are presented and compared with other data, partial-wave analyses (PWA's), and NN potential predictions in Sec. IV. Extrapolation of the data to the pion pole gives a value for the charged πNN coupling constant. The analysis and results are presented and discussed in

The TSL Neutron Beam Facility
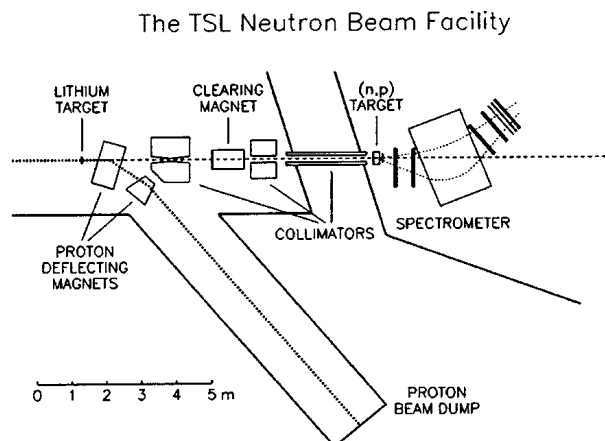
FIG. 1. Overview of the Uppsala neutron beam facility. The neutron production, shielding, and collimation are shown, as well as the magnetic spectrometer arrangement.

Sec. V. Finally, a summary and the conclusions are given in Sec. VI.

II. EXPERIMENTAL ARRANGEMENT

The experimental setup and procedure have been described in detail recently [2,15], and therefore only a brief summary will be given here.

The TSL neutron beam facility is shown in Fig. 1. Protons from the cyclotron impinge on the neutron production target from the left in the figure. Neutrons are produced by the $^7\text{Li}(p,n)^7\text{Be}$ reaction, using a 214-mg/cm^2-thick lithium target, enriched to 99.98% in ^7Li. After the target, the proton beam is bent into a well-shielded beam dump. The neutron beam is defined by a 1-m-long collimator, with two other collimators serving as beam scrapers. The vacuum system is terminated after the first collimator with a 1-mm-thick aluminum plate. Charged particles produced in this plate are deflected by a clearing dipole magnet. The diameter of the neutron beam at the np target position, 8 m from the neutron production target, is about 7 cm. The neutron yield is in the order of 10^6 s^{-1} over the full target area. The centroid of the full-energy peak in the neutron spectrum is determined to be 96 ± 0.5 MeV. The total energy spread in the peak is estimated to be 0.9 MeV [full width at half maximum (FWHM)].

To maximize the count rate without impairing the energy resolution, a sandwiched multitarget system is used. It consists of thin target layers interspaced by nine multiwire proportional chambers (MWPC's), each having an efficiency of $\geq99\%$. In this way, it is possible to determine in which target the scattering or reaction takes place, so that corrections for energy losses in the subsequent targets can be applied. The first two MWPC's provide veto signals for rejection of the few charged particles that contaminate the neutron beam. The target box contains five 35-mg/cm^2-thick CH$_2$ targets and two 85-mg/cm^2 ^{12}C targets, the latter for subtraction of the carbon contribution to the CH$_2$ spectra. The tar-

gets are stacked in the following (downstream) order: 2 CH_2, 2 carbon, and 3 CH_2 layers.

The momentum determination of the charged particles emitted from the targets is performed with a spectrometer consisting of a dipole magnet and four drift chambers (DCH's) [16], two in front of and two behind the magnet. The scattering angle is determined by the trajectory through the first two DCH's. The detection efficiency for a drift chamber plane is typically $\geq 98\%$. To minimize the multiple scattering of charged particles in air, the space between the first two DCH's and the volume in the pole gap is filled with helium gas.

The trigger signal is generated by a coincidence between a small 1-mm-thick plastic scintillator, located immediately after the multitarget box and a large 2-mm-thick plastic scintillator, positioned behind the last DCH. In addition, two large plastic scintillators of thicknesses 4 and 10 mm, respectively, are added behind the 2-mm plastic scintillator, to facilitate particle identification.

The entire setup can be rotated around a pivot point, located below the center of the multitarget box. With one position and one magnetic-field setting, the spectrometer has a horizontal angular acceptance of about 15° in the laboratory system. Measurements are performed with two different settings of the spectrometer position, covering the proton recoil angular ranges $\theta_{LAB} = 26°-41°$ and $35°-53°$, respectively. Under these conditions, the energy resolution in the measured spectra is typically in the range 3–5 MeV (FWHM). The angular resolution due to multiple scattering is estimated to be $0.6°-1.3°$ (rms).

III. DATA ANALYSIS

A. Data reduction and corrections

The data are analyzed off-line on an event-by-event basis. Before an event is accepted, a number of tests are applied. A brief summary of the analysis procedure is given below. More detailed information about the data reduction has been given in Ref. [2].

Events originating from charged particles contaminating the neutron beam, or from charged-particle production in the thin scintillator just after the target system, are rejected. The scattering angle is determined by calculating the particle trajectory through the first two DCH's, using both the horizontal and vertical coordinate information. The particle momentum is determined by a ray-tracing procedure, using magnetic field maps and position information from the DCH's. Three DCH's are required for this purpose. The use of the fourth DCH offers a possibility for a redundancy check. The few events with dubious energy determination, or with a trajectory outside the magnetic-field limits or an origin outside the neutron beam spot are rejected. To avoid vertical acceptance corrections, a narrow software gate of $\pm 0.8°$ is applied on the vertical scattering angle, ensuring that no events are lost in the magnetic gap. The momentum information, in combination with the pulse heights from two of the large scintillators, is used to discriminate between protons and other charged particles (almost exclusively deuterons).
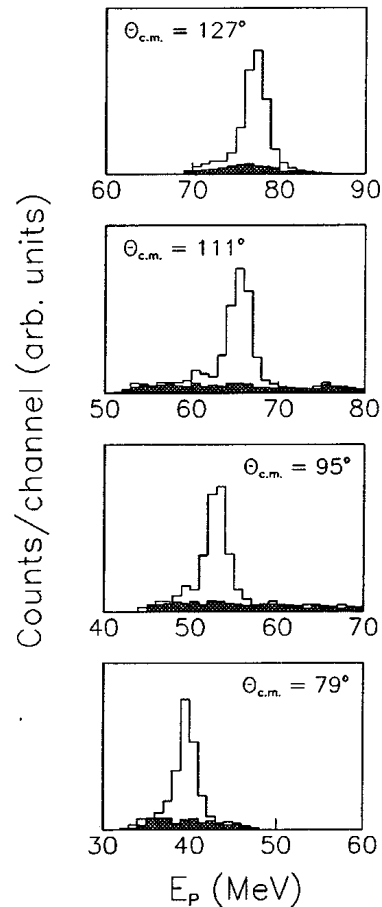
FIG. 2. Proton energy spectra from CH_2 (open histograms) and carbon (cross-hatched histograms) targets, respectively, at various scattering angles. The part of the CH_2 spectra at lower energies not accounted for by the carbon contribution originates from *np* scattering of neutrons from the low-energy neutron tail.

All accepted events are stored in matrices with angular and energy binning in the laboratory system of 1° and 0.25 MeV, respectively. Before extracting the hydrogen peak content, the carbon contribution to the CH_2 spectra is subtracted. This is illustrated for a few angles in Fig. 2, where an energy binning of 1 MeV is used. The open histograms represent the energy spectra from the CH_2 foils, while the cross-hatched histograms are those of the pure carbon targets, after normalization to the same number of target nuclei.

The *np* scattering peak contents are determined by integration. Since the energy resolution varies with angle, different integration windows are used. These are defined in a consistent way, and the final peak contents are determined by integrating the data in a region of $\pm \Delta E$ around the centroid, where ΔE is the peak FWHM. With this definition, the carbon background amounts to maximum 15% of the hydrogen peak for the largest recoil angles.

The variation of the width of the *np* peak with angle also causes an angular dependence in the background contribution from the low-energy continuum of the $^7Li(p,n)$ reaction. The data are corrected for this effect by using experi-
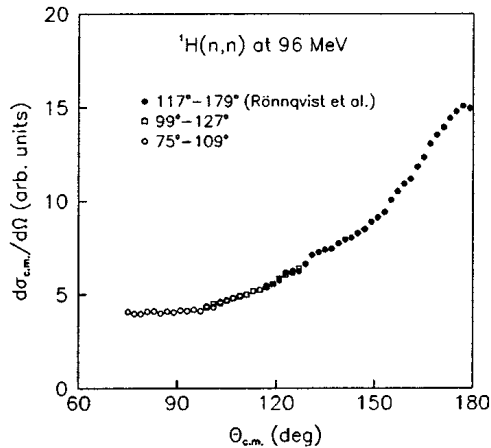
FIG. 3. Relative differential np scattering cross sections at E_n = 96 MeV. The open symbols represent data from the two magnetic settings, while the filled circles are the previously published backward-angle data [14]. The three data sets were normalized to each other in the overlapping regions.

mental neutron spectra from this reaction determined by Byrd and Sailor [17] at E_p = 90.1 and 139.9 MeV. To simulate the finite resolution of our experiment, the Byrd and Sailor spectra, which have a much better resolution than in the present experiment, are folded with Gaussian resolution functions. From these folded spectra, the neutron continuum contribution to the peak, as defined above, can be determined as a function of peak width, and appropriate relative correction factors ($<3\%$) can be determined.

Since the energy of the recoil protons varies with scattering angle, the variation of the proton absorption with energy in the detector system has to be taken into account. To first order, elastic in- and out-scattering of protons cancel, and thus only nonelastic losses have to be considered. We have calculated these losses in the targets, detectors, and helium gas, using the total reaction cross sections given by Carlson [18]. The proton attenuation gives non-negligible corrections only in the angular region $\theta_{c.m.} = 74° - 110°$, and the maximum correction amounts to 1.8% (at 74°).

B. Relative cross sections and uncertainties

The relative cross section data from the two different spectrometer settings, together covering the 74°–128° (c.m.) angular region, are used to extend the data of Rönnqvist *et al.* [14]. The three individual data sets, all treated as relative cross sections, are matched pairwise in the two uncorrelated overlapping regions using a minimum χ^2 criterion [2]. The result of this matching is shown in the c.m. system in Fig. 3. As can be seen, the agreement in shape in the overlapping regions is very good. Final relative np scattering cross sections are obtained by averaging the data from the different data sets in each 2° (c.m.) angular bin. A similar matching procedure was used by Rönnqvist *et al.* for five data sets to generate the full angular distribution. It should be pointed out that the five Rönnqvist sets, which were taken at different occasions, essentially fall into two main angular regions, i.e., 148°–180° and 116° to about 156°, respec-

tively. Thus there is a significant overlap of these two regions. Furthermore, there is no systematic shape difference between distributions with similar angular coverage, which is also verified by the small χ^2's mentioned.

Many sources of uncertainties contribute to the total error in the relative cross section. These errors are of both random and systematic character. Since the measurement is relative, only those systematic errors that affect the shape of the angular distribution have to be considered.

The random error is dominated by counting statistics, giving a contribution in the range 1.0–2.7 % per point for the new data. The smaller value is valid for the data points close to 127°. Another small, random error contribution is due to bin truncation when integrating the np peak. This error is at most 0.6% per point.

The most important contribution to the systematic error is related to the subtraction of the carbon background in the CH_2 energy spectra. Above about 145° the hydrogen peak is well separated from the carbon spectrum (Q value = −12.6 MeV), and below 125° the hydrogen peak is superimposed on a flat carbon continuum. In the latter region the uncertainty in the relative thickness of the CH_2 and pure carbon targets introduces an error in the np cross section. With an estimated relative thickness uncertainty of 5%, the error in the angular region 75°–127° is less than 0.7%.

In the angular range 125°–145° the hydrogen peak interferes with the rising slope of the carbon background. Hence a small error in the relative energy loss corrections for the CH_2 and carbon spectra, respectively, affects the background subtraction. This causes an error in the determined np cross section of $<2\%$, using an estimated relative energy uncertainty of ± 1 MeV. The problems arising from this effect can be seen in the Rönnqvist *et al.* [14] data around 133° in Fig. 3. Since the effect occurs in the middle of one of the Rönnqvist angular settings, it is not expected to contribute significantly to a possible progressive shape uncertainty arising from the overlap normalization procedure.

The correction ($<3\%$) for the contribution from the low-energy continuum of the $^7Li(p,n)$ spectrum to the np scattering peak introduces a systematic error that varies with the peak width and thus with the angle. Assuming a relative uncertainty of 10% in the correction, an error in the data of at most 0.3% arises.

The error from the small correction due to the energy-dependent attenuation of the protons is estimated to be less than 0.6%.

When adding the various systematic uncertainties quadratically, the total systematic error varies from 0.5 to 2.0 % in the full angular region. The largest errors are found in the range $\theta_{c.m.} = 125° - 145°$.

In addition to the random and systematic errors discussed, the shape of the full angular distribution is affected by the matching of the data sets. A quadratic addition of the uncertainties in the fitted coefficients, emerging mainly from the finite counting statistics, results in a shape error of $\pm 2.1\%$ between the most forward and most backward data sets, i.e., in the 75°/179° cross section ratio. This slope error includes the corresponding uncertainty of $\pm 1.3\%$ from the Rönnqvist *et al.* data. There could in principle be additional slope errors
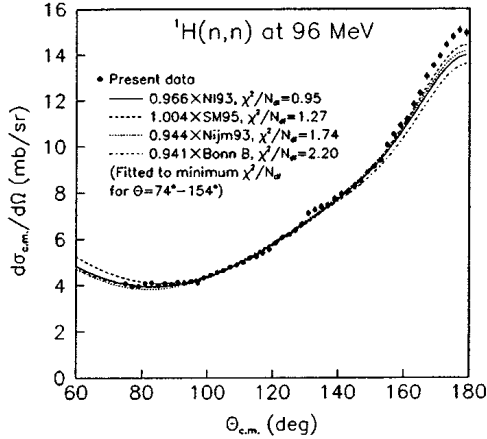
FIG. 4. Relative differential *np* scattering cross sections at E_n $=96$ MeV. The filled circles represent the present data, while the solid and dashed lines are the SM95 [20] and NI93 [27] PWA's, respectively, and the dotted and dot-dashed lines are the Nijm93 [27] and Bonn B [26] *NN* potentials, respectively, all least-squares fitted to the data in the angular region 74°–154°.

caused by small inhomogeneities in the drift chamber efficiencies, which could amplify from one setting to the next one. This does not seem probable, however, since 75% of the angular distribution, i.e., from 74° to 154°, is extremely well described by the PWA's. This is shown in Fig. 4, where the normalization of the NI93 [19] and SM95 [20] PWA's have been least-squares fitted to the experimental data in the angular range 74°–154°. The χ^2 per degree of freedom is 0.95 and 1.27 with respect to the NI93 and SM95 PWA's, respectively. Lowering the upper angle limit point by point results in fits with similar quality, while increasing it leads to a rapidly increasing χ^2 per degree of freedom. Thus shape deviations from these models are found only beyond 154°, which is within one of the angular settings, and more or less outside the overlap region for the next setting. For comparison we show also in this figure similar least-square fits for the Nijmegen (Nijm93) and Bonn B potentials with χ^2 per degree of freedom of 1.74 and 2.20, respectively. One can see that in the 74°–154° region the shape of the Nijm93 potential angular distribution is closer to that of the data than the shape of the Bonn B potential.

C. Normalization procedure

Absolute *np* scattering cross sections are obtained by normalization to the total *np* cross section, which can be done since other reaction channels are negligible at 96 MeV. The total cross section σ_T has been experimentally determined around 100 MeV by several groups, and is considered to be well known. If the entire angular range, i.e., from 0° to 180°, had been measured in the present experiment, it would have been possible to normalize the data to the total cross section directly by integration. Since that is not the case, we consider our angular distribution as a measurement of a *fraction* of the total cross section, i.e., the part between 74° and 180°. By using a number of PWA's or potential models, it is possible to estimate the magnitude F of this fraction, to which the
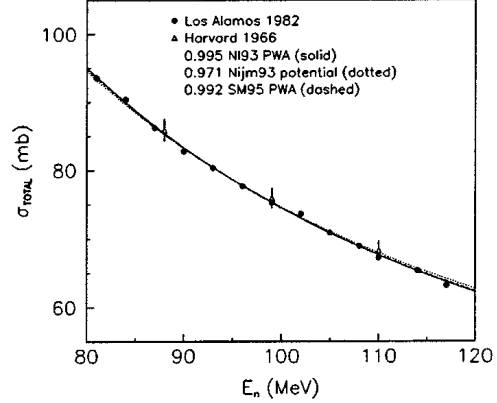
FIG. 5. Total *np* cross section versus energy in the range 80–120 MeV. The different symbols represent experimental data [21,22], while the lines are from PWA's and *NN* potentials, renormalized by us to the data in the shown energy region.

data should be normalized. Thus we require that the integral over the solid angle of our data should be equal to

$$\sigma_{74°-180°} = \int_{74°}^{180°} \frac{d\sigma}{d\Omega} d\Omega = F\sigma_T^{exp}, \qquad (1)$$

where

$$F = \sigma_{74°-180°}^{PWA}/\sigma_T^{PWA}. \qquad (2)$$

To obtain σ_T^{exp}, we have used the Los Alamos data of Lisowski *et al.* [21], and the Harvard data of Measday and Palmieri [22]. The total error of the former is below 1% and of the latter about 4%. These data are in very good agreement. At slightly higher energies, i.e., above 125 MeV, one has also excellent agreement between these data and those from PSI by Grundies *et al.* [23], for which the errors are less than 1.5%.

The total cross section at 96 MeV is determined by fitting the absolute scale of the Nijmegen energy-dependent PWA NI93 [19] to the experimental data in the energy region 80–120 MeV, as illustrated in Fig. 5. A slight renormalization of 0.995 is needed to obtain a good fit. Also other PWA's and potentials have been tested, but it is found that NI93 gives the best description of the energy dependence of σ_T^{exp}. The resulting total cross section at 96 MeV is

$$\sigma_T^{exp} = 77.74 \pm 0.78 \pm 0.43 = 77.74 \pm 0.89 \text{ mb}, \qquad (3)$$

where the first error corresponds to the 1% systematic error of the Lisowski data, and the second error is due to the ± 0.5 MeV uncertainty in the neutron beam energy, because the total cross section has a slope of 1.11%/MeV.

The fraction F of the total cross section covered in the present experiment is determined from the PWA's SM95 [20], VL40 [3], and VZ40 [24] of VPI, and NI93 of Nijmegen [19]. VL40, VZ40, and NI93 are energy-dependent PWA's based on data in the 0–350 or 400 MeV region, while SM95 was obtained by fitting up to 1.6 GeV. The result is given in Table I, together with integrated cross

TABLE I. Total cross sections (σ_T) and angular fractions ($F = \sigma_{74°-180°}/\sigma_T$) for different PWA's and NN potential models. The weighted experimental value is 77.74 mb (see the text for more details).

PWA or potential	σ_T	$\sigma_{0°-74°}$	$\sigma_{74°-180°}$	F	σ_T^{exp}/σ_T
SM95 [20]	78.22	30.88	47.34	0.6052	0.9939
VZ40 [24]	77.52	30.22	47.30	0.6102	1.0028
VL40 [3]	77.70	30.19	47.51	0.6115	1.0005
NI93 [19]	78.07	29.30	48.77	0.6247	0.9958
Average	77.88	30.15	47.73	0.6129	0.9982
Paris [25]	79.75	29.80	49.95	0.6263	0.9748
Bonn B [26]	77.96	28.95	49.01	0.6287	0.9972
Nijm93 [27]	79.99	30.12	49.87	0.6235	0.9719

sections and fractions for the Paris [25], Bonn B [26], and Nijmegen [27] (Nijm93) potentials for comparison. For the final value of F we take the average of the four mentioned PWA's to obtain $F = 0.613$. The potential models are not included in the determination, because we believe that the PWA's are more reliable since they describe the total cross section better. Thus the integrated np scattering data have been normalized to

$$\sigma_{74°-180°}^{exp} = F\sigma_T^{exp} = 0.613 \times 77.74 = 47.65 \text{ mb.} \quad (4)$$

The result is shown in Fig. 6(a), where the differential cross section has been multiplied with the solid angle element $2\pi \sin\theta$. In this representation, each angle bin directly shows its contribution to the total cross section. Also shown in the figure are the PWA's used to determine F, after normalization to $\sigma_T^{exp} = 77.74$ mb. As was discussed in the previous section, the data are well represented by any of the PWA's in most of the covered angular region. Deviations occur only at the extreme backward angles which, however, carry only small contributions to the total cross section [see Fig. 6(a)].

The spread in F for the various PWA's and NN potential models can be used to estimate the precision of this normalization procedure. One can see from Table I that the maximum deviation from the average value is -1.3% for the SM95 solution and $+2.6\%$ for the Bonn B potential. From this comparison, we believe that it is fair to say that the normalization uncertainty is within $\pm 1.5\%$. In addition, we have the "intrinsic" uncertainty in σ_T^{exp} of 1.1%. Summing these effects yields a total normalization uncertainty of $\pm 1.9\%$. However, a word of caution should be given here: The estimated uncertainty relies on the assumption that the various models give a reasonable account of the main characteristics of the angular distribution. If the balance between the two humps at about 40° and 130° seen in Fig. 6(a) is considerably different, our normalization would of course be affected. If, e.g., the cross section in the forward hemisphere is larger than predicted by the models, this has to be com-
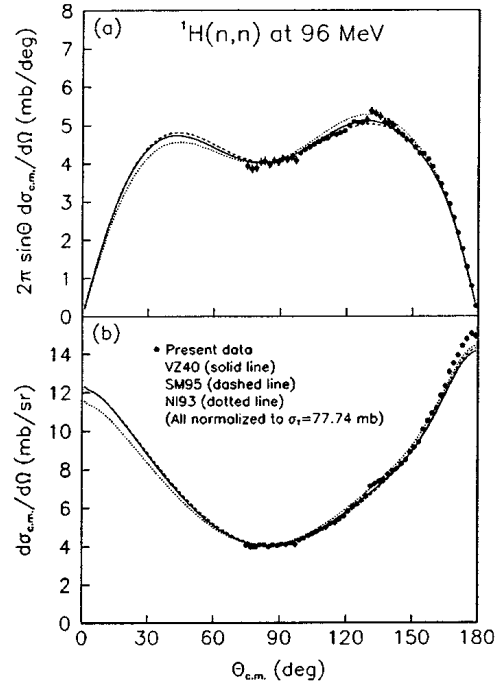
FIG. 6. Angular distributions for the SM95 [20], VZ40 [24], and NI93 [27] PWA's, and the present experimental data (filled circles) at 96 MeV. The VL40 [3] PWA solution is almost identical to VZ40 and is not shown for clarity. (a) Differential np scattering cross sections multiplied by the solid angle element $2\pi \sin\theta$. (b) Differential cross sections for np scattering.

pensated by lower backward cross sections to conserve the total cross section, and in this case our normalization would have to be lower.

IV. EXPERIMENTAL RESULTS

The final experimental differential cross sections are given in Table II and are shown as filled circles in Fig. 6(b). The errors given are the quadratic sums of the statistical and systematic uncertainties of the relative cross sections discussed above. They do not include, however, the normalization uncertainty of $\pm 1.9\%$ and the shape uncertainty of $\pm 2.1\%$ between the most forward and backward data sets, i.e., in the 75°/179° cross section ratio. These errors are correlated, and thus no individual point has a normalization error larger than about 2.2%. Also shown in the figure are the PWA's used to determine the normalization. As can be seen, the data are steeper than the PWA's in the 154°–180° region, while they are well described at smaller angles, as has been discussed earlier. As can be expected from the figure, and as has been mentioned in Ref. [8], these data and those of our previous measurement at 162 MeV [2] lead to a very high χ^2 for the PWA NI93 [19].

The present extension in angular range of the previous Rönnqvist *et al.* data [14] leads to a 1% higher normalization for the latter, which is well within the 4% normalization error stated in that work.

The new 96 MeV data are compared with other experi-

TABLE II. Differential cross sections for *np* scattering at 96 MeV.

$\theta_{c.m.}$ (deg.)	$d\sigma/d\Omega$ (mb/sr)	$\theta_{c.m.}$ (deg.)	$d\sigma/d\Omega$ (mb/sr)	$\theta_{c.m.}$ (deg.)	$d\sigma/d\Omega$ (mb/sr)
75.0	4.075±0.109	111.0	4.985±0.068	147.0	8.492±0.151
77.0	3.957±0.108	113.0	5.181±0.068	149.0	8.886±0.101
79.0	3.956±0.106	115.0	5.240±0.069	151.0	9.128±0.101
81.0	4.080±0.106	117.0	5.393±0.063	153.0	9.401±0.101
83.0	4.098±0.105	119.0	5.556±0.064	155.0	10.067±0.121
85.0	3.988±0.103	121.0	5.836±0.066	157.0	10.522±0.121
87.0	4.083±0.103	123.0	6.073±0.068	159.0	10.915±0.141
89.0	4.038±0.102	125.0	6.190±0.069	161.0	11.178±0.141
91.0	4.132±0.102	127.0	6.371±0.069	163.0	11.834±0.141
93.0	4.111±0.101	129.0	6.634±0.121	165.0	12.329±0.151
95.0	4.170±0.100	131.0	7.119±0.131	167.0	13.056±0.162
97.0	4.110±0.098	133.0	7.260±0.131	169.0	13.520±0.121
99.0	4.328±0.055	135.0	7.391±0.141	171.0	13.934±0.131
101.0	4.442±0.056	137.0	7.452±0.141	173.0	14.429±0.131
103.0	4.560±0.056	139.0	7.735±0.141	175.0	14.783±0.141
105.0	4.660±0.056	141.0	7.947±0.141	177.0	15.075±0.151
107.0	4.789±0.057	143.0	8.038±0.141	179.0	14.944±0.172
109.0	4.898±0.057	145.0	8.280±0.141		

mental data from measurements performed close to that energy in Fig. 7(a). Thus we give in the figure the data of Stahl and Ramsey [28], Chih and Powell [29], Scanlon *et al.* [30], and Bersbach *et al.* [31]. It can be seen in the figure that the present data are higher at the most backward angles, which indicates a larger steepness at those angles. The PWA's and the potential models have been adjusted to the Bonner data at higher energies, as well as to these earlier, not very precise, data. A comparison to the various models is therefore more instructive than a direct comparison to the data. From the study made in the last paragraph of Sec. III B, the result of which was shown in Fig. 4, one can conclude that the shape of our backward differential cross section, i.e., for angles beyond 154°, is clearly steeper than that of the models, and thus also steeper than the older data. Our data has also a larger 180°/90° cross section ratio.

The Stahl and Ramsey data [28] at 91 MeV from Harvard are included in the fits of the VPI PWA's, but not in that of the Nijmegen group. The experiment covered scattering angles between 60° and 180°, comprising in total 25 data points. The data were normalized to the total cross section, at that time believed to be 78.5±3 mb (the present value is 82.0 mb [21]). For the region not covered by the experiment, other *np* experimental data were used. The normalization error was assumed to be ±5%.

The Chih and Powell [29] data at 90 MeV consist of 18 points distributed over the angular range 8°–180°. The measurement, which was performed with a cloud chamber, was relative and was normalized to a total *np* cross section of 76.0 mb (the present value is 82.8 mb). The normalization uncertainty is not discussed in the paper. The data are included in the Nijmegen PWA fit, but are not present in the VPI data base.
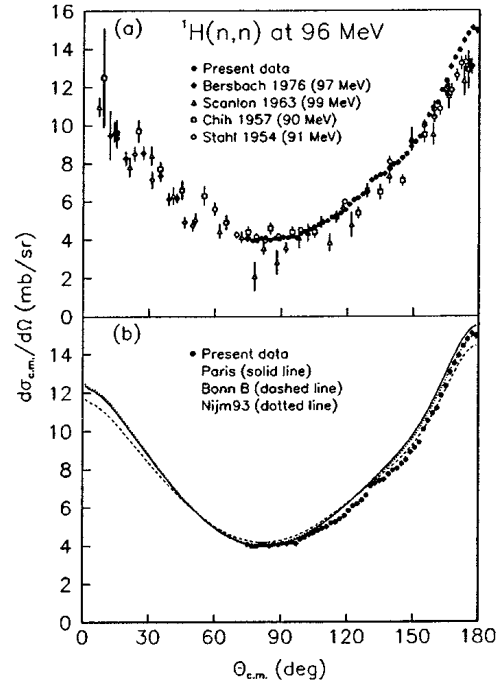
FIG. 7. (a) Differential *np* scattering cross sections of the present work (filled circles). Also plotted are other data from the literature at energies close to 96 MeV [28–31]. (b) The present differential cross sections plotted together with the Paris [25], Bonn B [26], and Nijm93 [27] *NN* potentials.

The Scanlon *et al.* data [30] at 99 MeV from Harwell cover the angular range from 7° to 173° in the c.m. system. Absolute cross sections between 7° and 120° were deduced by measuring the count-rate ratio between scattered neutrons and those of the direct neutron beam. Between 80° and 173°, the recoil protons were detected and only relative values for the cross sections could be obtained. This data set was normalized to the small-angle set in the 80°–120° region. Absolute values were also determined by normalizing to the *np* total cross section. The final differential cross sections, shown in Fig. 7(a), were obtained by combining the results of the two methods. The normalization uncertainty was claimed to be better than ±4%. The Scanlon data have been under critical examination by Hammans *et al.* [32] and Henneck [33], who recommend rejection of these data, based on experimental problems. The Nijmegen group has removed these data from their PWA fit, while the VPI group includes them in all their PWA versions.

The 97-MeV data of Bersbach *et al.* [31] were measured between 10° and 50° in the c.m. system, and are included in both the Nijmegen and VPI PWA fits. The normalization uncertainty was estimated to be ±10%. Like the Scanlon forward-angle data, absolute cross sections were obtained from scattered versus direct beam count-rate ratios.

The older data show a larger spread than the present ones, and it is therefore difficult to judge upon the degree of agreement. Furthermore, they are taken at slightly different energies, which affect the shape of the angular distribution. If the Stahl and Ramsey data, which show the smallest spread of

the old data sets, are corrected for the energy difference (91 vs 96 MeV) using the NI93 PWA, which increases the 180°/90° cross section ratio by about 7%, they agree fairly well with the present ones up to 175°, after upward renormalization of about 10%.

In Fig. 7(b), the present data are compared with three NN potential models, namely the Paris [25], Bonn B [26], and Nijm93 [27] potentials. The angular distributions of the Paris and Nijm93 potentials are rather similar, and describe the data reasonably well in the 160°–180° region, while a 7% overprediction is seen in the 110°–160° region. One should keep in mind, however, that both the Paris and Nijm93 potentials overpredict the total cross section by 3%. It is interesting to note that although the Nijm93 potential and the present data do not agree over the entire interval studied, the 180°/90° cross section ratio is in good agreement. The Bonn B potential is relatively close to the data in the 130°–165° region, but underpredicts it at 180° by 6%. This potential gives, on the other hand, a total np cross section which is in good agreement with the experimental one.

V. DETERMINATION OF THE πNN COUPLING CONSTANT

We have in the previous sections achieved our primary aim, which is to give normalized np cross sections. We now briefly explore the bearing these data have on the discussion of the πNN coupling constant. We closely follow the procedure previously discussed in our work at 162 MeV to which we refer for details [2]; here we only sketch the procedure. The analysis is based on the fact that the charged pion exchange contributes importantly to the np charge exchange at small momentum transfers. This was realized already in 1958 by Chew, who suggested a model-independent extrapolation to the pion pole for the determination of the coupling constant.

The Chew extrapolation procedure [34,35] is based on a polynomial expansion in the square of the momentum transfer, q^2. The technique used to extrapolate to the pion pole is to first construct a smooth physical function, the Chew function, by multiplying the cross section by $(q^2 + m_\pi^2)^2$, which removes the pole term, after which the extrapolation can be made far more safely and controlled. Here m_π is the charged pion mass. More exactly, in the physical region the function $y(x)$ is defined by

$$y(x) = \frac{sx^2}{m_\pi^4 g_R^4} \frac{d\sigma}{d\Omega}(x) = \sum_{i=0}^{n-1} a_i x^i.$$ (5)

Here s is the square of the total energy and $x = q^2 + m_\pi^2$. At the pion pole $x = 0$, the Chew function gives

$$y(0) \equiv a_0 \equiv g_{\pi^\pm}^4 / g_R^4$$ (6)

in terms of the pseudoscalar coupling constant $g_{\pi^\pm}^2 \approx 14$. The quantity g_R^2 is a reference scale for the coupling chosen for convenience. It is important to realize that the model-independent extrapolation requires accurate data with abso-

lute normalization of the differential cross section. If the differential cross section is incorrectly normalized by a factor N, the extrapolation gives $\sqrt{N} g_{\pi^\pm}^2$. This is one of the most important sources of uncertainty in the practical extrapolation from data.

An improvement on this rather slowly converging expansion is the difference method introduced in our previous work at 162 MeV [1,2], and also applied to $\bar{p}p$ charge exchange [36]. The difference method applies the Chew method to the difference between the function $y(x)$ obtained from a model with exactly known coupling constant and from the experimental data, i.e.,

$$y_M(x) - y_{exp}(x) = \sum_{i=0}^{n-1} d_i x^i$$ (7)

with g_R of Eqs. (5) and (6) replaced by the model value g_M. At the pole

$$y_M(0) - y_{exp}(0) \equiv d_0 \equiv \frac{g_M^4 - g_{\pi^\pm}^4}{g_M^4}.$$ (8)

This procedure should diminish systematic extrapolation errors and remove a substantial part of the irrelevant information at large momentum transfers, provided that the data and the model have a similar behavior at large momentum transfers. Otherwise, the difference method has little advantage as compared with the Chew approach.

As previously, we apply the difference method using four comparison models, i.e., the Nijm93 [27] and Bonn B [26] potentials, the Nijmegen energy-dependent PWA NI93 [19], and the VPI energy-dependent PWA SM95 [20]. The previous χ^2 study performed in the angular range 74°–154° has shown that the NI93 model agrees quite well with the data at large momentum transfers as does the Nijm93 one (cf. Fig. 4). For the region 74°–86° the SM95 model deviates markedly from the data and these are also not very well described by the Bonn B model. Already at this stage one should expect the difference method to work better for the NI93 and Nijm93 models than for the SM95 and Bonn B ones. For the case of the Bonn B potential, some minor modifications must be made in Eq. (8) to account for the fact that it uses an average pion mass of $\bar{m}_\pi = 138.03$ MeV, which shifts the pole position. This changes slightly the difference between the model and experimental Chew functions, and induces a small correction[1] for the relation between $g_{\pi^\pm}^2$ and d_0. The resulting $y_M(x) - y_{exp}(x)$ are shown in Figs. 8 and 9, together with polynomial fits in x of different orders $n-1$. As can be seen, the error bars blow up at large x, which is a

---

[1] In Eq. (8) one replaces $y_M(x)$ by $\bar{y}_M(\bar{x})$ $= (s\bar{x}^2/m_\pi^4 g_M^4) \, d\sigma/d\Omega_M(\bar{x})$ where $\bar{x} = x + \delta m^2$ with $\delta m^2 = \bar{m}_\pi^2 - m_\pi^2$. At the pion pole and to first order in δm^2, d_0 $= (\bar{m}_\pi/m_\pi)^4 [1 + \delta m^2 y_M'(0)] - g_{\pi^\pm}^4 / g_M^4$ with $y_M'(0)$ $= dy_M(\bar{x})/d\bar{x}|_{\bar{x}=0}$. This gives to first order in d_0, $g_{\pi^\pm}^2 = g_M^2 [1 - d_0/2 + \delta m^2 y_M'(0)/2]$. Here, $\delta m^2 y_M'(0)/2 \approx 0.01$.
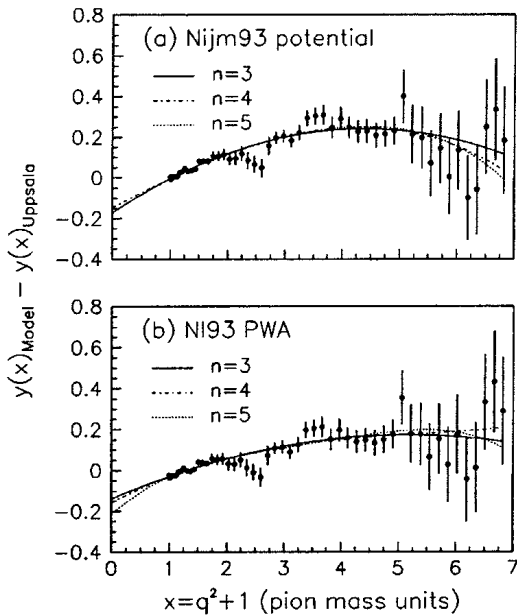
FIG. 8. Extrapolations of the Chew function $y(x)$ to the pion pole at 96 MeV with the difference method using different comparison functions and different polynomials orders. The comparison functions are (a) the Nijm93 potential model [27], (b) the Nijmegen energy-dependent PWA NI93 [19].

consequence of the multiplication of the cross section with x^2, leading to a smaller weight for the large q^2 region in the extrapolation. Already a visual extrapolation to $x=0$ gives $g^2_{\pi^\pm}$ to a precision of about 3% for any given comparison function in Figs. 8 and 9, especially if one ignores the few
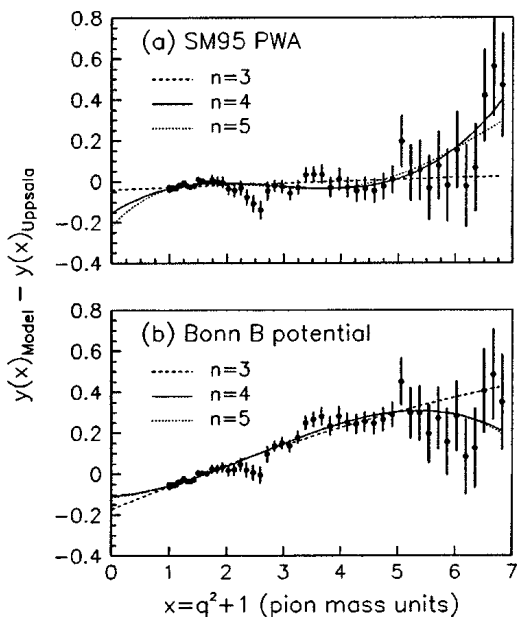

FIG. 9. Same as Fig. 8. The comparison functions are (a) the Virginia energy-dependent PWA SM95 [20], and (b) the Bonn B potential model [26].

points around $x=2.5$, which might be affected by the carbon background subtraction problem around 133° discussed in Sec. III B. For the Nijm93 potential [Fig. 8(a)], the NI93 PWA [Fig. 8(b)], and the SM95 PWA [Fig. 9(a)], $d_0 \simeq -0.15(5)$, leading to $g^2_{\pi^\pm} \simeq 14.60(34)$, 14.60(34), and 14.78(34), respectively. For the Bonn B potential [Fig. 9(b)], $d_0 \simeq -0.14(5)$, which gives $g^2_{\pi^\pm} \simeq 15.26(36)$. This is in agreement with the more sophisticated and accurate analysis below.

The values of the charged coupling constant obtained from the extrapolation using the polynomial fits are given in Table III for the four different comparison models considered here. Let us recall that n is the number of terms in the polynomial expansion, χ^2/N_{df} is the average χ^2 per degree of freedom and $g^2_{\pi^\pm}$ is the resulting value of the coupling constant, with its statistical and extrapolation error.[2] The behavior of χ^2/N_{df} as a function of n is characteristic. It falls with increasing n to a nearly constant value with variation less than 2%, corresponding to the usual criterion that a decrease in the total χ^2 by one unit when n is increased by one step, is an indication that the data are overparametrized. In the present case of 53 data points, this occurs when χ^2/N_{df} changes by less than 2%. Additional terms give only small gains, the data become rapidly overparameterized and the uncertainty large. The values of $g^2_{\pi^\pm}$ remain, however, compatible within errors. We determine $g^2_{\pi^\pm}$ from the first value of n for which χ^2/N_{df} becomes nearly constant. This is in accordance with standard statistical procedures. The value for χ^2/N_{df} of 0.93 to 0.95 in Table III is well within the statistically expected range. Note, however, that χ^2/N_{df} as expected becomes close to unity *on the average* for a large number of pseudoexperiments, when the number of parameters used is sufficient to describe the data well (see Table IV below).

With the Nijm93 potential and NI93 PWA our best choice of n is 3 according to the procedure described in the previous paragraph. This gives a small statistical extrapolation error. Going to $n=4$ gives approximately the same quality of fits and does not really change the extrapolated value of $g^2_{\pi^\pm}$, but the errors become larger. With the SM95 PWA of VPI and the Bonn B potential, the best choice of n is 4. The corresponding $g^2_{\pi^\pm}$ values are larger than those with the previous two models, and so are their uncertainties. While the $g^2_{\pi^\pm}$ using SM95 is compatible within errors to the Nijm93 and NI93 ones, that using Bonn B is slightly larger. The shape of the angular distribution of the Bonn B potential fits the data less well than those of the other models [see Figs. 4, 6(b), and 7(b)]. This difference is most probably responsible for the relatively large $g^2_{\pi^\pm}$ value obtained in this case.

As in our preceding work, we establish the systematic uncertainties of the extrapolation procedure from pseudodata with uncertainties corresponding to those of the present ex-

---

[2]Recall that this error has only a meaning when the χ^2/N_{df} is close to 1.

TABLE III. Values of the coupling constant obtained from polynomial fits with n terms to data at 96 MeV using the difference method for the full range of data ($0 < q^2 < 5.8$ m_π^2). The experimental values at the minimum χ^2/N_{df} are indicated in boldface. The comparison models are the Nijm93 [27] and Bonn B [26] potentials, and the NI93 [19] and SM95 [20] energy-dependent PWA's. The model coupling constants are $g_{\pi^\pm}^2$,(Nijm93) = $g_{\pi^\pm}^2$,(NI93) = 13.58, $g_{\pi^\pm}^2$,(SM95) = 13.75, and $g_{\pi^\pm}^2$,(Bonn B) = 14.40.

n	χ^2/N_{df}	$g_{\pi^\pm}^2$	χ^2/N_{df}	$g_{\pi^\pm}^2$	χ^2/N_{df}	$g_{\pi^\pm}^2$	χ^2/N_{df}	$g_{\pi^\pm}^2$
	Nijm93 − Uppsala		NI93 − Uppsala		SM95 − Uppsala		Bonn B − Uppsala	
2	1.917	14.11 ± 0.04	1.242	14.16 ± 0.04	1.333	14.02 ± 0.04	1.107	15.34 ± 0.03
3	0.956	**14.69 ± 0.09**	0.966	**14.49 ± 0.09**	1.359	14.03 ± 0.09	1.081	15.46 ± 0.08
4	0.956	14.54 ± 0.18	0.974	14.61 ± 0.18	0.962	**14.77 ± 0.18**	0.932	**15.01 ± 0.18**
5	0.971	14.71 ± 0.39	0.970	14.98 ± 0.39	0.955	15.17 ± 0.38	0.951	15.07 ± 0.38

periment, according to the following procedure. For each of the four models mentioned above, which all have a known coupling constant, we simulate our experimental data by generating 10 000 pseudoexperiments from the exact model values. The individual pseudodata are obtained by adding to these exact values a random error with a Gaussian distribution [6,37]. We then analyze each pseudoexperiment using the difference method, with the three other theoretical models as comparison models, and determine a value for the coupling constant. The average value for this sample of simulations is obtained to high accuracy. We list the result of this exercise, with all six permutations, in Table IV. The model in quotation marks is the one used to generate the "experimental" pseudodata. Here $g_{\pi^\pm}^2$ is the mean value of the coupling constant for the 10 000 pseudoexperiments, while the errors quoted are standard deviations for individual pseudoexperiments.

We now discuss the systematic deviations $\delta g_{\pi^\pm}^2$ of the mean value in the sample from that of the true value in the model (see Table IV). We first note that once χ^2/N_{df} has reached its minimum plateau close to 1 within a few percent, there are few systematic deviations clearly outside the statistical uncertainty. The principal one occurs in the Bonn B − "Nijm93" difference for $n = 4$ with $\delta g_{\pi^\pm}^2 = -0.50$ (-3.7%). The Bonn B − "NI93" difference also exhibits a

rather large systematic shift $\delta g_{\pi^\pm}^2 = -0.43$ for $n = 4$. This is to be expected, since the Bonn B − "NI93" difference follows mathematically from the NI93 − "Nijm93" one for $n = 4$, as seen from Table IV. One has

$$\delta g_{\pi^\pm}^2(\text{Bonn B} - \text{"NI93"})$$
$$= \delta g_{\pi^\pm}^2(\text{Bonn B} - \text{"Nijm93"})$$
$$- \delta g_{\pi^\pm}^2(\text{NI93} - \text{"Nijm93"})$$
$$= -0.50 + 0.07 = -0.43.$$

The Bonn B potential belongs to a previous generation of descriptions of NN observables as compared to the other models. It has a notably worse value for χ^2/N_{df} with respect to our data than the other models. After adjustment for normalization, the χ^2/N_{df} is 13.0, as compared to 5.02, 5.64, and 2.6 for Nijm93, NI93, and SM95, respectively. The Bonn B potential gives a larger systematic error than those of a typical realistic modern comparison function.

To summarize, polynomial fits using the difference method for the present experimental data give $n = 3$ for the NI93 and Nijm93 models and $n = 4$ for the SM95 and Bonn B models. The value for χ^2/N_{df} is systematically somewhat smaller than 1, which reflects the fact that ten points have

TABLE IV. Values of the coupling constant obtained from polynomial fits with n terms to "pseudodata" at 96 MeV using the difference method for the range $0 < q^2 < 5.8 m_\pi^2$. The comparison models and the model coupling constants are the same as in Table III. $\delta g_{\pi^\pm}^2$ is the systematic shift from the true model value.

n	χ^2/N_{df}	$g_{\pi^\pm}^2$	$\delta g_{\pi^\pm}^2$	χ^2/N_{df}	$g_{\pi^\pm}^2$	$\delta g_{\pi^\pm}^2$	χ^2/N_{df}	$g_{\pi^\pm}^2$	$\delta g_{\pi^\pm}^2$
	NI93 − "Nijm93"			SM95 − "Nijm93"			Bonn B − "Nijm93"		
2	1.27	13.63 ± 0.04	−0.05	2.56	13.49 ± 0.04	0.08	1.67	14.85 ± 0.04	−1.27
3	1.07	13.35 ± 0.10	0.23	1.62	12.86 ± 0.10	0.72	1.08	14.40 ± 0.09	−0.82
4	1.01	13.65 ± 0.20	−0.07	1.01	13.82 ± 0.19	−0.24	1.00	14.08 ± 0.19	−0.50
5	1.00	13.86 ± 0.42	−0.28	1.00	14.06 ± 0.42	−0.48	1.00	13.95 ± 0.42	−0.37
	Bonn B − "NI93"			Bonn B − "SM95"			NI93 − "SM95"		
2	1.39	14.79 ± 0.04	−1.21	2.15	15.09 ± 0.04	−1.34	1.56	13.90 ± 0.04	−0.15
3	1.29	14.61 ± 0.09	−1.03	2.13	15.21 ± 0.09	−1.46	1.29	14.22 ± 0.09	−0.47
4	1.02	14.01 ± 0.19	−0.43	1.02	14.01 ± 0.19	−0.26	1.00	13.58 ± 0.20	0.17
5	1.00	13.67 ± 0.42	−0.09	1.00	13.64 ± 0.42	0.11	1.00	13.55 ± 0.43	0.20

their errors increased by 25% to account for uncertainties in the carbon subtraction procedure [14], as previously noted. This leads to a decrease of the overall χ^2/N_{df} by about 0.07, quite apart from the fact that smaller or larger values than 1 normally occurs in a sample. We have chosen to average the values of the four comparison models, and find $g_{\pi^\pm}^2 = 14.74 \pm 0.14$. The systematic extrapolation uncertainty is determined from the spread of values to be $\pm 0.26(1.8\%)$, while the uncertainty from normalization is 1%, i.e., ± 0.15. Thus the final value for the charged πNN coupling constant from the present work is $\sqrt{N} g_{\pi^\pm}^2 = 14.74 \pm 0.14$ (extrapolation and statistical) ± 0.26 (systematic) ± 0.15 (normalization) $= 14.74 \pm 0.33$. This result is consistent with our previous finding, $\sqrt{N} g_{\pi^\pm}^2 = 14.52 \pm 0.13$ (extrapolation and statistical) ± 0.15 (systematic) ± 0.17 (normalization) $= 14.52 \pm 0.26$, extracted at 162 MeV [1,2].

VI. SUMMARY AND CONCLUSIONS

The *np* differential cross section has been measured at 96 MeV using the neutron beam facility at the The Svedberg Laboratory in Uppsala. The data from Rönnqvist *et al.* have been extended to cover the $74°-180°$ region. The data were normalized using the total *np* cross section, which has been experimentally determined with high precision by Lisowski *et al.* Since our data do not cover the full angular range, the experiment was considered as a measurement of a fraction of the total cross section. This fraction was determined by using the angular shape of a number of energy-dependent PWA's. The data were normalized to the average fraction, obtained from those PWA's, multiplied with the experimental total cross section. We estimate the normalization error to $\pm 1.9\%$.

A general feature is that our data have a steeper slope in the $150°-180°$ angular region than most of the existing data in the same energy region. As a consequence, the slope is also steeper than several of the current PWA's and *NN* potential models. A similar situation is also present at higher energies, where large data sets disagree significantly in shape.

The *np* scattering cross section at 180° is used as a primary standard for normalization of most other neutron-induced cross sections. Uncertainties of the order of 10% in this cross section are therefore unacceptable. Remeasuring the absolute *np* scattering cross sections with high precision and at several energies should be of high priority.

As a by-product of the present investigation we obtain an extrapolated value $g_{\pi^\pm}^2 = 14.74 \pm 0.33 (f_{\pi^\pm}^2 = 0.0814 \pm 0.0018)$ for the charged πNN coupling constant using the difference method. This is consistent with the value $= 14.52 \pm 0.26$ found in our previous work at 162 MeV [1,2]. Both these values are 3–6 % higher than those indicated by πN data and these problems are presently under debate [4,5]. It is noteworthy that the recent model-independent determination of the coupling constant from the Goldberger-Miyazawa-Oehme (GMO) relation gives a noticeably larger value than those derived from the indirect methods [38]. The present value is within about two standard deviations of this independent new value. Our values depend critically on the absolute normalization of the *np* cross sections, presently inferred indirectly using theoretical assumptions about the unmeasured cross section in the forward hemisphere. These missing data are urgently needed, and are expected to become available in the near future [39] (see below). In addition, directly measured absolutely normalized *np* cross sections in the backward hemisphere are expected to appear on the market within a few years [13].

Our future plans include measurements of *np* scattering between 10° and 170° (c.m.) at a few energies in the 50–180-MeV range. To this end, a new experimental setup is under construction [39]. The new detector system has been designed to detect either recoil protons or scattered neutrons. In this manner, it will be possible to cover both the backward angles by detecting the recoil protons and the forward angles by detecting the scattered neutrons. In particular, we plan to extend the data we have at 96 and 162 MeV to cover the full angular range, i.e., also the forward angles $\theta_{c.m.} = 10°-70°$. By including these forward-angle data, we could normalize our angular distributions to the total *np* cross section directly, without any assumptions about the angular shape.

[1] T.E.O. Ericson, B. Loiseau, J. Nilsson, N. Olsson, J. Blomgren, H. Condé, K. Elmgren, O. Jonsson, L. Nilsson, P.-U. Renberg, A. Ringbom, T. Rönnqvist, G. Tibell, and R. Zorro, Phys. Rev. Lett. **75**, 1046 (1995).

[2] J. Rahm, J. Blomgren, H. Condé, S. Dangtip, K. Elmgren, N. Olsson, T. Rönnqvist, R. Zorro, A. Ringbom, G. Tibell, O. Jonsson, L. Nilsson, P.-U. Renberg, T.E.O. Ericson, and B. Loiseau, Phys. Rev. C **57**, 1077 (1998).

[3] R. Arndt and R. L. Workman, *Nuclear Data Standards for Nuclear Measurements*, edited by H. Condé, NEANDC-311 "U"/INDC(SEC)-101 (OECD, Paris, 1992), p. 17; A.D. Carlson, S. Chiba, F.-J. Hambsch, N. Olsson, and A.N. Smirnov, *Update to Nuclear Data Standards for Nuclear Measurements*, edited by H. Wienke, INDC(NDS)-368 (IAEA, Vienna, 1997), p. 9. Data as given by SAID (see Ref. [20]).

[4] M. E. Sainio, *Working Group Summary: Pion-Nucleon Coupling Constant*, 8th International Symposium on Meson-Nucleon Physics and the Structure of the Nucleon, Zuoz, Swit-

zerland, 1999, πN Newsletter **15**, 171 (1999).

[5] *Proceedings of the Workshop on Critical Issues in the Determination of the Pion-Nucleon Coupling Constant*, Uppsala, 1999 [Phys. Scr. **T87**, 1 (2000)].

[6] B. Loiseau and T.E.O. Ericson, Phys. Scr. **T87**, 53 (2000).

[7] T.E.O. Ericson, B. Loiseau, J. Rahm, N. Olsson, J. Blomgren, H. Condé, K. Elmgren, O. Jonsson, L. Nilsson, P.-U. Renberg, A. Ringbom, T. Rönnqvist, G. Tibell, and R. Zorro, Phys. Rev. Lett. **81**, 5254 (1998).

[8] M.C.M. Rentmeester, R.A.M. Klomp, and J.J. de Swart, Phys. Rev. Lett. **81**, 5253 (1998).

[9] J. Blomgren, N. Olsson, and J. Rahm, Phys. Scr. **T87**, 33 (2000).

[10] B.E. Bonner, J.E. Simmons, C.L. Hollas, C.R. Newsom, P.J. Riley, G. Glass, and Mahavir Jain, Phys. Rev. Lett. **41**, 1200 (1978).

[11] W. Hürster, T. Fischer, G. Hammel, K. Kern, M. Kleinschmidt, L. Lehmann, H. Schmitt, L. Schmitt, and D.M. Sheppard, Phys. Lett. **90B**, 367 (1980); J. Franz, E. Rössle, H. Schmitt, and L. Schmitt, Phys. Scr. **T87**, 14 (2000).

[12] T. E. O. Ericson and W. Weise, *Pions and Nuclei* (Clarendon, Oxford, 1988).

[13] T. Peterson, Phys. Scr. **T87**, 22 (2000); T. Peterson, L.C. Bland, J. Blomgren, W.W. Jacobs, T. Kinashi, A. Klyachko, P. Nadel-Turonski, L. Nilsson, N. Olsson, J. Rapaport, T. Rinckel, E.J. Stephenson, S.E. Vigdor, S.W. Wissink, and Y. Zhou, Nucl. Phys. **A663&664**, 1057c (2000).

[14] T. Rönnqvist, H. Condé, N. Olsson, R. Zorro, J. Blomgren, G. Tibell, O. Jonsson, L. Nilsson, P.-U. Renberg, and S.Y. van der Werf, Phys. Rev. C **45**, R496 (1992).

[15] H. Condé, S. Hultqvist, N. Olsson, T. Rönnqvist, R. Zorro, J. Blomgren, G. Tibell, A. Håkansson, O. Jonsson, A. Lindholm, L. Nilsson, P.-U. Renberg, A. Brockstedt, P. Ekström, M. Österlund, F.P. Brady, and Z. Szeflinski, Nucl. Instrum. Methods Phys. Res. A **292**, 121 (1990).

[16] B. Höistad, E. Nilsson, J. Thun, S. Dahlgren, S. Isaksson, G.S. Adams, and H. Ikegami, Nucl. Instrum. Methods Phys. Res. A **295**, 172 (1990).

[17] R.C. Byrd and W.C. Sailor, Nucl. Instrum. Methods Phys. Res. A **264**, 494 (1989).

[18] R.F. Carlson, At. Data Nucl. Data Tables **63**, 93 (1996).

[19] V.G.J. Stoks, R.A.M. Klomp, M.C.M. Rentmeester, and J.J. de

Swart, Phys. Rev. C **48**, 792 (1993). Data as given by SAID (see Ref. [20]).

[20] R.A. Arndt, I.I. Strakovsky, and R.L. Workman, Phys. Rev. C **52**, 2246 (1995); **62**, 034005 (2000). Data as given by Scattering Analysis Interactive Dial-Up (SAID), Virginia Polytechnic Institute, Blacksburg, VA (R.A. Arndt, private communication).

[21] P.W. Lisowski, R.E. Shamu, G.F. Auchampaugh, N.S.P. King, M.S. Moore, G.L. Morgan, and T.S. Singleton, Phys. Rev. Lett. **49**, 255 (1982).

[22] D.F. Measday and J.N. Palmieri, Nucl. Phys. **85**, 142 (1966).

[23] V. Grundies, J. Franz, E. Rössle, and H. Schmitt, Phys. Lett. **158B**, 15 (1985).

[24] R.A. Arndt, I.I. Strakovsky, and R.L. Workman, Phys. Rev. C **50**, 2731 (1994).

[25] M. Lacombe, B. Loiseau, J.M. Richard, R. Vinh Mau, J. Côté, P. Pirès, and R. de Tourreil, Phys. Rev. C **21**, 861 (1980).

[26] R. Machleidt, Adv. Nucl. Phys. **19**, 189 (1989); (private communication).

[27] V.G.J. Stoks, R.A.M. Klomp, C.P.F. Terheggen, and J.J. de Swart, Phys. Rev. C **49**, 2950 (1994). Data as given by SAID (see Ref. [20]).

[28] R.H. Stahl and N.F. Ramsey, Phys. Rev. **96**, 1310 (1954).

[29] C.Y. Chih and W.M. Powell, Phys. Rev. **106**, 539 (1957).

[30] J.P. Scanlon, G.H. Stafford, J.J. Thresher, P.H. Bowen, and A. Langsford, Nucl. Phys. **41**, 401 (1963).

[31] A.J. Bersbach, R.E. Mischke, and T.J. Devlin, Phys. Rev. D **13**, 535 (1976).

[32] M. Hammans, C. Brogli-Gysin, S. Burzynski, J. Campbell, P. Haffter, R. Henneck, W. Lorenzon, M.A. Pickar, I. Sick, J.A. Konter, S. Mango, and B. van den Brandt, Phys. Rev. Lett. **66**, 2293 (1991).

[33] R. Henneck, Phys. Rev. C **47**, 1859 (1993).

[34] G.F. Chew, Phys. Rev. **112**, 1380 (1958).

[35] P. Cziffra and M.J. Moravcsik, Phys. Rev. **116**, 226 (1959).

[36] T.E.O. Ericson and B. Loiseau, Phys. Lett. B **393**, 167 (1996).

[37] See, e.g., William R. Gibbs, *Computation in Modern Physics* (World Scientific, Singapore, 1994), p. 35.

[38] T. E. O. Ericson, B. Loiseau, and A. W. Thomas, "Determination of the pion-nucleon coupling constant and scattering lengths," hep-ph/0009312, Phys. Rev. C (submitted).

[39] J. Blomgren, N. Olsson, and the Uppsala Neutron Collaboration, TSL exp. FA104.

Appendix VI

The response of a liquid scintillator detector to 21–100 MeV neutrons

J. Thun[a,b], J. Blomgren[a,*], K. Elmgren[a], J. Källne[a], N. Olsson[a], J.F. Lecolley[c],
F. Lefebvres[c], C. Varignon[c], F. Borne[d], X. Ledoux[d], Y. Patin[d], O. Jonsson[e],
P.-U. Renberg[e]

[a] *Department of Neutron Research, Uppsala University, P.O. Box 535, S-751, Uppsala, Sweden*
[b] *Laboratoire National Saturne, Gif-sur-Yvette, France*
[c] *LPC, ISMRA et Université de Caen, CNRS/IN2P3, France*
[d] *DPTA/SPN, Commissariat à l'Energie Atomique, Bruyères-le-Châtel, France*
[e] *The Svedberg Laboratory, Uppsala University, Sweden*

Abstract

A large volume (4 l) liquid NE213 scintillator detector for neutrons in the energy range up to 800 MeV has been calibrated using a high accuracy tagging technique at $E_n = 21, 34, 50, 60$ and 100 MeV. The experiment is described together with a discussion of the accuracy in the absolute efficiency calibration. Results are presented on total and differential detection efficiencies along with information on the underlying nuclear reactions causing the detector response, including both charged particles and γ-rays. The present results complement previous measurements for the same detector, so that an efficiency calibration now exists over an energy range of $E_n = 2$–800 MeV. The empirical results are compared with a calculated energy dependence of the detector response to neutrons. © 2001 Published by Elsevier Science B.V.

1. Introduction

Efficiency calibration of neutron detectors, such as liquid scintillators, is a general and persistent problem, making it a limiting factor in many nuclear physics studies involving neutrons. Experimental calibration studies (see Ref. [1] and references therein) have been performed for lower energies, but are scarce and of modest accuracy for energies above 20 MeV. Where data are missing, one has been referred to using calculated efficiency values and their dependence on neutron energy, besides the detector geometry dependent variation [1,2]. Efficiency calibration studies in the region $E_n > 20$ MeV are therefore highly desirable.

The present new calibration measurements were prompted by the interest in studies of

*Corresponding author. Tel.: +46-18-471-3788.
E-mail address:* jan.blomgren@tsl.uu.se (J. Blomgren).

high-intensity neutron production in spallation reactions with proton beams in the GeV range. High-flux neutron sources have gained recent interest because of their potential use in nuclear applications referred to as accelerator-driven transmutation [2]. This means that measurements of neutrons from a few MeV up to GeV energies are required. Such an experiment has recently been performed with the Saturne synchrotron in the energy range up to 1.6 GeV [3,4]. The neutrons were measured with a magnetic proton recoil (MPR) spectrometer covering an energy range from about 200 MeV and upwards [5], while neutrons of energies less than 400 MeV were measured with time of flight (TOF) techniques using NE213 liquid scintillation detectors (referred to as DEMON detectors) [6]. In the intermediate energy range, 200–400 MeV, the two methods overlapped, permitting cross checks between the TOF and MPR measurements [7]. For the MPR spectrometer, an ab initio calibration for the neutron detection efficiency can be derived (except for its dependency on the np scattering cross-section used as a reference), while the TOF measurements rely on specific knowledge of the neutron detection efficiency as a function of energy.

Neutrons can be produced at any energy that protons can be accelerated to, but to be useful in calibrations, they need to be well characterized which is not easily attained. This experiment employed the neutron facility at the The Svedberg Laboratory (TSL), which delivers quasi-monoenergetic neutron beams up to 180 MeV [8,9]. In the present study, the beam neutrons were scattered off a hydrogenous target, and those from elastic np scattering were determined with respect to momentum of the recoiling protons and their vertex of origin in the target. Each recoil is associated to a scattered neutron, which, in turn, is fully characterized by the kinematics of the measured recoil proton.

A novel feature of this type of experiments is the use of drift chambers, which allowed us to attain precise determination of the recoil protons. This high-accuracy neutron tagging (HANT) allows precise absolute efficiency calibration of neutron detectors. Besides information on the global neutron detection efficiency, this experiment has also provided new differential information on the response as a function of position of the neutron impact on the detector surface, and its dependence on the type of reaction constituting the detector response, for instance, in terms of the charged particle involved. Moreover, this study gives, as far as we know, the first detailed information on the response to γ-rays produced in the detector. This new differential response information is of particular interest as input in neutron detector response calculations, which can be used to reproduce calibration data or to predict experimental efficiencies for other conditions than those for which data exist.

This paper describes the HANT experiment, and presents the results on the calibration of the DEMON detector. Moreover, it discusses the implications of the experimental data with respect to the relevance for calibration of the mentioned detector; generally, it provides input to calculations of detector response properties for neutrons.

2. Experimental techniques

2.1. Outline of the experiment

The neutrons used to irradiate the neutron detector emanated from elastic scattering from target protons, where a target containing hydrogen was used. Measurement of the recoil proton assigned a tag to each neutron entering DEMON. Thus, the experiment had four distinctive parts: neutron production, np scattering target, neutron detector and proton detector system (see Fig. 1).

With a pencil neutron beam, the tagging measurement could, in principle, be done with a two-dimensional position sensitive recoil detector, as this would fully determine the hit position and energy of the neutrons impinging on the detector to be calibrated. In practice, mono-energetic neutron beams have a rather large diameter, and therefore the recoil production vertices have a significant spatial distribution. Thus, the tagging requires measurement of both trajectory and vertex for each recoil neutron of the scattered neutron flux.
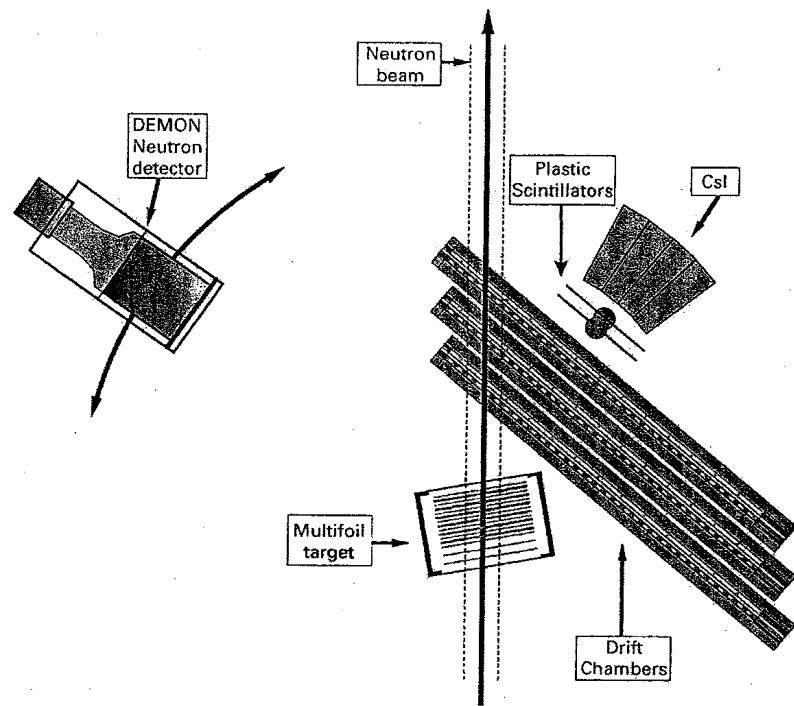
Fig. 1. Schematics of the experimental setup consisting of the neutron detector (DEMON), multi-layered target, neutron beam and the three components of the proton recoil detector (the drift chamber, plastic scintillator and CsI scintillator detectors).

It is desirable to use a rather thick target to boost the count rate in the experiment, however without impairing the energy resolution. This was achieved with a multi-layered target consisting of target foils interleaved with multi-wire proportional chambers (MWPC). The MWPCs recorded the charged particles produced, and hence the target from which the scattered neutron originated. Corrections for the energy loss in the subsequent target foils could then be applied in the analysis. Moreover, it is practical to use a composite hydrogen target, such as polyethene (CH_2), which was used in the present experiment. The use of a multi-target device allowed simultaneous determination of the background due to protons from carbon, which was subtracted in the analysis.

The quality of the background subtraction was improved by particle identification so that mainly protons and deuterons could be separated, and by charged-particle energy measurement. Any re-maining background in the elastic proton recoil flux should be small so that it can be handled as a correction in the neutron tagging. Thus, the proton detection system contained a stack of drift chambers to determine charged-particle trajectories, a set of large area scintillator detectors for energy loss measurements, and an array of CsI detectors for energy determination. Particle identification was accomplished by the latter two, i.e., by combined energy loss and full energy measurements.

It can be noted that the calibration was done in a neutron flux characterized by a localized source which the detector sees with an aspect angle of ± 0.1 rad.

2.2. The TSL neutron beam

The TSL neutron beam facility produces quasi-monoenergetic neutrons by the $^7Li(p,n)$ reaction, as shown in Fig. 2. The protons are delivered by a

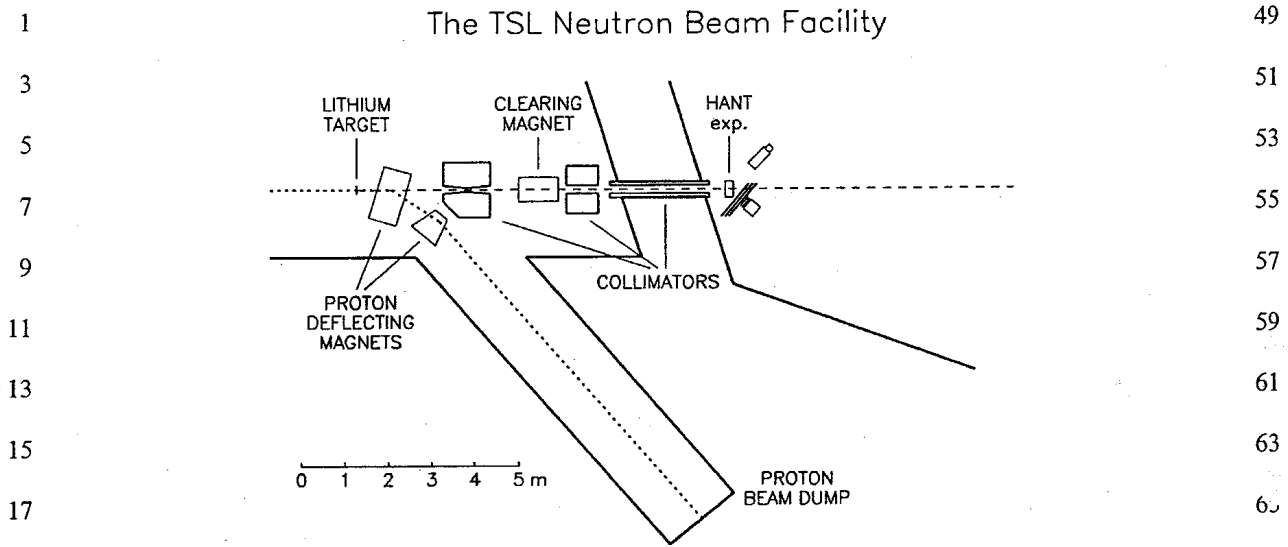# The TSL Neutron Beam Facility

Fig. 2. Schematics of the TSL neutron beam facility and the location of the present high-accuracy neutron tagging (HANT) detector calibration experiment.

sector-focused cyclotron which operates in continuous wave (CW) mode up to an energy of 100 MeV, and in frequency modulated (FM) mode up to 180 MeV. In the CW and FM modes, the maximum usable intensities are about 3 μA and 300 nA, respectively. The proton beam is bent away into a well-shielded dump downstream the production target. The neutrons are collimated so that they reach the experimental target with a well-defined beam spot size (the diameter was 7 cm and the divergence less than 5 mr). At 100 MeV, the maximum neutron flux using an 8-mm ^{7}Li target is about 2×10^{6} n/s. The energy distribution, in this case, has a width of about 1% (FWHM) with a low-energy tail. The contribution from this tail is reduced using TOF techniques. (The cyclotron has a 58 ns period for 100 MeV protons, and a microbeam pulse width of 3–5 ns.) The experiment was performed during two separate run periods, with proton beam energies of 100 and 160 MeV, respectively.

2.3. The target

The multi-target (area 10×18 cm^2) held two carbon foils (each 40 mg/cm^2 thick) and four CH$_2$

foils (100 mg/cm^2) each followed by a multiwire proportional counter (MWPC). There were also three MWPCs in front of the first target to identify any charged particle contamination in the neutron beam while the other MWPCs were used to determine the target of origin for charged particles observed in the recoil detector. The x–y coordinates were also determined with a resolution of about ± 6 mm, limited by the wire spacing. The total thickness of the target assembly was 515 mg/cm^2, of which 58 mg/cm^2 was hydrogen and 422 mg/cm^2 was carbon in target foils, and 35 mg/cm^2 was detector material (entrance foils, gas and wires). The carbon targets were used to assess and subtract the background due to protons from carbon, as well as that from other charged particles.

The target thickness is not negligible, so there is a finite probability that a scattered neutron or its associated proton recoil can suffer a nuclear collision in the target on their way out and be lost. Loss of protons means a reduction in the tagged neutron flux on the neutron detector, which is not directly affecting the final result, while a loss of neutrons has an effect on the calibration; i.e., the neutron detection efficiency becomes
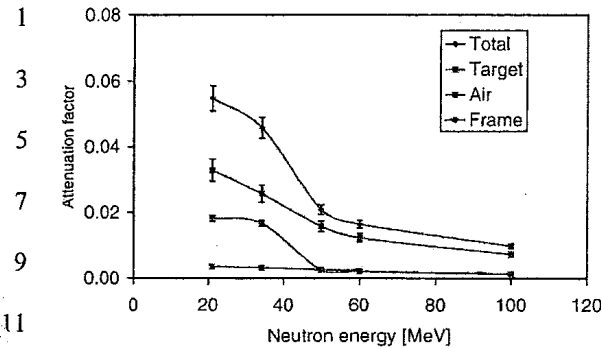
Fig. 3. The calculated attenuation of tagged neutrons imping-
ing on the DEMON detector as a function of energy; shown is
the total attenuation factor and its different contributions from
target foils (of CH_2 and C), frame of target and non-foil
material, and air.

underestimated in the measurement if not cor-
rected for. The neutron attenuation in the target
was calculated and was found to be a few percent.

The main contribution to the attenuation is due
to neutrons whose trajectories pass through the
frame of the multitarget (consisting of CH_2 and
Al) besides reactions in the target material and
foils (C and CH_2) and a smaller contribution from
air. The calculated attenuation as a function of
neutron energy is shown in Fig. 3. The result was
used as a correction factor in the determination of
the number of incident neutrons based on the
measured proton recoil tagging rate. This correc-
tion factor has an error estimated to less than
$\pm 0.5\%$. This attenuation is not exactly constant
across the detector area, but this effect was
estimated not to have any practical effect on
neither the total efficiency determination nor the
differential results. Finally, it should be noted that
protons are subject to Coulomb scattering, which
results in angular straggling. This introduces a
blurring of the neutron tagging kinematics, but is
otherwise not significant for the calibration.

2.4. Drift chambers

The charged-particle trajectories were deter-
mined with three drift chambers. The chambers
were mounted approximately perpendicular to the
trajectories of interest, and positioned so that the
neutron beam bypasses any massive parts. In
contrast to the rest of the detection system, the
chambers were surveyed and fixed directly with
respect to the beam and target to minimize
positioning errors that might affect the tagging
accuracy.

The characteristics of the drift chambers used
are described in detail in Ref. [10]. They are of the
double sense-wire type with two-dimensional x–y
readout. Assuming straight-line trajectories, the
charged-particle vertices in the target are deter-
mined, with additional information on the target
plane involved obtained by the multi-target device.

The position coordinates are derived from
recorded drift times (t_d) which are a function of
the drift distances (λ_d) from the ionization point in
the chamber to the nearest signal wire. The drift
time to distance (DTD) relationship is expressed
by functions $\lambda_d = f_{DTD}(t_d)$, where t_d is measured
with TDCs. These functions are determined
empirically and are assumed to be the same for
all wires in a plane. Because of the geometry of our
chambers, the functions are approximately linear.
Such a linear DTD relationship was assumed for
the on-line data analysis, performed for monitor-
ing and running of the experiment. It was also used
as initial assumption in the first of the two
methods used for the more precise DTD calibra-
tion described in Section 4.

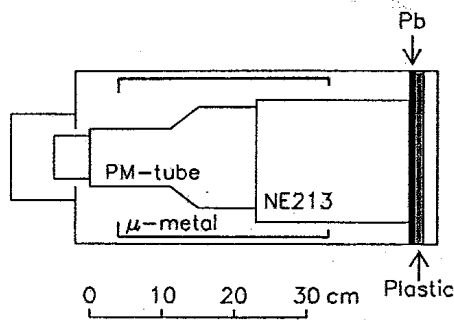## 2.5. Particle identification detectors and trigger

The charged-particle detector system, used for
particle identification and electronics triggering,
consists of a set of twelve cesium iodide (CsI)
crystals and two plastic scintillators (PSc). The
CsIs were mounted as an array of 3×4 units,
where each scintillator has a depth of 30 cm
(stopping protons up to 390 MeV) with a square
cross section area of 50×50 mm^2 at the front,
tapered up to 70×70 mm^2 at the back. The PSc
detectors had a thickness of 3 mm and an area of
24×20 cm^2. The CsIs were used to measure pulse
height for stopping particles, and were also
calibrated to provide energy (E_p) for identified
proton events. The PSc detectors were used to
provide differential energy information on passing

charged particles ($\Delta E1$ and $\Delta E2$), and also to provide trigger signals for read-out of the data acquisition system, as well as stop pulses for the TDCs connected to the drift chambers.

2.6. The neutron detector

The DEMON detector is a large volume NE213 liquid scintillator, intended for measuring neutrons in the energy range from 10 to about 400 MeV. It consists of a cylindrical aluminium container (diameter 160 mm and length 200 mm) with a 5 mm thick entrance sheet of lead to reduce the sensitivity to low-energy gamma rays. At the back, there is a lucite window to which a 5-in PM tube is connected. The whole assembly is contained in an outer housing providing mechanical support and also serving as an extra light-tight shield (Fig. 4). The detector was removed from other experimental structures to minimize background interference and thus check adverse effects on the calibration.

The high voltage of DEMON was biased against a discriminator setting of about 200 mV. The reference pulse height used corresponds to 670 keV γ-rays from a ^{137}Cs source, which give a Compton edge corresponding to an equivalent electron energy deposition of 490 keV$_{ee}$. For the purpose of verification, the pulse height spectrum for ^{88}Y ($E_\gamma = 898$ and 1836 keV, corresponding to deposition energies of 699 and 1612 keV$_{ee}$) was also used. These γ-ray spectra were recorded

Fig. 5. Example of a bias calibration spectrum recorded with DEMON using the gamma line at 670 keV of ^{137}Cs and a biasing threshold set at $E_b = 450$ keV$_{ee}$ (equivalent electron energy). The 898 and 1836 keV lines in ^{88}Y were used for verification and are also shown; the sharp cut-off at low pulse height shape the discriminator setting.

(Fig. 5) with the actual high voltage used and discriminator bias set at the maximum of the observed Compton pulse height distribution from ^{137}Cs.

The pulse-shape characteristics of the detector response to neutrons and γ-rays are different and was used to separate the two kinds of events in the neutron detector. Thus, the analog signal from DEMON was split and fed into two separate ADCs. One was read out with a prompt gate starting just before the leading edge of the pulse, and the other with a gate delayed to start at the point in time where the pulse has risen to its maximum. The pulse height ratio for delayed and prompt gating is characteristically smaller for γ-rays than for neutrons. The relative timing of the delayed and prompt gates was adjusted to give maximum separation between γ-rays and other particles when the data were presented as scatter plots (see Section 4). To adjust timing and verify the effectiveness of this pulse shape discrimination, the DEMON detector was irradiated with

Fig. 4. Sketch of the DEMON detector assembly showing the NE213 scintillator volume, the PM tube and the Pb entrance sheet besides mechanical and magnetic shielding structures.
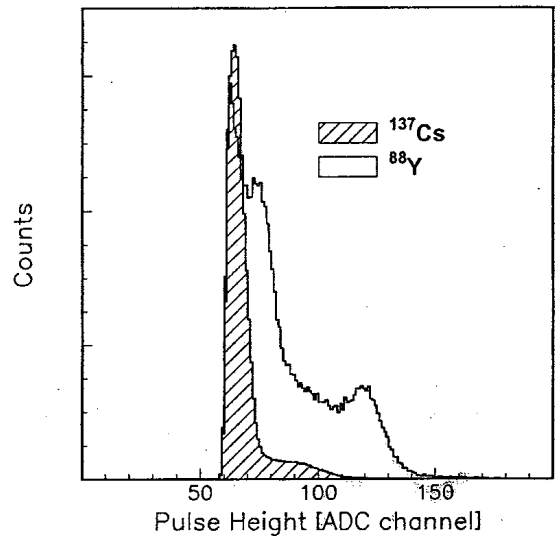
neutrons from an AmBe source. This gave neutrons of energies up to a few MeV which could be clearly distinguished from the ambient background of γ-rays.

3. Electronics and data acquisition

The electronics of the experiment was based on a CAMAC system placed in a counting room at a cable length distance of about 70 m from the experimental area. A single trigger was used for the readout and subsequent clear of all the electronic modules except the scalers. This trigger was defined by a coincidence between the two PSc signals. With a beam intensity of about 10^6 n/s, the trigger event rate in the experiment was a few tens of Hz, so dead time was not a problem.

The analog signals from the PSc detectors and CsIs were fed into ADCs. The DEMON detector signal was passively split into three branches in the counting room. One of these signal was used to generate a logic pulse to provide the prompt and delayed gates used in the pulse shape discrimination, while the other two were used as analog inputs into ADCs; ADC encoding was enabled when the main trigger was present. The logic signals from the CsIs and DEMON, as well as the cyclotron radio frequency pulse, were fed into TDCs and into scalers.

The drift chambers and the multitarget have in total 400 channels. They were read out with a LeCroy 4290 system that uses TDCs operated in common stop mode, placed in a dedicated CAMAC crate close to the chambers. The main trigger served as common stop and provided trigger signals for the chamber readout. Compacted data from the TDCs were sent to a data bus interface and memory module in the main CAMAC crate in the counting room.

The data acquisition system was VME based. It recorded data event by event and a pattern unit was used to characterize the events by type. The system also contained scalers, which recorded events continuously, and were read out at fixed time intervals.

4. Data reduction and analysis

4.1. Drift chamber data calibration

The precision in the proton tracking is one of the limiting factors of the present experiment, and therefore precise DTD relationships were determined, employing two different methods.

The first, iterative calibration method makes use of the coordinate information from two chambers to determine trajectories for projecting coordinates (sagitta) onto the third chamber. For the third chamber, the measured t_d-values were used to determine tentative λ_d-values which were, in turn, compared with the projected sagitta. The DTD function was determined in an iterative process, where the differences between the derived and measured drift distances ($\lambda'_d - \lambda''_d$) were minimized. For this iterative process to converge properly, it is necessary to have a sufficiently large data sample (of the order of 10^5 tracks). Moreover, this method requires that the relative position of the chambers is accurately known (to within ± 0.5 mm or better). This was attained in the DTD calibration so that a λ_d value was ascribed to each of the 512 TDC channels of the drift time measurement.

The second calibration method can be applied individually to each wire plane without auxiliary trajectory information from other planes or chambers. It requires, on the other hand, a homogeneous irradiation of the chambers. This means that the event distribution as a function of λ_d is constant, which is indeed a well-justified assumption for central wires. The time distributions for the selected cells can be summed, resulting in the distribution $N(t_d)$, whose integral $\int_0^{t_d} N(t'_d)\,dt'_d$ represents a monotonically increasing function of t_d. The integral $\int_0^{t_d} N(t'_d)(dt'_d/dx_d)\,dx_d$ is made into a linearly increasing function of t_d by adjusting dt_d/dx_d for all t_d values which thus determines the DTD calibration. These two calibrations agree within their uncertainties.

4.2. Charged particle identification

The forward-going charged particles were identified based on the full (E) and differential (ΔE) energy information obtained from the CsI and PSc
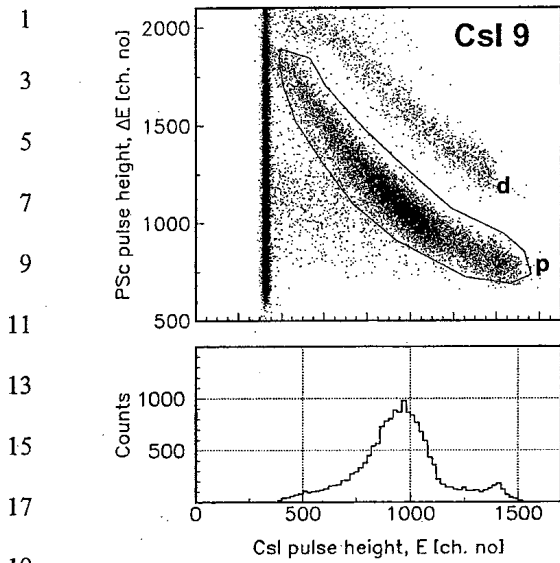
Fig. 6. Examples of $\Delta E - E$ results shown in detail for one CsI detector (E) and the PSc detector set (ΔE) indicating the selection of events (upper panel), and the projected energy spectrum of these selected elastic proton recoils (lower panel).

detectors, respectively. In the data on ΔE vs. E (Fig. 6a), bands of events due to protons and deuterons are visible. The projection of selected proton events on the E-axis (Fig. 6b) shows a peaked distribution consistent with the kinematics of proton recoils from elastic np scattering for the solid angle of the CsI detector viewing the finite target. The proton recoil angle is measured with the drift chamber system (see below), and this information is used to determine the energy of the proton recoil events (E_p). Comparison of the thus determined E_p-values and measured pulse heights (V_p) allows energy calibration of the CsI detector system (Fig. 7), using the events which come from a CH$_2$ target.

The relative importance of non-elastic protons can be seen in scatter plots of angle versus energy for targets of CH$_2$ and C (Fig. 8). Selection cuts were applied, and the projection of these reduced data onto the E-axis gave proton energy spectra for CH$_2$ and carbon targets. The result for CH$_2$ is a peaked energy distribution which is consistent with np scattering at a fixed angle. There is also a
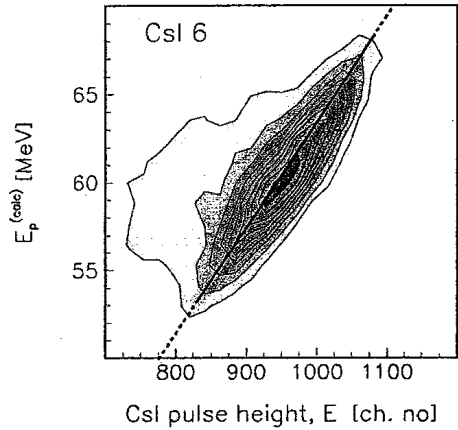

Fig. 7. Example of scatter plots showing results on the calculated elastic proton energy using the measured angle (E_p^{calc}) vs. measured pulse height (E) with a CsI detector. The line indicates the adopted energy calibration for the CsI detector.

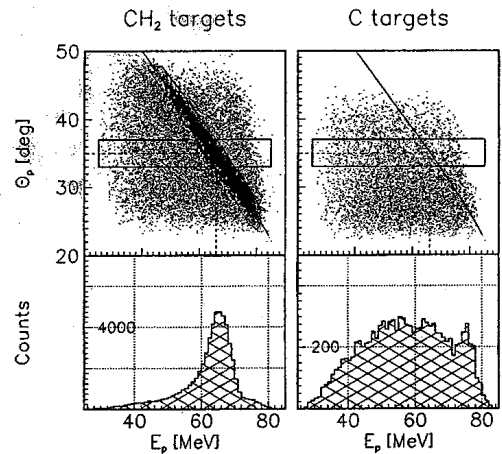Fig. 8. Example of scatter plots showing results on measured proton angle (θ_p) vs. energy (E_p) for events from CH$_2$ and carbon targets (upper panels). Projection onto the E_p-axis of selected events within the shown θ_p cuts gave the energy histograms presented in the lower panel.

weaker extended distribution which can be identified as C(n, p) reactions, which are determined using the carbon target data, and are subsequently corrected for. The background was further suppressed by applying energy restrictions, and this

9

Fig. 9. Examples of proton spectra measured with the CsI detectors for CH2 and C targets where the spectrum for C was normalized to represent the same proton emission contribution for CH2; also shown is the elastic np scattering part for CH2 as obtained by subtraction.

selected data set formed the elastic proton recoil events, each belonging to a tagged neutron (Fig. 9), i.e., $N_H(\text{tag}) = N_{CH_2}(\text{tag}) - N_C(\text{tag})$. Thus, the fraction of proton recoil tags, excluding background, is $N_H(\text{tag})/N_{CH_2}$, which is used to establish a correction factor in the determination of the DEMON detection efficiency, based on the recorded proton events in the forward detector system.

4.3. Neutron detector particle identification

The analog signals from DEMON were measured with prompt and delayed time integration gates (V_{PH1} and V_{PH2}). An example of data on V_{PH1} vs. V_{PH2} is shown in Fig. 10, where three bands are present, attributable to gamma Compton scattering in the DEMON scintillator (creating electrons) and neutron scattering on hydrogen (creating proton recoils), besides neutron reactions mainly in carbon (creating protons and α-particles, but also deuterons, tritons, etc.). The detector response is thus separated in the main groups of neutron and γ-ray signals.

The V_{PH1}–V_{PH2} data were subdivided in five sections (Fig. 10) and the events within each were selected for one-dimensional projection on the X'-axis according to the coordinate systems shown in Fig. 10. The resulting distributions (Fig. 11a–e)

Fig. 10. Scatter plot showing the correlation of results on V_{PH1} and V_{PH2} recorded with the DEMON using prompt and delayed time gates. It shows the cuts (solid lines) used to eliminate gamma events, and the subsection divisions (dashed lines) and coordinate system used for presentation in the form of histogram projections in Fig. 11.

show three well separated groups of events, especially for the highest pulse heights. The right-hand peak is due to γ-e events, and can be separated from the n-charged particle events, so the former can thus effectively be discriminated against using the cuts as indicated in Fig. 10. These γ-events are, in our case, most likely due to tagged neutrons hitting the detector as there is virtually no background. Still, the γ-like events are taken as a separate part of the detector response to extract a quantity which corresponds to the usual conditions for the use of a neutron detector of this type. The neutron-like events define the 'normal' detector response. The relative contribution to the detector response in terms of protons (including deuterons and tritons) and α-particles was also determined based on the distinct separation of these events in the V_{PH1} vs. V_{PH2} data. The detector response reactions are further discussed in Sections 5 and 6.

1

3

5

7

9

11

13

15

17

19

21

23

25

Fig. 11. Projection of the data shown in Fig. 10 in the form of histograms as function of the shape parameter X' for five subsections of data of increasing value of the Y' parameter (a–e). The three main groups represent neutrons causing doubly charged particles (α-particles) (left), singly charged particles (middle), and gamma response (right).

27

29

31

33

4.4. Tracking and vertex reconstruction

35

The target plane responsible for the event was determined by the most upstream MWPC that was triggered in the target assembly. Because of a small inefficiency of the chambers, only one was required to trigger and this defined the nearest up-stream target for the recoil produced; the chamber inefficiency lead to target misidentification affecting a few percent of the events. The x–y position on the target plane was extracted from the back projection of the particle trajectories determined with the forward drift chambers. The MWPC also provided coarse information on the x-coordinate of the charged particle vertex. The estimated

37

39

41

43

45

47

x-resolution in the projected vertex determination is better than ±2 mm. This comparison of target position data provides some confirmation of the drift chamber performance. If the target is misidentified one layer, this leads to a vertex translation of $\Delta x \approx 19$ mm in the scattering plane.

The charged-particle trajectories were determined from the measured particle coordinates in the drift chambers. The recoil trajectory and its vertex define the np scattering plane and the angle it forms relative to the horizontal plane. The trajectory determines also the recoil angle relative to the incoming beam direction. Through the kinematics of the np scattering, it is possible to establish the angle of the scattered neutron and, hence, also the neutron trajectory, which, in turn, gives the incident neutron coordinates on the DEMON detector surface so that the incident neutron flux distribution $N_{in}(x, y)$ can be determined. Furthermore, the tagged neutron energy was calculated from the measured proton angle and the known energy of the neutron beam; this was also verified through the measurement of E_p with the CsIs, taking into account the proton energy loss in the material traversed from the production vertex. For each incoming neutron, it was determined whether it gave a trigger in DEMON or not. The recorded events were characterized as being either of the neutron or γ-ray type, where the neutron events can be further differentiated in terms of protons, α-particles, etc.

49

51

53

55

57

59

61

63

6⌐

67

69

71

73

75

77

79

8₁

5. Results

83

The basic quantities measured in the present experiment are the spatial flux distribution of incident neutrons on the DEMON detector, $N_{in}(x, y)$, and the corresponding detected flux distribution, $N_{det}(x, y)$. The center position of the DEMON, $(x_0, y_0)_D$, was determined by inspecting the $N_{det}(x, y)$ distribution for its cylindrical symmetry. Using this symmetry, the incident and detected distributions can be expressed as functions of the radius ρ relative to the detector center, i.e., $N_{in}(\rho)$ and $N_{det}(\rho)$. The experimental alignment is estimated to be accurate to within a center offset of ±2 mm with respect to ρ. The differential

ɛ

87

89

91

93

95

detection efficiency, $\varepsilon(\rho)$, is defined as the ratio

$$\varepsilon(\rho) = N_{\text{det}}(\rho)/N_{\text{in}}(\rho),$$

where $N(\rho)$ is the number of particles (detected or incident) within a finite circular ring element of radius ρ and width $\Delta\rho$, i.e., a circular ring area from radius ρ to $\rho + \Delta\rho$. The neutron distribution $N_{\text{in}}(\rho)$ was derived from the number of proton recoil tags recorded, with a correction for the neutron attenuation; the attenuation correction amounts to 1–6% depending on E_n, as shown in Fig. 3.

Efficiency distributions, $\varepsilon(\rho)$, were measured for different fixed neutron beam energies and the range of scattering angles defined by DEMON, which gave tagged average neutron energies of $E_n = 21, 34, 50, 60$ and 100 MeV. The neutron energy has a spread across the DEMON detector area (radii from $\rho = 0$ to $\rho = R_D = 80$ mm) of about $\pm 6\%$ of the total beam energy. The results on the differential detection efficiency in the form of radial distributions are presented in Fig. 12; the errors shown are discussed below. The results are for the special conditions of a divergent neutron flux (± 0.1 rad) incident on the detector
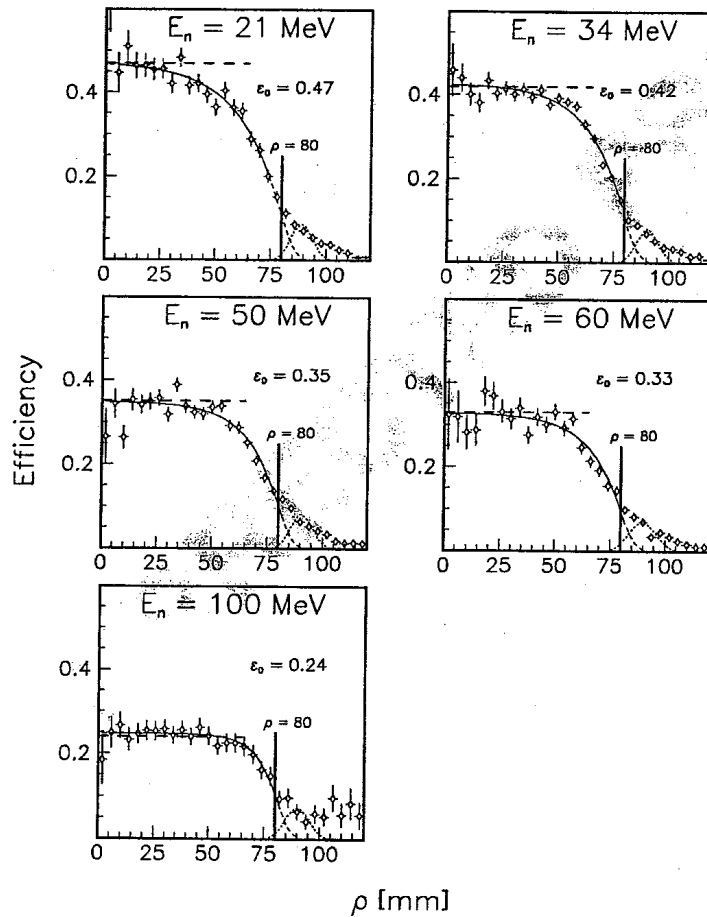
Fig. 12. Results on the measured spatially differential neutron detection efficiency as function of the radius, $\varepsilon(\rho)$, for neutron energies of $E_n = 21, 34, 50, 60$ and 100 MeV. Also shown are fits to the data as discussed in the text.

The distributions $\varepsilon(\rho)$ all show a radial dependence with a flat part in the middle and a fall-off towards the detector circumference at $\rho = R_D = 80$ mm. The edge effects are represented with the expression

$$F'_D(\rho) = \varepsilon_0(1 - e^{-(R_D - \rho)/\delta})$$

where ε_0 is the central detection efficiency and δ is the edge effect depth. This distribution was folded with a Gaussian representing the uncertainty in the position determination derived from the tagging, which has a width $\sigma = 3.4$ mm (or 8 mm FWHM). The functional form fitted to the measured $\varepsilon(\rho)$ distributions was

$$F(\rho) \propto (1/R) \int F'_D(\rho')e^{-[(\rho - \rho')/\sigma]^2} \, d\rho'$$

where ε_0 and δ were fitting parameters. The fitted curves are shown in Fig. 12 together with the data on $\varepsilon(\rho)$. The resulting values of the fitting parameters are summarized in Table 1. It can be noted that the fitted curves describe the main bulk of the measured $\varepsilon(\rho)$ distributions well. There is, however, some excess detection efficiency for the radial range $\rho > 90$ mm denoted $\varepsilon_x(\rho)$ which will be considered below.

The bulk fitting parameters were used to derive the detection efficiency characteristics for the DEMON detector. Among these, the area-integrated efficiency is

$$\varepsilon_A = (\pi/2) \int F(\rho)\rho \, d\rho$$

which represents an effective detection cross-section, or, 'flux efficiency'. The average efficiency is defined as $\varepsilon_{avg} = \varepsilon_A/A_D$, where A_D is the area of the neutron detector ($A_D = \pi R_D^2$). The results on

ε_0, ε_A, ε_{avg} and δ as function of neutron energy are presented in Fig. 13 and Table 1. It can be noted that in general the efficiencies decrease with energy, but ε_{avg} is less than ε_0 (Fig. 13a,b). The latter difference can be illustrated by the ratio $\varepsilon_{avg}/\varepsilon_0$, which can be taken as the apparent relative detector area, that seems to increase monotonically with E_n (Fig. 13c). This trend could be attributed to an increasing role of non-detector material (see below) in enhancing the detection efficiency, which could also explain the apparent decrease in edge effect thickness with increasing energy (Fig. 13d).

The appearance of events extending outside the fit, $\varepsilon_x(\rho > R_D)$, is attributed to neutrons interacting in the oversized front lead sheet or the scintillator canister of the DEMON assembly (see Fig. 4), leading to in-scattering of neutrons. The apparent relative efficiency $\varepsilon_x(\rho)/\varepsilon_0$ is at the 5–10% level, and its relative contribution to the flux efficiency ε_A is estimated to be in the same range; the estimates were based on fitting a Gaussian to $\varepsilon_x(\rho)$ being the difference between the data and the fit of $\varepsilon(\rho)$ in Fig. 12.

When neutron events are differentiated with respect to the type of response particles (protons and α-particles), we find charged particle pulse height distributions of the type illustrated in Fig. 14. These spectra are for 34-MeV incident neutrons which means that the full energy of the neutron (E_n) can be deposited in DEMON in the case of protons, while the α-particle energies are limited to a maximum of $E_n + Q$, where the Q-value is typically -5 MeV. The data for protons and α-particles taken for $\rho < 20$, $20 < \rho < 40$, $40 < \rho < 60$ and $60 < \rho < 80$ mm show no clear

Table 1
Summary of results on the central (ε_0), area integrated (flux) (ε_A) and average (ε_{avg}) efficiencies besides the ratio $\varepsilon_{avg}/\varepsilon_0$ and the edge thickness parameter δ for the DEMON detector at different neutrons energies

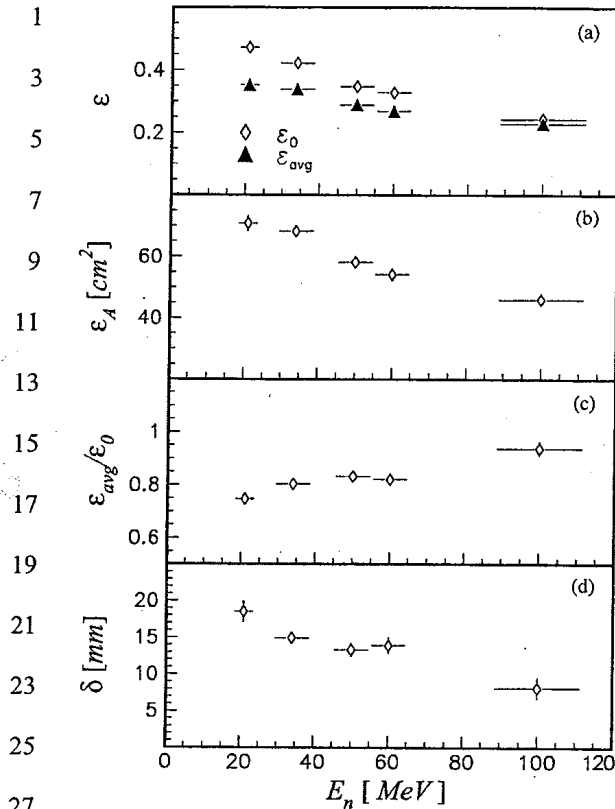| E_n (MeV)	ε_0	ε_A (cm^2)	ε_{avg}	$\varepsilon_{avg}/\varepsilon_0$	δ (mm)
21 ± 2.4	0.472 ± 0.017	71 ± 2	0.352 ± 0.012	0.75 ± 0.01	18.5 ± 1.4
34 ± 4.6	0.422 ± 0.007	68 ± 1	0.340 ± 0.005	0.80 ± 0.01	14.9 ± 0.6
50 ± 4.5	0.347 ± 0.007	58 ± 1	0.289 ± 0.006	0.83 ± 0.01	13.3 ± 0.9
60 ± 4.4	0.328 ± 0.012	54 ± 2	0.269 ± 0.010	0.82 ± 0.02	13.9 ± 1.1
100 ± 11.2	0.244 ± 0.008	46 ± 2	0.229 ± 0.008	0.94 ± 0.02	8.1 ± 1.4

Fig. 13. Results on the energy dependence of the central detection efficiency ε_0 and effective average efficiency ε_{avg} (a), the integrated (flux) efficiency (ε_A) (b), the flux efficiency $\varepsilon_{avg}/\varepsilon_0$ (c), and the edge depth parameter δ (d); the horizontal bars indicate the neutron energy spread across the detector.

trend of different ρ-dependencies between them. We have also examined the differential detection efficiency based on α-particles, $\varepsilon_\alpha(\rho)$, relative to the one based on protons, $\varepsilon_p(\rho)$, and find that there is no obvious difference between them as a function of ρ. The results for the full detector area are, therefore, used as representative numbers for estimating the relative importance of protons and α-particles.

The results on the ratio $\varepsilon_\alpha/\varepsilon_p$ as a function of neutron energy (Fig. 15) show that the ratio increases rapidly from $E_n = 21$–34 MeV. This can be understood as the threshold biasing effect for ε_α discussed earlier. From $E_n = 34$ MeV and upwards, the $\varepsilon_\alpha/\varepsilon_p$ ratio stays at a rather constant

level of about 0.2 up to $E_n = 100$ MeV. Similarly, by distinguishing neutron and γ-ray like events, the DEMON response ratio $\varepsilon_\gamma/\varepsilon$ (where $\varepsilon = \varepsilon_p + \varepsilon_\alpha$) can be determined. It is found that $\varepsilon_\gamma/\varepsilon$ varies in the range 0.20–0.28, but without clear evidence of an energy dependence. It should be stressed that the exact numbers of these effects depend strongly on the discriminator used, i.e., $E_b = 490$ keV$_{ee}$.

The experimental error for the total efficiencies (ε) is mainly due to the binomial statistics of the ratio N_{det}/N_{in} including correction for background in N_{in}. The ascribed statistical errors in ε_0 are determined to be 1.8%, 1.2%, 1.6%, 2.1% and 2.8% at $E_n = 21, 34, 50, 60$ and 100 MeV, respectively. Another important source of uncertainty is the correction for the carbon background. This correction factor varies with neutron energy between 1.16 and 1.20 (with relative errors of 3%, 1%, 1%, 3% and 2% as estimated from applying different geometrical cuts). Other error sources are estimated to be small so that, for instance, the correction for neutron attenuation has an error of less than $\pm 0.5\%$. The ε values determined relate to the specific detector bias used, i.e., $E_b = 490$ keV$_{ee}$ (cf. Fig. 3) which was set relative to the 670-keV γ-ray line as reference. The stability of the bias setting was carefully checked during the course of the measurements. The biasing uncertainties are not considered to be a significant error source, except for ambiguities of procedure in setting the bias.

The neutron tagging is determined from the measured kinematics of elastic recoil protons. Moreover, there are detected recoils in uninteresting parts of the phase space, besides extraneous particles, which are eliminated as they appear outside the selected ranges of the measured parameters used to characterize the forward-going charged particles. This selection of defined events is the main source of systematic error in the determination of ε. However, ε is not critically dependent on these selection cuts and the systematic errors are therefore estimated to be small compared to the statistical ones. Thus, the efficiencies and errors given should be taken as absolute values.

What concerns the energy dependence, the neutrons received by the detector have an energy
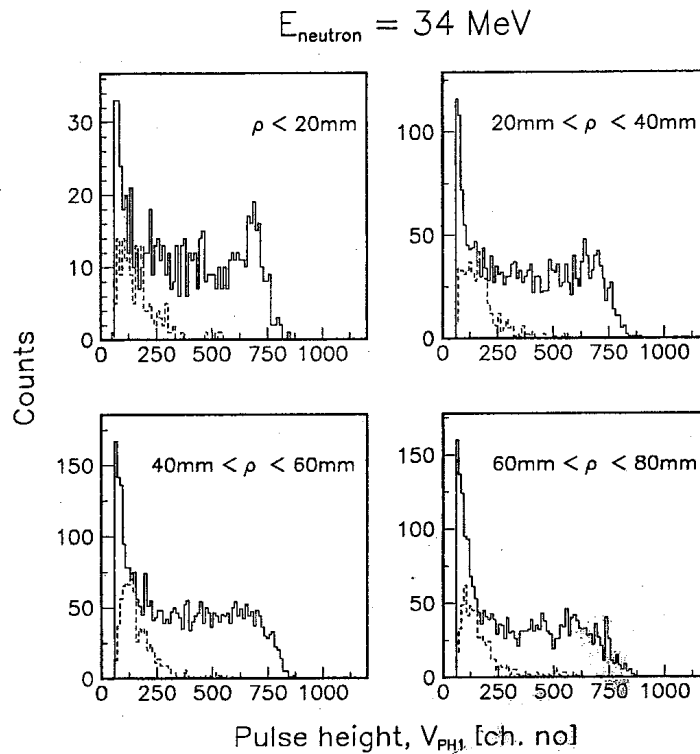
Fig. 14. Comparison of the pulse height spectra measured with DEMON for detected neutrons of 34 MeV with distinction made between responses in terms of proton (solid lines) and α-particle recoils (dashed lines) for selected detector areas of different radii.

spread depending on geometry. This spread together with the uncertainty in the beam energy means that the efficiency is given for the energy brackets of ± 2.4, ± 4.6, ± 4.5, ± 4.4 and ± 11.2 MeV around central E_n-values of 21, 34, 50, 60 and 100 MeV, respectively The differential efficiencies $\varepsilon(\rho)$ determined are subject to the same type of errors as the ε-values with the addition of the uncertainty in ρ.

6. Discussion

Before proceeding, we note that what is meant with the neutron detection efficiency is intrinsically a matter of definition. That is demonstrated by the present measurement, which provides the first detailed information on the spatial response dependence. Our basic efficiency result is given by the ε_0-value. A global efficiency of the 'bare'

detector is given by our derived results denoted ε_{avg} (Fig. 13). To obtain the effective overall efficiency for the DEMON detector assembly, ε_x should also be added. This overall efficiency happens to be not too different from ε_0. Therefore, ε_0 can be used for comparison with calibration results obtained in measurements without spatial differentiation. For the purpose of illustrating the energy dependence of the neutron detection efficiency of DEMON, it makes sense to use our results on ε_0 in comparison with the global efficiencies of other calibration measurements. It is clear that a more quantitative comparison can be made, but that would also require consideration of the differences in neutron flux conditions. That in turn would require modeling calculations, which is beyond the scope of the present study.

Extended calibration data now exist for the energy range 2–800 MeV for the DEMON
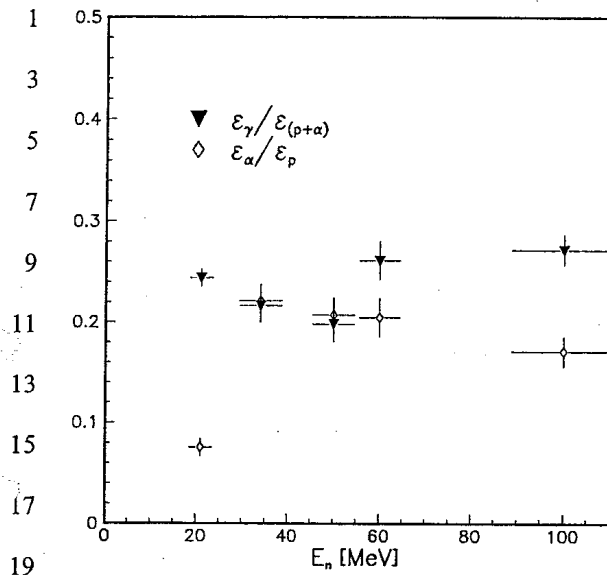
Fig. 15. Results on relative central detection efficiencies as function of neutron energy for registered gamma events compared to charged particles events $(\varepsilon_\gamma/\varepsilon_{p+\alpha})$, and α-particles compared to protons $(\varepsilon_\alpha/\varepsilon_p)$, obtained with a discriminator setting of $E_b = 4900$ keV$_{ee}$.
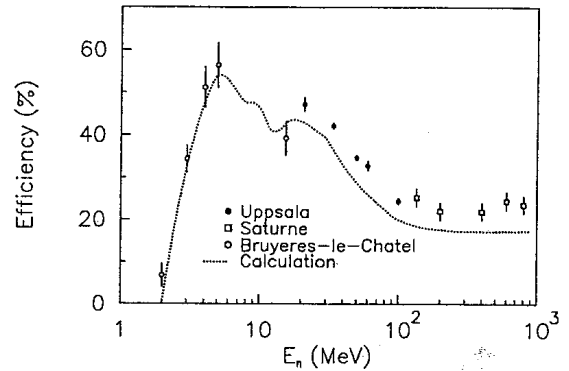

Fig. 16. Results on the measured central detection efficiency (ε_0) of the DEMON detector from the present experiment compared with those from other experiments at lower $(E_n < 20$ MeV) and higher $(E_n > 140$ MeV) [6,5]. Calculated results for the same detectors are also shown as a broken curve [4].

detector (Fig. 16). Besides our new data, covering the medium energy range 21–100 MeV, there are low energy data for neutrons of $E_n < 20$ MeV produced with the deuteron beam of a Tandem accelerator using the reactions $d + d \rightarrow^3$ He+n and $d + t \rightarrow^4$ He+n [6]. These data extend down to $E_n = 2$ MeV, which is the practical lower limit for the bias threshold used $(E_b = 490$ keV$_{ee})$. For higher energies, there are data from Saturne using neutrons produced in the forward direction through break-up of deuterons on ^{9}Be. In such reactions, $E_n \approx E_d/2$, and the useful range of E_d was from 0.3 to 1.6 GeV in the Saturne experiment. A consistency check is possible using spallation neutron spectra measured with a TOF spectrometer DEMON detector compared with a MPR spectrometer [5] whose calibration is based on the np cross-section. This method is less successful below $E_n = 100$ MeV, so only the > 100-MeV data are shown in Fig. 16. These high energy data bring the DEMON calibration into the region where inelastic np channels open up, starting with pion production for $E_n > 275$ MeV.

The detailed energy dependence of the neutron detection efficiency, $\varepsilon(E_n)$, shows some gross features reflecting the principle detector response. It is interesting to consider this in terms of the type of charged particles created, their initial energy and the amount of scintillation light (i.e., pulse height) they produce when slowing down. The light production is charge dependent and it is a strong function of particle velocity, resulting in a rapid decrease in $\varepsilon(E_n)$ at low energies where the corresponding pulse height approaches the bias threshold $(E_b = 0.5$ MeV$_{ee})$. Thus, the strong rise in ε from $E_n = 1.9$ to 5 MeV (Fig. 16) can be attributed to the change in light production for recoil protons whose maximum energy $E_n = E_p$ is increased just above $E_b = 1.9$ MeV$_p$ corresponding to $E_b = 0.5$ MeV$_{ee}$. From $E_n = 5$ to 13 MeV, $\varepsilon(E_n)$ is determined by the energy dependence of the np elastic scattering (varies as $1/E_n$).

Protons from reactions in carbon contribute to ε_0 first above $E_n = 14.6$ MeV because of their negative Q-values $(Q = -12.6$ MeV for ^{12}C(n,p)^{12}B). Similarly, (n,d) and (n,t) reactions start to contribute at $E_n = 15.9$ and 21.4 MeV, respectively; as estimated from their respective Q-values of -13.7 and -10.0 MeV and biasing thresholds of $E_b = 2.4$ MeV$_d$ and 2.7 MeV$_t$. Alpha particles start contributing to ε_0 first at $E_n = 10.4$ MeV because of the high threshold $(E_b = 5.5$ MeV$_\alpha$ and $Q = -5.7$ MeV for ^{12}C(n,α)^{9}Be).

1   Above $E_n = 15$ MeV, the relative importance of
inelastic n-charged particle reactions would in-
3   crease both due to the rise in cross-section and
light production effects. They are responsible for
5   the enhancement of the detector response above
the detection efficiency level of elastic recoil
7   protons, which decreases monotonically with
energy. Our measurement establishes the energy
9   dependence of $\varepsilon(E_n)$ in this energy region up to
$E_n = 100$ MeV showing a falling trend that con-
11 tinues up to about $E_n = 200$ MeV; a possible
enhancement at the highest energy might reflect
13 the opening up of pion production channels.

It can be noted that neutrons which undergo
15 reactions leading to undetected particles can
attenuate the incoming flux or lower its energy;
17 both can reduce the neutron detection efficiency.
One such strong reaction channel is inelastic
19 scattering in carbon, $^{12}C(n, n')^{12}C^*$ leading to
the 4.4-MeV excited state. It would affect the
21 efficiency from $E_n = 5.5$ MeV where the cross-
section starts to be significant, to reach a
23 maximum between 6 and 8 MeV [11]. On the
other hand, the 4.4-MeV γ-rays from the decay is a
25 likely contribution to the γ-events registered in the
detector. In our case, these γ-rays are indeed
27 detected but they are not included in the efficiency
and would therefore contribute to the mentioned
29 attenuation as do the $(n, n'\gamma)$ interactions resulting
in γ-rays that escape detection altogether.

31 A fraction of the neutrons from $(n, n'\gamma)$ events
can subsequently suffer elastic np scattering. These
33 are basically gamma-triggered events but with a
possible upshift in V_{PH2} for a given V_{PH1} because
35 of the admixture of protons in the response. The
extended distribution on the left-hand side of the
37 gamma peak in Fig. 11 could be attributed to this
type of double interaction events. Another possible
39 double interaction event is np scattering preceding
the $(n, n'\gamma)$ reaction in which case the trigger is the
41 proton recoil signal. These events appear as proton
events in the V_{PH1} vs. V_{PH2} diagram but with an
43 extra spread up and down in the V_{PH2} value.
Lower values are obtained because of the gamma
45 admixture. Higher values occur because of the
delay between the proton recoil and gamma
47 production times (up to a few ns); the latter would
enhance V_{PH2}, making it approaching the value of

V_{PH1} as more of the pulse falls inside the timing   49
gate. These mixed n- and γ-type of response events
can be seen to fill in the region between the   51
respective single type events in the V_{PH1}–V_{PH2}
diagram (Fig. 10) and the histogram projections   53
(Fig. 11).

For the largest pulse heights (Fig. 11), it can be   55
seen that the proton recoil group is split into two,
and possibly even three components. These can be   57
ascribed to neutron reactions producing proton,
deuteron and triton recoils while the α-particle   59
group is well distinguished, except for the very
lowest pulse heights. With better resolution, it is   61
possible to resolve these components to perform
detailed studies of the charged-particle responses   63
of the detector and, hence, the relative weights of
the underlying reaction cross-sections as functions   65
of energy.

Moreover, one can also note the possibility for a   67
more detailed study of the γ-ray response of the
detector and to make a distinction between pure   69
γ–e reactions and mixed ones. In the case of mixed
ones, the delay time spread of the sequences $n \to p$ 71
followed by $\gamma \to e$, or $\gamma \to e$ followed by $n \to p$, could
be scanned by varying the time gate for the V_{PH1} 73
and V_{PH2} pulse height signals.

The present study has determined that with the   75
present bias setting ($E_b = 490$ keV$_{ee}$), the α-parti-
cle recoils constitute about 20% of the detector   77
efficiency in the energy range $E_n = 34$–100 MeV.
We find that out of the detected fraction of   79
impinging neutrons, between 16% and 21% is
due to gamma events which are eliminated when   81
gamma discrimination is applied as it is in the
normal measurement mode.   83

The detection efficiency of the DEMON detec-
tor has been calculated with the Kent State   85
University (KSU) code with standard reaction
cross-sections [12,4] as well as with modified ones;   87
the latter was undertaken to describe the DEMON
response. The results of the standard cross-   89
sections are compared with the experimental data
in Fig. 16 which describe the general features of   91
the measured $\varepsilon(E_n)$ but tend to be too low above
20 MeV. The present results, covering the pre-   93
viously unmeasured energy range 20–100 MeV,
confirms that the code calculations with standard   95
cross-sections is too low up to $E_n = 100$ MeV and

that modifications are needed. The underestimation above 200 MeV can still have other causes, such as the onset of pion production contributions. To shed some further light on this, one should perform a response calculation that differentiates between production of proton and α-particle recoils for comparison with our data in Fig. 15. Moreover, future measurements could be extended upwards in energy (the experimental limit being at present about 180 MeV at the TSL neutron facility) for better overlap and cross calibration with, for instance, MPR spectrometer data. Similarly, extension downwards from 21 to 10 MeV would reach the range where the np elastic scattering dominates the response function. This would provide an overlap with the energy range which can be covered with Tandem experiments. In general, the present type of measurements can eventually be extended to cover the energy region 10–180 MeV (at TSL).

To improve the quality of the measurements, the statistical error can be reduced by increasing the experimental running time. It would also be advantageous if the systematic uncertainties in the background subtraction (CH_2 vs. C targets) could be further reduced. An accompanying improvement in the determination of the detailed energy dependence would add value to the data. This tagging measurement is intrinsically absolute, but it is directly related to the bias setting. Thus, it would be justified to measure quantitatively the sensitivity to how this bias is set which could be done by measuring the variation in ε as a function of E_b. In all, this might allow measurements at a general overall accuracy level of about 1% in the determination of detection efficiencies, global and differential ones.

It was shown in this study that not only the global detection efficiency can be measured, but also the differential detection efficiency, both the radial detector dependence and the dependencies on energy and type of recoil particle. These measurements can be improved even further, which is especially true for the recoil energy dependence which was limited to the very low pulse height region in the present experiment. This would be useful for benchmarking the codes used to calculate neutron detection response functions.

At the indicated level of detailed experimental information that can be obtained, this can be done at a rather specific level which would allow the codes to be used for detectors of other geometries than that of the DEMON.

7. Summary and conclusions

The response of a large neutron detector (DEMON) has been studied with tagged neutrons in the energy range 21–100 MeV. Results are presented on the total (ε) and differential neutron detection efficiencies, which fill a gap in the information on energy dependence of the detection efficiency for DEMON, so that $\varepsilon(E_n)$ is now known experimentally from 2 to 800 MeV for this detector. This information was essential for recent high-accuracy measurements of the energy distribution of the neutron emission in spallation reactions with a GeV proton beam. The efficiency calibration data were compared with code calculations, which describe the general trend of the energy dependence of the efficiency. However, our new results confirm that the standard reaction cross-sections for neutrons on carbon give too low efficiency values in the energy range $E_n > 20$ MeV. It is shown that the tagging technique is very efficient to obtain both the absolute integral detection efficiency ε as well as the differential response characteristics. Especially, new information has been provided on the neutron-induced reactions in the scintillator that normally are eliminated by pulse shape discrimination to avoid interference from extraneous γ-rays. Finally, this experiment has demonstrated the capabilities of high-accuracy neutron tagging techniques, and possible extensions of this method have been presented, as well as their usefulness for benchmarking codes for calculating neutron response functions.

Acknowledgements

References

[1] N. Olsson, P.-O. Söderman, L. Nilsson, H. Laurent, Nucl. Instr. and Meth. A 349 (1994) 231.

[2] S. Leray et al., Proceedings of Second International Conference on Accelerator Driven Transmutation Technologies and Applications, Uppsala University, 1997, p. 455; G.S. Bauer, Proceedings of Second International Conference on Accelerator Driven Transmutation Technologies and Applications, Uppsala University, 1997, p. 159.

[3] X. Ledoux, et al., Phys. Rev. Lett. 82 (1999) 4412.

[4] F. Borne, Ph.D. Thesis, Université de Bordeaux I, France, 1998.

[5] E. Martinez, et al., Nucl. Instr. and Meth. A 385 (1997) 345.

[6] F. Borne, et al., Nucl. Instr. and Meth. A 385 (1997) 339.

[7] J. Thun, J. Källne, J. Frenje, J. Nilsson, E. Traneus, Proceedings of Second International Conference on Accelerator Driven Transmutation Technologies and Applications, Uppsala University, 1997, p. 624.

[8] H. Condé, et al., Nucl. Instr. and Meth. A 292 (1990) 121.

[9] J. Klug et al., to be published.

[10] B. Höistad, et al., Nucl. Instr. and Meth. A 295 (1990) 172.

[11] J.K. Dickens, Oak Ridge Nat. Lab. Report, ORNL/TM-11812, 1991; J.K. Dickens, Oak Ridge Nat. Lab. Report, ORNL-6463, 1988.

[12] R.R. Cecil, B.D. Anderson, R. Madey, Nucl. Instr. and Meth. 161 (1979) 439.

Appendix VII

THE SCANDAL FACILITY –
HOW TO MEASURE
ELASTIC NEUTRON SCATTERING
IN THE 50–130 MEV RANGE

JOAKIM KLUG

PH.L. THESIS

THE SCANDAL FACILITY –
HOW TO MEASURE
ELASTIC NEUTRON SCATTERING
IN THE 50–130 MEV RANGE

Joakim Klug

Department of Neutron Research, Uppsala University, Sweden

THESIS FOR THE DEGREE OF LICENTIATE OF PHILOSOPHY

Contents

I Summary

II J. Klug *et al.*, *SCANDAL – a facility for elastic neutron scattering studies in the 50–130 MeV range*, to be published

The SCANDAL facility – how to measure elastic neutron scattering in the 50–130 MeV range

Joakim Klug

Department of Neutron Research, Uppsala University, Sweden

Licentiate thesis

January 2001

Abstract

The interest in neutrons of energies above 20 MeV is growing rapidly, since new applications are being developed or have been identified. Transmutation of nuclear waste and cancer therapy with neutron beams are two research fields that would benefit from new neutron scattering data at these energies.

A facility for detection of scattered neutrons in the energy interval 50–130 MeV, SCANDAL (SCAttered Nucleon Detection AssembLy), has been developed and installed at the neutron beam facility of the The Svedberg Laboratory in Uppsala. It can be used to study the (n,n), (n,p) and (n,d) reactions.

This thesis describes the layout of the setup, the experimental procedure, and data analysis principles. The performance of the spectrometer is illustrated with measurements of the (n,p) and (n,n) reactions on ^{1}H and ^{12}C. In addition, the neutron beam facility is described in some detail.

1 Introduction

Nuclear waste management and cancer therapy may seem to have little in common, but there are at least two aspects that concern both topics: great public interest, and neutron physics.

The recent development of high-intensity proton accelerators has resulted in ideas to use subcritical reactors, fed by externally produced neutrons, for transmutation of waste from nuclear power reactors or nuclear weapons material. This has the potential to simplify the requirements for long-term storage of such materials.

Conventional radiation treatment of tumours is carried out using photons or electrons. Some common types of tumours, however, cannot be treated successfully in this way. For some of these, very good treatment results have been reached with fast neutron therapy, making it the largest non-conventional therapy world-wide.

It has also become evident that electronics in aeroplanes suffer effects from cosmic-ray neutrons [1, 2]. These can induce nuclear reactions in the silicon substrate of a memory device, releasing free charges, which in turn can flip the memory content. This random re-programming is obviously not wanted.

Furthermore, neutrons at aircraft altitudes give a significant radiation dose to airplane personnel. This poses a relatively new dosimetry problem, which is currently under investigation [3].

All these applications involve neutrons at energies above 20 MeV. As there is very little data available in this region, the interest in new data is growing rapidly.

This thesis work has been part of the neutron scattering programme at the Department of Neutron Research at Uppsala University. A facility for detection of scattered neutrons – SCANDAL – at energies relevant for the applications described above has been installed at the The Svedberg Laboratory (TSL) in Uppsala. Since the equipment can be used to study the (n,p) and (n,d) reactions in addition to neutron elastic scattering, the acronym should be interpreted as SCAttered Nucleon Detection AssembLy. The focus of this work, and the subject of the paper presented here, has been to characterize the performance of the equipment, by analyzing measurements of elastic and inelastic neutron scattering from hydrogen and carbon.

2 Transmutation of nuclear waste

All elements heavier than tungsten are known to fission with a large energy release if irradiated by neutrons. Thus, all heavy elements are potential sources of enormous amounts of energy. In reality, however, only one reasonably abundant element in nature, ^{235}U, can be utilized today on a technical scale, using reactors based on a self-sustained chain reaction.

In a nuclear reactor, fission is not the only occurring process as there are also those building up elements heavier than uranium. These transuranic actinides con-

stitute the bulk of the long-lived waste, with plutonium being the most abundant nuclide.

In the opinion of many people, a major drawback of nuclear power production lies in the fact that the radioactive waste has to be stored safely for many years. However, a concept for dealing with the waste problem, acting as a complement to storage in a deep geological repository, is being investigated. By irradiation of actinides and long-lived fission products in spent fuel with an intense neutron flux, transmutation into elements with shorter lifetimes could be attained [4].

Besides providing a means for the reduction of nuclear waste, the same techniques might be used to destroy nuclear weapons material, especially plutonium which is difficult to incinerate in standard reactors. On a very long time scale, the strong neutron sources we are considering here can also be used to drive reactors that can make use of natural uranium and thorium, which are immense energy sources.

A limiting factor in the self-sustaining fission reactors of today is the neutron economy. Fission is induced by neutrons, but neutrons are also released after fission, which makes a chain reaction possible. Some of the released neutrons, however, are lost in other reactions. In addition, for a self-sustaining reactor, it is important for safety reasons that a reasonable fraction of the neutrons are released later in time (beta-delayed neutrons), making reactivity changes sufficiently slow to be possible to control.

These problems are making self-sustaining reactors, that can incinerate the long-lived wastes from the reactors of today, very difficult (or even impossible) to build. Subcritical reactors, where some neutrons are produced externally and fed into the reactor, are not limited by these shortcomings. This has made hybrid solutions, where an external neutron source is coupled to a reactor, a field of intense research during the last few years.

Presently, there seems to be some consensus about the basic design of a possible future device. The extra neutrons are created in spallation processes, generated by a beam of protons or deuterons (1–2 GeV, 20–100 mA) that is stopped in a heavy target material, e.g. lead. The spallation neutron flux can be several orders of magnitude higher than that in a conventional reactor.

After creation in the spallation target, the neutrons enter a surrounding blanket containing long-lived transuranic elements from spent nuclear fuel. Due to the intense neutron irradiation, these elements can be transformed into stable or short-lived ones by fission processes. This lessens in principle the requirements on the geological repository. In addition, the transmutation facility has a potential of producing energy, not only for the ion accelerator, but for the electric power grid as well.

In order to construct the core and to predict its performance, simulations have to be done. These require knowledge of the underlying fundamental nuclear reactions, i.e., cross sections for production of neutrons and charged particles in the target,

and for reactions that are relevant for neutron transport and moderation.

The spallation neutron spectrum is different from the neutron spectrum of standard nuclear reactors, especially in the high energy region. The nuclear data libraries developed for reactors of today go up to about 20 MeV, but in a transmutation facility, neutrons with energies up to 1–2 GeV will be present. Although a large majority of the neutrons will be below 20 MeV, the relatively small fraction at higher energies still has to be characterized. Spallation results in neutron spectra with an intensity distribution roughly like $1/E_n$. The small number of neutrons at very high energies, say above 200 MeV, make data in this region not being as important as mid-range data. Direct reaction models assuming a single interaction also work reasonably well above 200 MeV. In other words, there is a significant need for neutron scattering data in the 20–200 MeV region. Existing theoretical models and computation codes, together with the parameters used therein, have to be reviewed thoroughly. Experimental measurements are essential in order to verify these models and parameters.

3 Fast neutron cancer therapy and dosimetry

Radiation treatment of tumours is, in most cases, carried out using electron beams and bremsstrahlung photon beams. Unfortunately, not all tumours respond positively to this kind of radiation. A large number of patients could benefit from therapy with more densely ionizing radiation [5, 6].

Cancer therapy with fast neutrons can provide such radiation to a reasonable cost. In this case, ionizing charged particles are produced by nuclear reactions in the tissue. To fully investigate the potential of this therapy, the dose delivery has to be known with the same precision as in common photon therapy. This requires determination of the fundamental cross sections for conversion of neutrons into charged particles. Another important quantity is elastic scattering, which through the heavy recoils is responsible for 10–15 % of the dose in cancer therapy.

Modern neutron therapy beams extend up to 70 MeV, while most evaluated data bases go up to 20 MeV, as mentioned above. This makes it difficult to correctly estimate the dose given, and to plan and optimize the therapy. Hence, the needs of data for cancer therapy coincide in energy with those for transmutation applications.

4 The optical model

For transmutation purposes, neutron elastic scattering is the single most important intermediate energy quantity that remains to be measured. It also plays a key role in describing reactions that are relevant for medical purposes. There are several reasons for this, the most important one being that elastic scattering allows determination of the optical potential, which plays a role in every microscopic calculation that

involves neutrons in either the entrance or the exit channel. The optical model for protons is well known, while this is not the case for neutrons.

Coulomb repulsion of protons creates a neutron excess in all stable nuclei with mass number $A > 40$. Incident protons and neutrons interact differently with nuclei, depending on the neutron excess. To account for this, an isovector coupling term has been introduced in the optical model by Lane [7], giving the nuclear part of the potential the form

$$U_N(E) = U_0(E) + (4/A)U_1(E)\vec{t} \cdot \vec{T}$$

where $\vec{t}$ is the isospin of the projectile and $\vec{T}$ is the isospin of the target. The origin of this term may be traced to the $\vec{\tau_i} \cdot \vec{\tau_j}$ term in the nucleon-nucleon interaction. The diagonal elements of the $\vec{t} \cdot \vec{T}$ matrix display the differences between proton-nucleus and neutron-nucleus elastic scattering, i.e.,

$$U_N(E) = U_0(E) \pm \epsilon U_1(E) + \Delta U_c$$

where $\epsilon = (N - Z)/A$ and $\Delta U_c = 0$ for neutrons.

This expression shows that the proton-nucleus optical potential contains both an isovector term, U_1, and a Coulomb correction term, ΔU_c. This means that the proton kinetic energy is lower inside the nucleus, compared to that of a neutron. Once ΔU_c is known, the isovector potential U_1 can be deduced by a comparison of neutron and proton elastic scattering from the same $T \neq 0$ nucleus at the same energy.

Given the time and cost to carry out elastic scattering experiments, the first nuclei to study are those being interesting for developing theoretical models, i.e. magic or semi-magic ones like ^{12}C, ^{16}O, ^{40}Ca, ^{90}Zr and ^{208}Pb. Fortunately, these elements are also important in transmutation and therapy applications.

The optical model provides additional support for measuring elastic scattering; it follows from the model itself that the elastic cross section must constitute at least half the total cross section.

5   Elastic scattering data

The major part of neutron elastic scattering data above 20 MeV comes from the period 1950–1960. Due to difficulties at that time in extracting particle beams from cyclotrons, experiments were performed by placing a neutron production target inside a cyclotron, at a radius corresponding to the desired charged particle energy. For neutron production, the Be(d,n) and C(p,n) reactions were utilized. The extension of the neutron production target, and the small radial difference between consequtive beam turns inside the cyclotron, resulted in neutron beam energy resolutions of typically 20–35 % (FWHM), and energy uncertainties of several MeV. There are elastic

neutron scattering data from 80 to 350 MeV from this period [8, 9, 10, 11, 12], but due to the characteristics mentioned, their quality is considered too low for today's requirements.

In 1994, neutron elastic scattering data from UC Davis at 65 MeV on a few nuclei were published [13]. The neutron beam was produced by the ^{7}Li(p,n) reaction, and had a resolution of 1.2 MeV (FWHM). Cross sections were measured for targets of C, Si, Cd, Fe, Sn and Pb, at laboratory angles from 6° to 45°. Besides this, there are unpublished data for a few nuclei, from Los Alamos [14].

The neutron beam facilities at UC Davis and Los Alamos serve as representatives for the two main means of producing neutrons using accelerated particle beams. At the Los Alamos Meson Production Facility (LAMPF), 800 MeV protons collide with a tungsten target, producing spallation neutrons with a continuous energy distribution (a white spectrum) up to the proton beam energy. Even if data can be recorded simultaneously over a wide range of energies, there is one obvious disadvantage in the fact that the flux per energy unit decreases like $1/E_n$ – measurements at high energies become very time consuming.

The ^{7}Li(p,n) reaction, employed at UC Davis as well as at TSL, yields a quasi-monoenergetic spectrum of neutrons having roughly the same energy as the incident protons. The advantage of using a monoenergetic beam when studying reactions at a specific energy is shown in figure 1. Here, a ^{12}C(n,n) excitation spectrum obtained at TSL is compared with a corresponding spectrum from Los Alamos [14]. It illustrates the difference in time needed to obtain the same amount of data – a few hours using a monoenergetic beam, compared to some months for a white source.

6 Neutron detection principles

When measuring neutron scattering at energies up to 20 or 30 MeV, time-of-flight (TOF) techniques are normally used to determine the neutron energies. In the low end of the interval, the flight paths can be kept to a length of a few metres to obtain the desired energy resolution. Thus, it is also possible to rotate the detector around the scattering sample, to measure angular distributions. At the high end, however, the required flight path must be increased, meaning that rotation becomes unpractical. The solution is to use a beam swinger with which the incident beam angle can be changed by rotating a set of magnets.

At still higher neutron energies, the TOF techniques become less favourable. For instance, 20 MeV neutrons can be measured with an energy resolution of 0.5 MeV, given a time resolution of 1 ns and a flight path of 5 m. In contrast, 100 MeV neutrons require a 60 m flight path for the same energy resolution. Even if a resolution of 2 MeV is accepted, the flight path will be 15 m. In addition, a large array of neutron detectors is needed to maintain a reasonable solid angle and count rate.
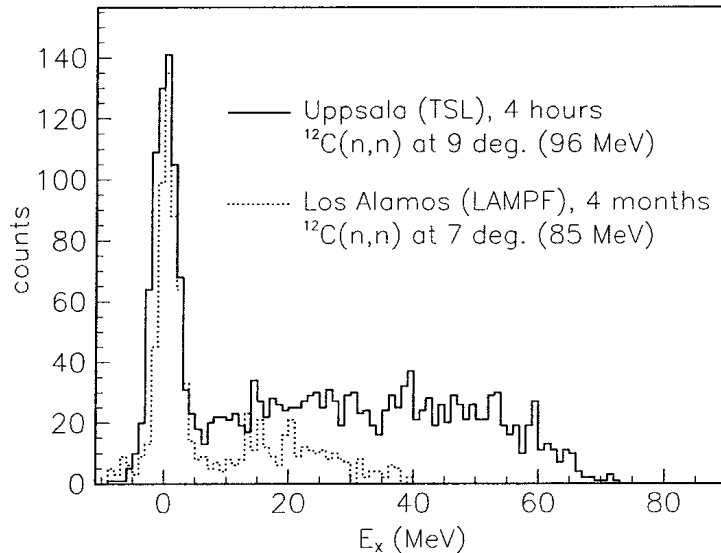
Figure 1: Comparison between a monoenergetic (Uppsala) and a white (Los Alamos) neutron source.

Another problem is related to the dumping of the charged particle beam. When a 100 MeV beam is stopped, a huge background of neutrons will be created. A solution is to bend the beam between the neutron production target and the scattering sample, and bring it far away to a well-shielded beam dump. Unfortunately, this leads to an increase in the neutron flight distance before they reach the target, resulting in reduced count rate.

A different approach is to increase the distance between the neutron production target and the scatterer, thereby enabling collimation of the neutrons into a well-defined, high-quality beam, as well as good shielding of the charged particle beam dump. By converting the neutrons to recoil protons in a hydrogenous converter near the scatterer (about 1 m), a large solid angle is guaranteed. The recoil protons can then be detected with a $\Delta E - E$ telescope.

This method has been employed for the SCANDAL setup at the TSL neutron beam facility. The assembly consists of two identical systems that can be rotated around the scattering target, normally covering a total angular range from 10 to 70 degrees. Neutrons are converted into protons in the H(n,p) reaction in a 10 mm thick plastic scintillator. Two additional scintillators act as ΔE detectors, while a stack of CsI detectors are used for energy determination. When measuring elastic neutron scattering, veto detectors in front of the converters are used for fast charged particle rejection. In addition to the ΔE and E detectors, drift chambers are used

for tracking of the recoil protons and improvement of the angular resolution.

Measurements of the H(n,p), ^{12}C(n,p), and ^{12}C(n,n) reactions have been performed at a neutron beam energy of 96 MeV, using scattering targets of CH$_2$ and carbon, respectively. Principles of the experimental procedure and the analysis, as well as technical details on the equipment, are given in the paper presented.

The results of the analysis are illustrated in proton energy and excitation energy spectra. A response function for the SCANDAL setup, constructed from basic principles, describes the data very well; hence it is concluded that the performance of SCANDAL is under good control. The total energy resolution is 3.7 MeV.

Acknowledgements

References

[1] J.F. Ziegler, IBM J. Res. Develop. **40** (1996) 19.

[2] H.H.K. Tang, IBM J. Res. Develop. **40** (1996) 91.

[3] D. O'Sullivan, private communication. EU Cosmic Radiation and Dosimetry Group.

[4] Proceedings of the 3rd International Conference on Accelerator Driven Transmutation Technologies (ADTTA99), Prague, Czech Republic, June 7-11, 1999. www.fjfi.cvut.cz/con_adtt99/.

[5] A. Wambersie, P. Pihet, H.G. Menzel, Radiat. Prot. Dosim. **31** (1990) 421.

[6] M. Tubiana, J. Dutreix, A. Wambersie, Introduction to Radiobiology (Taylor & Francis, 1990).

[7] A.M. Lane, Nucl. Phys. **35** (1962) 676.

[8] A. Bratenahl, S. Fernbach, R.H. Hildebrand, C.E. Leith, B.J. Moyer, Phys. Rev. **77** (1950) 597.

[9] C.P. van Zyl, R.G.P. Voss, R. Wilson, Phil. Mag. **1** (1956) 1003.

[10] A. Ashmore, D.S. Mather, S.K. Sen, Proc. Phys. Soc. A **71** (1958) 552.

[11] R.S. Harding, Phys. Rev. **111** (1958) 1164.

[12] G.L. Salmon, Nucl. Phys. **21** (1960) 15.

[13] E.L. Hjort, F.P. Brady, J.L. Romero, J.R. Drummond, D.S. Sorenson, J.H. Osborne, B. McEachern, L.F. Hansen, Phys. Rev. C **50** (1994) 275.

[14] J. Rapaport, private communication. J. Osborne, thesis, unpublished.

SCANDAL – A facility for elastic neutron scattering studies in the 50–130 MeV range

J. Klug[a], J. Blomgren[a1], A. Ataç[a], B. Bergenwall[a], S. Dangtip[a],
K. Elmgren[a], C. Johansson[a], N. Olsson[a], A.V. Prokofiev[a,j],
J. Rahm[a], O. Jonsson[b], L. Nilsson[b], P.-U. Renberg[b],
P. Nadel-Turonski[c], A. Ringbom[d], A. Oberstedt[e], F. Tovesson[e],
C. Le Brun[f], J.F. Lecolley[f], F.R. Lecolley[f], M. Louvel[f], N. Marie[f],
C. Schweitzer[f], C. Varignon[f], Ph. Eudes[g], F. Haddad[g], M. Kerveno[g],
T. Kirchner[g], C. Lebrun[g], L. Stuttgé[h], I. Slypen[i], A.N. Smirnov[j],
R. Michel[k], S. Neumann[k], U. Herpers[l]

[a]Department of Neutron Research, Uppsala University, Sweden
[b]The Svedberg Laboratory, Uppsala University, Sweden
[c]Department of Radiation Sciences, Uppsala University, Sweden
[d]Swedish Defence Research Establishment (FOA), Stockholm, Sweden
[e]Department of Technology and Science, Örebro University, Sweden
[f]LPC, ISMRA et Université de Caen, CNRS/IN2P3, France
[g]SUBATECH, Université de Nantes, CNRS/IN2P3, France
[h]IReS, Strasbourg, France
[i]Institute de Physique Nucleaire, Université Catholique de Louvain, Belgium
[j]V.G. Khlopin Radium Institute, St. Petersburg, Russia
[k]Zentrum für Strahlenschutz und Radioökologie, Universität Hannover, Germany
[l]Abteilung Nuklearchemie, Universität zu Köln, Germany

Abstract

A facility for detection of scattered neutrons in the energy interval 50–130 MeV, SCANDAL (SCAttered Nucleon Detection AssembLy), has recently been installed at the 20–180 MeV neutron beam facility of the The Svedberg Laboratory, Uppsala. It is primarily intended for studies of elastic neutron scattering, but can be used for the (n,p) and (n,d) reaction experiments as well. The performance of the spectrometer is illustrated in measurements of the (n,p) and (n,n) reactions on ^{1}H and ^{12}C. In addition, the neutron beam facility is described in some detail.

[1]Corresponding author. Tel. +46 18 471 3788. E-mail address: jan.blomgren@tsl.uu.se (J. Blomgren)

1 Introduction

The interest in high-energy neutrons is rapidly growing. This is due to a number of potential large-scale applications involving fast neutrons, either having been identified or being under development. These applications primarily fall into three sectors; nuclear energy and waste, medicine and electronics effects.

The recent development of high-intensity proton accelerators has resulted in ideas to use subcritical reactors, fed by external spallation-produced neutrons, for transmutation of waste from nuclear power reactors or nuclear weapons material. This might result in less problematic waste material and/or energy production [1].

Conventional radiation treatment of tumours, i. e. by photons or electrons, is a cornerstone in modern cancer therapy. Some rather common types of tumours, however, cannot be treated successfully. For some of these, very good treatment results have been reached with neutron therapy, which is the largest non-conventional therapy world-wide [2, 3].

The last few years, it has become evident that electronics in aeroplanes suffer effects from cosmic-ray neutrons [4, 5]. The now most well-known effect is that a neutron can induce a nuclear reaction in the silicon substrate of a memory device, releasing a free charge, which in turn flips the memory content. This random reprogramming is obviously not wanted. Similar effects causing hardware damage have recently been identified also on ground level.

Neutrons at aircraft altitudes give a significant radiation dose to airplane personnel. This poses a relatively new dosimetry problem, which is currently under intensive investigation [6].

Finally, fundamental nuclear physics with intermediate-energy neutrons has recently got widespread attention due to the experimental studies of the absolute strength of the strong interaction in the nuclear sector, derived from neutron-proton scattering data [7].

Elastic neutron scattering plays a key role for the understanding of all these areas. The most important reason is that it allows a determination of the optical potential, which plays a decisive role in every microscopic calculation including neutrons in either the entrance or exit channel. In addition, the elastic cross section is also the largest of the individual partial cross sections contributing to the total cross section. In fact, a consequence of the optical model is that the elastic cross section must constitute at least half the total cross section.

All the applications mentioned above involve neutrons at much higher energies than for the traditional applied areas, e.g. nuclear power. Extensive evaluated data libraries have been established for the development of nuclear fission and fusion for energy production, which have a 20 MeV upper limit. Very little high-quality neutron-induced data exist above this energy. Only the total cross section [8] and the (n,p) reaction have been investigated extensively [9, 10]. There are high-quality neutron total cross section data on a series of nuclei all over this energy range. In addition, there are (n,p) data in the forward angular range at modest excitation energies available at a few energies and for a rather large number of nuclei.

Besides this, there are data on neutron elastic scattering from UC Davis at 65 MeV on a few nuclei [11]. Programmes to measure neutron elastic scattering have been proposed or begun at Los Alamos [12] and IUCF [13], with the former resulting in a thesis on data in the 5–30° range on a few nuclei [12]. The design of SCANDAL has been based on the experiences from the latter two projects.

Besides the role of elastic neutron scattering data for determining the neutron optical potential, there are also cases where they can be of direct use. Examples are in neutronics of spallation systems, including accelerator-driven transmutation cores, and fast-neutron cancer therapy, where 10–15 % of the dose comes from elastic neutron scattering.

All these research areas are represented at the neutron beam facility of the The Svedberg Laboratory (TSL). The facility has previously been described in a NIM publication [14]. Major recent upgrades in the neutron production motivate a renewed description of it, which is found in section 2. An overview of the experimental area is given in section 3, and the SCANDAL setup is described in section 4. Section 5 is devoted to experimental tests of the performance of the device, while the experimental programme is discussed in section 6, and finally, a summary and the conclusions are presented in section 7.

2 Neutron beam production

2.1 Neutron production techniques above 50 MeV

Neutron beam facilities above 50 MeV have traditionally been of two types; white sources and quasi-monoenergetic. White spallation sources have been used at Los Alamos [15] and Paul Scherrer Institute [16], and a new source is presently being installed at CERN [17]. Typically, the energy-integrated flux is significantly larger than for monoenergetic sources, on the expense that the flux per energy unit is much smaller. For elastic neutron scattering measurements, i.e. the scope of this paper, this smaller flux per energy unit is a clear disadvantage. This is illustrated by the fact that no data on elastic neutron scattering at intermediate energies have been published from white sources.

3

Monoenergetic sources are, like the Uppsala facility, in most cases employing the ^{7}Li(p,n) reaction. Such installations have been operated at UC Davis [18], IUCF [19], TRIUMF [20], NAC [21], TIARA [22], UCL [23], and RIKEN [24].

Recently, a novel technique has been developed at IUCF to produce tagged neutrons at a cooler ring [25]. This technique can be used to provide neutron beams with well-defined energy and intensity, but with the drawback that the intensity is very poor. A programme is underway to measure neutron-proton scattering, for which the intensity is sufficient, while it is inadequate for elastic scattering from nuclei.

Finally, the D(p,n) reaction has been extensively used to produce intense neutron beams with a slightly worse intrinsic resolution than the ^{7}Li(p,n) reaction, but with the advantage that reasonably polarized neutrons can be obtained. The limited beam resolution, however, prevents resolved studies of (polarized) elastic neutron scattering from nuclei.

2.2 The TSL neutron beam

An overview of the neutron beam facility at the The Svedberg Laboratory (TSL) is presented in fig. 1. Protons from the cyclotron impinge on a neutron production target from the left. After the target, the remaining proton beam is bent into a beam dump tunnel. A narrow neutron beam is defined by a system of three collimators. The major experimental devices are installed in a separate hall. The different parts are given detailed descriptions below.

Lithium targets of 100–800 mg/cm^2 thickness (2-15 mm), enriched to 99.98 % in ^{7}Li, are mounted in a remotely controlled water-cooled stainless-steel rig with four target holders, each with a diameter of 26 mm. One of the target positions contains a fluorescent screen viewed by a TV camera, which is used for beam alignment and focussing. Targets can be changed without breaking the vacuum; a vacuum lock reduces the exposure of the lithium targets to air to a few seconds. Previously, a cold trap was located close to the lithium target arrangement. Increased pumping capacity has made this cold trap unnecessary.

After passage of the target, the proton beam is deflected in two magnets and bent into an 8 m long tunnel, where it is focussed onto a water-cooled graphite beam dump. The integrated current from this Faraday cup is used for proton beam monitoring, which is also a relative monitoring of the neutron beam. An efficient dumping of the high-intensity proton beam is important for various reasons. A high beam transmission through the magnet elements reduces the irradiation around the beam tubes, making activation a smaller problem. In addition, the reliability of the proton current for relative neutron intensity monitoring improves.

A low-cost system has been installed to handle automatically the high-intensity beams in the beam dump line. It is based on placing electrically insulated 1 mm
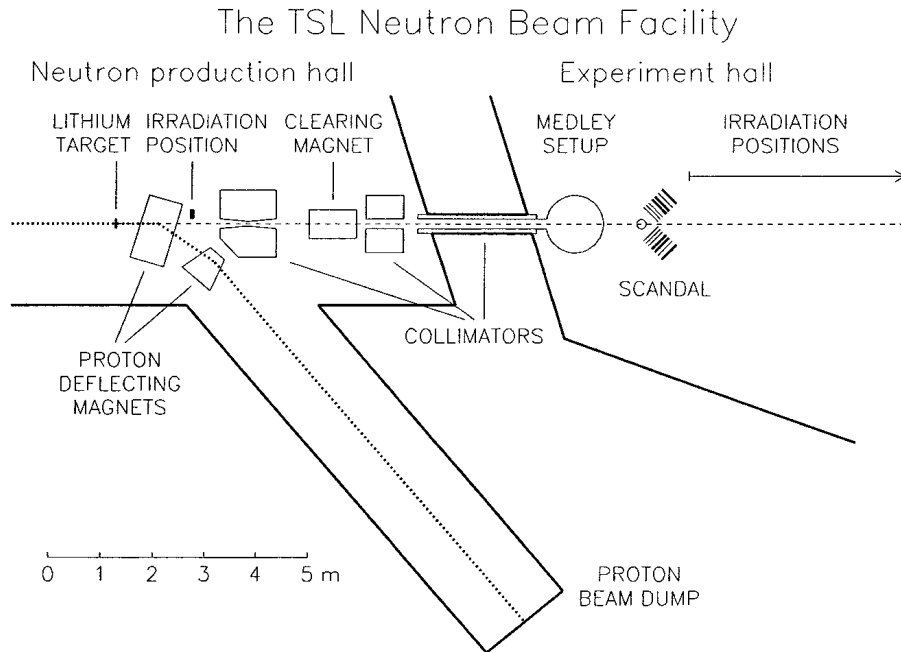
Figure 1: Overview of the Uppsala neutron beam facility.

stainless-steel pins vertically along the diameter of the beam tube in the path of the beam at two positions in the bending section. The beam profile is measured by scanning the beam with an upstream steering magnet. The beam is centered on the two pins by an automatic routine. An example of measured profiles for 180 MeV protons with and without production target is shown in fig. 2, which was obtained by scanning the preceding bending magnet current from 135 to 150 A. The effect of inserting the target is clearly visible. The centroid has shifted due to the lower energy in the beam after having passed it, and the width has increased due to energy and angular straggling.

The neutron beam produced in the forward direction is geometrically defined by a system of three collimators. The first one consists of a 1.1 m long iron cylinder of revolver type with four axial holes of different diameter. The cylinder is remotely controlled to collimate the neutron beam to solid angles of 60, 80, or 100 μsr. The fourth hole has the beam tube diameter, and can be used e. g. for alignment purposes when free sight through the collimator is required. The collimators are doubly conical in shape, with a central waist defining the solid angle.

The second collimator is 0.8 m thick and consists of iron and paraffin slabs, while the third one, about 2 m thick, is made of iron only. Neither of these two collimators shape the neutron beam, but serve as scrapers of the beam halo from
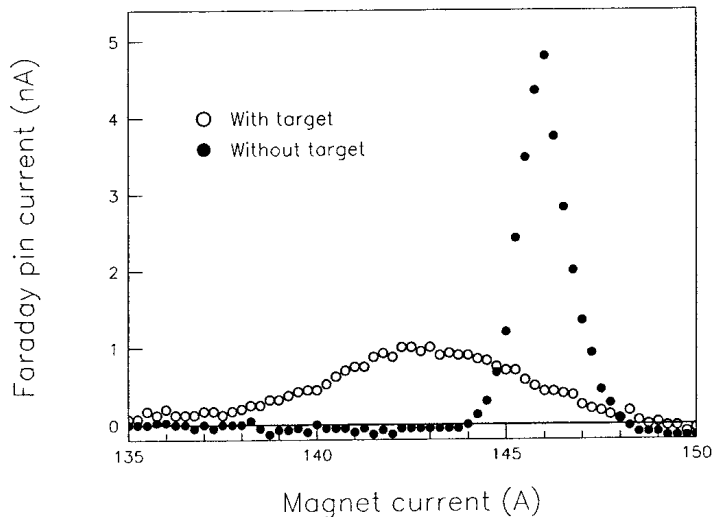
5

Figure 2: Example of a measured beam profile. The open and filled circles shows the profile with and without a lithium target, respectively.

the first collimator. The third collimator is conical in shape, with entrance and exit diameters of 60 and 75 mm, respectively. It is located in a wall separating the neutron-production area and the main experimental hall, and it also contains a beam shutter.

Protons passing through the lithium target have a small probability to pick up an electron and become hydrogen atoms, which are not deflected by the magnet after the target. For some experiments, this H^0 flux can be a problem. If so, a 1 mm thick aluminium valve after the first collimator can be closed, which results in H^0 breakup, and a dipole after the valve is used to clean the beam.

All the neutron production and collimation takes place in vacuum. The first major installation in the experimental hall, MEDLEY, is part of the vacuum system, which is terminated by a 0.1 mm stainless-steel foil at the exit of the MEDLEY scattering chamber.

In applications where the proton contamination of the beam has to be minimal, the aluminium valve and the clearing magnet described above can be used, with the valve terminating the vacuum, i.e. the MEDLEY exit foil is removed and the neutrons pass through the downstream fraction of the neutron beam line in air. With such precautions, the charged particle contamination of the neutron beam has been measured to be about 10^{-5}.

A prominent feature of the neutron production facility is the very good shield-

ing between the dumping and the experimental area, which gives low experimental background. The long distance between the neutron production and experiment area allows rejection of low-energy neutrons by time-of-flight techniques. A fast switching magnet upstream the neutron production facility allows it to be run in beam-share mode with other experiments at the laboratory, making very efficient use of the beam possible.

2.3 High-intensity irradiation facility

The main experimental devices are installed in a separate hall, well shielded from the neutron production. There is, however, one notable exception. Activation experiments can benefit from higher intensities and require very little space. A neutron irradiation facility for activation targets of maximum diameter 25 mm and length 60 mm is available 1.9 m downstream the neutron production target, located just after the proton bending magnet. It makes use of neutrons produced at an angle about 1° off the initial beam axis, and it does not interfere with other ongoing experiments further downstream.

2.4 Beam intensity monitors

Relative monitoring is provided by the proton beam Faraday cup (see above). In addition, absolute monitoring of the neutron fluence is obtained from a fission detector, based on thin-film breakdown counters (TFBCs) [26]. It consists of a double-sided ^{nat}U target and two TFBCs placed close to the target surfaces at its both sides. The fissile layers are deposited onto a 0.1 mm thick aluminium foil. The diameters of the fissile layers and the sensitive surfaces of the TFBCs are about 36 mm. The detectors and the target are placed in a non-vacuum aluminium chamber for electrical shielding and mechanical protection of the detectors. The device includes also a pulse amplifier placed in a separate box.

Depending on the required counting rate and the statistical accuracy, it is possible to use either one of the detectors or both of them simultaneously. The single-side mode is useful for neutron energies in the 20–100 MeV range when the proton beam current is in the range of a few μA. The double-side mode provides maximum sensitivity of the monitor, which is useful in the 100–180 MeV range where proton beam currents are commonly in the range of a few hundred nA.

Because of the nature of TFBC operation [27], detectors of this type can sustain only a limited number of breakdowns. Thus, for reliable and long-time operation of a TFBC, its counting rate should not exceed what is required to get a reasonably small statistical error. Under normal conditions this means about one breakdown per second, or a few thousand counts per hour. The tentative lifetime of the TFBC under such conditions is about 1500 proton μA·hours. The counting rate can be

optimized by adjusting the monitor sensitivity, which can be regulated within a rather wide range by varying the applied voltages or by using different targets, as well as by selecting the optimum mode of operation, i.e. single- or double-sided. The absolute uncertainties in the measured neutron fluence are about 10 %.

2.5 Neutron beam characteristics

The ^{7}Li(p,n) reaction produces a neutron spectrum consisting of a full-energy peak and a continuum of neutrons at lower energies, roughly evenly distributed in energy. The intensity is approximately equally distributed on these two regions. The full-energy peak is due to excitation of the ground state and first excited state (E_X = 0.43 MeV) in ^{7}Be. The energy of it is slightly lower than the initial proton energy ($Q = -1.6$ MeV), and the width is primarily given by the thickness of the lithium target. Typically, widths in the 1–4 MeV region have been used.

The intensity of the full-energy peak over the full beam area with the 60 μsr solid angle collimator is $5 \cdot 10^4$ neutrons per mm ^{7}Li target and μA of incident proton beam. The cyclotron is operated in isochronous mode up to 100 MeV, with proton beam intensities up to about 5 μA. Above 100 MeV, it employs frequency modulation, which results in much less intensity, about 200 nA at the highest proton energy, 180 MeV. To some extent this loss in proton intensity is compensated for by a lower energy loss in lithium, allowing thicker targets to be used for the same energy resolution. Thereby a loss in proton beam intensity by a factor ten gives a neutron intensity reduction by a factor five.

Low-energy neutrons can be rejected by time-of-flight techniques, which is illustrated in fig. 3. The pulse width of the cyclotron is about 4 ns, which corresponds to a neutron energy interval of 13 MeV at 100 MeV neutrons 8 m from the production target. This is the main reason for the incomplete rejection.

For a 100 MeV energy and a 8 m flight path to the experimental setup, the first three wrap-around neutron energies are at 24, 11 and 6 MeV. Thereby, for all measurements of ejectiles with higher energies, this is normally not a problem. For some experiments, however, this can be a major obstacle. A system to increase the pulse separation with preserved intensity is under consideration. One possible technique might be to select pulses with a sweeping system at an early stage of the acceleration where the activation of the lost beam is small, combined with an increased ion source intensity.

The magnetic spectrometer LISA [14] has been used for characterization of the high-energy part of the neutron spectrum. By measuring the (n,p) reaction on CH_2 and pure carbon targets, the H(n,p) reaction spectrum can be constructed. Knowing the energy variation of the H(n,p) cross section, i.e. the np scattering cross section, the energy distribution of the incident neutrons can be derived. This technique has shown that the energy distribution within 40 MeV of the full-energy peak is
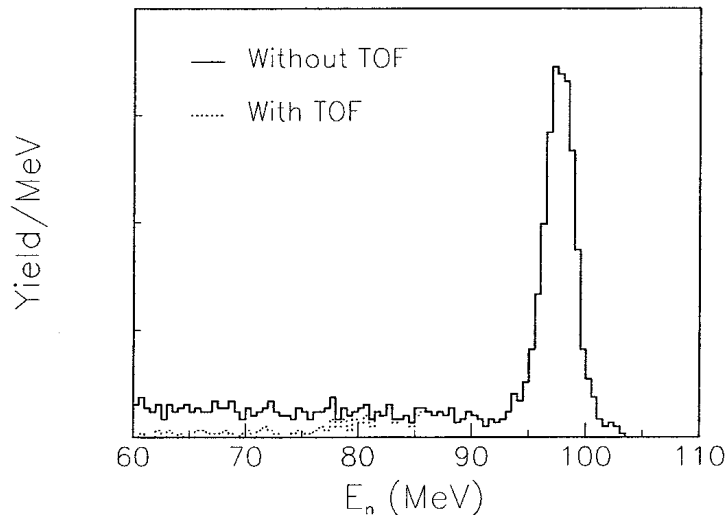
8

Figure 3: Reconstructed energy spectra of incoming neutrons, using a proton spectrum in the angular range 0 − 5° measured with the LISA magnetic spectrometer. The solid line shows the spectrum without time-of-flight conditions, and the dashed spectrum is obtained with such a cut.

in good agreement with the data on the ^{7}Li(p,n) reaction by Byrd and Sailor [28], while measurements at lower neutron energies have not been carried out with this method, due to the limited momentum bite of the magnetic spectrometer.

In fission measurements on fissile targets, like ^{235}U, wrap-around neutrons can be a major problem all the way down to zero energy. This has motivated an investigation of the low-energy neutron content in the beam. The measurements were based on time-of-flight (TOF) techniques in conjunction with neutron-induced fission reactions. Targets of ^{232}Th, ^{235}U, ^{238}U, and ^{nat}U were used in different runs. Fission fragments were detected by TFBCs with fast timing properties. The TFBCs were mounted close to the targets as sandwiches. In addition, one of the sandwiches with a ^{235}U target was surrounded by a 1 mm thick Cd foil. Since cadmium possesses a very high capture cross section at neutron energies below about 0.5 eV, the foil attenuated the neutron flux in this energy region by many orders of magnitude. On the other hand, neutrons with energies above about 10 eV interacted with the foil material with a probability of only 2–3 %. Thus, a comparison of data obtained with two ^{235}U targets with and without cadmium surrounding them allowed an estimation of the neutron flux in the near-thermal energy region.

As an example of the results, fig. 4 shows time spectra of fission events obtained

in the neutron production hall in the vicinity of the irradiation position described in section 2, with a peak neutron energy of 44 MeV. The spectra of ^{232}Th and ^{nat}U fission events reflect the high-energy part of the neutron spectrum, while the ones of ^{235}U are affected by wrap-around of low-energy neutrons. A comparison of the spectra obtained for ^{235}U targets with and without cadmium surrounding them, makes it evident that the neutron spectrum includes a measurable component at energies below 0.5 eV. Assuming a Maxwellian energy distribution for the low-energy component, its time-averaged flux was found to be about 1 % of the high-energy peak neutron flux. Similar investigations were made in the experimental hall. TOF spectra of fission events were obtained for ^{235}U and ^{238}U targets, placed alternately in the beam, and out of the beam. The resulting thermal/peak flux ratio was found to be not more than $2 \cdot 10^{-4}$.
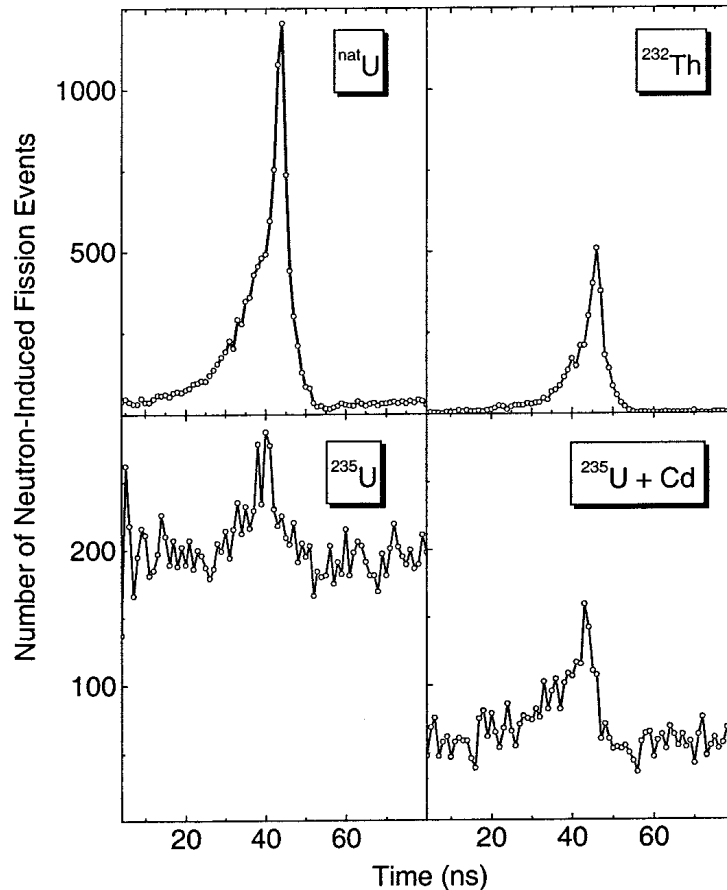

Figure 4: The fission reaction rate versus time measured in the neutron production hall. The peak neutron energy is 44 MeV (see the text for details).

The uniformity of the beam at the high-intensity irradiation position has been verified by activation techniques, where foils covering different regions of the beam spot were activated. No deviations from uniformity was found beyond a 4 % uncertainty given by statistics and the systematic uncertainty of the measurement.

3 Experimental area

The experimental hall contains three major devices. The Light Ion Spectrometer Assembly (LISA) is a magnetic spectrometer [14] for (n,p) studies. It has been used for extensive studies of the (n,p) reaction on nuclei in the $A = 9 - 208$ mass range [29, 30, 31, 32, 33, 34], and on precise experiments on np scattering [35, 36, 37, 38].

The MEDLEY detector array [39] has been designed for measurements of neutron-induced light-ion production cross sections of medical relevance, i. e. for fast-neutron cancer therapy and related dosimetry. It consists of eight particle telescopes, placed at 20-160 degrees with 20 degrees separation. Each telescope is a $\Delta E - \Delta E - E$ detector combination, with sufficient dynamic range to distinguish all charged particles from a few MeV up to about 130 MeV. All the equipment is housed in a 100 cm diameter scattering chamber, so that the charged particles can travel in vacuum.

The SCAttered Nucleon Detection AssembLy (SCANDAL) is primarily intended for studies of elastic neutron scattering, but can be used for the (n,p) and (n,d) reactions as well. It is described in some detail below.

Finally, there is about 8 m of neutron beam line between SCANDAL and the beam dump. This is used for other kinds of experiments, like fast-neutron fission [40], studies of neutron-induced electronics failures [41, 42] or dosimetry research.

4 The SCANDAL setup

4.1 General layout

The setup is primarily intended for studies of elastic neutron scattering, i. e., (n,n) reactions. The neutron detection is accomplished via conversion to protons by the H(n,p) reaction. In addition, (n,p) reactions in nuclei can be studied by direct detection of protons. This is also used for calibration of the setup. Therefore, it has been designed for a quick and simple change from one mode to the other.

The device is illustrated in fig. 5. It consists of two identical systems, in most cases located on each side of the neutron beam. The design allows the neutron beam to pass through the drift chambers on the left side of each setup, making low-background measurements close to zero degrees feasible.

In neutron detection mode, each arm consists of a 2 mm thick veto scintillator for fast charged-particle rejection, a neutron-to-proton converter which is a 10 mm thick plastic scintillator, a 2 mm thick plastic scintillator for triggering, two drift chambers for proton tracking, a 2 mm thick ΔE plastic scintillator which is also part of the trigger, and an array of CsI detectors for energy determination. The trigger is provided by a coincidence of the two trigger scintillators, vetoed by the front scintillator. If used for (n,p) studies, the veto and converter scintillators can be removed, and additional drift chambers can be mounted if desired.

In neutron detection mode, a large solid angle of protons emitted from the converter is of crucial importance to get reasonable statistics. This implies that the distance from the converter to the CsI hodoscope should be as short as possible, while proton tracking is required. Inserting a third drift chamber would improve the proton tracking, both in position accuracy and in overall efficiency, but at the expense that the proton solid angle decreases dramatically. Therefore, only two drift chambers are used, but the design allows a third chamber to be installed if desired.

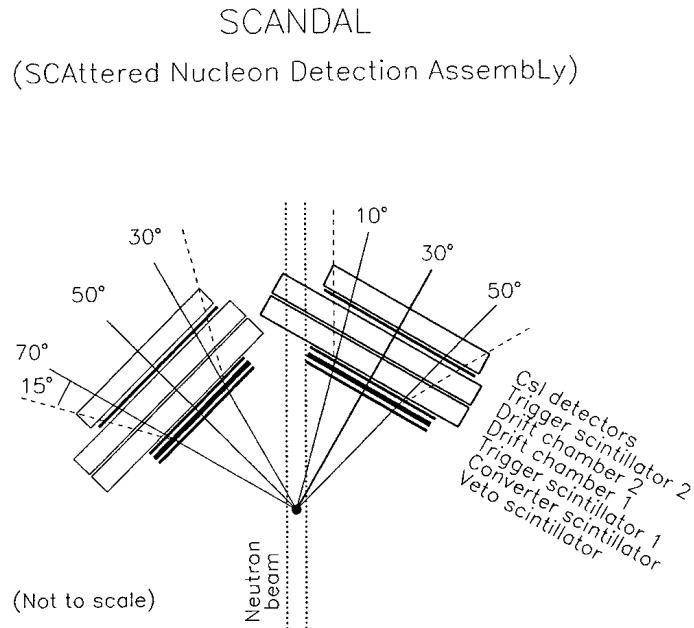SCANDAL

(SCAttered Nucleon Detection AssembLy)

Figure 5: Schematic figure of the SCANDAL setup.

4.2 Converter scintillator

Neutrons have to be converted to charged particles to be detected. We have chosen the H(n,p) reaction for neutron-to-proton conversion because it has a large cross section (above 50 mb/sr at small angles in the 50–130 MeV range), and it populates no excited states in a residual nucleus. Two main approaches can in principle be used; passive or active converters.

Active converters have the advantage that they can be thicker, because the proton straggling on the way out of the scintillator can be measured and compensated for. The maximum thickness of an active converter is thereby set by the energy resolution of the detector. A typical plastic scintillator has a resolution in the 10–15 % range, and the proton energy loss is about 0.7–1.0 MeV/mm for 70–100 MeV protons. Thereby, a converter thickness of 10 mm gives up to 10 MeV deposited energy, and the resolution contribution is henceforth up to about 1 MeV.

The most frequently used converters contain hydrogen and carbon, which allows unambiguous measurements up to 12 MeV excitation energy. For higher excitation energies, the ^{12}C(n,p) channel opens in the converter, and therefore a unique identification of the target excitation is no longer possible. This is obviously not a problem for elastic scattering, or inelastic scattering to low-lying states, but complicates experiments where low-energy neutron emission is under study. This problem is, however, present both for active and passive converters.

The problems above can be circumvented by using a passive liquid hydrogen converter, but the technique is both non-trivial and expensive. Another prize to pay is that the converter must be an order of magnitude thinner for the same resolution. Based on these discussions, we have chosen to use active plastic scintillator converters.

4.3 CsI hodoscope

The setup has in total 24 CsI(Na) detectors, 12 in each system. These detectors are trapezoidal in shape, 30 cm high with a $7 \cdot 7$ cm^2 cross section area at the PM tube end, and a $5 \cdot 5$ cm^2 area in the other end. By placing them in alternating directions, a 72 cm wide CsI hodoscope has been installed. This geometric shape is not optimal; the crystals were manufactured for another experiment and have been recycled. The shape makes the light output position-dependent, and this effect has to be compensated for in the offline analysis.

An average energy resolution of 3.0 MeV has been demonstrated for 77 MeV protons. As each detector has an individual resolution, it may deviate significantly from this figure; ranging from less than 2 MeV up to around 5 MeV in the worst case.

CsI crystals are frequently doped with tallium, which allows particle identifica-

tion through pulse-shape analysis. Doping with sodium, like in the present case, makes the crystals much more resistent to radiation damage, at the expense that the particle identification capability is lost. In the present application, this is not an important matter. The only particle identification needed is proton-deuteron separation, which is easily accomplished with $\Delta E - E$ techniques.

4.4 Drift chambers

The drift chambers serve two main purposes; they improve the angular resolution and they allow rejection of spurious events. The H(n,p) cross section close to zero degrees is rather flat over several degrees in the lab system. This effect, combined with the rather large front-area of the CsI's, makes the effective subtended angular range for each detector quite large. This would be a major contribution to the energy and angular resolution without proton tracking.

Furthermore, the Q-value for ^{12}C(n,p) is -12.6 MeV. Thus, at forward angles energy detection can isolate the protons which are due to conversion via H(n,p). At about 20° conversion angle, the proton energies from the two processes are the same, and thereby it can no longer be determined whether the energy lost was due to excitations in the neutron scattering sample or in the conversion. By applying a maximum opening angle criterion on the conversion (see fig. 5), such problems can be avoided.

Sufficient angular information is obtained by placing drift chambers between the converter and the CsI's. Hence, the conversion point is well determined. This has also the potential of allowing rejection of spurious events. With this technique, the remaining contribution to the angular resolution is the width of the neutron beam (or the scattering sample). The only way to improve the angular resolution further would be to use a narrower beam or target, but that would be at the expense of count rate.

The drift chambers are of double sense-wire type with two-dimensional readout. The horizontal coordinate is determined from one out of 40 drift cells, and the vertical from one out of eight. Each drift cell is 24 mm wide, making the total active area $960 \cdot 192$ mm^2. The position within each cell is determined by measuring the electron drift time. The position resolution is 0.3 mm (FWHM) for each coordinate. The chambers are described in more detail in reference [43].

The maximum detection efficiency possible to obtain for a single coordinate is about 98 %, when defining a good event as having at least one hit in a plane. There is, however, a non-zero probability of cross-talk between adjacent wires. For most events, the time information can be used to select the correct wire, but not all. In elastic neutron scattering measurements with SCANDAL, these double-hit events have to be rejected. By lowering the high voltage biasing the chambers, the nominal efficiency is slightly reduced, but the fraction of double hits is reduced even more,

14

increasing the figure-of-merit for good events. For optimum conditions, the efficiency for a single coordinate is in the 90–97 % range.

4.5 Multitarget

For (n,p) measurements, a multitarget arrangement can be used to increase the target content without impairing the energy resolution. This multitarget box allows up to seven targets to be mounted simultaneously, interspaced with multi-wire proportional counters. In this way it is possible to determine in which target the reaction took place, and corrections for energy loss in the subsequent targets can be applied. In (n,n) measurements, the multitarget is placed empty upstreams the scattering target, and used as charged-particle veto. A more detailed description can be found in reference [14].

4.6 Resolution

The energy resolution in neutron mode has contributions from the neutron beam (1.2 MeV at FWHM), the converter (1.4 MeV), the two trigger scintillators (0.3 MeV each), straggling in non-detector materials (0.25 MeV), kinematics (1.2 MeV), and the CsI detectors (3.0 MeV). This makes a total excitation-energy resolution of 3.7 MeV in elastic scattering measurements. This resolution is comparable with the distance from the ground state to the first excited state in most of the nuclei of interest, e. g., ^{12}C (4.4 MeV), ^{16}O (6.1 MeV), ^{40}Ca (3.3 MeV), ^{90}Zr (1.8 MeV), and ^{208}Pb (2.6 MeV).

The angular resolution is solely due to the neutron beam and target width. With the present setup dimensions and a 5 cm wide sample, it is about 1.4° (rms). The angular resolution is most crucial at small angles, where the cross section falls very rapidly. For these angles, the cross section is also very large, and thereby a narrow strip target could be used to improve the angular resolution, without making the total beam time considerably longer.

4.7 Solid angle and count rate

The solid angle subtended by each system in the proton detection mode is about 240 msr for a point target. Applying the maximum opening angle criterion on the second scattering in the converter (see above), required for neutron detection, makes the effective solid angle smaller – about 130 msr per setup at full coverage of the 15° cone. The conversion efficiency is then about $5 \cdot 10^{-4}$.

In a typical experiment, the two arms will be located such as to cover 10–50°, and 30–70°, respectively. For a one-week run on ^{208}Pb, the total number of counts

15

for a one-degree angular bin is expected to be about 5 000 at 10°, and 1 at 70°, illustrating that the cross section falls off rapidly with angle.

4.8 Electronics and data acquisition

Each plastic scintillator has two PM tubes, mounted adjacent to each other on one of the longer, horizontal sides of the scintillator. The signals are lead to a remote counting room, where they are handled using mainly standard electronic units.

The signal from each plastic scintillator PM tube is split into an energy and a timing branch using a linear fan-in/fan-out. The pulse height of the energy signal is registered by a charge-integrating ADC (QDC), which is gated by a MASTER signal (see below).

The timing signal is fed to a constant fraction discriminator (CFD), which generates a stop signal for a TDC. In addition, for the veto and trigger PM tubes, a second CFD signal is utilized for event definition. A logic OR between the two PM tubes is used to define a hit in the respective detector. A logic AND between the two trigger (T1 and T2) signals, vetoed by the veto detector (V) signal, is used to define an event in the left- or right-side setup, i.e. a SCANDAL LEFT or SCANDAL RIGHT event. These signals are fed to a pattern unit to register which setup triggered the event. Furthermore, an OR between SCANDAL LEFT and SCANDAL RIGHT defines the MASTER signal, which announces the presence of an event in one of the setups. The MASTER signal causes a read-out of the system, starts the TDCs, and gates the energy signals (ADCs) and the pattern unit.

The CsI signals are processed by preamplifiers placed close to the detectors. After transport to the counting room, the signals are fed into a spectroscopic amplifier and registered by peak-sensing ADCs.

Drift chamber amplifiers and discriminators are mounted directly on the chambers. The output signals are fed to a LeCroy 4290 TDC system, situated in the experimental area, and read out by CAMAC.

The radiofrequency (RF) signal from the cyclotron is used as a time-of-flight reference signal, and is recorded as a stop signal in a TDC which is started by the MASTER signal. At the same time, the complementary of the RF signal is used to veto the OR unit that defines the MASTER signal; i.e., if there is no RF signal, no MASTER signal will be created. In addition to this, a computer busy signal from the data acquisition system (see below) acts as a veto on the MASTER signal.

A scaler unit is used to monitor the dead time of the data acquisition system and the intensity of the neutron beam. The number of pulses from a 100 Hz clock, both with and without a computer busy veto, is registered for the dead time determination, giving typical values of 5–10 %. Signals from the proton beam Faraday cup and the fission counter give two independent values of the neutron flux.

Data are recorded on an event-by-event basis using SVEDAQ, a general-purpose

16

data acquisition system employed at the TSL [44]. Data are read out through a CAMAC branch highway and sent to a VME-based event-builder. From the event-builder system, data are split into two independent branches; to an Exabyte tape station for recording, and to online analysis. A SUN workstation is used for online sorting, monitoring and control. Typical online spectra that can be displayed are pulse heights from scintillator detectors, time-of-flight (TOF) and drift chamber hit position distributions.

5 Experimental tests, data analysis and results

5.1 Experimental procedure

To investigate the characteristics of the SCANDAL setup and to illustrate the experimental procedures, we have performed measurements both in proton and in neutron detection mode, at a neutron beam energy of 96 MeV.

The proton mode runs were used for studies of the H(n,p), ^{12}C(n,p) and ^{12}C(n,d) reactions, as well as for calibration purposes. In order to get enough statistics for the calibration of all CsI detectors, each arm was consecutively placed at both sides of the beam, giving sufficient data for the six detectors closest to the beam at each setting.

In the (n,p) measurements, the multitarget box was filled with CH_2 targets of total thickness 0.26 mg/cm^2, and with carbon targets of total thickness 0.34 g/cm^2. A background run was made with the multitarget box containing only one CH_2 foil for reference.

In neutron mode, a carbon cylinder of 5 cm height and 5 cm diameter was used as a target, while the multitarget box was empty and acting as a charged-particle veto. Here, the angular ranges 10–50° and 30–70°, respectively, were covered by the two arms.

5.2 Proton mode test experiment

5.2.1 Energy calibration

For the analysis of both proton and neutron mode data, the scintillator detector pulse heights (PH) have to be converted into energy. This calibration is done using protons from H(n,p) reactions in one of the CH_2 foils in the multitarget box.

In the CsI cases, two calibration points are identified for each detector: a pedestal channel due to events detected in other CsIs, and thus associated with zero energy; and a H(n,p) proton peak. A centroid channel is found by fitting a Gaussian to the proton peak, and the deposited energy represented by that channel is obtained by calculating the energy loss of protons between the target and the CsI in question.

Assuming a linear correspondence between PH and energy gives a simple relation between these quantities. However, due to detector geometry and local variations in the light output of a CsI crystal, the PH depends on the proton hit position. If not compensated for, this effect will contribute with up to half the intrinsic energy resolution in the CsIs. Therefore, a polynomial describing the PH as a function of the vertical hit position is employed instead of a constant value in the PH–energy relation.

The plastic scintillator detectors are calibrated using events where protons hit a narrow, central section of the scintillator, i.e. where the distance is approximately the same to both PM tubes, and where it can be assumed that both of these detect half of the energy deposited. Each PM tube is calibrated separately. The energy represented by the peak channel in a PH spectrum is obtained by calculating the preceding losses, as in the CsI case. A pedestal channel gives a second calibration point for each PM tube, and a linear correspondence is assumed. Finally, the total energy detected by a plastic scintillator is the sum of the energies in the two PM tubes.

The total energy of a particle emitted in the target is obtained by adding the energies from the ΔE and E detectors, as well as the energy loss that the particle undergoes in materials where it is not detected, such as detector wrapping, drift chamber foils and air. The latter contributions are calculated.

5.2.2 Particle identification

A $\Delta E - E$ technique is used to separate protons and deuterons originating in the target. Fig. 6 shows a typical $\Delta E - E$ scatter plot from 96 MeV neutron-induced charged-particle production reactions in carbon and CH_2 in the multitarget box, detected at 7°. Here, ΔE is the sum of the detected energy losses in the two trigger detectors (T1 and T2). The separation between protons and deuterons is good enough to make the assignment of particle ID a straight-forward procedure. Two-dimensional contours can be applied to the scatter plot for both particle types, facilitating the analysis of a specific reaction.

5.2.3 Low-energy neutron rejection

In order to reject low-energy neutrons, the neutron TOF can be constructed. A TDC registers the time difference between the MASTER signal and the cyclotron RF. The measured TOF is thus the sum of the flight times for the neutron and the charged particle. Since the energy of the charged particle is measured, and the particle mass is known by selecting protons or deuterons, its flight time over the known target-to-detector distance can be calculated. Subtraction of the charged-particle flight time from the total, measured TOF then yields the neutron TOF.
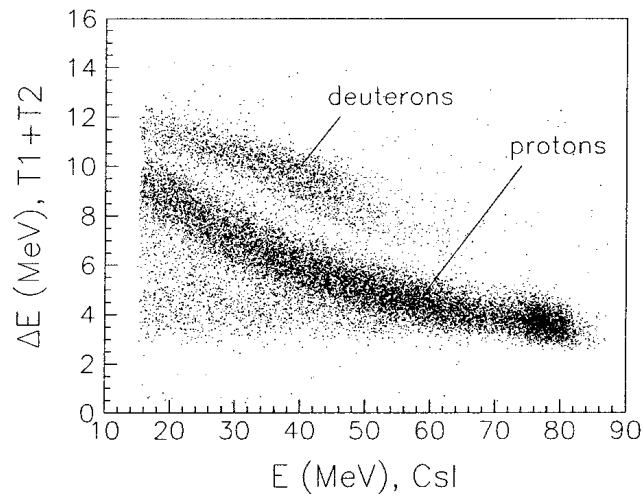
18

Figure 6: Two-dimensional scatter plot of the sum of the energies detected in the trigger scintillators versus the energy in a CsI detector at 7°. The data are obtained accepting protons from both carbon and CH_2 planes in the multitarget.
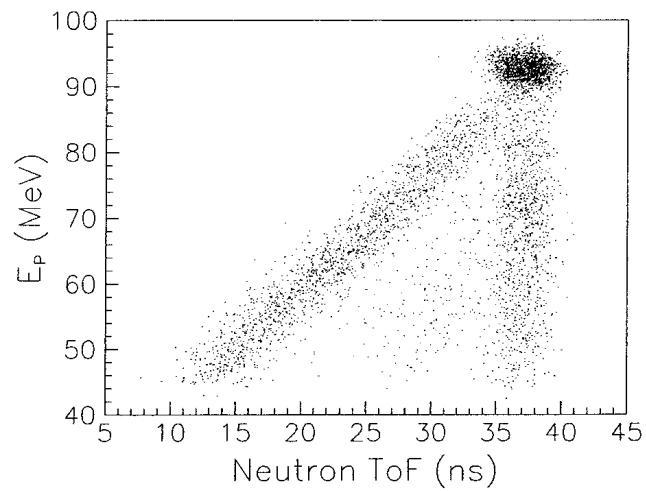

Figure 7: Proton energy versus neutron time-of-flight for (n,p) events, obtained using a CH_2 target. Neutrons corresponding to the full-energy peak appear as a vertical band to the right.

Fig. 7 is a scatter plot of proton energy versus neutron TOF, recorded using a CH_2 target. It illustrates the fact that the full energy neutron peak is accompanied by

19

a low-energy tail, generating the diagonal band. By making a cut around the full-energy events in the vertical band in the neutron TOF spectrum, the low-energy tail can be reduced. This tail is dominated by protons from H(n,p) reactions, while protons induced by full-energy neutrons, but having energies less than 85 MeV, come from reactions in carbon.

5.2.4 Energy resolution

By normalizing $^{12}C(n,p)$ spectra with respect to the carbon content in CH_2 and the integrated neutron flux, carbon spectra can be subtracted from those of CH_2, giving pure np scattering spectra as illustrated in fig. 8. A TOF rejection of low-energy neutrons has been applied. Furthermore, a gate on proton hit positions on the CsI front area has been employed to ensure that the protons are stopped in the E detector, i.e. particles too close to a detector edge are rejected. The hit positions are calculated using drift chamber data.

The resolution of the np scattering peak varies due to the differences in intrinsic resolution in the CsI detectors, but an average value of 3.7 MeV (FWHM) has been found. Apart from the CsI detectors, the main contributions to the resolution come from the neutron beam, the plastic scintillators and straggling in non-detector
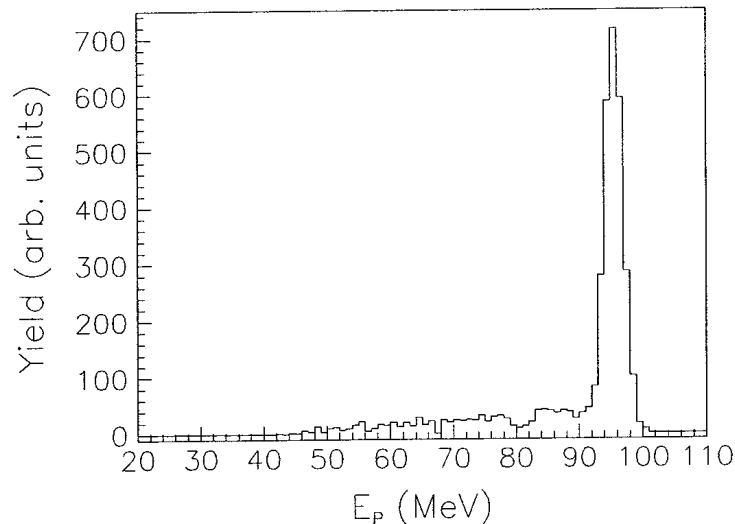

Figure 8: Proton energy spectrum for (n,p) reactions in hydrogen, induced by 96 MeV neutrons, in the angular range 6–7°. The spectrum has been obtained by subtracting a $^{12}C(n,p)$ spectrum from a proton spectrum coming from CH_2, after normalization.

materials. These are estimated to be 1.2, 1.7 and 0.7 MeV (FWHM), respectively; implying an average intrinsic CsI resolution of 3.0 MeV.

A ^{12}C(n,p) spectrum has been obtained by gating on the carbon planes in the multitarget box. In fig. 9, SCANDAL data are compared with data collected on the same reaction with the LISA spectrometer [31]. For this purpose, LISA data have been folded with a Gaussian representing the resolution in SCANDAL, and data from the SCANDAL measurement have been normalized to the LISA cross section scale. It is obvious that SCANDAL reproduces the data. A low energy cut has been made at 60 MeV, as no low-energy corrections, e. g. for lost particles, are made. The errors are statistical.
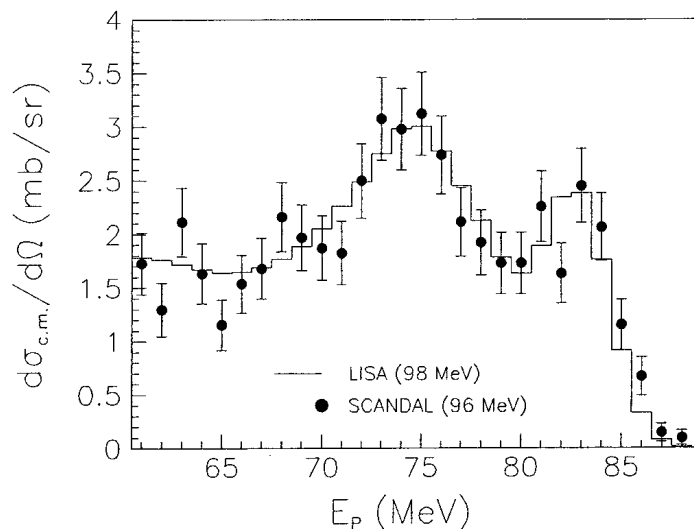

Figure 9: Comparison of SCANDAL and LISA proton energy spectra, from (n,p) reactions in carbon. LISA data have been folded with the SCANDAL resolution, while SCANDAL data have been normalized to the cross section scale of the LISA measurement.

5.3   Neutron mode test experiment

In neutron mode, charged particles contaminating the beam are rejected by the empty multitarget box, while charged particles produced in the scattering target are rejected by the veto detector.

Particle identification is used to separate protons from deuterons, both originating in neutron-induced reactions in the converter. Furthermore, in order to accept protons due to conversion via H(n,p) reactions, and reject those coming from carbon, a maximum opening angle criterion is applied (see section 4).

21

5.3.1 SCANDAL response function

Fig. 10 shows excitation energy spectra for ^{12}C(n,n) at 96 MeV and 9° scattering angle. A maximum opening angle of 10° has been employed for the (n,p) conversion. The large peak at $E_X = 0$ MeV is due to elastic scattering, and the excited states at 9.6 MeV, and possibly at 4.4 MeV, are small but visible.

A response function for the SCANDAL setup has been constructed. The upper plot of fig. 10 shows different components of this function. A Gaussian has been fitted to the H(n,p) peak in the converter, reflecting elastic scattering from the ground state in ^{12}C. Knowing the relative cross section of ^{12}C(n,p) reactions in the converter with respect to that of (n,p) reactions in hydrogen, a ^{12}C(n,p) spectrum

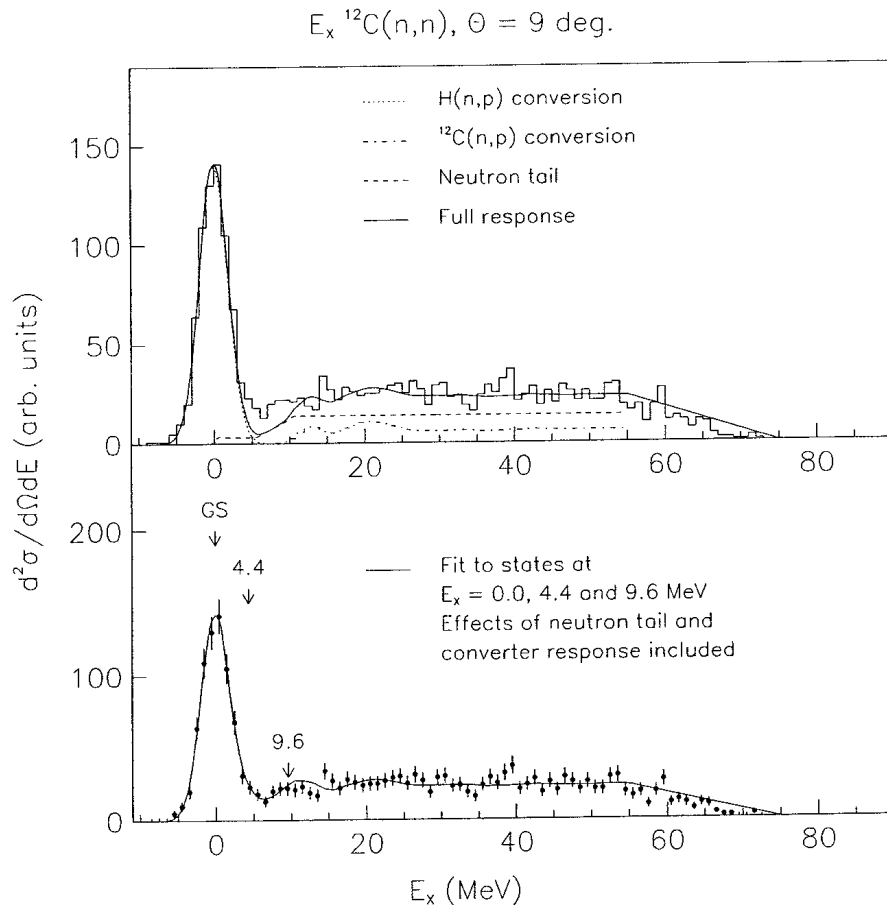Figure 10: Excitation energy spectra for ^{12}C(n,n) at 9°. See the text for details on the response function and its contributions.

has been added. Also, a low-energy neutron tail has been included by knowing the ^{7}Li(p,n) cross section, again with respect to that of H(n,p) in the converter.

At an excitation energy of 75 MeV, the energy of the scattered neutron is 20 MeV, giving an energy of 0–10 MeV for the protons reaching the CsI detector. Protons with these energies are rejected in the analysis; thus there are no events in the E_X spectrum above 75 MeV. For $E_X = 55$ MeV, the resulting proton energies are high enough for all events to be recorded. Thus, a straight line describing the cut-off at high excitation energies has been employed between $E_X = 55$ and 75 MeV.

Adding the contributions from the hydrogen peak, the ^{12}C(n,p) and the low-energy neutron backgrounds, as well as the cut-off at high E_X, gives the full response function shown in the upper plot.

In the lower plot of fig. 10, Gaussians have been fitted to the excited states at 4.4 and 9.6 MeV, in addition to the ground state fit. Contributions from ^{12}C(n,p) reactions in the converter and from the low-energy neutron tail, relative to these states, have been included in the response function.

It is concluded that the full spectrum can be explained in terms of the effects described here, and that no unexpected contributions are seen.

The energy resolution is 3.7 MeV (FWHM), as shown in section 4.

5.3.2   Detection efficiency

The detection efficiency of the SCANDAL setup consists of the probability for a H(n,p) reaction to take place in the converter, i.e. the conversion efficiency, and the efficiency of detecting the proton.

The probability for a conversion in hydrogen is obtained by integrating the cross section for the H(n,p) reaction over the solid angle given by the maximum opening angle criterion. As was mentioned in section 4, for a converter thickness of 1 cm and a maximum opening angle of 15°, the conversion efficiency is estimated to be $5 \cdot 10^{-4}$.

The detection efficiency has contributions from the efficiencies in each drift chamber plane (four per SCANDAL arm), the efficiency of selecting the correct wire when there are double-hit events in the drift chambers, the CsI response (see below), and reaction losses of neutrons in the target. The contributions are measured or estimated to be 0.75 (from an average of 0.93 per plane, as discussed in section 4), 0.93, 0.92, and 0.93, respectively. This makes a total proton detection efficiency of 0.60.

5.4 CsI response measurement

There is a finite probability that a proton stopping in CsI undergoes a nuclear reaction before coming to rest. Since the light yield is smaller for other ions than protons, this results in loss of light, which manifests itself as a tail in the response function.

This effect has been studied experimentally using H(n,p) data at small angles. By applying gates on energy loss in the trigger scintillators and on incident neutron energy (via time of flight), data sets with a limited range of proton energies incident on the CsI detectors were defined. The response, i. e. the pulse height distribution, for the same data in the CsI crystals display a full-energy peak and a tail.

This behaviour has been modeled by assuming that all nuclear reactions result in total light loss. Thereby, the experimentally well-known total reaction cross section can be used for an estimation of this effect. In general, good agreement between the data and this simple model has been found, as can be seen in fig. 11. Hence, the line in the figure is not a fit to the measured data.
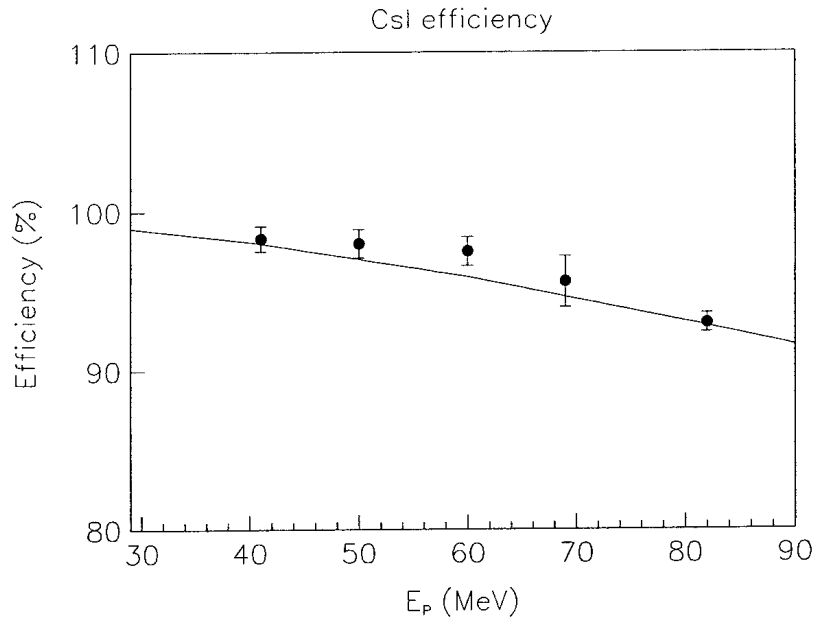

Figure 11: The experimentally determined energy dependence of the CsI full-energy peak efficiency. The line is due to a model based on the reaction cross section. See the text for details.

5.5 Normalization

Normalization of neutron-induced cross sections is a notorious problem because of the difficulties in monitoring the absolute intensity of neutron beams. Precisions better than 10 % have very rarely been achieved. Therefore, most data have been measured relative to another cross section assumed to be known. Most often, the neutron-proton scattering cross section has been used as the primary standard.

Recent experimental investigations [35, 36, 37, 38] have indicated that the np scattering cross section above 50 MeV might have larger uncertainties than previously estimated. It seems now that the cross section can be uncertain by as much as 10–15 % in the energy range of 100 MeV and up [45].

A recent high-precision measurement of np scattering at 96 MeV in the 74–180 degree range claims an absolute uncertainty of 1.9 % [38], but this is outside our angular range. This is where the planned H(n,n) measurement comes in. By making a relative measurement of the angular distribution of H(n,n) from (close to) zero degrees and out to angles overlapping with the existing data, a normalization to the total cross section can be made with a very small uncertainty (about 1 %) [46].

The reason for this high precision is that the total cross section has been possible to determine with a very high precision (1 %), because knowledge of the absolute beam intensity is not required. Instead, it can be inferred from intensity ratio measurements in attenuation experiments. Furthermore, in the case of hydrogen, integration of the elastic scattering cross section accounts for more than 99 % of the total cross section, with very small corrections for capture and bremsstrahlung processes.

For practical experimental reasons, we plan to measure this in a CH_2-vs-C difference measurement. By this technique, we can normalize the C(n,n) cross section to the H(n,n) cross section. This is very useful, because thereby we can establish the much larger C(n,n) cross section as a secondary standard, allowing all other nuclei to be measured relative to C(n,n).

A second normalization method will be provided by comparisons with the total elastic cross section. This cross section has been derived from the difference of the total cross section and the total inelastic cross section. Both these quantities have been measured in attenuation experiments, and are therefore known to high precision, i.e. 1–2 %. (See for example ref. [47]). By covering 0–70 degrees, far more than 99 % of the contribution to the total elastic cross section will be accounted for, providing a second normalization technique. This method works the best with light nuclei, and is therefore well suited for e.g. C(n,n), but is not as reliable for ^{208}Pb(n,n). Hence, this is another reason to establish C(n,n) as a secondary standard. A detailed account of these issues is underway [48].

6 Experimental programme

Given the time and cost to carry out elastic scattering experiments, the main focus must be on developing theoretical models rather than systematically measuring all nuclei. The obvious nuclei to study are then the magic or semi-magic nuclei, i.e. ^{12}C, ^{16}O, ^{40}Ca, ^{90}Zr and ^{208}Pb. Here it is fortunate that lead and zirconium are also important materials in future transmutation facilities, and carbon, oxygen and calcium are all of direct medical and dosimetric relevance, so the gain is twofold. Besides the elements above, H(n,n) will be studied for normalization purposes. Important materials for transmutation cores, like iron, chromium, bismuth, thorium and uranium might be investigated in a second phase.

Studies of (n,xp) reactions on nuclei of interest for transmutation applications are carried out using SCANDAL in proton mode [49]. Data on ^{208}Pb and ^{56}Fe have been acquired, and experiments on ^{238}U are planned.

A programme to study (n,xn) reactions is underway [50], i.e. neutron emission spectra over a wide secondary energy range. For this project, a new multi-layer converter is being developed, allowing the conversion from ^{12}C(n,p) to be subtracted.

The large solid angle and versatile operation of SCANDAL allows it to be used also for other applications. Recently, parts of SCANDAL were employed as proton detector in a tagged-neutron measurement of the absolute efficiency in the 20–100 MeV range of liquid neutron detectors [51]. This experiment did not only provide an overall efficiency determination, but the spatial efficiency variation could also be mapped, for the first time at these energies.

7 Summary and conclusions

In this paper, we have presented the new SCANDAL facility (SCAttered Nucleon Detection AssembLy), intended for measurements of elastic neutron scattering in the 50–130 MeV range, but also useful for (n,xp) studies in the same energy range. Such data are relevant for applications in transmutation technologies, spallation neutron sources, fast-neutron cancer therapy, dosimetry, neutron-induced electronics failures as well as in basic physics. The neutron production facility is also described in some detail.

The setup consists of two identical detection systems, each having a veto scintillator for fast charged-particle rejection, a plastic scintillator neutron-to-proton converter, two plastic scintillators for triggering and particle identification, two drift chambers for proton tracking, and an array of CsI detectors for energy determination.

The facility subtends a very large solid angle, making experiments with reasonable count rates possible in the first place. It can be used to acquire data with good energy and angular resolutions, very small background, and very good particle

identification. In addition, the timing properties allow suppression of events due to the low-energy neutron tail. When employed for proton detection, simultaneous studies of up to seven targets can be accomplished by means of a segmented target device.

The performance of the facility is illustrated with data from experiments on neutron and proton emission from carbon and CH_2 targets at 96 MeV incident neutron energy.

Acknowledgements

References

[1] Proceedings of the 3rd International Conference on Accelerator Driven Transmutation Technologies (ADTTA99), Prague, Czech Republic, June 7-11, 1999. www.fjfi.cvut.cz/con_adtt99/.

[2] A. Wambersie, P. Pihet, H.G. Menzel, Radiat. Prot. Dosim. **31** (1990) 421.

[3] M. Tubiana, J. Dutreix, A. Wambersie, Introduction to Radiobiology (Taylor & Francis, 1990).

[4] J.F. Ziegler, IBM J. Res. Develop. **40** (1996) 19.

[5] H.H.K. Tang, IBM J. Res. Develop. **40** (1996) 91.

[6] D. O'Sullivan, private communication. EU Cosmic Radiation and Dosimetry Group.

[7] Proceedings of Workshop on Critical Issues in the Determination of the Pion-Nucleon Coupling Constant, ed. J. Blomgren, Physica Scripta T87 (2000).

[8] R.W. Finlay, W.P. Abfalterer, G. Fink, E. Montei, T. Adami, P.W. Lisowski, G.L. Morgan, R.C. Haight, Phys. Rev. C **47** (1993) 237.

[9] J. Rapaport and E. Sugarbaker, Annu. Rev. Nucl. Part. Sci. **44** (1994) 109.

[10] W.P. Alford and B.M. Spicer, Advances in Nuclear Physics **24** (1998) 1.

[11] E.L. Hjort, F.P. Brady, J.L. Romero, J.R. Drummond, D.S. Sorenson, J.H. Osborne, B. McEachern, L.F. Hansen, Phys. Rev. C **50** (1994) 275.

[12] J. Rapaport, private communication. J. Osborne, thesis, unpublished.

[13] R.W. Finlay, private communication. *Proposal to the NSF for the support of CHICANE/SPECTROMETER SYSTEM FOR THE IUCF COOLER RING*, (1992).

[14] H. Condé, S. Hultqvist, N. Olsson, T. Rönnqvist, R. Zorro, J. Blomgren, G. Tibell, A. Håkansson, O. Jonsson, A. Lindholm, L. Nilsson, P.-U. Renberg, A. Brockstedt, P. Ekström, M. Österlund, F.P. Brady, Z. Szeflinski, Nucl. Instr. Meth. **A292** (1990) 121.

[15] P.W. Lisowski, C.D. Bowman, G.J. Russell, S.A. Wender, Nucl. Sci. Eng. **106** (1990) 208.

[16] W. Hürster, Th. Fischer, G. Hammel, K. Kern, M. Kleinschmidt, L. Lehmann, H. Schmitt, L. Schmitt, D.M. Sheppard, Phys. Lett. **B90** (1980) 367.

[17] E. Radermacher, private communication. C. Rubbia, S. Andriamonje, D. Bouvet-Bensimon, S. Buono, R. Cappi, P. Cennini, C. Gelès, I. Goulas, Y. Kadi, P. Pavlopoulos, J.P. Revol, A. Tzima, V. Vlachoudis, CERN internal report CERN/LHC/98-02.

[18] J.A. Jungerman and F.P. Brady, Nucl. Instr. Meth. **89** (1970) 167.

[19] S.S. Hanna, C.J. Martoff, D. Pocanić, K. Wang, R.C. Byrd, C.C. Foster, I.J. van Heerden, Nucl. Instr. Meth. **A401** (1997) 345.

[20] R. Helmer, Can. J. Phys. **65** (1987) 588.

[21] W.R. McMurray, D.G. Aschman, K. Bharuth-Ram, R.W. Fearick, Nucl. Instr. Meth. **A329** (1993) 217.

[22] M. Baba, Y. Nauchi, T. Iwasaki, T. Kiyosumi, M. Yoshioka, S. Matsuyama, N. Hirakawa, T. Nakamura, Su. Tanaka, S. Meigo, H. Nakashima, Sh. Tanaka, N. Nakao, Nucl. Instr. Meth. **A428** (1999) 454.

[23] H. Schuhmacher, H.J. Brede, V. Dangendorf, M. Kuhfuss, J.P. Meulders, W.D. Newhauser, R. Nolte, Nucl. Instr. Meth. **A421** (1999) 284.

[24] N. Nakao, Y. Uwamino, T. Nakamura, T. Shibata, N. Nakanishi, M. Takada, E. Kim, T. Kurosawa, Nucl. Instr. Meth. **A420** (1999) 218.

[25] T. Peterson, Impact on the πNN Coupling Constant of the IUCF Measurement with a Tagged Neutron Beam, in Proceedings of Workshop on Critical Issues in the Determination of the Pion-Nucleon Coupling Constant, Physica Scripta T87 (2000) 22 [7].

[26] A.N. Smirnov, V.P. Eismont, A.V. Prokofiev, Rad. Meas. **25** (1995) 151.

[27] L. Tommasino, N. Klein, P. Solomon, J. Appl. Phys. **46**, No. 4 (1975) 1484.

[28] R.C. Byrd and W.C. Sailor, Nucl. Instr. Meth. **A264** (1989) 494.

[29] S. Dangtip, J. Blomgren, N. Olsson, H. Condé, K. Elmgren, J. Rahm, A. Ringbom, G. Tibell, O. Jonsson, L. Nilsson, P.-U. Renberg, S.Y. van der Werf, Nucl. Phys. **A677** (2000) 3.

[30] A. Ringbom, G. Tibell, J. Blomgren, H. Condé, K. Elmgren, N. Olsson, J. Rahm, T. Rönnqvist, O. Jonsson, L. Nilsson, P.-U. Renberg, Chr. Bargholtz, K. Fransson, K. Lindh, P.-E. Tegnér, P. Thörngren-Engblom, S.Y. van der Werf, Nucl. Phys. **A679** (2000) 231.

[31] N. Olsson, H. Condé, E. Ramström, T. Rönnqvist, R. Zorro, J. Blomgren, A. Håkansson, G. Tibell, O. Jonsson, L. Nilsson, P.-U. Renberg, A. Brockstedt, P. Ekström, M. Österlund, S.Y. van der Werf, D.J. Millener, G. Szeflinska, Z. Szeflinski, Nucl. Phys. **A559** (1993) 368.

[32] T. Rönnqvist, H. Condé, N. Olsson, E. Ramström, R. Zorro, J. Blomgren, A. Håkansson, A. Ringbom, G. Tibell, O. Jonsson, L. Nilsson, P.-U. Renberg, S.Y. van der Werf, W. Unkelbach, F.P. Brady, Nucl. Phys. **A563** (1993) 225.

[33] H. Condé, N. Olsson, E. Ramström, T. Rönnqvist, R. Zorro, J. Blomgren, A. Håkansson, G. Tibell, O. Jonsson, L. Nilsson, P.-U. Renberg, M. Österlund, W. Unkelbach, J. Wambach, S.Y. van der Werf, J. Ullmann, S.A. Wender, Nucl. Phys. **A545** (1992) 785.

[34] A. Ringbom, A. Håkansson, G. Tibell, R. Zorro, J. Blomgren, H. Condé, N. Olsson, J. Rahm, E. Ramström, T. Rönnqvist, O. Jonsson, L. Nilsson, P.-U. Renberg, S.Y. van der Werf, H. Lenske, Nucl. Phys. **A617** (1997) 316.

[35] T. Rönnqvist, H. Condé, N. Olsson, R. Zorro, J. Blomgren, G. Tibell, O. Jonsson, L. Nilsson, P.-U. Renberg, S.Y. van der Werf, Phys. Rev. **C45** (1992) R496.

[36] T.E.O. Ericson, B. Loiseau, J. Nilsson, N. Olsson, J. Blomgren, H. Condé, K. Elmgren, O. Jonsson, L. Nilsson, P.-U. Renberg, A. Ringbom, T. Rönnqvist, G. Tibell, R. Zorro, Phys. Rev. Lett. **75** (1995) 1046.

[37] J. Rahm, J. Blomgren, H. Condé, S. Dangtip, K. Elmgren, N. Olsson, T. Rönnqvist, R. Zorro, A. Ringbom, G. Tibell, O. Jonsson, L. Nilsson, P.-U. Renberg, T.E.O. Ericson, B. Loiseau, Phys. Rev. **C57** (1998) 1077.

[38] J. Rahm, J. Blomgren, H. Condé, K. Elmgren, N. Olsson, T. Rönnqvist, R. Zorro, A. Ringbom, G. Tibell, O. Jonsson, L. Nilsson, P.-U. Renberg, T.E.O. Ericson, B. Loiseau, np scattering measurements at 96 MeV, (in manuscript).

[39] S. Dangtip, A. Ataç, B. Bergenwall, J. Blomgren, K. Elmgren, C. Johansson, J. Klug, N. Olsson, G. Alm Carlsson, J. Söderberg, O. Jonsson, L. Nilsson, P.-U. Renberg, P. Nadel-Turonski, C. Le Brun, F.R. Lecolley, J.F. Lecolley, C. Varignon, Ph. Eudes, F. Haddad, M. Kerveno, T. Kirchner, C. Lebrun, Nucl. Instr. Meth. **A452** (2000) 484.

[40] V.P. Eismont, A.V. Prokofiev, A.N. Smirnov, K. Elmgren, J. Blomgren, H. Condé, J. Nilsson, N. Olsson, T. Rönnqvist, E. Tranéus, Phys. Rev. **C53** (1996) 2911.

[41] K. Johansson, P. Dyreklev, B. Granbom, N. Olsson, J. Blomgren, P.-U. Renberg, IEEE transactions on Nuclear Science I **45** (1998) 2519.

[42] K. Johansson, M. Ohlsson, N. Olsson, J. Blomgren, P.-U. Renberg, IEEE transactions on Nuclear Science I **46** (1999) 1427.

[43] B. Höistad, E. Nilsson, J. Thun, S. Dahlgren, S. Isaksson, G.S. Adams, H. Ikegami, Nucl. Instr. Meth. **A295** (1990) 172.

[44] T. Sundqvist and J. Nyberg, TSL Progress Report 1996-1997, p. 21.

[45] J. Blomgren, N. Olsson, J. Rahm, How Strong is the Strong Interaction? – The πNN Coupling Constant and the Shape and Normalization of np Scattering Cross Sections, in Proceedings of Workshop on Critical Issues in the Determination of the Pion-Nucleon Coupling Constant, Physica Scripta T87 (2000) 33.

[46] C. Johansson, *et al.*, to be published.

[47] J. DeJuren and N. Knable, Phys. Rev. **77** (1950) 606.

[48] J. Klug, *et al.*, to be published.

[49] J.F. Lecolley, *et al.*, TSL experiment FA118.

[50] J.F. Lecolley, *et al.*, TSL experiment FA131.

[51] J. Thun, J. Källne, C. Varignon, J. Blomgren, F. Borne, K. Elmgren, O. Jonsson, J.F. Lecolley, X. Ledoux, F. Lefebvres, N. Olsson, Y. Patin, P.-U. Renberg, The response of a liquid scintillator detector to neutrons of energies between 21 and 100 MeV, to be published.

Appendix VIII

Minnesanteckningar från möte med
OECD/NEA Nuclear Science Committee (NSC)
Paris, 2001-06-11—13

T. Lefvert och N. Olsson, 2001-06-27

Detta dokument utgör en kort och sammanfattande rapport över de viktigaste besluten
och rapporteringarna till rubricerade möte. Svenska delegater till NEA/NSC är T.
Lefvert och N. Olsson. T. Lefvert är dessutom NSC:s ordförande för närvarande.
Ytterligare information eller kopior av underliggande dokument kan fås från någon av
dessa.

Dagordningen för mötet framgår av bil. 1, medan mötesdeltagarna återfinns i bil. 2.

1. NEA:s Generaldirektör, L. Echávarri, hälsade välkommen och informerade
   om att
   - NEA:s nyligen framtagna rapport om " Nuclear Energy in a Sustainable
     Development Perspective" blivit mycket väl mottagen av OECD. Med
     detta menade han att kärnenergi åter hamnat på dagordningen. Bland länder
     som ligger långt framme nämndes Japan, Frankrike och Finland.
   - MoU-förhandlingarna mellan IAEA och NEA pågår fortfarande. Bl a
     Ryssland, Kina och Indien vill öppna NEA mer för medlemsländer i IAEA.
   - NEA:s styrkommitté beslutat att budget för NEA:s aktiviteter framöver ska
     ges för två år i taget. På detta vis kan en bättre stabilitet erhållas.
   - NEA har en uppgift att hjälpa medlemsländernas regeringar när det gäller
     att överbrygga gapet mellan kärnenergi och samhället i övrigt, i syfte att
     åstadkomma ett globalt synsätt på kärnenergin.
   - Vidare kommer NEA att arbeta med frågor rörande bibehållande av
     kärnenergins infrastruktur, i synnerhet när det gäller rekrytering av yngre
     personer. Detta ska ses i perspektivet att man nu diskuterar att en reaktor
     kan ha en teknisk livslängd av 60 år.
   - Slutligen nämnde Echávarri att NEA tagit initiativ till en workshop,
     tillsammans med IAEA, för att enas om hur alla kostnader för olika
     energikällor ska beräknas.
   NEA:s nye "Deputy Director" för "Science and Development", T. Dujardin,
   presenterade sig, liksom också de nya ledamöterna från Portugal, Sverige,
   Schweitz och EU.

2. Godkändes.

3. NEA/SEN/NSC(2000)3 godkändes.

4. Lägesrapporter för kommitténs projekt, NEA/SEN/NSC(2001)2 och muntliga
   presentationer:
   4.1   NSC-finansierade workshops och möten.
          - En workshop om "Nuclear Production of Hydrogen" hölls i
            oktober 2000. IAEA har gjort en liknande studie. Som ett resultat
            fanns ett förslag att tillsätta en expertgrupp för detta område
            (NEA/NSC/DOC(2001)11). Kommittén ansåg att ytterligare

1

studier av nämnda rapporter behövdes, liksom en konsultation med NDC (NEA Nuclear Development Committee). Ärendet bordlades därför till arbetsutskottets möte i december.

4.2   Kommittéaktiviteter.

- A. Nouri rapporterade från "Working Party on Nuclear Criticality Safety" (WPNCS), som leds av Y. Nomura från JAERI (NEA/SEN/NSC/WPNCS(2001)1). Vid sitt senaste möte i September 2000 gick WPNCS igenom rapporterna från de olika expertgrupperna: Burnup Credit, Source Convergence Analyses, Int. Criticality Safety Benchmark Evaluation Project, Experimental Needs och Minimum Critical Values. Flera NSC-finansierade konferenser och workshops har hållits inom området, och detta kommer att ske också framöver.

- C. Nordborg rapporterade från "Working Party on Int. Nuclear Data Evaluation Cooperation" (WPEC), NEA/SEN/NSC/WPEC (2000)2 och NEA/SEN/NSC/WPEC(2001)2. Gruppen koordinerar datautvecklingen i de olika evalueringsgrupperna, såsom ENDF (USA), JEFF (väsentligen EU), JENDL (Japan), BROND (Ryssland), CENDL (Kina) och FENDL. Dessutom deltar KAERI (Korea) som observatörer. Vidare försöker man stimulera de experimentella ansträngningarna genom att tillsätta expertgrupper för att lösa specifika problem, på kort såväl som på lång sikt. Det föreslogs att nästa internationella konferens i serien "Nuclear Data for Science and Technology" skulle hållas i Santa Fe, USA, vilket gdkändes av NSC. Vidare godkände NSC att en Workshop om kärnmodeller hålls i Paris 2002.

- K. Hesketh rapporterade från "Working Party on Physics of Plutonium Fuel and Innovative Fuel Cycles" (WPPR), NEA/SEN/ NSC/WPPR(2000)2 och NEA/SEN/NSC/WPPR(2001)2. Gruppen har under det senaste året haft två möten, där man fokuserat på: BWR MOX benchmark, High Temperature Reactor (HTR) Pu physics benchmark och Advanced Reactors with Innovative Fuels (ARWIF). Vidare har man diskuterat gränsdragningen mot den nystartade WPPT (se nedan).

- P. D'Hondt rapporterade från "Expert Group on Reactor-based Plutonium Disposition" (TFRPD), NEA/NSC/DOC(2000)23 och NEA/NSC/DOC(2001)3.

- B-C. Na, NEA, rapporterade från "Working Party on Partitioning and Transmutation" (WPPT). Frågan restes om detta arbete var en duplikation av motsvarande verksamhet vid IAEA, men det konstaterades att IAEA mest fokuserar på icke-spridnings-aspekter. NSC godkände det föreliggande mandatet för WPPT, i vilket man tagit hänsyn till gränslinjerna mot WPPR och mellan NDC och NSC.

- T. Lefvert redogjorde för problemen i "Expert Group on Radiation Damage under Irradiation", som inte haft någon aktivitet under året. Området ansågs viktigt, men verksamheten lider av den dåliga kontakten med NSC. Lefvert lämnade ett förslag på en något förändrad inriktning, genom att till gruppen knyta några Uppsala-

2

forskare. NSC beslutade dock vänta med detta till nästa år, då den gamla gruppens mandat ändå löper ut.

- W. Wiesenack rapporterade från "Expert Group on Basic Phenomena in Fuel Behaviour". Framförallt arbetar man för att tillsammans med IAEA etablera en databas över "International Fuel Performance Experiments" (IFPE) och problem relaterade till dess användande.
- M. Aragones Beltram rapporterade från "Expert Group on Transients Benchmarks and Codes. Bl a har ett slutdokument publicerats om "Forsmark 1 & 2 BWR Stability Benchmark", NEA/NSC/ DOC(99)9 och NEA/NSC/DOC(2001)2. Vidare har resultaten från fas 1 av "PWR Main Steam-Line Break Benchmark publicerats, NEA/NSC/DOC(2000)21, liksom från "BWR Turbine Trip Benchmark", NEA/NSC/DOC(2000)22 och NEA/NSC/DOC (2001)1. Det föreslogs också att nya expertgrupper skulle tillsättas om "Benchmark for VVER-1000" och för "Uncertainties", den sistnämnda först nästa år. Detta stöddes av NSC.
- E. Sartori rapporterade från "Expert Group on Radiation Shielding and Transport". Arbete har här bedrivits inom "Shielding Aspects of Accelerators, Targets and Irradiation Facilities" (SATIF), NEA/ NSC/DOC(2000)19, och "Radiation Shielding Experiments Database" (SINBAD). Vidare har Kobayashis Benchmark för 3D strålningstransport publicerats under år 2000.

4.3   NSC-finansierade workshops och möten 2001-2002. Följande möten kommer att hållas:
- "High Temperature Engineering", Paris, Frankrike, 10-12 oktober 2001.
- ARWIF'01 ("Advanced Reactors with Innovative Fuels"), Chester, Storbritannien, 22-24 oktober 2001.
- "Reliability of High Power Accelerators", Santa Fe, USA, maj 2002.
- "Reactor Noise" (SMORN), Göteborg, Sverige, 27-31 maj 2002.

5. Diskussion om "R&D Needs in Nuclear Science". Det föreslogs att en Exper Group skulle tillsättas, uppgift att se över det framtida behovet av forskning och försöksanläggningar. Frågan hänsköts till NSC:s arbetsutskott i december, för senare, förnyad diskussion i NSC. De aspekter som togs upp var.
- Bevarande av integrala data. Ett förslag till åtgärder förelåg från J. Gado, Ungern, med en indelning i olika nivåer. Det framfördes att lägsta nivån, dvs att få in data i databaser, är det mest angelägna, men även benchmarking för att kontrollera att alla nödvändiga data finns med måste göras. NSC var positivt till Gados förslag, och uppmuntrade en fortsättning längs dess linjer. De resurser som frivilligt ställts till förfogande från Japan och Korea togs tacksamt emot, samtidigt som det ansågs viktigt med lokalt stöd för att få samman alla data. Sådant lokalt stöd utlovades från Frankrike och Belgien.
- Relaterade NEA-aktiviteter i CSNI och NDC. Det rapporterades om CSNI:s "Code Validation Matrix", som har en web-baserad plattform, med data på CD-rom. Vidare informerades om den omfattande verksamhet som bedrivs inom Nuclear Safety Division, och om de ansträngningar som görs

inom NDC för att få till stånd en internationell forskarskola inom kärn-
teknikområdet.
- Aktiviteter i medlemsländerna. Utförliga presentationer gavs av verksam-
  heterna i Frankrike, USA och Japan. Speciellt kan nämnas det amerikanska
  "Generation IV"-initiativet.
- Framtida NSC-program om R&D needs. En grupp av NSC medlemmar,
  bestående av P. D'Hondt (Nederländerna), R. Chawla (Schweitz), E.
  Menapace (Italien) och A. Zaetta (Frankrike), utsågs att förbereda ett
  förslag till Working Party eller Expert Group. Förslaget ska vara klart till
  arbetsutskottsmötet i december, så att verksamheten kan starta tidigt nästa
  år.

6. P. D'Hondt, ordförande i Executive Group (EG), rapporterade från mötet
   2001-06-11. EG har till uppgift att monitorera verksamheten vid NEA Nuclear
   Data Bank. NSC godkände programförslag och budget för år 2002. Budgeten
   är gjord på samma nivå som för innevarande år.

7. Ett förslag från sekretariatet till att förbättra kommunikationen mellan NSC
   och dess WP- och EG-aktiviteter diskuterades (NEA/NSC/DEC(2001)5).
   Följande punkter fanns i förslaget:
   - Gå igenom situationen i varje WP och EG vid varje NSC möte, speciellt
     med avseende på "deliverables" och tidtabell.
   - Strikt följa varaktigheten för varje grupp, och bara bevilja förlängning efter
     förnyad evaluering.
   - Undvika att förlänga problemorienterade aktiviteter, utan istället försöka få
     stöd för att starta nya aktiviteter.
   - Försäkra sig om att tillräckliga resurser står till förfogande, både i
     medlemsländerna och vid NEA:s sekretariat, innan en ny aktivitet startas.
   I diskussionen föreslogs dessutom att för varje WP eller EG ska en "liaising
   member" från NSC utses, som kan tillse att kontakter med och rapportering till
   NSC fungerar på ett effektivt sätt. Några sådana medlemmar utsågs vid mötet.
   Det föreslogs vidare att varje aktivitet regelbundet ska rapportera till NSC
   genom en standardiserad blankett på max en sida. Förslag till fler liaising
   members kommer att behandlas av arbetsutskottet.

8. Rapporter från andra NEA divisioner och internationella organisationer.
   Rapporter gavs från NEA Nuclear Development Division and Nuclear Safety
   Division. Vidare gavs rapporter från IAEA:s Division of Nuclear Power och
   Nuclear Data Section, liksom från EU och IRMM i Geel, Belgien. Viss
   documentation för dessa presentationer delades ut.

9. K. Suyama från NEA Data Bank presenterade ingående den nya strukturen på
   NEA:s website. Där kan aktuell information hittas om NEA:s organisation,
   aktuella möten, konferenser och publikationer.

10. Förslag till ämne för fördjupad diskussion på nästa NSC möte diskuterades. Bl
    a föreslogs "High-Priority Request List" (hur man kan undvika "self-
    refereeing), kvantkemi (för att förstå aktiniders egenskaper), hög utbränning
    av bränsle och transienter i reaktorer. Förslagen kommer att behandlas av
    arbetsutskottet.

11. Nästa NSC-möte beslutades äga rum 3-5 juni 2002 i Paris.

12. T. Lefvert, Sverige, omvaldes till ordförande för NSC fram till nästa möte. P. D'Hondt, Nederländerna, A. Zaetta, Frankrike, T. Osugi, Japan, och N. Haberman, USA, omvaldes till vice-ordförande. De nämnda delegaterna utgör också arbetsutskott för NSC.

13. Övriga frågor.
   - Slovenien har begärt att få observatörsstatus i NSC, trots att man inte är medlem av OECD. Frågan ställdes om Slovenien kan anses vara (i) en relevant partner, och (ii) kan ge ett ömsesidigt utbyte. Båda dessa frågor besvarades positivt, varför NSC gärna ser Slovenien som observatör.
   - Det nämndes att Slovakien också är på väg in, eftersom Slovakien nu är medlem av OECD.
   - De "fem stora", dvs Ryssland, Kina, Indien, Brasilien och Indonesien, har också uttryckt intresse av ökade kontakter med OECD, och då också med NEA.

14. Mötet avslutades.